Demagnetisatie- en excentriciteitsdetectie
in permanentemagneetbekrachtigde synchrone machines met axiale flux

Demagnetization and Eccentricity Detection
in Axial Flux Permanent Magnet Synchronous Machines

Jan De Bisschop

Promotoren: prof. dr. ir. P. Sergeant, prof. dr. ir. L. Dupré
Proefschrift ingediend tot het behalen van de graad van
Doctor in de ingenieurswetenschappen: werktuigkunde-elektrotechniek

UNIVERSITEIT
GENT

Vakgroep Elektrische Energie, Metalen, Mechanische Constructies en Systemen
Voorzitter: prof. dr. ir. L. Dupré
Faculteit Ingenieurswetenschappen en Architectuur
Academiejaar 2018 - 2019

ISBN 978-94-6355-246-2
NUR 959
Wettelijk depot: D/2019/10.500/54

Demagnetization and Eccentricity Detection in Axial Flux Permanent Magnet Synchronous Machines

Jan De Bisschop

Dissertation submitted to obtain the academic degree of
Doctor of Electromechanical Engineering

Supervisors:
Prof. dr. ir. Peter Sergeant
Prof. dr. ir. Luc Dupré
Electrical Energy Laboratory (EELAB)
Department of Electrical Energy, Metals, Mechanical Constructions and Systems (EEMMeCS)
Faculty of Engineering and Architecture
Ghent University
Tech Lane Ghent Science Park 131
B-9052 Zwijnaarde, Belgium

Members of the examining board:

Prof. dr. ir. Filip De Turck (chairman)	INTEC, Ghent University
Dr. ir. Hendrik Vansompel (secretary)	EEMMeCS, Ghent University
Prof. dr. ir. Luc Dupré (supervisor)	EEMMeCS, Ghent University
Prof. dr. ir. Peter Sergeant (supervisor)	EEMMeCS, Ghent University
Prof. dr. ing. Jos Knockaert	EEMMeCS, Ghent University
Dr. ir. Henk Polinder	Delft University of Technology
Dr. ir. Ahmed Abdallh	Flanders Make
Prof. dr. Tanja Van Hecke	INTEC, Ghent University

FACULTY OF ENGINEERING AND ARCHITECTURE

GHENT UNIVERSITY

Preface

Electrical motors have become the backbone of the industry, consuming approximately 70% of the industrial electricity consumption. The emphasis on energy efficiency and reliability has only increased throughout the years. Due to the large share in this energy consumption, slight improvements in efficiency have a great effect. This has triggered a race to design highly efficient machines. Especially the axial flux permanent magnet synchronous machines have the literature's interest because of their high efficiency, high power density and high torque density.

Reliability, on the other hand, is important as unexpected downtime of a production process can be very costly. Added to this, the periodic maintenance to prevent this downtime can become costly as well, especially if it is done too frequently or the machine is not easy to access (e.g. offshore wind turbines). The increased desire for reliability has led to many studies about the progression of the faults within the machine and how they led to premature failures. Beside that, there is a need to actually measure the condition of the machine and it's components. This has led to the field of condition monitoring: by means of sensory data of the machine, the internal health of the machine is predicted and the time-to-failure is estimated. This allows for a predictive maintenance program.

It was clear that there is a need for an analytical model that can give insight of the effects of demagnetization and eccentricity defects in the axial flux permanent magnet synchronous machines. Furthermore, a detection technique is needed to detect the presence of these defects in the machine by only measuring the stator voltages and currents. Therefore, prof. dr. ir. Peter Sergeant and prof. dr. ir. Luc Dupré decided to start up research at the Ghent University in 2012 to study these defects and build both the analytical model and the detection technique.

PhDs are known for being challenging, and the last six years have been difficult. But through all those obstacles I always had the support of my promotor prof. dr. ir. Peter Sergeant. Peter, I would like to thank you for never giving up on me, even at my toughest moments. You were always there to guide me with your expertise and helped me reach the finish line. I know my troubles gave you plenty of stress, but you always pushed through and kept motivating me. This, I really appreciate.

I also would like to thank my second promotor prof. dr. ir. Luc Dupré for giving me the opportunity to do this PhD and for periodically giving me your insights and

constructive feedback. I would also like to express my gratitude for always finding time in your busy schedule for helping me when I'm stuck and when I'm trying to meet a deadline.

Besides my two promotors, I would like to express my appreciation to dr. ir. Ahmed Abdallh, dr. ir. Hendrik Vansompel, ir. Lynn Verkroost, Tony Boone and Vincent Gevaert for the good collaboration and their technical contributions to this PhD. I couldn't have done this without you.

Further, I would like to thank all of my colleagues at both Campus Schoonmeersen and at campus Tech Lane Ghent Science Park in Zwijnaarde for the pleasant work environment. Many of you have become friends throughout the years, especially Bart, Paul, Nele and Sam. I also would like to thank Gianni, Maarten, David, Dries, Robbe, Johnny and Seppe for the many interesting, in-depth and enlightening conversations during our coffee and lunch breaks. Those conversations were often the highlights of my days.

I would also like to show my gratitude to Dimitri. Through the years, we had plenty of interesting conversations that helped my grow as a person. You were always available at difficult times and your psychological advise and support, especially this last year, helped me overcome my obstacles. Thank you for looking out for me.

And of course I would like to thank Ahmed Hemeida, Mohamed N. Ibrahim, Jasper Vandermeulen, and in this regard Ahmed Abdallh again, for all the wonderful moments we had. For those I had the pleasure of traveling together with, I remember the trips to Germany and China we did pretty well. I also appreciate the good conversations we had about our spiritual and cultural views. I especially want to thank Mohamed and Jasper for the many funny moments we had together.

I want to give a special thank you to my parents for the opportunities they gave me in both my path toward as during this PhD. You were always there to help and support me, which allowed me to become the person I am today. I also appreciate the care and emotional support you gave me during all the rough times in the last years. I know it has been turbulent, to say the least.

Furthermore, I would like to thank my brother Pieter, and my dear friends Sibron and Ine for listening to me whining about all the troubles I had. And also for giving me constructive support and psychological insight when I needed it the most, sometimes even when I didn't want to hear it. You spared no time nor effort to help me get through this. Thank you very much for everything. I love you guys, you're the best!

Charlotte, we've only met near the end of my PhD, but you had a great contribution to my well-being in this challenging time. I really appreciate all the support, help and care you provided. All those times we worked together really helped me to keep moving forward. I would like to thank you for all the interesting conversations we had and all the times you listened to my frustrations. You really pulled me through this last months.

I'm very grateful to all my friend in both my home region as in Ghent for the

social support and all the good times we had together that kept me going. More specifically, thank you Nick, Elias, Jorg, Daphne, Trixie, Bram, Merlijn, Tuur, Laurens, Jelien, Peter, Elisa and Joachim. And an extra thank you to Joachim for helping with the lay-out of that one annoying table.

My gratitude also goes to Mégane and Wouter for the many pleasant train rides and –on strike days– car rides together throughout the years. I'll definitely miss those.

Lastly, I want to thank Stephan for always believing in me and for encouraging me to dream big.

Jan De Bisschop, Juni 2019

Table of contents

Summary

A study of the International Energy Agency shows that about 50% of the electrical energy globally produced is used by electric rotating machinery. Electrical motors have become the backbone of the industry, consuming approximately 70% of the industrial electricity consumption. The emphasis on energy efficiency and reliability has only increased throughout the years. Due to the large share in this energy consumption, slight improvements in efficiency have a great effect. This has triggered a race to design highly efficient machines. Thanks to the use of rare-earth permanent magnets, synchronous machines with a high power density have been developed. Especially the axial flux permanent magnet synchronous machines have the literature's interest because of their high efficiency, high power density and high torque density. Their simple structure allows them to be designed for both low-speed-high-torque applications like direct-drive wind turbines and (in-wheel) electric vehicles, and for high-speed-low-torque applications like pump or fan applications, and very compact motors for electrical vehicles used with a speed reduction.

Although these machines are quite robust and reliable, unexpected premature failures still happen. Literature shows that on average 9% of all electric machines fail prematurely. The problem is that unexpected fallout of a machine can heavily disrupt a company's production processes. The actual cost of the machine itself is only a fraction of the total economic cost resulting from this. Therefore, reliability is important as unexpected downtime of a production process can be very costly. In addition, the periodic maintenance to prevent this downtime can become costly as well, especially if it is done too frequently or the machine is not easy to access (e.g. offshore wind turbines). Due to the rise of sustainable energy applications, and the development of the fourth industrial revolution, reliability has become increasingly significant. The increased desire for reliability has yielded many studies about the progression of the faults within the machine and how they led to premature failures. In maintenance, the insights learned from these studies were used to adapt the maintenance program to increase robustness. The learned knowledge also contributed to more fault tolerant machine designs.

Nonetheless, there is a need to actually measure the condition of the machine and components. This has led to the field of condition monitoring by means of sensory data of the machine. The internal health of the machine is predicted and

the time-to-failure is estimated. This allows for a predictive maintenance program. Most common analyzes use vibration data, stator currents, stator voltages, temperature data and flux measurements. These systems continuously monitor the retrieved data and report to the machine's operator if anything alarming occurs.

The goal of this dissertation is firstly to build an analytical model that is fast and can give insight in the effects of demagnetization and eccentricity defects in double-rotor single-stator axial flux permanent magnet synchronous machines. The studied type of machine is commonly indicated by the term "YASA" (Yokeless and Segmented Armature). A second goal is to use this model to detect the presence of these defects in the machine by only measuring the stator voltages and currents.

The dissertation starts by explaining the motivation, objectives and outline of this dissertation. Then, it explains the working principles of the machine. After explaining the possible topologies, the YASA machine type, which is studied in this PhD, is explained more thoroughly. This machine is praised because of its high power density, high efficiency and modular stator design. Afterwards, the maintenance strategies are explained and based on this it is explained why condition monitoring is so important. Thereafter, the condition monitoring techniques studied in literature are shown, starting with a broad overview and afterwards an overview of detection techniques for demagnetization and eccentricity specifically. From this study, it was clear that there was a lack of an analytical model of the YASA axial flux permanent magnet synchronous machine with two air gaps. This model must be able to account for both demagnetization and eccentricity defects. The literature also shows the need for flexible defect detection techniques that can handle both demagnetization and eccentricity defects.

Chapter 3 starts with a comparison of three typical modeling techniques for analytical models. After selecting the most suitable technique, the model of the machine is mathematically constructed and all technical details are explained thoroughly. Afterwards, the model is validated with numeric simulations performed on different topologies, for healthy and several defected situations.

Chapter 4 proposes a technique for solving an inverse problem that uses the analytical model of the previous chapter to detect demagnetization and eccentricity defects. This technique uses the terminal voltages and phase currents of the stator, and is from now on called the "terminal voltage technique". As calculation time is an important element, the chapter explains the theoretical elements for analyzing what harmonics are more sensitive to the occurrence of demagnetization defects. The last part of this chapter provides an alternative technique using sensing coils. This technique gives a solution for an inherent limitation of the terminal voltage technique: the inability of determining in which rotor the defect has occurred. For this sensing coil technique, the analytical model of Chapter 3 and the inverse problem method are modified to work with sensing coils for demagnetization detection.

The next chapter applies the techniques explained in the previous chapter for demagnetization defects. The detection technique with the terminal voltage analytical model is tested for a wide variety of demagnetization defects, noise levels and

machine topologies with different numbers of rotor poles and stator slots. In the second part of this chapter, the technique for analyzing the sensitivity of harmonics has been used on demagnetization defects. Lastly, the sensing coil technique is applied on demagnetization defects, and the results are compared with the terminal voltage technique.

In Chapter 6, the terminal voltage technique is applied on eccentricity defects. First, eccentricity only is tested for a wide variety of defects, noise levels and topologies. Secondly, combined demagnetization and eccentricity defects are studied to determine if the algorithm can accurately differentiate between the two types of defects.

Finally, the last chapter introduces the prototype of the studied machine constructed at the Electrical Energy Laboratory of Ghent University and describes the test setup in which this prototype is placed in the laboratory. The setup allows measurements of the phase and sensing coils voltages. This data is then used to validate the terminal voltage and the sensing coil analytical model with experimental data, proving the correctness of the models. Lastly, an example is given of the advantages of having this detection technique and the analytical model by using it in a deadbeat control.

After this, a general conclusion of this work is given.

Samenvatting

Een studie van de International Energy Agency toont aan dat ongeveer 50% van de globale wereldwijde energieproductie geconsumeerd wordt door elektrische rotationele machines. Elektrische motoren zijn de ruggengraat van de industrie geworden. Samen consumeren ze ongeveer 70% van de elektriciteitsconsumptie van de industrie. Door de jaren heen is de nadruk op energie-efficiëntie en betrouwbaarheid enkel maar toegenomen. Door het grote aandeel van deze machines in de energieconsumptie, hebben kleine verbeteringen op de efficiëntie een groot effect. Dit heeft een race veroorzaakt om machines met hoge efficiënte te ontwerpen. Dankzij het gebruik van zeldzame-aarde permanente magneten zijn er synchrone machines met een hoge vermogensdichtheid kunnen worden ontwikkeld. Hierbij hebben vooral de permantemagneetbekrachtigde synchrone machines met axiale flux de interesse van de literatuur verkregen door hun hoge efficiëntie, hoge vermogensdichtheid en hun hoge koppeldichtheid. Hun simpele structuur laat toe om deze machines te ontwerpen voor zowel lage-snelheid-hoog-koppel toepassingen zoals direct-drive wind turbines en (in-wheel) elektrische voertuigen, als voor hoge-snelheid-laag-koppel zoals bij pompen, ventilatoren, en zeer compacte motoren voor elektrische voertuigen die via een snelheidsreductie worden gebruikt.

Ook al zijn deze machines vrij robust en betrouwbaar, onverwachtse uitval gebeurt nog steeds. De literatuur toont dat gemiddeld 9% van de elektrische machines vroegtijdig faalt. Het probleem is dat de onverwachtse uitval van de machine de normale productie in een bedrijf hevig kan verstoren. De eigenlijke kost van de machine zelf is maar een fractie van de totale economische kost die hieruit voortvloeit. Bijgevolg is betrouwbaarheid belangrijk omdat onverwachtse uitval van het productieproces heel kostelijk kan zijn. Daarbovenop kan de kostprijs van het periodieke onderhoud om uitval te voorkomen ook oplopen, vooral als het te frequent gebeurt of indien de machine niet makkelijk toegankelijk is (bijvoorbeeld bij offshore wind turbines). Door de opmars van duurzame energietoepassingen, en het ontwikkelen van de vierde industriële revolutie, is betrouwbaarheid steeds meer significant geworden. De toegenomen vereiste qua betrouwbaarheid heeft tot vele studies geleid over de propagatie van de fouten in de machine en hoe deze leiden tot vroegtijdig falen. In onderhoud werden de verkregen inzichten van deze studies gebruikt om het onderhoudsprogramma aan te passen met als doel een verhoogde robuustheid te verkrijgen. De verkregen kennis heeft ook bijgedragen tot

een meer fouttolerant machineontwerp.

Niettemin is er een nood om de eigenlijke toestand van de machine en de onderdelen te meten. Dit heeft geleid tot het vakgebied van condition monitoring waarbij door middel van sensor data van de machine de interne gezondheid van de machine voorspeld wordt en de time-to-failure geschat wordt. Dit laat een voorspellend onderhoudsprogramma toe. De meest voorkomende analyses gebruiken vibratiedata, statorstromen, statorspanningen, temperatuurdata en fluxmetingen. Deze systemen monitoren de verkregen data constant en rapporteren bij de machine operator indien het nodig is.

Het doel van dit proefschrift is in de eerste plaats om een analytisch model te bouwen dat snel is en inzicht kan geven in de effecten van demagnetisatie- en excentriciteitsdefecten. De bestudeerde machines zijn permantemagneetbekrachtigde synchrone machines met axiale flux, opgebouwd uit een dubbele rotor en een enkele stator van het jukloos en gesegmenteerde type. Deze machine wordt vaak aangegeven met de term "YASA" (Yokeless and Segmented Armature). Een tweede doel is om dit model te gebruiken om de aanwezigheid van deze defecten in de machine te meten door enkel de statorspanningen en -stromen te gebruiken.

Het proefschrift start met de motivatie, de doelstellingen en het plan van deze dissertatie uit te leggen. Daarna legt het de werkingsprincipes van de machine uit. Nadat de verschillende topologieën besproken zijn, wordt de machine waarop gefocust wordt, dieper uitgewerkt. Deze machine is geprezen voor haar hoge vermogensdichtheid, haar hoge efficiëntie en haar modulair statorontwerp. Daarna worden de verschillende onderhoudsstrategieën beschreven en op basis hiervan is het belang van "condition monitoring" uitgewerkt. Vervolgens worden de condition monitoring technieken in de literatuur bekeken, startende met een breed overzicht om daarna een overzicht te geven van de detectietechnieken specifiek voor demagnetisatie en excentriciteit. Hieruit is duidelijk zichtbaar dat er een gebrek is aan een analytisch model dat de permantemagneetbekrachtigde synchrone machines van het YASA-type beschrijft, rekening houdende met zowel demagnetisatie- als excentriciteitsdefecten.

Hoofdstuk 3 start met een vergelijking tussen drie veel gebruikte modeleringstechnieken voor analytische modellen en kiest hier één uit. Daarna wordt het model van de machine wiskundig opgebouwd en worden alle technische details diepgaand uitgelegd. Vervolgens wordt het model gevalideerd met numerieke simulaties voor verschillende topologieën, voor gezonde toestand en voor verschillende defecte situaties.

Hoofdstuk 4 stelt een techniek voor om inverse problemen op te lossen, die gebruikmaakt van het analytisch model van het vorig hoofdstuk om demagnetisatie- en excentriciteitsdefecten te detecteren. Deze techniek maakt gebruik van klemspanningen in de stator en statorstromen, en wordt verderop "klemspanningstechniek" genoemd. Omdat rekentijd zo belangrijk is, legt het hoofdstuk de theoretische elementen uit om te analyseren welke harmonischen het meest gevoelig zijn voor het voorkomen van demagnetisatiedefecten. Het laatste deel

van het hoofdstuk voorziet een alternatieve techniek die gebruik maakt van zoekspoelen. Deze techniek biedt een oplossing voor een inherente beperking van de klemspanningstechniek: het niet kunnen bepalen in welke rotor een bepaald defect voorkomt. Voor deze zoekspoeltechniek is het analytische model in hoofdstuk 3 en de inverse probleem methode aangepast om met zoekspoelen demagnetisatie te kunnen detecteren.

Het volgende hoofdstuk past de techniek die in het vorige hoofdstuk werd uitgelegd toe op demagnetisatiedefecten. De detectietechniek die gebruik maakt van het analytisch model met klemspanningen is getest voor een grote waaier van demagnetisatiedefecten, ruisniveaus en machinetopologieën met verschillende aantallen rotorpolen en statorgleuven. In het tweede deel van het hoofdstuk is de techniek voor het analyseren van de gevoeligheid van harmonischen gebruikt op demagnetisatiedefecten. Tot slot is de zoekspoeltechniek toegepast op demagnetisatiedefecten en de resultaten zijn vergeleken met de klemspanningstechniek.

In hoofdstuk 6 wordt de klemspanningstechniek toegepast op excentriciteitsdefecten. Eerst wordt enkel excentriciteit getest bij een waaier van defecten, ruis niveaus en topologieën. Daarna worden defecten met demagnetisatie en excentriciteit gecombineerd bestudeerd om te bepalen of het algoritme het onderscheid kan maken tussen de twee defecten.

Ten slotte introduceert het laatste hoofdstuk het prototype van de bestudeerde machine welke verwezenlijkt is in het Elektrische Energie Laboratorium van de Universiteit Gent. Het hoofdstuk beschrijft de testopstelling waarin dit prototype is opgesteld in het laboratorium. De opstelling voorziet de mogelijkheid om de fase- en zoekspoelspanning te meten. Deze data is daarna gebruikt om het analytische model voor klemspanningen en dat van zoekspoelen te valideren met experimentele data, om zo de correctheid van de modellen te bewijzen. Als laatste is een voorbeeld gegeven van het voordeel om deze detectietechniek en dit analytisch model te hebben door het te gebruiken in een deadbeat sturing.

Het geheel wordt afgerond door een algemene conclusie van dit werk te geven.

List of Abbreviations

AFIR	Axial Flux Internal Rotor
AFPMSM	Axial Flux Permanent Magnet Synchronous Machine
AI	Artificial Intelligence
AR	Armature Reaction
ASBC	Amplitude of the Side-Band Components
BLDC	Brushless Direct Current
CM	Condition Monitoring
CRLB	Cramér-Rao Lower Bound
DB	Deadbeat
DE	Dynamic Eccentricity
DSSR	Double-Stator Single-Rotor
EMF	Electro-Motive Force
FEM	Finite Element Method
FFT	Fast Fourier Transform
FSCW	Fractional Slot Concentrated Windings
HV	High-Voltage
IP	Inverse Problem
LF Model	Lateral Force Model
LV	Low-Voltage
MCSA	Motor Current Spectrum Analysis
ME	Mixed Eccentricity
MLE	maximum-likelihood estimation

MLP	Multi-Layered Perceptron
MMF	Magneto-Motive Force
MPU	Minimum Path of the Uncertainty
MSMR	Multi-Stator Multi-Rotor
MTBF	Mean Time Between Failures
MTTF	Mean Time To Failures
MV	Medium-Voltage
MVU	Minimum Variance Unbiased
OF	Objective Function
PM	Permanent Magnet
PWM	Pulse Width Modulation
RCFA	Root Cause Failure Analysis
RMS	Root Mean Squared
SC Model	Schwarz-Christoffel Model
SCADA	Supervisory Control And Data Acquisition
SD Model	Subdomain model
SE	Static Eccentricity
SQP	Sequential Quadratic Programming
SSDR	Single-Stator Double-Rotor
SSSR	Single-Stator Single-Rotor
TDE	Time Delay Embedding
TRR	Trust-Region-Reflective
UMP	Unbalanced Magnetic Pull
YASA	Yokeless And Segmented Armature
ZSVC	Zero Sequence Voltage Component

List of Symbols

A	Magnetic vector potential [Vs/m]
B_{r}	Residual induction of the PMs [T]
B	Magnetic flux density [T]
C_r	The Cramér-Rao Lower Bound [/]
D_{info}	Defect information, which are the parameters describing the eccentricity defect together with the magnetization factors K
E_{Ecc}	The error of the optimization algorithm in the eccentricity parameters [/]
$E_{K,\mathrm{perc}}$	The relative error of the optimization algorithm in the magnetization factors [/]
E_K	The error of the optimization algorithm in the magnetization factors [/]
E_{phase}	Phase back-EMF [V]
E_{sens}	Back-EMF of a sensing coil [V]
E_{tooth}	Back-EMF of stator coil [V]
F_m	Fisher Information Matrix [/]
F	Fisher Information [/]
H	Magnetic field [A/m]
I_d	Direct current [A]
I_k	The current in the slot with number k [A]
I_{phase}	Phase current [A]
J_k	The current density in the slot with number k [A/m^2]
J_{S}	Surface current density [A/m^2]
K	Array of magnetization factors [/]
L'_d	Instantaneous inductance via the direct direction [H]
L_d	Inductance via the direct direction [H]
L_σ	Leakage inductance [H]
L	Linear coefficient of the quadratic programming solver [/]

M	Magnetization waveform of the permanent magnets [A/m]
N_S	Number of stator slots [/]
N_p	Number of pole pairs in the machine [/]
$N_{\mathrm{har,acc}}$	The minimum number of harmonics per phase of the terminal voltages needed to find an accurate solution to the IP [/]
$N_{\mathrm{har,min}}$	The minimum number of harmonics per phase of the terminal voltages needed to find the unknown parameters of the IP [/]
N_{har}	The number of harmonics per phase of the terminal voltages [/]
N_{sens}	Number of turns in a sensing coil [/]
N_{ph}	Number of phases [/]
N_{stator}	Number of turns in the stator coils [/]
P_{cool}	The evacuated power of a cooling system [W]
P	Polynomial [/]
P	The probability of a certain set of data and parameters [/]
Q	Quadratic coefficient of the quadratic programming solver [/]
Q	The flow rate of the cooling liquid in the cooling system [m^3/s]
R_{a}	Armature resistance [Ω]
S_T	Tooth surface [m^2]
S_{PM}	Area of the magnet [m^2]
S	The score of a certain set of data and parameters [/]
T_{in}	The inlet temperature of a cooling circuit [K]
T_{out}	The outlet temperature of a cooling circuit [K]
V_{d}	Direct voltage [V]
V_{q}	Quadrature voltage [V]
V_{term}	Phase terminal voltages of the machine [V]
V	The variance of the likelihood function [/]
X_m	Measurement data [/]
α_{p}	The ratio of magnet to pole pitch in the compared analytical models [/]
α	A constant in the MPU OF fitted to minimize the impact of uncertain parameters [/]
β	General deterministic parameter [/]
$\mathbb{Z}_{\neq 0}$	Set of integer numbers without zero
g_{L}	Left air gap width [m]
g_{R}	Right air gap width [m]

g_Δ	Deviation of the air gap width due to eccentricity [m]
$g_{healthy}$	Air gap width of the left and the right air gap with in healthy state [m]
ρ_{DE}	DE amplitude coefficient [/]
ρ_{SE}	SE amplitude coefficient [/]
θ_{MDE}	Angle of the position of minimum air gap for DE [rad]
θ_{MSE}	Angle of the position of minimum air gap for SE [rad]
H_{AR}	AR magnetic field generated only by the stator currents [A/m]
H_{PM}	No-load magnetic field generated only by the permanent magnets [A/m]
B_{AR}	AR magnetic flux density generated only by the stator currents [T]
B_{PM}	No-load magnetic flux density generated only by the permanent magnets [T]
μ_S	The mean value of the score [/]
μ_0	Absolute permeability of vaccum [H/m]
μ_M	Absolute permeability of the PMs [H/m]
μ_S	Absolute permeability of the stator iron [H/m]
$\mu_{r,M}$	Relative permeability of the PMs [/]
$\mu_{r,S}$	Relative permeability of the stator iron [/]
$\hat{D}_{info}$	Estimated value of the defect information, which are the parameters describing the eccentricity defect together with the magnetization factors K
$\hat{\beta}$	Estimator of the deterministic parameter β [/]
$\hat{K}$	Estimator of the array of magnetisation factors [/]
λ_d	The direct axis flux linkage [Wb]
λ_m	The flux linkage in the stator coil at no-load [Wb]
λ_{sl}	Permeance function describing the stator slot effect [/]
$\mathbb{E}$	The function calculates the expected value of a set of data [/]
$\mathbb{Z}$	Set of integer numbers
$\mathcal{F}_{\mathrm{AR}}$	MMF of the stator coils for the fraction of the flux that crosses the air gap [Aw]
$\mathcal{F}_{\mathrm{PM}}$	Equivalent MMF of the magnets [Aw]
$\mathcal{L}$	The likelihood of a certain set of data and parameters [/]
$\mathcal{R}_{\mathrm{PM}}$	Reluctance of the permanent magnets in axial direction [H^{-1}]

$\mathcal{R}_{\mathrm{g,L}}$	Reluctance of the left air gap in axial direction [H^{-1}]
$\mathcal{R}_{\mathrm{g,R}}$	Reluctance of the right air gap in axial direction [H^{-1}]
μ	Absolute permeability [H/m]
ω_{m}	Mechanical angular rotation velocity [rad/s]
$\overline{\beta}$	The assumed value of the deterministic parameter β [/]
$\overline{K}$	The assumed value of the array of magnetisation factors [/]
ϕ_{PM}	Residual flux of the magnets [Wb]
ϕ	Magnetic scalar potential [A]
ph	Phase number [/]
τ_{m}	Half a base period, equal to half the machine circumference [m]
τ_{p}	The pole pitch in the compared analytical models [m]
θ_m	Angular space variable in the circumference direction [rad]
θ_q	Angle of center of the slot before stator tooth q [rad]
θ_{s}	Mechanical start angle [rad]
υ	The periodicity of the machine, in respect to the number of stator slots and pole pairs [/]
ε_1	Border position of region I in the 5-region model [m]
ε_2	Border position between region I and region II in the 5-region model [m]
ε_3	Border position between region II and region III in the 5-region model [m]
φ_{sens}	Flux through a sensing coil [Wb]
φ_{stator}	Flux through a tooth [Wb]
ζ	This value is 1 or 2 if N_S / υ is odd or even respectively [/]
b	Stator slot width [m]
c_{p}	The heat capacity of the cooling liquid of a cooling system [J/K]
d_{l}	Layer thickness [m]
d_{tooth}	Stack height of the stator teeth [m]
e	Statistical efficiency [/]
f_{sq}	The "defects waveform" constructed by the magnetization factors K [/]
g	Air gap in general, this can either be g_{R} or g_{L} [m]

h_{PM}	PM axial width [m]
h	Stator slot length in axial direction [m]
i_q	The instantaneous quadrature current [A]
i	Polynomial index [/]
j	Imaginary constant [/]
k_w	The winding factor [/]
k	The slot number [/]
l	Layer number [/]
m''	Time harmonic number of the demagnetized no-load field [/]
m'	Space harmonic number of the "defect waveform" [/]
m	Time harmonic number of the no-load field and the stator current field [/]
n_{l}	Number of layers [/]
nl_{ampl}	The amplitude of the noise level [V]
nl	The noise level in percentage [/]
n	Polynomial degree [/]
n	Time harmonic number of the tooth back-EMF, the phase back-EMF, the terminal voltages and the current [/]
p	Time harmonic number of the eccentricity permeance function [/]
q	Tooth number [/]
$r_{\max}$	Radius where eccentricity will lead to collision between the rotor and the stator [m]
r	Radius of the cylindrical 2D calculation plane [m]
s	Magnet number [/]
t	Time variable [s]
$u^{\bullet}$	An array of the mean values of the uncertain parameters of the analytical model [/]
u	Space harmonic number of the stator current field [/]
u	An array of the uncertain parameters of the analytical model [/]
v	Space harmonic number of the slot permeance function [/]
w	Space harmonic number of the eccentricity permeance function [/]
w	An array of the well-known parameters of the analytical model [/]
x	Polynomial indeterminate [/]

x	Unknown variable in the quadratic programming solver [/]
x	Space variable in circumference direction in meters [m]
y	Space variable in the axial direction [m]
$\lambda_{\mathrm{LF}i}$	Permeance function in the LF Model [/]
λ_{ecc}	Permeance function describing the eccentricity effect on the magnetic flux density [/]
λ_{gap}	Permeance function mapping the change in the air gap width due to eccentricity [/]
$\mathcal{R}_{tang}$	Tangential reluctance of the stator [H^{-1}]
DE	Index used to denote dynamic eccentricity
L	Index used to denote the left air gap
R	Index used to denote the right air gap
SE	Index used to denote static eccentricity

Chapter 1

General introduction and outline of the thesis

This first chapter will explain the motivations behind this work. It shows the necessity for solutions in condition monitoring and sets the objectives and scope of this research.

1.1 Motivation

The International Energy Agency published a study which shows that about 50% of the electrical energy globally produced is used by electric rotating machinery [1]. Electrical motors have become the backbone of the industry, consuming approximately 70% of the industrial electricity consumption [1]. Energy efficiency and reliability have gotten an increased emphasis throughout the years. Due to the large share in this energy consumption, slight improvements in efficiency have a great effect. This has triggered a race to design highly efficient machines. Because rare-earth permanent magnets have become more available, synchronous machines with a high power density have been developed. Especially the axial flux permanent magnet synchronous machines have the literature's interest because of their high efficiency, high power density and high torque density. Their simple structure allows them to be designed for both low-speed-high-torque applications like direct-drive wind turbines and (in-wheel) electric vehicles, and for high-speed-low-torque applications like pump or fan applications, and very compact motors for electrical vehicles used with a speed reduction.

These machines are build quite robust and reliable, but yet unexpected premature failures still happen. Literature shows that on average 9% of all electric machines fail prematurely [2]. This unexpected fallout of a machine can heavily disrupt a company's production processes. The actual cost of the machine itself is only a fraction of the total economic cost resulting from this. As unexpected downtime of a production process can be very costly, reliability is important. In

addition, the periodic maintenance to prevent this downtime can become costly as well, especially if it is done too frequently or the machine is not easy to access (e.g. offshore wind turbines). The rise of sustainable energy applications and the development of the fourth industrial revolution have made reliability even more significant. The increased desire for reliability has yielded many studies about the progression of the faults within the machine and how they led to premature failures. The insights learned from these studies were used to adapt the maintenance program to increase robustness and to contributed to more fault tolerant machine designs.

This all makes it clear that there is a need to actually measure the condition of the machine and it's components. For this, the field of condition monitoring was born, meanly by means of sensory data of the machine. The internal health of the machine is predicted and the time-to-failure is estimated, which makes a predictive maintenance program possible. Analyzes use vibration data, stator currents, stator voltages, temperature data and flux measurements are most frequently used. These systems continuously monitor the retrieved data and report to the machine's operator if anything alarming occurs.

Based on the literature, of which a thorough overview is given in Chapter 2, it is clear that there is a need for detection technique to detect the presence of defects in the machine by only measuring the stator voltages and currents. For this, an analytical model is required that can give insight in the machine and the effects of the defects. The machine used in this thesis is the axial flux permanent magnet synchronous machines and the defects this dissertation will study are demagnetization and eccentricity defects, which also explained more thoroughly in Chapter 2.

1.2 Objectives

The objectives of this PhD are the following:

- As the most condition monitoring techniques described above are performed on radial machines with only one air gap, mostly induction machines and Brushless Direct Current (BLDC) machines, there is a lack of a model of Axial Flux Permanent Magnet Synchronous Machines (AFPMSMs), especially for Yokeless And Segmented Armature (YASA) type machines. The modeling that has been done, is always under healthy conditions and mostly with Finite Element Method (FEM) modeling techniques. The literature lacks a model of the chosen machine in defected situations. So the first objective is to build such model capable of simulating the machine with defects. This model needs to be accurate and fast enough for condition monitoring. In the work, this model is an analytical model and is called the forward model.

- This research limits itself to demagnetization of the Permanent Magnets (PMs) and eccentricity of the rotors, because both defects have not been

studied sufficiently in the literature, but do occur quite often. As machine operators show interest to push their machines to the limit, information about the demagnetization of the PMs caused by temperature rises due to machine load is required. As both defects can occur asymmetrically, meaning both rotors will not experience the same identical defect, this needs to be accounted for in the model and detection technique.

- The detection of the demagnetization and eccentricity defect with as little as possible sensors is needed for condition monitoring. For this, the model of the machine is used together with an Inverse Problem (IP) to perform the detection.
- The speed of the detection technique is important as it is intended for online condition monitoring. Analysis of the model and the IP have been performed to optimize the calculation speed and thus to increase the detection speed of the proposed technique.
- Operators generally are not only interested in knowing if a machine is healthy or not, but also want to know what type of defect occurred (i.e. demagnetization, static or dynamic eccentricity), how severe the defect is and where in the machine it occurred. To meet this demand, this has been taken into account throughout the design of the forward model and the IP.

1.3 Outline

In Chapter 2, a brief overview of the AFPMSM and more specifically the topologies leading to the YASA is given. Afterwards the maintenance strategies are explained and based on this it is explained why condition monitoring is so important. Then the condition monitoring techniques are shown, starting with a broad overview and afterwards an overview of detection techniques for demagnetization and eccentricity specifically.

Secondly, in Chapter 3, the model of the machine is examined. A comparison between three typical analytical modeling techniques for of AFPMSMs is done and one technique is chosen for this PhD. The mathematical construction and the chosen techniques are explained in detail. The focus is on modeling the machine 3D using a multislice technique with the purpose of condition monitoring. This means that some assumptions are made based on this that will speed up the model, but makes it inaccurate for e.g. loss calculations. The mathematical solidity of the model is validated with FEM simulations.

In Chapter 4, the forward model described in Chapter 3 is used in an IP to detect demagnetization defects and eccentricity. The elements of this IP, e.g. which solver is chosen, stop conditions, etc. are touched upon, but it should be noted that a deep study of solvers and IPs is outside the scope of this work. Afterwards an analysis of the harmonics on the detection of defects is performed. It is clear that certain

harmonics are more sensitive to the defect occurrence than others, so by selecting the most sensitive harmonics for the simulations, the calculation time is reduced. Lastly, in this chapter, an alternative using sensing coils is described that is able to estimate in which rotor the defect occurred as this is an unavoidable limit of the main proposed technique of this work.

In Chapter 5, the techniques from Chapter 4 are put to the test by applying them to some cases with demagnetization defects. The results of this tests are discussed and conclusions are drawn. In the second part of this chapter, the technique for analyzing the sensitivity has been used on demagnetization defects. Lastly, the sensing coil technique is applied on demagnetization defects, and the results are compared with the terminal voltage technique.

In Chapter 6, the techniques for detecting the demagnetization defect with the terminal voltages is broadened to also detect static and dynamic eccentricity. Here, it is also shown that it is possible to distinguish between demagnetization defects and eccentricity defects.

Finally, Chapter 7 introduces the prototype AFPMSM constructed at the Electrical Energy Laboratory of Ghent University and describes the test setup in the laboratory. The setup allows measurements of the three phase terminal voltages and the sensing coils back-Electro-Motive Force (EMF). This data is then used to validate the terminal voltage and the sensing coil analytical model, and the terminal voltage detection technique with experimental data. Lastly, an example is given of the advantages of having this detection technique and the analytical model by using it in a deadbeat control.

Chapter 8 draws some final conclusions about the techniques of this work and points out the future work that is required for the further development of this technology.

1.4 Scientific publications in International SCI Journals

An overview of journal papers published in peer-reviewed international journals at the time of publication of this thesis:

- J. De Bisschop, A. Abdallh, P. Sergeant, and L. Dupré, "Identification of demagnetization faults in axial flux permanent magnet synchronous machines using an inverse problem coupled with an analytical model," *IEEE Transactions on Magnetics*, vol. 50, no. 11, pp. 14, 2014.

- J. De Bisschop, A. A. Abdallh, P. Sergeant, and L. Dupré, "Analysis and selection of Harmonics sensitive to Demagnetization Faults intended for Condition Monitoring of Double Rotor Axial Flux Permanent Magnet Synchronous Machines," *IET Electric Power Applications*, vol. 12, no. 4, pp. 486493, 2015.

- J. De Bisschop, H. Vansompel, P. Sergeant, and L. Dupré, "Demagnetization Fault Detection in Axial Flux PM Machines by using Sensing Coils and an Analytical Model," *IEEE Transactions on Magnetics*, vol. 53, no. 6, pp. 14, 2017.
- J. De Bisschop, P. Sergeant, A. Hemeida, H. Vansompel, and L. Dupré, "Analytical Model for Combined Study of Magnet Demagnetization and Eccentricity Defects in Axial Flux Permanent Magnet Synchronous Machines," *IEEE Transactions on Magnetics*, vol. 53, no. 9, 2017.
- L. Verkroost, H. Vansompel, P. Sergeant, F. De Belie, and J. De Bisschop, "Active Demagnetization Fault Compensation for Axial Flux Permanent Magnet Synchronous Machines Using an Analytical Inverse Model," *IEEE Transactions on Energy Conversion*, submitted October 2018.

Chapter 2

Introduction to Axial Flux Permanent Magnet Synchronous Machines and Condition Monitoring

This chapter will give an overview of the current state of the technology and show the necessity for the work done in this dissertation. The chapter starts by introducing the machine topology on which the condition monitoring will be performed and explaining the working principles. Secondly, the importance of condition monitoring is explained based on the maintenance strategies. Furthermore, the condition monitoring techniques described in literature are shown: a broad overview of existing techniques to detect several types of defects, and a more specific overview of detection techniques for demagnetization and eccentricity.

2.1 Axial flux permanent magnet synchronous machines

2.1.1 Introduction

The name of synchronous machines refers to the synchronous rotation speed of the rotor and the rotating magnetic field of the stator. In order to achieve this, in contrast to induction machines, the rotor has either PMs or excited windings as source for the rotor magnetic field.

The machine can be divided based on the flux paths: radial, axial and transverse flux machines. The operating principles of radial and axial flux machines only differ in the direction of the rotor magnetic field with respect to the machine's rotation axis, i.e. in the radial and axial direction for radial and axial flux machines respectively. Assuming a sufficiently large radius, the electromagnetic aspects of the axial flux machines are similar to those of the radial machines. Transverse

flux machines use 3D shapes in their stator flux paths, which makes them more complicated [3]. The scope of this work exclusively considers AFPMSM.

In [4], an overview of the recent machine's development in electromagnetic, mechanical and thermal modeling as well as the improved assembling methods is given and it is clear that these AFPMSMs have become a mature technology. The main reasons why AFPMSMs are preferred are [5]:

- By changing the numbers of magnets and the diameter of the machine, AFPMSMs perform well for a large range of rotational speeds. This flexible design makes them useful in a wide range of areas. A machine with a high number of PMs and a larger diameter is perfect for low-speed-high-torque applications like small to medium range direct-drive wind turbines and (in-wheel) electric vehicles [6]. In contrast, a machine with a low number of PMs and a smaller diameter is perfect for high-speed-low-torque like pump, fan, valve control and centrifuge applications [7].

- The compactness of these machines makes them very convenient for built-in applications. Based on [8], axial flux machines can be 45% smaller in material volume than a radial flux machine with similar power and torque specifications, as can be seen in figure 2.1. This in turn increases the power density and the torque density of the machine. This again makes them interesting for electric vehicles because space and mass are restricted in such systems. Furthermore, the torque of axial flux machines scales with the third power of the radius, while in radial flux machines the torque scales with the square of the radius multiplied by the active axial length. So in axial flux machines, high torque can be achieved with a lower radius (smaller machine) compared to radial flux machines. The rotor is relatively larger in axial flux machines compared to radial flux machines with similar dimensions. This inertia can be used as a flywheel.

- By choosing to excite the rotor with PMs instead of excited windings, no power is needed to energize the rotor. This increases the efficiency due to the absents of copper losses in the rotor. This advantage is shared with other types of PM machines.

These advantages make AFPMSMs not only interesting for academic research, but also for industrial applications. Several studies show that AFPMSMs are intensively used in electric vehicle applications [9–12] and wind energy systems [13–18]. This is confirmed by the use or production of this machine by businesses like Axco-motors (Finland), YASA Motors Ltd (UK), Evo-Electric (UK), Magnax (Belgium) and ESSET (Belgium).

The applications are divided into high-speed motor applications and high-torque-low-speed applications [19]. The first group focuses on electric vehicles. The machine can be used as range extenders due to its compact design and short

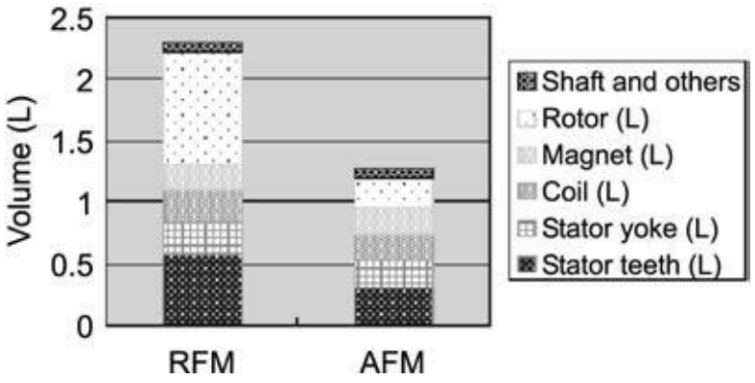

Figure 2.1: Comparison of volume between radial and axial flux machines [8].

axial length. Also, it introduced little losses at no-load spinning. The machine is also used in direct-drive applications like in-wheel setups. The removal of the gear-box increases the efficiency. The machine is as well used in E-axle concepts, where the motor, gears and shafts to the wheels are designed in one optimized component.

The high-torque-low-speed applications mainly focuses on wind power, but can be used in many industrial processes using rotating machines where a high torque is needed at relatively low RPM. Often gearboxes are used in these setups, but by replacing the motor and gearbox with and AFPMSM, improvements in efficiency, weight, size, reliability and costs can be made.

2.1.2 Basic operating principles

The AFPMSM operates by the interaction between two magnetic fields, one produced by the PMs on the rotor and the other by currents in the coils on the stator. This is not very different than the operating principle of its radial counterpart. Figure 2.2 shows the most basic construction of the AFPMSM. The PMs are placed on the rotor, with the adjacent PMs alternately magnetized in the axial direction i.e. perpendicular to the rotor disc surface. The iron part of the rotor disc is called the rotor back-iron, and its function is to close the magnetic flux path at the rotor side of the machine.

The stator is constructed of a disc with teeth upon it. The disc is called the stator back-iron or stator yoke, and it has a similar function as the rotor back-iron i.e. closing the magnetic flux path at the stator side of the machine. Windings are inserted in the spaces between the stator teeth (called the stator slots). These windings are combined to form the stator coils. In practice, the air gap – the space between the rotor and the stator – is kept as small as possible. The reason for this is that air increases the reluctance for the magnetic fields drastically. The limit for

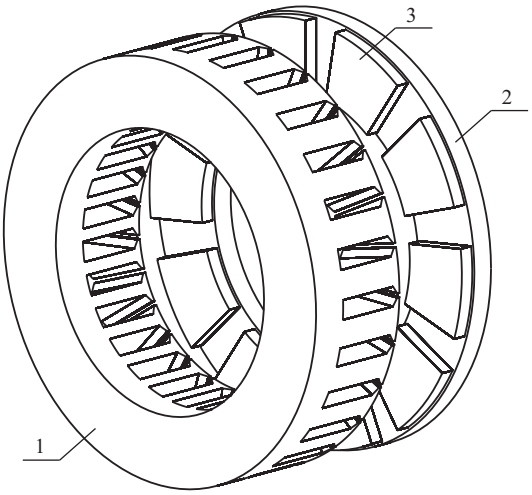

Figure 2.2: Basic AFPMSM constructed of one stator (1) and one rotor (2) with the permanent magnets (3) [20].

the air gap width is based on the mechanical tolerances and the constraints. In an ideal case, the net flux crossing the air gap is zero, which means that the path of the magnetic flux through the stator and the rotor will always be closed.

This machine contains one stator and one rotor. This setup is called the single-sided construction of the AFPMSM. It is simpler than a double-sided construction (see later), but it also has a lower torque. The operating principles are similar to that of its radial flux counterpart:

- In generator mode, the rotor is rotated due to an external force (e.g. a gas turbine, a wind turbine, a combustion engine, etc.). Because of this rotation, the magnetic field of the PMs induces a back-EMF (voltage) in the stator coils and thus also in the terminals of the machine. Here, mechanical power is transferred to electrical power.
- In motor mode, a source introduces a current in the stator coils. This leads to an alternating magnetic field that interacts with the magnetic field of the PMs and forces the rotor to rotate. Here, electrical power is transferred to mechanical power.

From the perspective of one stator coil, one period passes for every two passing magnets. This is also the electrical period. So if the machine has a rotor with e.g. 16 magnets, the magnetic field of the rotor has eight periods, and the stator coil will sense eight electrical periods per revolution. Two adjacent magnets that form one magnetic period are called a pole pair. The example machine thus has eight pole pairs (N_p).

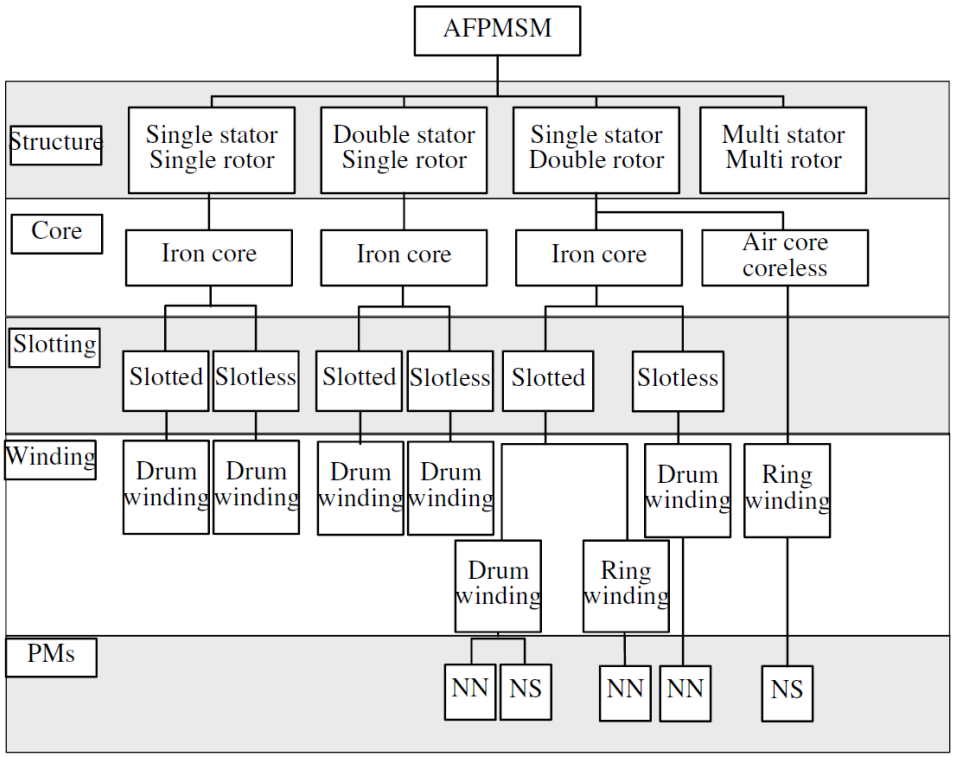

Figure 2.3: AFPMSM topology overview [21, 22].

The rotor iron mainly experiences the flux produced by the magnets. As this is a constant flux, the induced eddy currents are limited and therefore the rotor can be constructed out of solid construction steel. On the other hand, the flux through the stator is time varying, and therefore would induce eddy currents that results in increased losses. To prevent the eddy currents from flowing, the stator is either laminated or constructed in a material with low electric conductivity like e.g. Soft Magnetic Composite material. The magnetic properties of the material are not the only constraints. Due to the high axial attractive forces between the stator and the rotor, the mechanical properties are essential as well. The high axial forces originate from the high magnetic conductive stator and rotor material and the small air gap. The construction and its components like the bearings should be designed for this. Even elastic deformation of the parts could result in a smaller air gap and therefore should be considered in the design process.

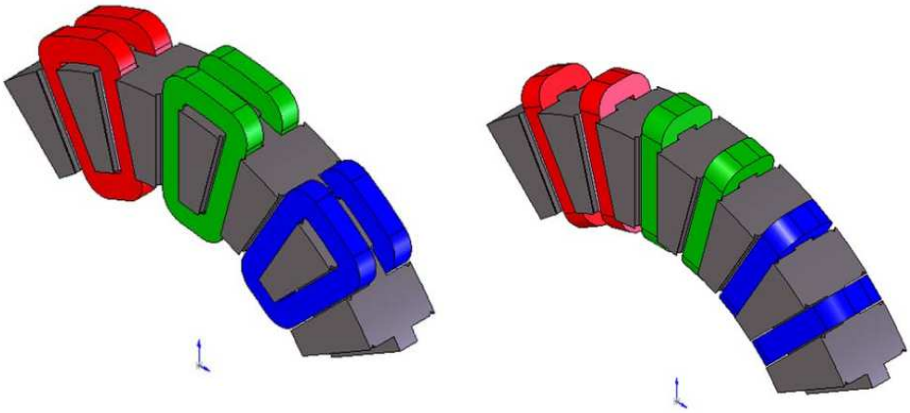

(a) (b)

Figure 2.4: AFPMSM winding types: (a) drum (tooth wound) and (b) ring (core wound). [4, 21]

2.1.3 Topologies of axial flux permanent magnet machines

Many variants of axial flux machines can be found, a.o. induction machine [23] and the switched reluctance versions [24], next to permanent magnet versions. As the latter show higher efficiency and power density, we focus on the permanent magnet version of axial flux machines.

For the permanent magnet synchronous machines with axial flux, many other topologies [25] are found apart from the topology with one rotor and one stator.

Figure 2.3 gives a graphical overview of the most common topologies. They are separated from each other based on the following properties: [4, 21].

- The number of stators and rotors (number of stages)
- The presence or absence of an iron core
- The presence or absence of stator slots
- The winding configuration: drum winding or ring winding. Figure 2.4 (a) and (b) give the details of drum winding and a ring winding respectively.
- The permanent magnet (PM) configuration: surface mounted magnets or interior magnets. In the case of double rotors, the permanent magnets on both rotors can face each other with either the same polarity, or with the opposite polarity. This concepts of different polarities is described in figures 2.6 (c) and (d).

From all the possibilities in the above list, as illustration, four topologies are described in more detail in the following paragraphs: Single-Stator Single-Rotor (SSSR), Single-Stator Double-Rotor (SSDR), Double-Stator Single-Rotor (DSSR), or Multi-Stator Multi-Rotor (MSMR).

Single-Stator Single-Rotor (SSSR)

As described above, the simplest version of an AFPMSM is composed of only a SSSR [26, 27]. This configuration can be seen in figure 2.2.

To summarize, in this topology, the yoke and the teeth form the stator iron core as shown in figure 2.2. The windings are placed in the slots between the teeth. The yoke acts as a return path for the flux density through the stator. It is also a mechanical fixation of the stator within the structure of the machine. The PMs are placed on the rotor and are magnetized in the axial direction.

The PMs and the currents in the windings produce the magnetic flux, which flows axially in the PMs and the teeth and circumferentially in the rotor and the stator yoke.

Due to the unbalanced axial force between the rotor and the stator, the construction may deform in axial direction as a result of the uncompensated axial force [26]. This is the biggest disadvantage of this machine. The dimensioning of the bearing needs to account for the greater axial force.

Double-Stator Single-Rotor (DSSR)

Secondly, DSSR topology, also known as the Axial Flux Internal Rotor [25, 28] is shown in figure 2.5. A 2D representation of the construction showing the magnetic flux path is given in figure 2.6 (b). From this, it can be seen that the flux flows only axially through the rotor. This means that the rotor back-iron is optional for this machine. Both figures show a cored version of the machine, which offers more reliability since it can operate with only one functioning stator [29]. Both stators produce an equal amount of stator losses, but due to the large surface of the stator, cooling them by air is not a problem. Gluing the magnets on the surface of the rotor or burying the magnets inside the rotor has been studied thoroughly [28].

Single-Stator Double-Rotor (SSDR)

In this topology, the stator is positioned between two rotors [30], as can be seen in figure 2.7. This can result in different versions as is shown in figure 2.6 (a), (c) and (d). figures 2.8(a) and 2.8(b) show two types of cored stator windings for this machine represented in 2.6 (c) and (d) respectively, which are called the toroidally wound internal stator (torus) machine [29]. Typically for these machines is the stator between the two rotors, consisting of a yoke with double sided teeth on both axial sides. As shown in figures 2.6 (c) and (d), the arrangement of the magnets influences the flux paths in the machine [31]. The two types can be described as:

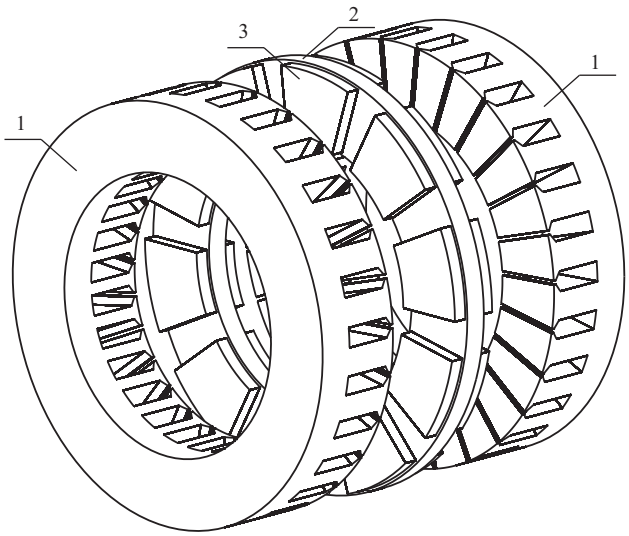

Figure 2.5: Schematic representation of the double stator single rotor AFPMSM topology. Stator (1), rotor (2), permanent magnet (3) [20].

- On the other hand, figure 2.6 (c) shows a configuration where the magnets facing each other have the same polarity. This type of torus machine is called a north-north (NN) torus configuration. The flux crosses the stator teeth axially but closes through the stator yoke circumferentially. Adhering to this, the windings are placed toroidally wound around the stator yoke. This can be seen in figure 2.8(a).

- Figure 2.6 (d) shows that two magnets facing each other on the machine have an opposite polarity ('N' for north pole and 'S' for south pole). This type of torus machine is called a north-south (NS) torus configuration. The flux crosses the stator axially and through the rotor back-irons circumferentially. There is no flux flowing through the stator yoke. Adhering to this, the windings are placed toroidally wound around the stator teeth. This can be seen in figure 2.8(b).

For the NN torus machine, a higher filling factor can also be achieved in this machine [9]. The downside of the NN torus compared to the NS torus is the need for a thicker stator yoke to carry the magnetic flux passing through it. Therefore, iron losses and the mass of the stator core are larger than in the NS configuration.

A differentiation can also be made on the stator core: materials with high permeability as cores, slot-less stator with only a stator yoke and coreless stator [32–34].

If a stator core is used, it is made of a material with high permeability e.g. lam-

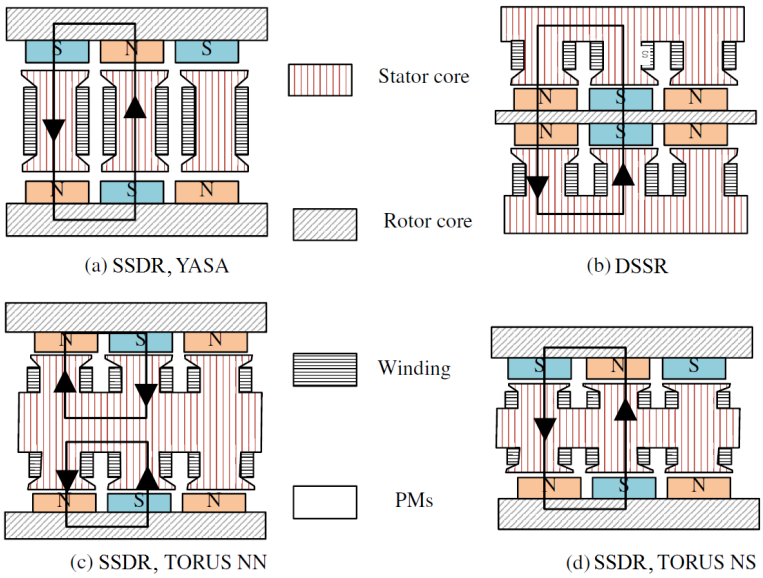

Figure 2.6: Schematic representation of different configurations of the AFPMSM [21].

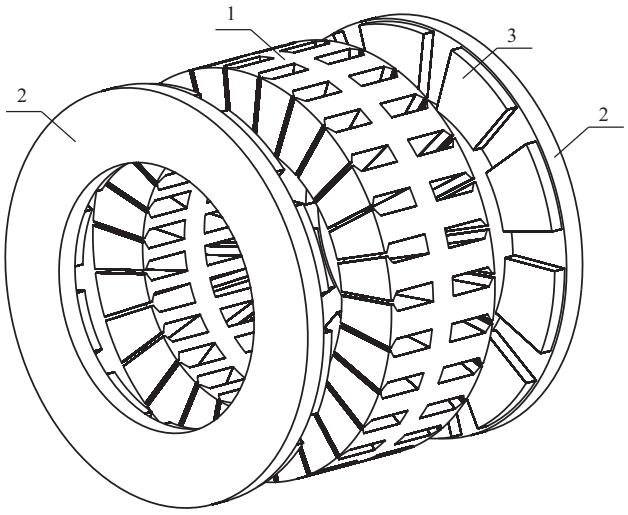

Figure 2.7: Schematic representation of the single stator double rotor AFPMSM topology. Stator (1), rotor (2), permanent magnet (3) [20].

inated silicon steel, soft magnetic composite, or amorphous iron. As the winding is then placed in the stator slots this is called a slotted winding. The main disadvantage of such topology is the rise of cogging torque, which is a ripple in the torque at no-load. This is created by the difference in permeance for different rotor positions

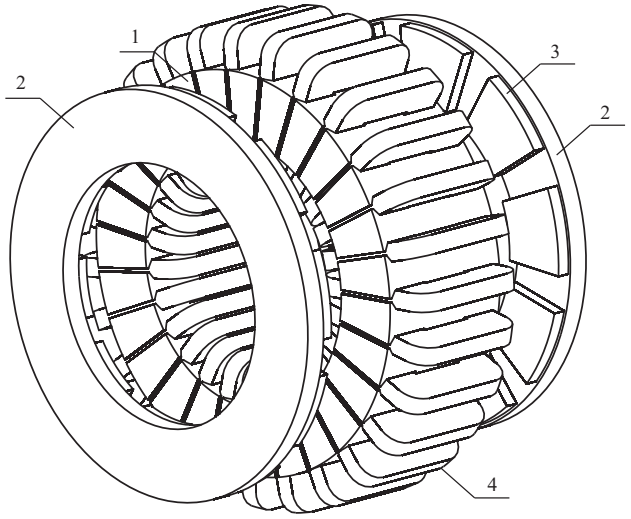

(a)

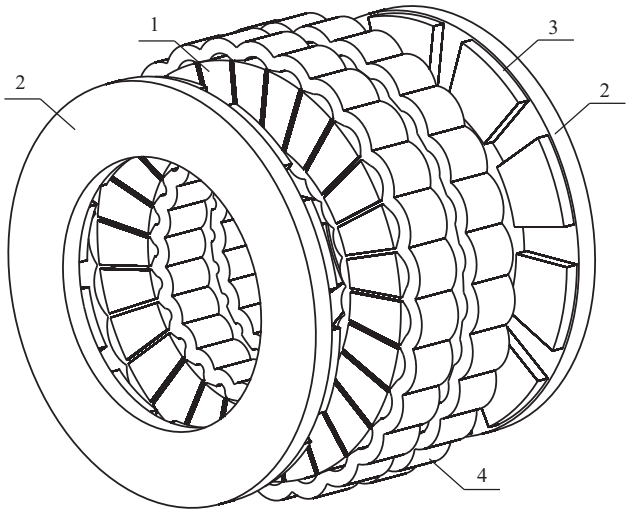

(b)

Figure 2.8: Schematic representation of (a) the NN torus and (b) the NS torus AFPMSM topology. Stator (1), rotor (2), permanent magnet (3), winding (4) [20].

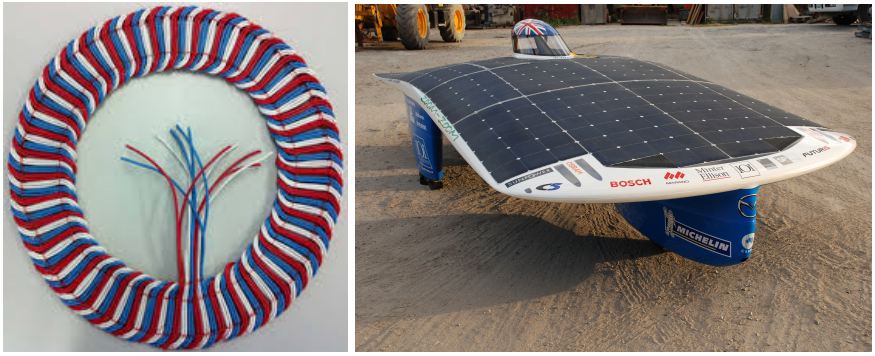

(a) (b)

Figure 2.9: (a) Coreless stator windings for the Marand 2010 DSSR axial flux machine [35] and (b) the Aurora solar car of 2007 World Solar Challenge [36].

due to the stator slots. The magnetic field of the PMs interacts with the stator slot opening near the air gap.

The prevent cogging torque, coreless windings are used in e.g. wind turbine applications. The core can be replaced by air, but in many cases the windings are embedded in an epoxy resin with similar permeability as air. This helps containing the windings in the proper place and improves the mechanical construction compared to air cored windings. Although this has big advantages like the absence of cogging torque, the lower mass of the machine and the absence of core losses, the downside of the high equivalent air gap thickness is significant. The absence of a stator core increases the reluctance of the magnetic flux path. In order to obtain sufficiently high magnetic fluxes in the windings, relatively high permanent magnet volumes are needed. In the production of permanent magnets rare earth materials such as Neodymium, Samarium, Dysprosium are very often used, which are costly compared to silicon steel. To prevent this cost, the reduction of cogging torque in AFPMSMs with slotted windings is studied intensively in scientific research.

Multi-Stator Multi-Rotor (MSMR)

A multistage AFPMSM can be formed from either DSSR or SSDR configurations [37]. The construction consist of N stators and $N + 1$ rotors, which have the same mechanical shaft. There is flexibility in the stator winding connections: they can be connected either in parallel or in series. The main advantage of the multistage configuration it the increased torque and power density without increasing the machine diameter.

For wind energy applications, this allows for a reduced outer diameter of the machine for a similar torque [38, 39]. This then reduces the total structural mass of the construction. A downside to consider is the increased axial length of the machine.

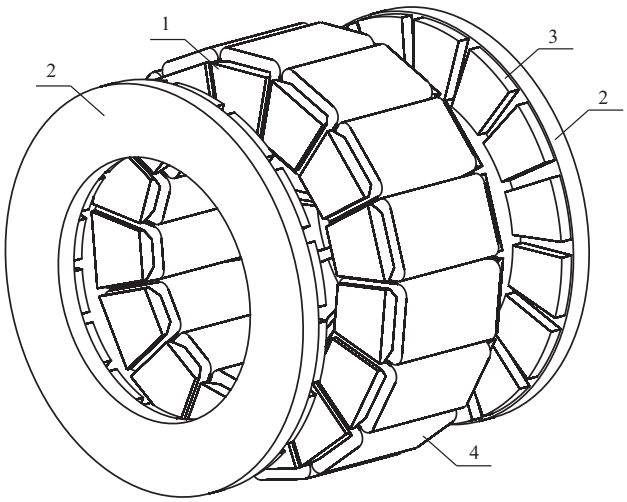

Figure 2.10: The yokeless and segmented armature AFPMSM topology. Stator consisting of multiple stator core elements (1) around which a tooth coil winding (4) is wound, rotor (2), permanent magnet (3) [20].

2.1.4 From the torus to the YASA topology

Within the field of the AFPMSM topology with one stator and two rotors, special attention is drawn towards the slotted torus machines. It is indicated that the NN torus (figure 2.8(a)) and the NS torus (figure 2.8(b)) are the best performing AFPMSM topologies [40]. [9] shows that the efficiency and power density of the NS torus are slightly higher than those of the NN torus.

From this NS torus, the YASA machine topology was derived, which can be seen in figure 2.10. This topology combines the advantages of the reduced stator yoke and a good winding arrangement. This combination of the advantages of both machine topologies was introduced in [9], where the yokeless and segmented armature was derived. This is achieved by implementing the following adjustments to the original NS torus:

- As described above, the magnetic flux path through the stator is purely axially and closes through the rotor yokes. This means there is no magnetic flux flowing through the stator yoke. As this yoke is not used, it can be removed, hereby removing weight of the machine. By removing the magnetic and mechanical link between the different stator teeth, the stator exists of individually segmented armature elements [20].

- By opting for a Fractional Slot Concentrated Windings (FSCW), each windings can be wound around a single tooth. This changes the stator teeth pitch

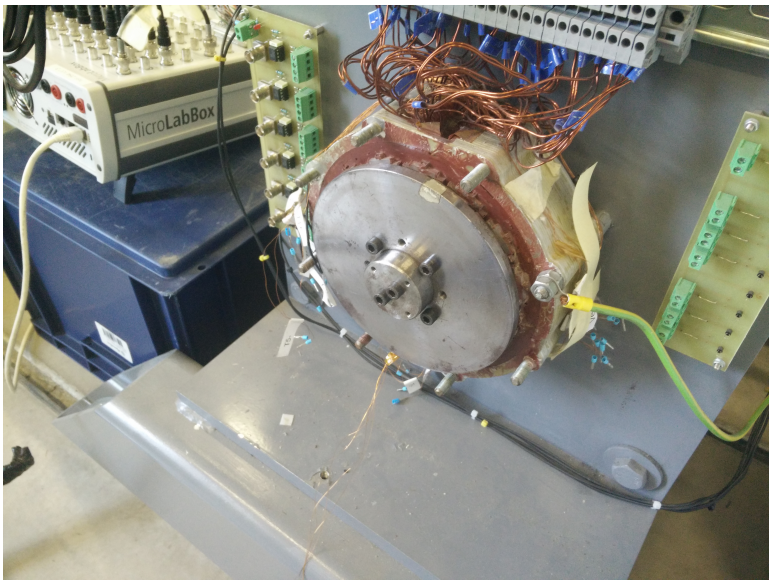

Figure 2.11: Laboratory setup of the AFPMSM including access of all stator teeth connections.

to be similar to the PMs width. This alteration improves the ease of manufacturing.

- The implementation of a double layer concentrated fractional pitch winding improves the winding arrangement by reducing its complexity: every winding can be wound around a single individual armature segment to establish a modular design. The windings are then called a tooth coil (figure 2.10). This construction improves the manufacturing process even further.

The power density and the stator core losses are greatly improved by the absence of a stator yoke. The improved winding arrangement enables short end-windings. Lastly, by using wires with a rectangular cross-section, a good filling factor of the conductor in the slots is obtained. Overall this topology has a superior power density and is considered to be an excellent energy efficient machine.

In this thesis, the machine is used in generator mode, powered by a induction machine. The test setup allows access to all stator teeth windings separately, as shown in figure 2.11, but the machine is connected as a three phase with neutral. This allows measurements of the three phase terminal voltages and three phase stator currents.

Although the yokeless and segmented armature torus machine topology is considered a superior machine, some quantities in the machine design had to be improved even further.

Several papers in the literature and several patents deal with many variants of the YASA machine, and many aspects to improve it in terms of efficiency, power density, manufacturing techniques and thermal design. The work of Dr. Woolmer and Dr. McCulloch of the University of Oxford [9, 24, 38, 39, 41–43] used Finite Element (FE) analysis to accurately determine the machine losses. The work was done on a machine with a peak torque of 120 Nm and top rotational speed of 3600 RPM. This increased the torque density with 20% by the removal of the stator yoke, i.e. a reduction of 50% of the iron was achieved. The machine performed at an efficiency of above 94% in a wide range of operating conditions, with a peak of 96% at a speed between 3200 to 3600 RPM and a torque of 50-60 Nm.

In the group of Dr. Pyrhönen and Dr. Parviainen, extensive work has been performed on the design of the machine and the influence of the geometrical parameters [44–47]. In [18], a 1.6kW AFPMSM generator was designed to operate in small-scale wind power applications. The phase voltage and current were pure sinusoidal and a reasonably low torque ripple was achieved. A simpler and cheaper mechanical structure was obtained.

At the University of Rome, Dr. Capponi has performed thorough research about hybrid-excited axial flux synchronous machines [48–50]. They also developed a tailor-made machine for situations with restricted shaft height [51] and studied coreless [32] and multistage [37] AFPMSMs. In [10], an experimental study is done on reducing the cogging torque and the no-load losses in AFPMSM. This could be done by using magnetic wedges for closing the slot openings. Alternatively, the proper magnet width, shorting the magnet pitch and skewing of the permanent magnets reduced the cogging torque as well.

Dr. Marignetti (Cassino, Italy) together with Dr. Mirimani (Iran University of Science and Technology) studied the effect of eccentricity on the performance of the machine [27, 52, 53]. They also used sensing coils to detect eccentricity [54].

In Milan, the group of Dr. Di Gerlando performed extensive research in the machine design of the AFPMSM, the effects of slots, manufacturing dissymmetries, flux stray paths, torque ripple reduction, thermal modeling, modeling of unbalanced magnetic pull. They also studied the design of the power rectifier that can be used to control the machine [14, 55–60].

At University of Tehran, Dr. Ebrahimi and Dr. Faiz have studied the design, modeling, control, and fault diagnosis of electrical machines. They analyze the spectrum of the stator current (see Section 2.3.2) to detect demagnetization and eccentricity detection [61–67].

At Delft University of Technology, Dr. Polinder together with Dr. Ferreira performed research about short circuits and interturn faults in machines [68, 69]. Furthermore, they studied fault tolerant designs in machines in e.g. wind turbines [70–73].

Condition monitoring systems are becoming available as a plug&play solution in the industry [74, 75], based on e.g. vibration, terminal voltage and phase current spectrum analyzes.

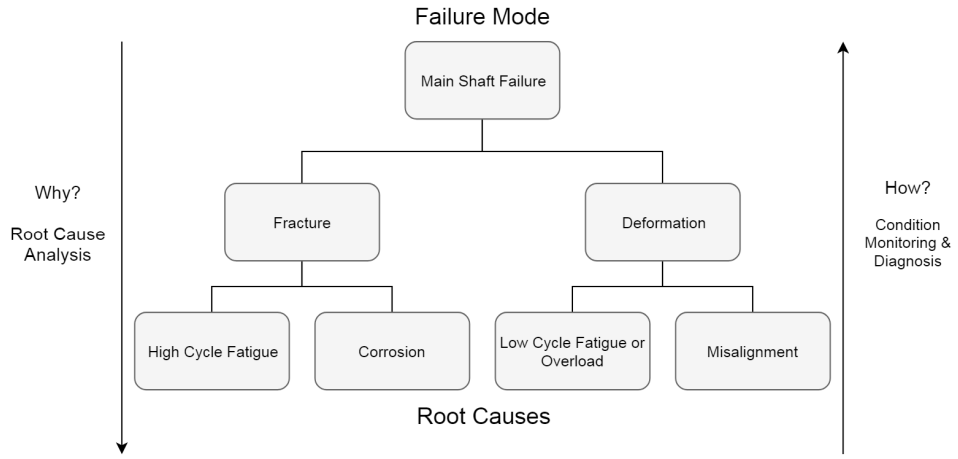

Figure 2.12: Example of a causal sequence from root cause to failure mode [93].

Many aspects were studied at the Electrical Energy Laboratory of Ghent University, by dr. H. Vansompel, dr. A. Hemeida, dr. A. Rasekh, dr. B. Scheerlinck and L. Verkroost. [20] studied and improved this machine intensively. First of all, the magnetic materials where improved by using grain oriented magnetic material instead of conventional non-oriented material [76]. Secondly by segmenting the magnets, the eddy currents losses in the magnets are reduced tremendously [77]. Thirdly, the back-EMF was increased slightly by connecting the stator coils with a combined star-delta winding layout [78]. Finally, a study was done about several geometry parameters: the slot opening, the magnets shape and the stator teeth shape. The impact of the fringing flux on the machine losses is studied by [3, 79, 80]. The heat production, heat transfer, convective cooling and other elements of the thermal analysis of the machine have been investigated [81–86]. An intensive modeling and investigation of the machine has been done by [21, 87–89] to create an efficient design toolbox. Based on the results from this PhD, studies about the control of the machine by e.g. a deadbeat control in defected conditions have been performed [90–92].

Some aspects of the YASA machine are not yet much investigated in literature. Behavior in case of defects is one of them. This is one of the key points in this PhD. Identifying defects makes condition monitoring possible. The following sections give an overview of existing condition monitoring techniques.

2.2 Overview of condition monitoring techniques

2.2.1 Faults in electrical machines

Although electrical machines are usually very reliable, several faults can occur that may cause failure of the machine. An overview of several faults that can happen, and their probability is given in several papers. The probability depends strongly on the type of machine and the application.

Firstly, it needs to be understood that a machine failure is the end of a causal sequence. At the beginning of that sequence is the root cause of the failure. The effect of this cause will eventually lead to the failure of some component of the machine. The failure mode is the type of defect that eventually forced the machine to terminate. Figure 2.12 shows an example of such a sequence. It can be seen that multiple root causes can lead to the same failure mode. Failure is defined as shutting down where a restart is impossible. A premature failure is a failure before the specified lifetime of the machine.

When a machine terminates due to a defect, operators trace the causal sequence from the failure mode back to the root cause. This is called Root Cause Failure Analysis (RCFA), and by doing this the root cause of every failure can be found, which could significantly reduce future failures [94]. For condition monitoring it is more important to understand the opposite direction i.e. how the root cause propagates through the machine and leads eventually to the failure mode. The root cause of a failure can occur in a different part of the machine than where the failure mode forced shut-down of the machine. A broken rotor bar, for example, could lead to overheating of the rotor, which axially overloads the bearing and triggers a bearing failure as failure mode. Alternatively, that same broken rotor bar can instead lead to overheating of the stator windings due to loss of efficiency and trigger a winding short-circuit. It is therefore important to make a distinction between the direct and the indirect cause of the failure. While the direct cause of the failure (failure mode) is the bearing defect or the winding short-circuit in the example, the indirect cause (root cause) is the broken rotor bar.

The duration of the sequence from root cause to failure mode depends on many parameters: the sequence itself, the operation conditions of the machine and ambient conditions of the environment. Figure 2.13 shows a fault with a fast sequence (a) and a fault with a slow sequence (b). In both cases, the average of the probability distribution of the failure is at 50% of the component's life time. In the first case, it can be seen that the reliability transitions from reliable to unreliable very quickly and suddenly. An example could be a short-circuit that triggers the component short-circuit protection, where the duration of the action may be only a few seconds or cycles. It is nearly impossible to do condition monitoring on this defect. On the other hand, if the duration of the causal sequence is weeks or months, as in figure 2.13(b), condition monitoring is a possibility to prompt an early warning and prevent terminal failure. From this, is can be concluded that faults with a slow causal sequence must be the focus of condition monitoring.

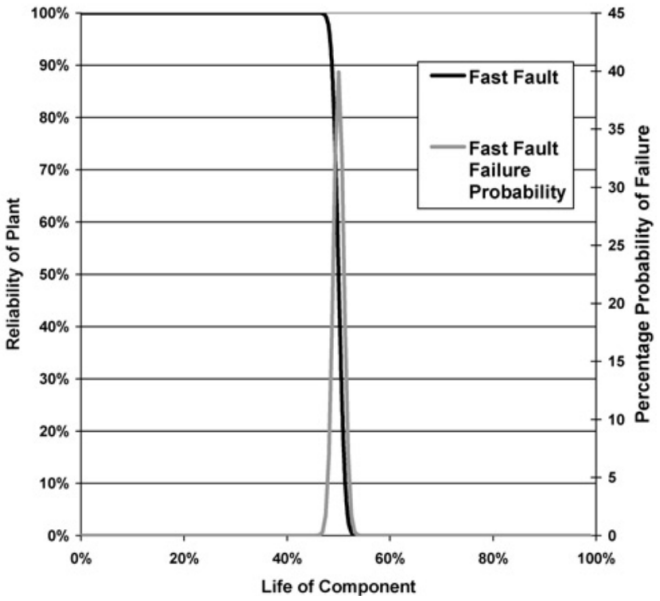

(a)

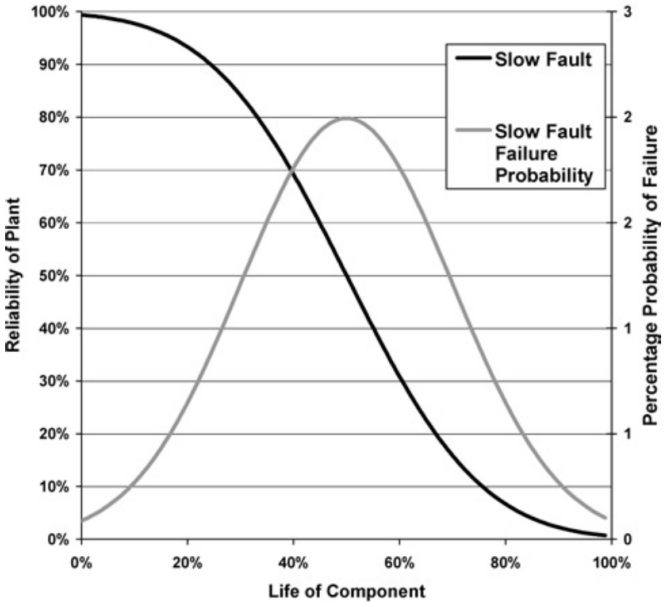

(b)

Figure 2.13: A timeline of the reliability of a component for a failure around 50% of the life time and a normal distribution showing the probability of the failure, for a fast failure sequence (a) and a slow failure sequence (b) [93].

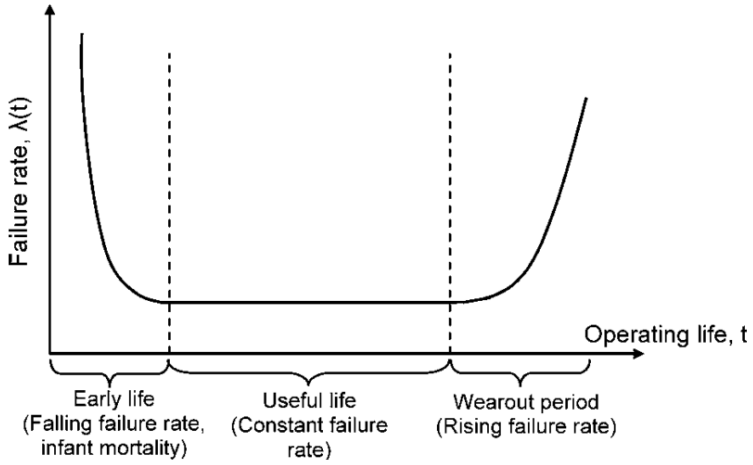

Figure 2.14: Failure rate in function of the lifetime for a population of components forming a piece of machinery. This is also called the bath-tub curve [93].

In [93], a quite detailed survey is given. The author of the paper has used information on Mean Time Between Failures (MTBF). This gives an indication about the reliability. MTBF data should always be interpreted with care, as it can be deceptive. It assumes a constant failure rate as in the middle region in figure 2.14. This means that there is a 50% chance that the failure will occur before the MTBF and 50% chance that it will occur afterwards. The examined surveys are conducted in the USA together with IEEE in [95–102] and later in the defense and wind industries [103, 104]. The surveys are dominated by induction machines due to there ubiquity. The defects are categorized in three areas: the bearings, stator related and rotor related. Table 2.1 shows the distribution of the defects for the several surveys. The distribution is influenced by the size, the voltage and the type of the machine.

This can be seen in the first two columns, where small, Low-Voltage (LV) machines mainly exhibit bearing failures. This is explained because windings are not under much dielectric stress and vibrations due to the LV and small machine, while mostly rolling element bearings are used in this machine, which failure rate largely depends on the maintenance.

On the other hand, in the next three columns, machines with High-Voltage (HV) result in more stator winding defects, due to the higher dielectric stress. The bearings in this type of machines are generally sleeve bearings, which are less prone to failure when constantly lubricated. In larger machines, stator related defects and bearing defects are similar significant.

As this dissertation focuses on Permanent Magnet Synchronous Machine (AFPMSM), data about these machines is required. The survey in [105] shows the fail-

Table 2.1: Overview of failure occurrence in subassemblies of electrical machines [93]

Subassemblies	Predicted by an OEM through FMEA techniques, 1995-7 [*]	MOD survey, tavner, 1999 [103]	IEEE large motor survey, 1985, ODonnell, 1985 [101]	Motors in Utility Applications, Albrecht, 1986 [102]	Motor Survey Offshore and Petrochemical, Thorsen, 1995 [97]	Proportion of 80 Journal Papers published in IEEE and IEE on these subject areas over the past 26 years [93]
Types of machines	Small to medium LV motors and generators <150 kW, generally squirrel cage induction motors	Small LV motors and generators <750 kW, generally squirrel cage induction motors	Motors greater than 150 kW generally Medium-Voltage (MV) and HV induction motors	Motors greater than 75 kW generally MV & HV induction motors	Motors greater than 11 kW generally MV & HV induction motors	All machines
Bearings	75%	95%	41%	41%	42%	21%
Stator related	9%	2%	37%	36%	13%	35%
Rotor related	6%	1%	10%	9%	8%	44%
Other	10%	2%	12%	14%	38%	–

* Private communication from Laurence, Scott & Electromotors Ltd [93].

ure modes of both Induction Machine (IM) and AFPMSM together. An overview of this survey is given in Table 2.2. It shows 7% occurrence rate for demagnetization, 69% bearing defects, which often lead to eccentricity and 3% eccentricity due to assembly inaccuracies. The authors of [106] give an indication for AFPMSM specifically. They classify the faults into magnetic, electrical and mechanical faults. They state that about 35-40% failures are related to stator winding insulation and core (electrical) and almost 40-50% of all motor failures are related to mechanical faults involve bearing and eccentricity faults. It is noted that 80% of the mechanical faults lead to eccentricity. The literature lacks thorough and comprehensive data about the occurrence of demagnetization and eccentricity defects, but generally states that both defects are important and detection of these defects should be performed [27, 105, 107–110].

2.2.2 Why condition monitoring?

Failure and Maintenance

Data shows that about 50% of the electrical energy globally produced is used by electric rotating machinery [1]. These machines transform electrical energy into mechanical energy. They achieve this efficiently and reliably. Furthermore their operations can be reversed, meaning e.g. a motor can often be used as a generator as

Table 2.2: Failure modes and effects in IM and AFPMSM [105]

Fault (%)	Fault Mode	Failure Effects
Stator (21%)	Winding asymmetry such as open phase, Winding short circuit	Reduced torque, Catastrophic failure
Rotor (7%)	Broken bars (IM only), Cracked end-ring (IM only), Demagnetization (AFPMSM only)	Torque pulsations, speed fluctuations, vibrations, overheating.
Bearing (69%)	Damage in rolling element bearing	Vibration and noise, flaking or spalling, increase in wear.
Stator/Rotor Assembly (3%)	Air-gap eccentricities: static and dynamic	Increase in bearing wear, stator windings exposure to harmful vibration, rotor-to-stator contact.

.

well. This can be interesting in applications where rapid deceleration with energy recovery is preferred e.g. electrical vehicles.

As a result, these machine are widely used in industrial environments [94]. Therefore, around 70% of energy consumed by electric rotating machines is allocated to the industry. The machines are used in a wide range of applications, from a simple ventilation of a fabrication hall to actuating highly crucial and precise production processes such as plastic extrusion.

Although these machines are quite robust and reliable, unexpected premature failure still happen. Literature shows that on average 9% of all electric machines fail prematurely [2]. The problem is that unexpected fallout of a machine can heavily disrupt a company's normal operations. The actual cost of the machine itself is only a fraction of the total economic cost leading from this. There might be a loss of production, need for demounting components, reassembling after repairing or replacing the components, re-initialization of the production process, etc. Especially in the food industry and in general all continuous manufacturing processes where high quality is required, sudden failure of one of the machines in the chain of production leads to extremely high costs [2].

As the cost of premature or unexpected failure is so high, it is important to assure the up-time of these critical machines. This is performed by carefully elaborated maintenance programs. Research has shown that the maintenance cost of the critical machines is negligible compared to the cost of a premature failure in the production chain. The authors of [111] show that there are four main maintenance strategies called corrective, periodic, predictive and proactive maintenance.

In **corrective maintenance**, no effort has been done to reduce the risk of unexpected failures. It is also called the run-to-failure-strategy, as the machine is quite literally used until it breaks down. Once it breaks down, the machine or the com-

ponent that triggered the failure is replaced. This is a solution if the cost of the downtime is smaller than the cost of replacing the machine or component itself, it may be economically optimal to use corrective maintenance and no maintenance efforts should be made. Sometimes this strategy is applied to machines with a higher cost at fallout if the machine itself is cheap. In this case, redundancy is created by installing a second and sometimes even a third machine or drivetrain in parallel. If a failure occurs in one of the machines, the other ones will take over the functionalities instantaneously. The production process is safeguarded of a shutdown, but the lifetime of the drivetrain itself is not affected.

Periodic maintenance is frequently used and is a preventive maintenance strategy. The machine is periodically inspected and maintained. This can range from a brief visual inspection to an extended accurate measuring inspection of a set of electrical and/or mechanical parameters. This is used to determine the condition of the machine and its components, e.g. insulation resistance test to diagnose the condition of the winding insulation. The problem is that most of these inspections and maintenance are performed when the machine is off-line. Sometimes this can be scheduled at moments that the production is low, or completely down, but this is not a possibility in all cases. To account for this, more and more vibrations and/or thermal analysis is applied to conduct an on-line inspection of the machine's condition. The maintenance itself can also vary, i.e. from a simple cleaning of the machines or certain parts, to a re-lubrication or even replacing certain parts like the bearings completely. Periodic maintenance can be developed in an extensive maintenance schedule for every important machine in a production chain, but this can also result in increased cost. Therefore it is paramount that a balance is found between the cost of the periodic maintenance and the gained profit in prevented cost of the unexpected and premature breakdowns and increased machine life time. Healthy machines that show little to no indication of failure can have maintenance less frequently, e.g. once a month, while machines that show signs of degradation by for example increased or abnormal vibrations and/or temperatures, can be maintained more frequently, e.g. once a week or every day. The downside of this technique is that unexpected failures between the interventions is still highly possible.

In **predictive maintenance**, the state of the machine is constantly monitored and estimated. Based on this data, maintenance is scheduled. So maintenance is done on demand, instead of periodically. This is the most advanced, efficient and effective way of doing maintenance. By doing maintenance only when needed, the cost of maintenance itself is lower, but because more expensive equipment for analyzing the state of the machine is needed, predictive maintenance is the most expensive strategy. Fault indicating parameters are measured and used continuously to predict the MTBF or the Mean Time To Failures (MTTF). Based on this data, and the type of fault that is occurring in the machine, operators can estimate the urgency and the proper actions for the maintenance intervention. This continuous monitoring of certain fault parameters to estimate the fault severity is called Condition Monitoring (CM), and they can be implemented in a larger Supervisory

Control And Data Acquisition (SCADA) system to monitor a whole plant. A great variety of CM techniques are developed using vibrations, temperature, stator current and voltage, air gap flux, torque data, etc. For example, based on vibration data of machine defects like bearing faults, misalignment and rotor unbalance can be diagnosed. It should be noted that the sensors used for CM e.g. accelerometers for vibration analysis, are placed on or in the machine and therefore are often subjected to harsh environments e.g. temperature swings, large impacts, excessive vibrations, dust, moisture, etc. Because of this, high maintenance of the sensory equipment is necessary. This includes remounting the sensors, sensor recalibration, broken wiring, cleaning, etc. and makes CM often very expensive. It is only interesting to use more expensive CM if the total cost of the machine unexpected fallout is significantly high.

The fourth maintenance strategy is **proactive maintenance**. In this strategy, after a failure, the root cause is determined with RCFA. Once this is known, the maintenance will do extra effort to prevent the same root cause from triggering a failure again. This strategy can be combined with one of the previous three strategies. The learned knowledge and feedback can improve the machine, the mounting structure, the maintenance schedules, the maintenance quality or any desired combination of these possibilities. Re-dimensioning of the machine itself is rarely needed. Often changes to the mounting structure, correcting alignment, better balancing of the rotors, etc. prevents the defect from reoccurring. As a result, after years of successful operations, no proactive maintenance is required anymore. Proactive maintenance is especially used for new or re-initialized machines.

Condition Monitoring

As described above, the breakdown of very critical machines leads to a large total cost. To prevent this, predictive maintenance using CM is the chosen maintenance strategy [94]. Beside this, CM is also a key element in industry 4.0, which involves an increase in extracted data from the machines and the components of a production process and combining all this data to make better operational and management decisions.

CM primarily involves the continuous analysis of operational equipment and the identification of problems before component breakage or machine failure. CM has mostly been associated with the analysis of rotating and reciprocating equipment. Almost any equipment, be it electrical, hydraulic, mechanical, or thermal, generates characteristic signals or “signature” during optimal performance. A change in this signal, even if marginal, could be an early warning regarding potential equipment failure [112].

Industrial equipment is a major investment for any company to make. Keeping that equipment up and running is critical. Establishing and following a careful maintenance program is essential for this process. However, condition monitoring must also be part of the program. Without this kind of observation, critical clues

could be missed and unexpected repairs could bring the equipment to a halt [113].

Condition monitoring looks at the key conditions that indicate how well a given piece of equipment is working. Some examples of this kind of monitoring include oil analysis, vibration monitoring, or acoustic emissions testing. The exact factors involved with condition monitoring will vary from one piece of equipment to another.

For many companies, condition monitoring is important for routine maintenance. A schedule for regular maintenance is critical to ensure sufficient lifetime of industrial devices. But the frequency of doing maintenance is to be chosen carefully. Doing maintenance too often means more downtime and additional cost. Postponing maintenance too long may cause irreversible damage to components and eventually also leads to downtime and additional cost.

This is where condition monitoring comes into play. Closely observing the condition of industrial equipment can indicate when maintenance should be performed. In this PhD, the focus will be on condition monitoring only, not on maintenance.

Note that there are other advantages to condition monitoring for industrial equipment. Close observation helps engineers to understand the equipment better, or to predict based on previous observations and behavior, when and which future problems will arise. For example, vibrational analysis can be used to monitor the vibrations of a device, which usually have some typical vibration frequency. If that frequency starts to vary, or changes substantially, it could mean something inside the machine is starting to fail or needs to be replaced. Monitoring allows engineers to anticipate a potential failure and take action. Condition monitoring helps engineers to make better decisions about performance optimization and maintenance needs.

Condition monitoring helps to save money, time, and resources. Although monitoring itself costs money, it is usually minimal compared to the downtime associated with doing maintenance too often or making unexpected repairs [114].

Specifically for rotating electrical machinery – which is the most relevant for this PhD about axial flux permanent magnet synchronous machines –, the following sections give an overview of well-known possible techniques for condition monitoring. The overview is based on a review paper of P. Tavner [93], and is about detecting all possible types of defects. After this overview, Section 2.3 gives a more detailed analysis of techniques for demagnetization and eccentricity detection as this PhD studies mainly these techniques.

For the general overview, there are three restrictions given by [93]: only online techniques for rotating machines are considered, no variable speed drives are studied, and the paper focuses on conventional rather than emerging brushless, reluctance and permanent magnet machines of unusual topology. Nevertheless, most techniques are also applicable to variable speed drives and permanent magnet machines, such as the ones considered in this PhD.

2.2.3 Temperature monitoring

Temperature is an important aspect of an electrical machine. Overloading the machine can lead to too high temperatures that can damage the insulation of the wiring and cause short-circuits. Therefore, machines are rated at certain maximum temperatures and load levels. The temperature can also be used as detection parameter as inter-turn shorts and increased friction can alter the local temperature. The temperature can be measured in three ways: local point measurement, thermography, and bulk temperature measurement. These three techniques are explained in the following paragraphs.

Local point measurement

To measure the temperature in a local point, embedded temperature sensors are needed like thermocouples, resistance temperature detectors (RTD) like PT100 or PT1000, etc. They have to be placed in the heat generating parts of the machine, mostly in the windings, the stator core and the bearings [115]. Determining the exact position of the sensors demands careful consideration and knowledge of the temperature distribution within the machine, in particular the knowledge of the hotspot locations, e.g. placing the sensor at the hottest side in case of asymmetrical cooling.

The downside is that the above mentioned sensors need electrical isolation to measure e.g. the temperature in the stator windings. Because of the limited heat conductivity of the isolation, a temperature difference between the sensor and the windings will occur. A fiber-optical technique counters this by using the polarization of the light as indicator [116]. A second problem with thermocouples and RTD's is the difficulty of using them for rotating parts: mainly in large induction machines where heat is produced on the rotor side, the temperature measurement on the rotor is very useful but the wiring from the rotating sensors to the static parts of the machine can become complicated [117].

In recent work, a fiber Bragg grating-based system was made to detect a wide set of parameters of the machine: temperature distribution along the windings and rotor surface, vibrations rotor speed, torque and spin direction. The all-optical approach avoids electrical interference and is a natural insulator for the sensors. [118].

Thermography

The problem with local point measurements is that a hotspot due to a defect, e.g. an inter-turn fault, might not be at the measured position. To find these hotspots, thermography or thermal imaging can be used. The application of these techniques is limited, although the results are promising. In [119–121], a technique using a thermal model, ambient air temperature and stator winding current measurements

is developed to predict the temperature at a set of chosen points in small enclosed fan-cooled induction motors.

Bulk temperature measurement

By measuring the temperature of internal or external coolant, an overall average of the temperature can be estimated. This is indicative for general overload problems, but is insensitive for hotspots. The advantage is that sensors can be placed on relatively easily accessible locations. [122] uses a fiber that is temperature sensitive over a certain length adjacent to the windings to detect an increase in temperature.

2.2.4 Chemical and wear monitoring

Fault detection by means of chemical and wear analysis has a very broad spectrum of possibilities. For instance if the temperature rises, thermal degradation of the insulation material starts. First, the lighter solvents will vaporize. After that, the heavier materials start to vaporize. By detecting the composition of the released gas/smoke, the level of degradation can be estimated. The gas/smoke can be detected by classical ion chamber smoke detectors [123–125].

Alternatively, the gas/smoke can be analyzed chemically with a chromatogram [126], or with ultra-violet light (based on the fluorescence effect of some materials). It is possible to insert easily identifiable materials in the machine to make the analysis of the fault easier. The difficulty of gas detection lies within the complexity of the analysis and the problem of converting it to an electrical signal [127].

Some machines use a continuous oil supply for the lubrication of their bearings. As a defect like increased temperature (e.g. by magnetically induced shaft voltages that generate a current in the bearings) can increase the oil degradation, monitoring the oil supply can be a good estimator to prompt an early warning. When bearings wear, small debris is released in the lubrication oil, which can be detected [128].

2.2.5 Mechanical vibration monitoring

Due to the torque spectrum and the other air gap magnetic field forces, vibrations are introduced on the mechanical structure of the machine. Each component of the machine will have each own response to vibrations it receives. The vibrations can also be caused by mechanical and electrical faults:

- Pure mechanical defects like shaft whirl and mechanical unbalance cause transverse motions.
- Bearing wear can cause eccentricity, which in turn results in dynamic or static Unbalanced Magnetic Pull (UMP) and also causes transverse motions.
- Electical defects in the stator coils result in vibrations in the shaft.

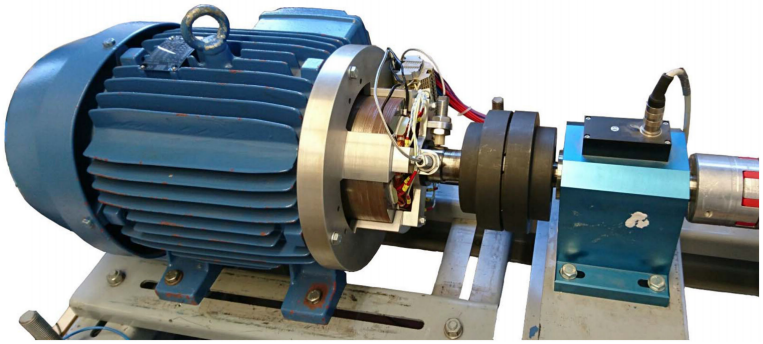

Figure 2.15: Setup of the induction machine with controllable magnetic bearing [135].

It should be noted that vibrations from different machines in the plant can be received by the analyzed machine and disturb the measurements. These vibrations can be picked up by accelerometers and velocimeters on the vibrating part, and by proximeters adjacent to the vibrating part. Such a sensor can be placed on the machine stator. The Root Mean Squared (RMS) value of the vibrations is used as an indicator for the machine's health. So there is no diagnosis of the actual defect, but a set of guidelines is constructed for when maintenance is required.

The most widely used method is to analyze the spectrum of the measured vibration [129–132]. A baseline is needed to know the vibrational content of a healthy machine. Above the healthy baseline, an operational limit is placed. As each defect has different influences on the vibrational spectrum, a diagnosis can be made. To simplify the diagnosis, the impact of certain defects on the frequencies is examined. This allows for a focused analyzes on only the reacting frequencies.

With strain gauges, the torsional vibration on the shaft can be detected. Because this is not always preferred (wiring from the shaft can be problematic), an alternative is used: by measuring the angular displacement between the non-driving ends of the motor and the load, the vibrations are assimilated as well [133, 134].

A different approach has been performed in the research group EELAB of Ghent university. Here bearing faults are detected by the analyzing the movement of the outgoing axis of the machine. In order to simulate defects in a healthy machine, a magnetic bearing is created able of reproducing a given movement by the controls (figure 2.15). This setup allows for great insight in the behavior of bearing defects and their propagation to the machine axis [135].

As rolling element bearings deteriorate, small pits and imperfections are created in the path of the moving objects. As these moving objects pass over these imperfections, shock pulses are generated. These shock pulses are in the ultrasonic frequency spectrum and can be measured with piezoelectric transducers [136–138].

In recent work, electrical measurements of the machine are combined with a model simulating the torsional resonance of the machine. From this information, the bearing defect can be extracted. This technique is advantageous in comparison

with the traditional vibration-based methods in sensor cost, installation complexity and detection reliability [139].

2.2.6 Electrical current, flux and power monitoring

Brushgears of DC machines need regular maintenance to prevent sparking. A possibility for detecting the need for maintenance is to place a dipole antenna near the brushgear and analyze the radio frequency signal. The higher the power of the signal, the greater the sparking activity [140].

Earth leakage faults are no problem if only one occurs, but a second connection to the earth can create large currents leading to damaged insulation and thermal hotspots. The simplest way is to apply a DC voltage to the wiring and measure the current via the earth connection. Operational pressures prefer that the machine is only shut down when a second defect occurs. The earth leakage fault detection technique monitors the leakage currents. After a first earth leakage defect, the detected current remains low and no action is taken in order to keep the drive operational. If there is any significant change in current detected, it means that a second defect has occurred. An alternative is to use a potentiometer and a sensitive relay to create a balance with a bridge circuit. When a second fault occurs, the balance is disturbed and the relay is triggered. The problem with both techniques is that a second fault close to the first fault may not change the current enough to be detected.

Turn-to-turn faults change the magnetic field in the air gap. This can directly be detected with a search coil placed on the rotor. As it passes by the stator coils, it maps the magnetic field and can alert for unusual deviations [141].

Any deviations in the air gap such as caused by eccentricity, will result in alterations in the stator currents [142], as can be seen in figure 2.16. This current can be spectrally analyzed to diagnose the defect, this is called Motor Current Spectrum Analysis (MCSA). Other defects occurring on the drivetrain (e.g. in the gearbox, the load, etc.) can propagate to the rotor of the machine and can also be picked up by the analysis of the current spectrum [143].

Winding short circuits, voltage imbalance, rotor demagnetization lead to an asymmetry in the machine. By destroying the natural symmetry of the machine, an axial leakage flux or shaft flux occurs. The flux is detected with a search coil wound around the shaft, spectral analyzed and it leads back to the fault that caused it [145–149].

Similarly, the terminal power spectrum can be used in condition monitoring as well. Combining the voltage and current spectrum information creates a simpler overview that can lead to diagnostic conclusions more easily [150, 151].

In recent work, a holistic technique uses MCSA, partial discharge monitoring (explained in Section 2.2.7), power quality monitoring and vibration monitoring as a combined CM method for machines in the oil and gas sector. The sensor information is combined with a CM database for benchmarking and trending pur-

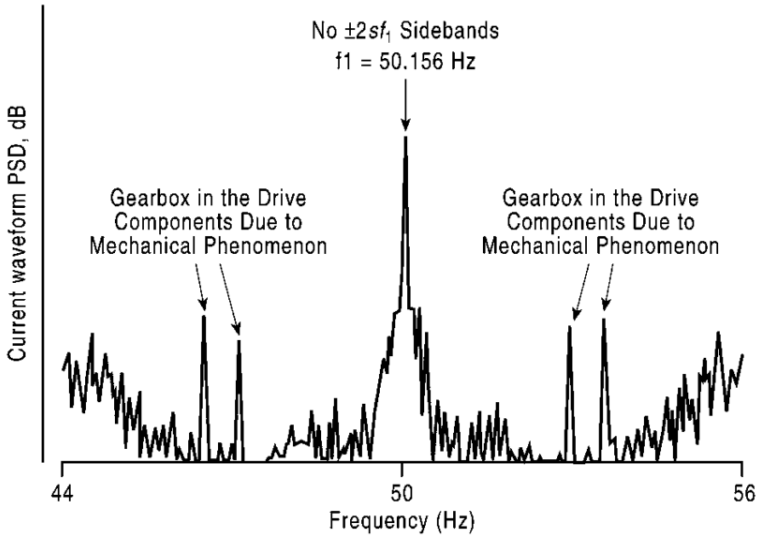

Figure 2.16: Current spectrom of a 1220 horse power motor, 3 of the 46 rotor bars have been fractured [144].

poses [152].

2.2.7 Electrical discharge monitoring

Electrical discharges detection is another technique to indicate when insulation deteriorates. The types of discharges in ascending order of damage and energy are:

- Corona discharge: the voltage causes the surrounding air to ionize, which causes a blue glow.
- Partial discharge: small voids inside the insulation weakens it and allows for a small leakage current.
- Spark discharge: the leakage is large enough for sparks to show.
- Arc discharge: the insulating properties are so deteriorated that an arc of current forms.

These discharges progress onto the voltage and the current waveforms. By coupling a radio frequency current transformer with the neutral cable of the machine, the signal caused by the discharging can be measured. The neutral is a good measuring point because every possible discharge in the machine causes radio frequency current flow in the neutral. However, the variation in the current signal level due to the discharge is not large, making it hard for this signal to be used as

alarm trigger. Also signals can originate from multiple discharge sources and it is not possible to discriminate between them [153–155].

Capacitors are coupled to the machine terminals, and connected to a device that analyzes the signal's harmonic content. This can capture the signals (see figure 2.17) from the partial discharge without interfering with the machine's operations. An analysis is performed at regular intervals during the machine's life time to monitor the condition [156, 157].

Experiments have shown that sparking and arcing discharge have faster rise-times than corona and partial discharge. This means they introduce energy at higher frequencies. A broad-band radio frequency method tries to obtain this information by placing a broad-band antenna in the machine [158]. This technique is able to detect the defects, but has the disadvantage of having no location information about the defect.

In recent work, this technique was applied to detect bearing damage in variable speed drives, which are known to be sensitive to bearing currents and damage resulting to these currents. Usually, bearing monitoring is done via vibration analysis, but this paper uses electrical discharge combined with time- and frequency domain signal processing [159].

2.2.8 AI techniques

As condition monitoring tries to connect the measurable signals of the machine with the underlying defects, much effort has been made to use Artificial Intelligence (AI) to solve this problem. Expert systems, fuzzy logic and artificial neural networks have been used, which take the measurable signals as input and result in the underlying defects as output.

Expert systems

In an expert system, the expert knowledge of the operators is combined with measured signals of the machine to determine the machine condition. Figure 2.18 shows an example of the architecture of such system.

An expert system was created to monitor the insulation condition of turbo-generators [160]. The conclusion is based on trend analysis, maintenance records, present operating point, vibration, visual inspection, fleet experience, comparison with other generators, earlier off-line test results, and temperature measurements. Based on human expert knowledge, a set of rules is created to use this data and diagnose the partial discharge activity.

Fuzzy logic

Fuzzy logic allows states to be represented as not only '1' or '0' ('true' or 'false') as with Boolean logic, but also the entire range between it. By using this for condition monitoring, the state of the machine is not necessary 'good' or 'bad', but

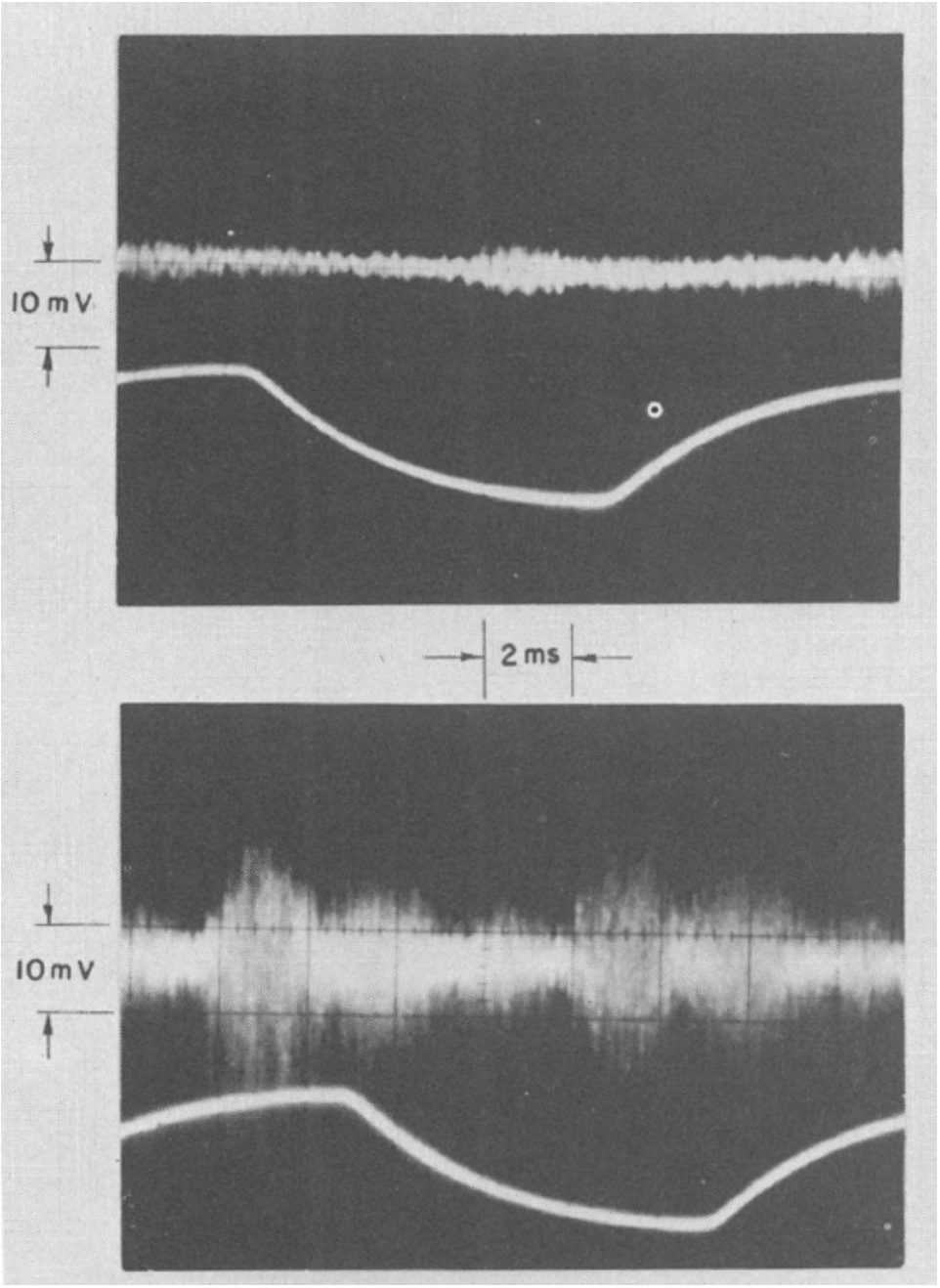

Figure 2.17: Partial discharge of one phase and a power-frequency reference signal. Both graphs are from identical machines, where the winding of the upper graph is 3 years old and the winding of the lower graph is 24 years old [156].

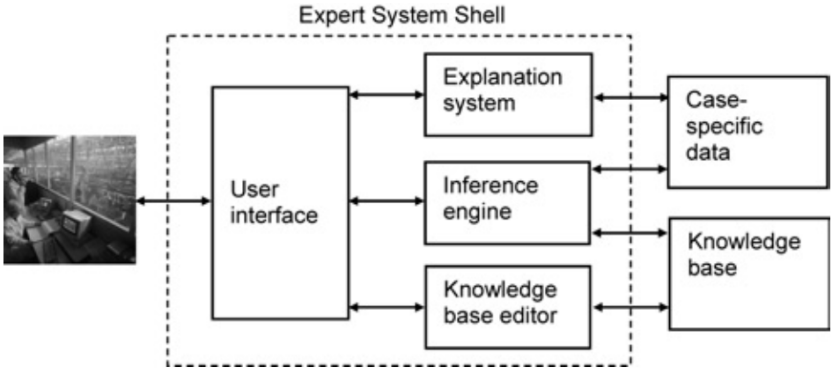

Figure 2.18: The general architecture of an expert system [93].

can lay in between. This is a more accurate representation of reality and allows to describe the machine's state linguistically. Fuzzy logic maps the input signals with membership functions. By doing so, linguistic variables are connected with signals like temperature and negative sequence current. Constructing this requires insight in the internal working of the machine and the meaning of the signals, thus experience and knowledge is essential [161]. [162] shows that a linear induction motor can be equipped with a fuzzy diagnostic system to do condition monitoring. Both expert systems and fuzzy logic use experience and knowledge, but have a different approach in how the knowledge is implemented to do the condition monitoring.

Artificial neural networks

An artificial neural network uses training data to learn how the measurement signals correlate to the underlying defects (self-learning). It is capable of recognizing patterns in complex, non-linear systems. It can also account for other parameters like the machine load, operation point, etc. The machine is seen as a black box, but the most relevant signals are selected to diagnose the machine. Again, knowledge of the machine is required. The most popular structure is the Multi-Layered Perceptron (MLP). In case of supervised learning, the MLP is trained using labeled training data and e.g. the back-propagation algorithm. [163] uses this to detect a broken rotor bar in induction motors.

It is also possible to use artificial neural networks unsupervised, meaning no labeled training data is used for the learning of the network [164]. The network analyzes the data and clusters it in groups with similar characteristics, constantly training itself to better classify new data to the existing groups. This is simpler, but takes more time to get better results. As labeled training data is not always available, this technique can be more practical than supervised learning. On the other hand, if the data can be categorized into groups in different ways, then the network might not use the groups the user prefers.

In recent work, an artificial neural network has been used to diagnose bearing problems in wind turbines. Vibration measurement data is used as input in the time domain, the frequency domain and the time-frequency domain. The network was trained unsupervised to extract the required features and perform the necessary classification [165].

2.3 Demagnetization and Eccentricity

Out of all possible faults in rotating machinery, this PhD studies two types of faults: demagnetization and eccentricity.

As shown in Table 2.1 and explained in Section 2.2.1, eccentricity is occurring frequently: for bearing failures, which cause often eccentricity, it was found for small to medium LV motors and generators below 150 kW that these bearing failures are 75% of all observed failures. For other types of machines, generally MV and HV, the percentages were around 40%. Although demagnetization is not the most frequently occurring fault in machines, it is relevant to monitor because it can greatly impact the performance and healthy of the machine.

The most direct way to detect defects is to measure the magnetic flux density directly with a Gauss meter. In [166], this is used to map the flux pattern of the PMs, in order to diagnose demagnetization defects. The measurement requires dismantling the machine, which makes it an offline test. Because the flux pattern is measured directly, the technique is reliable and accurate. The invasive process of dismantling and measuring is time-consuming, which makes this method only suitable for laboratories and not for real life applications. Therefore, most detection techniques utilize more accessible parameters to retrieve the information about the defects.

This section will first explain the failure mechanisms for demagnetization and eccentricity, show some some practical cases and will then discuss current-based, voltage-based, torque-based and loss-based fault detection techniques.

2.3.1 Failure mechanisms

Demagnetization

NdFeB magnets are easy to crack, brittle and easy to erode. This allows for a wide range of possible causes for demagnetization.

- Due to stator short-circuit faults, it is possible that the magnetic field succeeds the coercivity of the magnets, demagnetizing the magnets.
- Heat can be created by many causes: by the stator copper losses (possibly even due to fault currents), by eddy currents losses in magnets, by interturn short-circuits of windings and fault in the cooling system. This can raise the magnet temperature and make the magnets demagnetize.

- Due to different expansion rates between magnets and rotor iron mechanical stresses are introduced. This can be solved by choosing a glue that is flexible yet strong.

- During the installation process of the magnets on the rotor disc, the magnets are subject to mechanical pressure. This can lead to small cracks in the magnets.

- High humidity, contaminants, dust pollution, salt and cooling lubricants can all lead to erosion. Oxidation and corrosion change the metallurgical properties of the magnets resulting in irreversible demagnetization.

If the magnets in the motor are starting to demagnetize and the operator requires a certain amount of torque, than this can result stator currents higher than normal. These higher stator currents in turn will result in higher copper losses, which leads to more heat, and thus even more demagnetization. This can even lead to a stall of the machine. Note that if all magnets are similarly demagnetized, this may result in an uniformal temperature rise, while a local demagnetization due to breakage may lead to a local heating of the machine.

Demagnetization in turn can lead to other faults in the machine. For instance, UMP which can result in bearing erosion and bending of the shaft [167]. This may introduce eccentricity in the machine. The extra harmonics in the magnetic forces may result in acoustic noise, vibration and torque ripple (unless if all magnets demagnetize equally). Demagnetization will reduce considerably the mechanical torque of the machine. Also broken pieces of the magnets may fall in the air-gap and possibly damage the stator windings. In machines with parallel branches in the stator windings, it causes circulating currents between the branches [168].

Eccentricity

The authors of [106] show that 80% of the mechanical defects lead to eccentricity, especially bearing defects. Bearing defects are caused by poor mounting or alignment, heavy radial and axial stress (sometimes due to inherent eccentricity or UMP), vibrations, electrical stresses due to bearing currents, improper lubrication, contamination and corrosion. But even under normal operating conditions fatigue failures may take place due to normal internal operating stresses.

In turn, eccentricity defects are caused by misalignment of bearings, bearing deficiency/defects and wear of the bearings, bending of the rotor/shaft, mechanical resonance at critical speeds (sometimes called rotor whirl), unbalanced load, unbalanced mass due to manufacturing imprecision, improper assembly and excessive tolerances (looseness). Eccentricity defects can lead to bearing damage and therefore result in more eccentricity.

Example cases

Lets take an electrical vehicle with the AFPMSM as a first example case. Lets state that the machine is heated up during operation, and because it is a warm day, it is not demagnetized, but near the maximum temperature. Lets state that this vehicle tries to drive on a high curb, but it cannot deliver the required torque. As this happens, a high quadrature current will flow in the stator currents, trying to generate the required torque. As the motor is in standstill, the five magnets who are in the quadrature field will receive a opposing magnetic field. If this field is high enough, this can result in demagnetization of those five magnets, while the other magnets will remain healthy.

A second scenario can be an operator requiring higher performance of the machine that it is rated for. The losses due to the operation will heat up the machine uniformly. As the machine is pushed over its limits regularly, the temperature can demagnetize the magnets. First this will result in reversible demagnetization, but with increased temperature the magnets become irreversible demagnetized. This will reduce the performance of the machine. As the operator still demands high performance, higher currents are injected. This will increase the heat production and accelerate the demagnetization process.

Thirdly, an electrical vehicle hitting the curb introduces a mechanical shock on the shaft. The same can happen in wind turbines by sudden wind gusts. If the machine is connected in direct drive, the mechanical shocks can reach the AFPMSM and for instance bent the shaft. By bending the shaft, the rotors will exhibit a dynamic eccentricity. Typically, the angle of the dynamic eccentricity of both air gaps will be the same. If this mechanical shock keep occurring, a point may be reached where the rotors will make contact with the stator, increasing the damage to the machine even more.

Lastly, because of fatigue, rolling of the bearings or faulty assembly the bearing may not be able to keep the shaft centered. This lower the shaft at that bearing, will still being centered at the other bearing. Because of this, the rotors will exhibit and angle toward the stator, meaning a static eccentricity defect has occurred in both air gaps. Typically in this situation, the angle of the static eccentricity of both air gaps will have a 180° offset between each other.

2.3.2 Current-based detection

Current-based detection techniques are described first. These techniques are very popular and common because the current waveforms are easily accessible and more understandable. Of course these techniques also have their limitations, which the introduced techniques in this section try to overcome.

One of the basic current-based detection techniques is MCSA, which was mentioned briefly in Section 2.2.6. This uses an analysis of the frequencies of the current spectrum. In a defected machine, extra harmonics are introduced in the current due to the defect. These current harmonics in the stator coils are a result of the in-

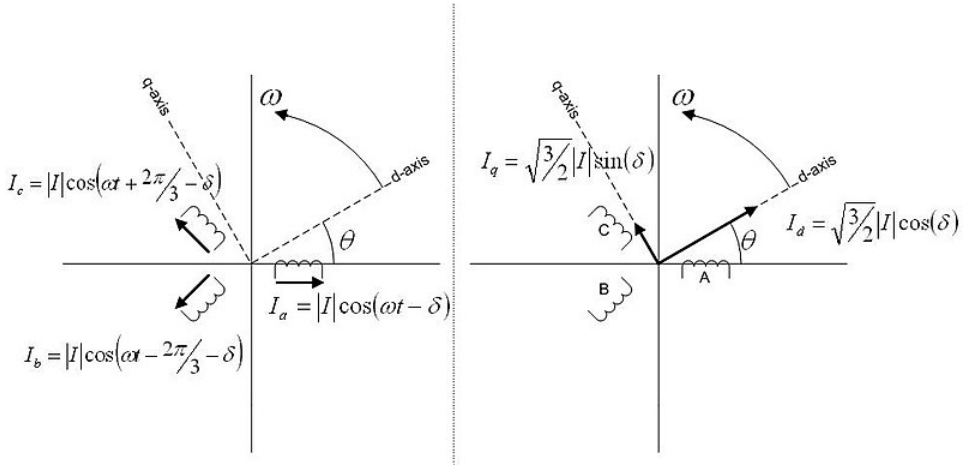

Figure 2.19: Graphical interpretation of the d-q-transformation [174].

duced harmonics within the back-EMF. With a Fast Fourier Transform (FFT), the time signal of the current can be transformed to the frequency domain. This clearly shows what harmonics occur in the machine. In [61, 169–172], this technique was used: both demagnetization and eccentricity can be detected. The authors of [173] succeeds in differentiating between demagnetization and static eccentricity. Uniformal demagnetization cannot be detected because it injects no extra harmonics. These methods base themselves on numeric and experimental data. This drastically reduces their flexibility toward different topologies. It also requires stationary conditions due to the use of a FFT and is intensively sensitive for faults in the inverter because these faults often also introduce extra current harmonics. It has the advantage of being non-invasive and can be used online.

In [172], the authors also describes a method using the stator current together with the voltage, speed and some machine parameters to estimating the d-axis flux. The reduction of the estimated flux is different for demagnetization defects and for eccentricity, speed variations and load level variations. The technique is non-invasive and can detect uniform machine demagnetization but is prone to estimation errors.

In [110], a current based technique is presented that can detect demagnetization and eccentricity without using FFT, but by using the machine's inductance. Like the previous technique, this method is also able to distinguish between the two types of defects. To do this, the machine is considered in a d-q-reference frame: If the injected current and terminal voltages of a machine are symmetrical and sinusoidal (or the harmonics are not considered), they can be represented by a single current and voltage vector rotating at the rotation speed of the rotor. If these current and voltage vector are seen from a reference frame with the same rotation speed as the rotor, the current and voltage vector are seen as stationary.

The abscess and ordinate are called the direct and quadrature axis respectively. This tranformation can be seen in figure 2.19. In this d-q-reference frame, two parameters are defined for this detection technique:

$$L_d = \frac{\lambda_d - \lambda_m}{I_d} \tag{2.1}$$

$$L'_d = \frac{d\lambda_d}{dI_d} \tag{2.2}$$

where L_d is the d-axis inductance, L'_d is the d-axis differential inductance, λ_d is the d-axis flux linkage and λ_m is the flux linkage in the coil with I_d = 0. In the linear part of the magnetization curve of a material, the two inductances are equal: $L_d = L'_d$. If the material saturates, both inductances will decrease, but at a different rate. Therefore they will not be equal anymore. This allows for detecting when the machine is saturating. A small AC current is injected in order to detect L'_d. At I_d = 0, L_d in the linear part is determined with this as well. In a healthy situation, the PMs will inject a magnetic field in the machine that puts it at the end of the linear region. A direct current I_d is injected so that the core materials start saturating. The magnitude of the direct current indicates the magnitude of the PM field. In case of demagnetization defects, the PM field will be lower. A larger I_d will be needed to saturate. This allows for demagnetization detection. In case of eccentricity, there is an increase in magnetic flux at the shortest air gap length which will reduce L'_d due to saturation. At the longest air gap length, there is a decrease of magnetic flux, but due to the linear region, L'_d does not change. The total impact of eccentricity is a lower L'_d at I_d = 0, which is different from the demagnetized case. It is thus possible to differentiate between demagnetization and eccentricity. The technique can even detect both uniform and partial demagnetization defects. The downside of this technique is that it requires standstill conditions and an additional inverter for injecting DC and AC I_d. The sensitivity of the index to the fault is dependent of the type of machine.

Another technique exploiting saturation is given in [175], by placing a pulsating square wave voltage source on the stator coils. The voltages are chosen to generate a normally distributed, but pulsating, magnetic field in the machine. When this magnetic field is aligned with the magnetic field of the PMs, the core will saturate and the current will be higher than without saturation. If on the other hand the magnetic field of the coils is in the opposite direction of the magnetic field of the PMs, the core will be in the linear region and the current will not change. By changing the spatial direction of the magnetic field of the current, the amplitude and phase of the magnetic field of the PMs can be estimated. In case of uniform demagnetization, the amplitude will change, but not the phase. On the other hand, in case of local demagnetization, the phase will change as well. It has the same drawbacks: it requires standstill conditions and an additional inverter.

To counter the stationary constraint of the MCSA technique with FFT, [176–

180] use different types of wavelet transformations in order to extract the harmonic content though time. This results in a frequency-time distribution of the stator current signal. From this the demagnetization defect can be diagnosed in non-stationary conditions.

The authors of [181, 182] developed an analytical model to diagnose interturn defects in the stator coils using the phase current waveform and the freewheeling current through the inverter diodes as inputs. These interturn defects can cause unwanted local increases in magnetic flux that cause (partial) demagnetization of the PMs. In order to account for this, they included this demagnetization in their model. This is done by estimating the magnetic flux density in the air gap based on the stator currents and healthy PMs in the machine. From this information, it can be deducted where the magnets operate below the knee point of the B-H curve, causing irreversible demagnetization to that part of the magnets. Their algorithm then updates the remanent magnetization value of the PMs and calculates the air gap magnetic field again. After some iterations, a solution is found and both the demagnetization defect as the interturn defect are diagnosed.

2.3.3 Voltage-based detection

In this section, voltage-based detection techniques, each with their merits and drawbacks are described. These techniques are interesting when fault harmonics are filtered out of the stator current spectrum by the winding configuration. As expected, these techniques have their limitations and downsides as well, which will be discussed below.

The authors of [183, 184] made an analytical model of a radial machine to simulate demagnetization defects. The back-EMF of the machine is calculated. By combining these data with data from the defected machine, a gradient-based algorithm is used to extract the demagnetization defect information.

By the introduction of extra harmonic content because of demagnetization defects, a Zero Sequence Voltage Component (ZSVC) will occur. In [107, 185, 186], this voltage component is measured and used as an index for the demagnetization fault. Although this requires low computational time, a connection to the neutral point of the stator winding phase connections is needed. The Pulse Width Modulation (PWM) of the inverter injects ZSVC into the machine. This can be eliminated from the measurements by inserting resistors in star connection between the inverter and the machine to create a neutral point as measuring reference of the ZSVC measurement. Speed variations can impact the ZSVC as well.

The authors of [187] used the direct V_{d} and quadrature voltage V_{q} as indicator to diagnose demagnetization, static eccentricity and interturn faults. They succeeded in discriminating between the three defects. In vector control, the d-q current are used in order to control the machine. The machine is compared at the same d-q current. This means the d-q voltage is free to change depending on the defect. In case of a demagnetization defect, both the Vdirect and the V_{q} will de-

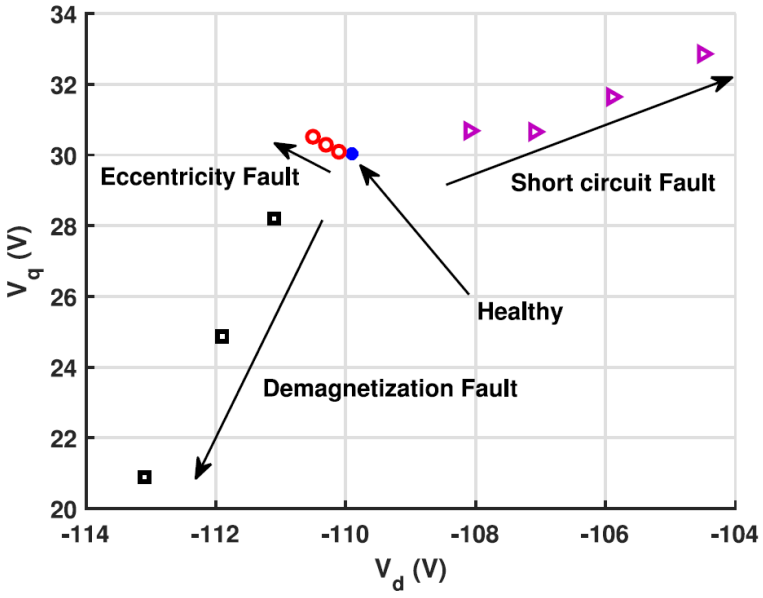

Figure 2.20: V_{d}-V_{q} diagram of experimental results showing the alterations of caused by the defects [187].

crease, moving the working point to the lower left side in a V_{d}-V_{q} diagram. If the machine has a static eccentricity defect, the Vdirect will decrease and the V_{q} will increase, moving the working point to the upper left side of the V_{d}-V_{q} diagram. When a interturn defect is introduced, both the Vdirect and V_{q} is increased, moving the working point to the upper right side of the V_{d}-V_{q} diagram. An example of this can be seen in figure 2.20.

The authors of [54] used sensing coils to detect eccentricity online. Three sensing coils are placed on the stator cores, but with an angle of 120 degrees between each of them. The three sensing coils are connected in series. In healthy situations, the vector sum of the voltages of the three sensing coils is zero. But if eccentricity occurs, this balance is disturbed and the vector sum results in a non-zero voltage vector. The angle of the voltage vector can be used to determine the position of the minimum air gap width caused by the eccentricity. It is possible to differentiate between static and dynamic eccentricity, because the voltage vector is stationary in the former case and rotating in the latter.

2.3.4 Torque-based detection

Torque sensors are commonly used to extract the torque signal data from the machine. These sensors are more expensive and are prone to vibrations of the machine causing higher noise in the raw data. This is why this type of detection techniques

are less common.

The air gap flux density is modified by demagnetization defects. This increases the torque ripple of the machine. The defect also increases the Amplitude of the Side-Band Components (ASBC) of the torque. The authors of [62] uses the normalized ASBC of the torque for demagnetization detection. The ASBC pattern is influenced by saturation, supply voltage harmonic content and speed variations. Due to the normalization, it is independent of the machine load. The authors were not able to distinguish between eccentricity and demagnetization defects.

The technique based on the ASBC has been extracted by [62] with the Time Delay Embedding (TDE) technique. This method can be used for fault detection on itself as well. TDE represents the torque time signal in a 2-D plot. The data forms a circle. A smaller radius of the circle indicates a higher demagnetization defect. This parameter is influenced by the load, which means that the diagnoses needs to be done for the same load as the healthy reference. The advantages and disadvantages are similar to the ASBC technique. TDE can also be used to detect eccentricity as was done in [188]. Here, no circle is formed, but the shape is indicative for the eccentricity defect.

The authors of [169] proposed a certain parameter as an index to estimate demagnetization. This parameter is the torque divided by the current of the DC-link, which is a constant in certain conditions. Demagnetization will alter this parameter. In [169], a method for estimating the proposed parameter by estimating the back-EMF and dividing it by the rotation speed was provided. The back-EMF is calculated by the measured terminal voltages and currents. The downside of the method is the error on the estimation. This is countered in [189] by calculating the parameter more directly. This increases the precision, but has several disadvantages as well. The parameter is obtained by supplying the motor with a direct current and rotating it with an external device. By measuring the terminal voltages and by using the direct current and the rotation speed, the parameter is determined. This makes it an offline method. Although it does not require dismantling the motor, it does require disconnecting the load and attaching an external device for rotation.

Demagnetization and eccentricity create a force unbalance in the machine, the so-called unbalanced magnetic pull. This will influence the shaft trajectory. By tracking a point on the shaft, the defect can be estimated [167]. The measurement must be done without altering the shaft trajectory, so a non-contact measurement system, i.e. two interferometers are used: one for each axis. Uniform demagnetization over the whole machine cannot be detected with this technique. The advantages are that this technique is online and non-invasive.

2.3.5 Loss-based detection

As the defects in a machine alter the internal flux distribution, current flows, etc. extra losses will occur. Loss-based detection techniques make use of this effect to

estimate the machine's health and diagnose the specific defect.

In demagnetized conditions, the extra induced harmonics in the back-EMF of the machine introduce circulating currents in machines with parallel branches in the stator coils. These currents increase the losses of the machine. In [168], the total losses are measured at no-load. This is used as an indicator to estimate the demagnetization defect. This requires reference data of the healthy machine and no-load conditions during measurement. They introduced a demagnetization by removing 25% of the magnets in one pole of there machine. This increases the total losses at 1200 RPM in no-load from 54.60 J to 55.87 J. According to the authors, this difference can be measured and used as a demagnetization detection index.

2.3.6 Conclusion

This chapter introduces the axial flux permanent magnet synchronous machine and explains why this is an interesting machine for sustainable applications. It gives an overview of the maintenance programs and explains why predictive maintenance and condition monitoring is important. Finally, it gives an overview of the current condition monitoring techniques and shows a lack for sensorless demagnetization and eccentricity detection in axial flux permanent magnet machines.

Chapter 3

Forward model

In Chapter 2, we have given an overview of the literature regarding the models and detection techniques currently examined. The literature lacks an accurate analytical model that makes combined detection of eccentricity and demagnetization possible for machines with two air gaps. Therefore, a model is developed with the following properties.

- The model describes a single-stator double-rotor AFPMSM topology with two air gaps, which allows for asymmetrical defects.
- The combination of eccentricity and demagnetization defects is studied.
- The model needs to be useful for sensorless fault detection, based on the frequency spectrum of computed back-EMF and terminal voltages.
- Due to the iterative detection technique, the model is required to have a short computation time of a few seconds. The proposed model achieves approximately 1 s.
- The rotor back-iron is assumed to have an infinite permeability. The stator permeability is that of real silicon steel.
- The model functions for both distributed and concentrated windings.

3.1 Schematic overview of the forward model

The authors of [190] compared three common techniques of analytically modeling an AFPMSM. The models where compared with FEM model data. Both CPU time and flux density are compared and based on this, it can be concluded that the Schwarz-Christoffel Model (SC Model) is a good compromise between speed and accuracy. Therefore, the analytical model of this work will be build based on the SC Model design described in [190].

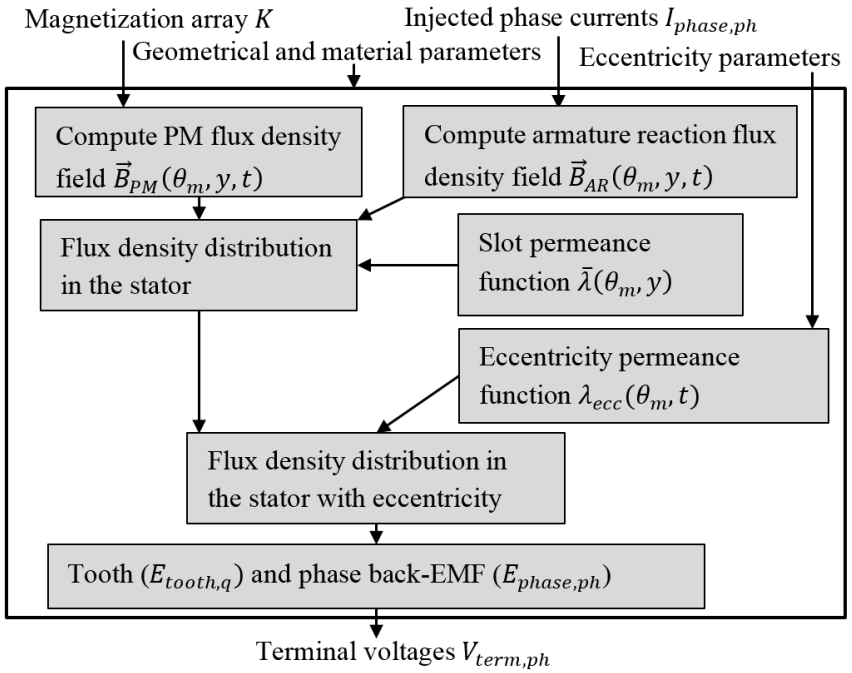

Figure 3.1: Flowchart of the analytical model.

A flowchart of the analytical model is shown in figure 3.1. It will be used in further chapters to study demagnetization and eccentricity defects. This section gives an overview of the structure, while the next sections explain the details of each part of the model.

The four types of inputs of this model are: the geometry, the currents injected in the machine, magnetization factors for each magnet and eccentricity defect coefficients. The last two types contain information about the defects.

The model computes the flux density caused by the magnets only, and the flux density caused by the stator currents (armature reaction). The two models - explained in Sections 3.2.2 and 3.2.3 – neglect slotting effect. Both flux density distributions are superimposed, which means of course that saturation is not taken into account. To account for the slotting effect, the flux density distribution is modified via a permeance function, explained in Section 3.2.4. A second permeance function is used for modeling the effect of eccentricity (Section 3.3). Finally, the total flux density is obtained, and post-processing quantities are computed such as EMFs and terminal voltages. This is explained in Section 3.4.

The output of the model is the terminal voltage in the different phases.

3.2 Forward model with demagnetization defects

3.2.1 Magnetization of permanent magnets including defects

First, a 2D calculation plan is defined to simulate the machine. This is done by placing a cylindrical cross-section in the machine, as can be seen in figure 3.2. Unrolling this cross-section results in a 2D calculation plane with periodicity constraints at the boundaries in the circumference direction. The radius of the cylinder is large enough so that curvature effects can be neglected. A cartesian coordinate system is defined in the plane with x and y denoting the circumferential and axial direction. As x is used for the circumferential distance, θ_m is used for the mechanical circumferential angle, which is defined as:

$$\theta_m = \frac{\pi}{\tau_{\mathrm{m}}} x \tag{3.1}$$

with τ_{m} defined as half of the circumference. To perform a multislice 2D calculation [191], the simulations are performed for several 2D calculation planes at multiple radial positions. This results in a quasi-3D simulation. This assumes that the radial flux is negligible. When the machine is evaluated only in healthy operation, symmetry can be used to limit the calculation plane to half of the machine. However, the model developed in this chapter simulates the whole machine because the model needs to allow asymmetrical defects.

The source of the magnetic flux density at no-load are the PMs. The magnetization M of the PMs can be represented by a square wave in function of the circumference as shown in figure 3.3. Every square represents one magnet. A magnetization that induces a magnetic field directed from the left to the right rotor is defined as a positive magnetization. It can been seen that the magnet direction alternates along the circumferential direction. As discussed in Chapter 2, the magnets magnetization on the two rotors is chosen so that they induce a magnetic field in the same direction. This means that in healthy state, the left rotor's magnetization square wave will be identical to the right rotor's magnetization square wave. The magnetization square waves of the two rotors will not be identical when an asymmetrical demagnetization defect occurs.

In a healthy state, the magnetization can be divided in N_p identical parts, with N_p the number of pole pairs. This would suggest that only a period of $2\pi/N_p$ should be examined. But in faulty operations, the magnets will not have identical magnetization, and therefore breaking the periodicity of the pole pairs. This means the complete circumference of the machine is the base period. τ_{m} was defined as half of the circumference, making the base period $2\tau_{\mathrm{m}}$.

The widths of the squares in the magnetization square wave are determined by the width of the magnets. The space between the squares with zero magnetization corresponds with the space between the magnets. The amplitude of the magnetization square of each separate magnet is given by:

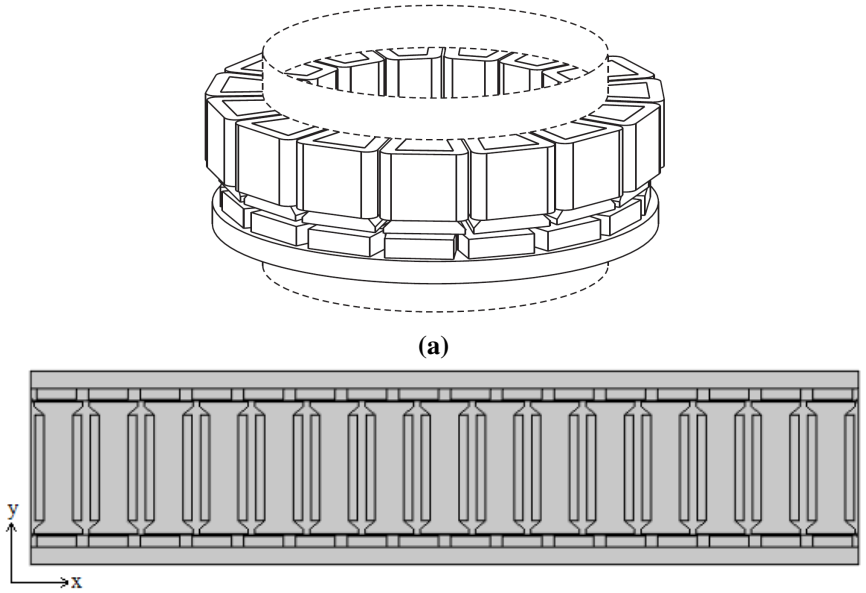

(a)

(b)

Figure 3.2: (a) The cylindrical calculation plane across a 16 pole pair 15 stator slot machine at a certain radius [20]. Half of the machine is shown for clarity, but the calculations of the model later in this chapter are performed on the whole machine. (b) Unrolling this cylindrical calculation plane results in a 2D calculation plane [20].

$$M_{rt,s} = (-1)^s \frac{B_\mathrm{r}}{\mu_0 \mu_{r,M}} K_{,rt,s} \tag{3.2}$$

where B_r is the residual flux density of the PMs, μ_0 is the permeability of vacuum, $\mu_{r,M}$ is the relative permeability of the magnets, s is the magnet number and rt is the index of the rotor. This can either be 'L' or 'R' to denote the left or right rotor respectively. Furthermore, $K_{,rt,s}$ is the magnetization factor for magnet s of every rotor rt. $M_{rt,s}$ is thus the amplitude of the s-th square in the square wave $M(\theta_m)$ of the rt-th rotor.

The magnetization factor $K_{,rt,s}$ contains the demagnetization defect information for that magnet. It ranges between 0 and 1, where 0 represents total demagnetization and 1 represents a healthy magnet. It can be seen as the relative magnetization of that magnet. The magnetization factors of all magnets are contained in an array K. With N_p pole pairs and the machine having two rotors, there are $4N_p$ magnets and therefore $4N_p$ magnetization factors in K. This array therefore contains the complete demagnetization defect information.

The model assumes that the residual flux density per magnet in a partially de-

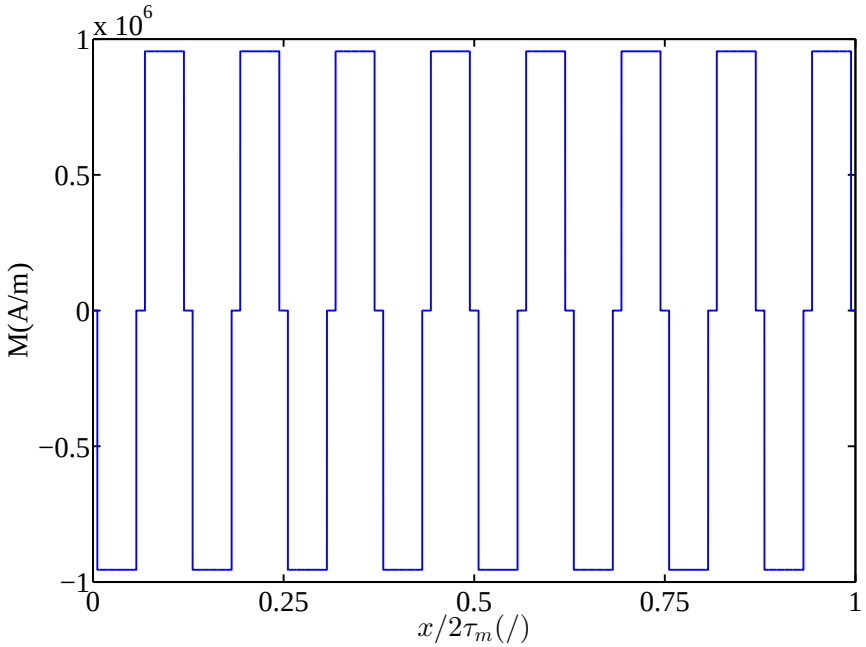

Figure 3.3: Magnetization pattern of the magnets of the right rotor with 8 pole pairs in healthy state.

magnetized state is uniformly distributed in the magnet volume. Evidently, partial demagnetization occurs usually in a non-uniform way in a part of the magnet volume [192]. However, as the analytical model is intended for condition monitoring, it is more important to assess the total flux reduction than to know exactly what part of the magnets is affected. An example of a partially demagnetized rotor is shown in figure 3.4.

The magnetization waveforms of figure 3.3 or figure 3.4 can be written in the frequency domain by using the Fourier form in the stator reference frame:

$$\begin{cases} M_{\mathrm{R}}(x,t) = \sum\limits_{m=-\infty}^{+\infty} M_{\mathrm{R},m} e^{j(\frac{m\pi x}{\tau_{\mathrm{m}}} + \omega_{\mathrm{m}} m t)} \\ M_{\mathrm{L}}(x,t) = \sum\limits_{m=-\infty}^{+\infty} M_{\mathrm{L},m} e^{j(\frac{m\pi x}{\tau_{\mathrm{m}}} + \omega_{\mathrm{m}} m t)} \end{cases} \tag{3.3}$$

with t the time variable, ω_{m} the pulsation, $M_{\mathrm{R},-m} = M_{\mathrm{R},m}^*$ and $M_{\mathrm{L},-m} = M_{\mathrm{L},m}^*$. $M_{\mathrm{R},m}$ and $M_{\mathrm{L},m}$ are the Fourier components for the m-th harmonic of the right and the left rotor respectively. This magnetization is then used to simulate the magnetic fluxes in the machine. By carefully choosing the definition of the magnetization as shown above with the magnetization factors as controllable parameters, demagnetization defects can be imposed in a flexible, fast and accurate way.

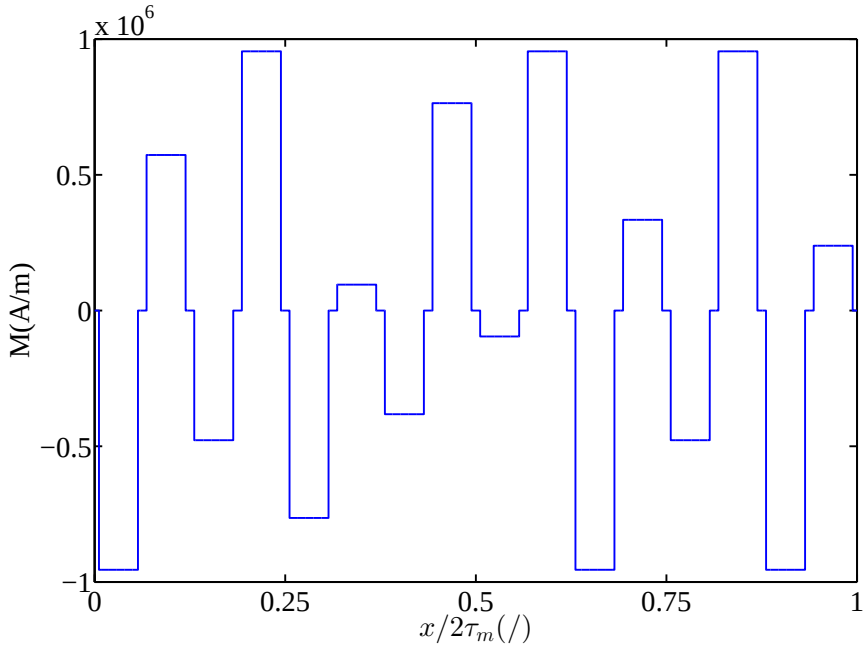

Figure 3.4: Magnetization pattern with partial demagnetization of a number of magnets in the right rotor with N_p = 8. The magnetization pattern is chosen arbitrarily to illustrate the methodology of the magnetization factors.

Note that the space harmonics and time harmonics in the magnetization waveform are the same. The reason for this is that the magnetization of the PM can be considered constant. As the rotor rotates, the flux density field of the magnets simply rotates as well, but furthermore does not change in time. The stator slots will modify the air gap flux density field of the magnets, but this influence cannot be detected by the stator coils because the stator slots are obviously stationary. Therefore, both the space and the time harmonics of the no-load field will be denoted by m as well.

To determine the defects unambiguously, the following notation is used: a demagnetization defect is denoted by a set of three parameters $D = [d_1, d_2, d_3]$ where d_1 is the magnet number s i.e. $d_1 \in [1, \ldots, 2N_p]$, d_2 is the rotor on which the defect occurs rt, i.e. $d_2 \in [\mathrm{L}, \mathrm{R}]$ and d_3 is the magnetization factor $K_{,rt,s}$ corresponding with this magnet number and rotor index, i.e. $0 \leq d_3 \leq 1$.

3.2.2 Permanent Magnet Flux Density Field

The defined magnetization of the previous section is the source term used to calculate the magnetic flux density field in the air gaps of the machine caused by the PMs. This is also called the no-load magnetic flux density field because this

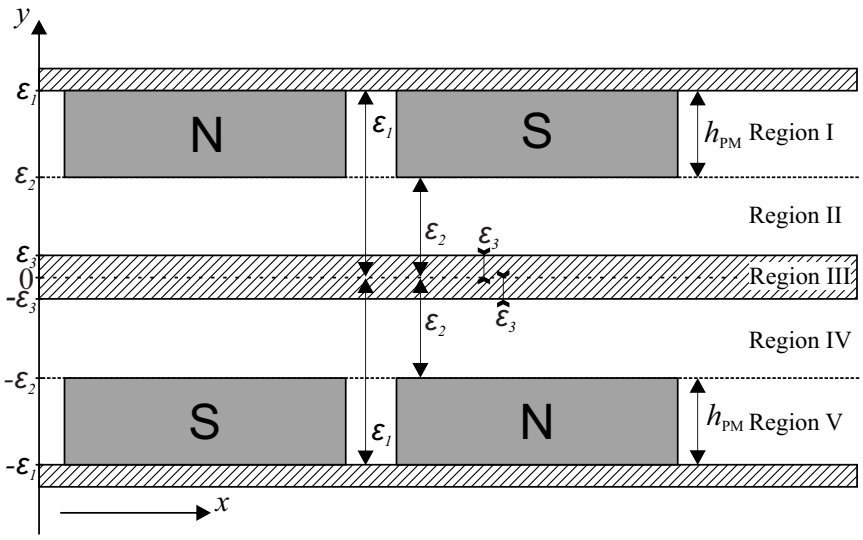

Figure 3.5: 5-region model for PM flux density fields.

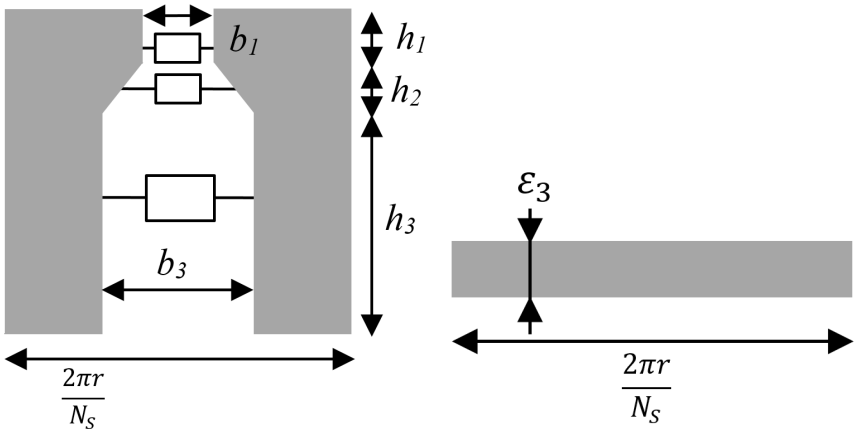

Figure 3.6: One slot pitch with half of the adjacent stator teeth of the real stator (a) and one slot pitch of the homogenized model with equal tangential reluctance (b).

field correspond with the machine operating at no-load i.e. with no current flowing through the stator coils and no torque being produced to drive a load. The PM flux density field in the machine is determined by using a 5-region model in the 2D plane shown in figure 3.5. The machine can be divided into 5 regions: Region I and II are the magnets and the air gap of the right rotor respectively, Region IV and V are the air gap and the magnets of the left rotor and Region III represents a simplified version of the stator.

It is possible to model the stator in full detail including slots with the subdomain model [193, 194], but because the internal fluxes in the stator are not needed for condition monitoring, modeling the detailed stator would be unnecessarily complicated. Therefore, the stator is modeled as a homogenized domain (Region III) with thickness $2\varepsilon_3$. The value ε_3 is determined such that the tangential reluctance of the modeled stator equals that of the real stator, as shown in figure 3.6. This allows a tangential leakage flux similar to the real fluxes. For the real stator, the tangential reluctance is calculated using the geometric parameters defined in figure 3.6a. This is done by calculating the three simple reluctances in the slot shown in figure 3.6a and combining them in parallel. This results in:

$$\mathcal{R}_{tang,real} = \frac{1}{\mu_0 d_{tooth}\left(\frac{h_1}{b_1} + \frac{h_2 \ln\frac{b_3}{b_1}}{b_3 - b_1} + \frac{h_3}{b_3}\right)} \tag{3.4}$$

with d_{tooth} as the stack height. The tangential reluctance of the homogenized domain (Region III) is calculated with the parameters defined in figure 3.6b, and results in:

$$\mathcal{R}_{tang,model} = \frac{2\pi r}{N_S \mu_{r,S} \varepsilon_3 d_{tooth}} \tag{3.5}$$

with r the radius, N_S the number of stator slots and $\mu_{r,S}$ the relative permeability of the real stator. By making $\mathcal{R}_{tang,real}$ = $\mathcal{R}_{tang,model}$, using (3.4) and (3.5), ε_3 is found:

$$\varepsilon_3 = \frac{2\pi r \mu_0}{N_S \mu_{r,S}}\left(\frac{h_1}{b_1} + \frac{h_2 \ln\frac{b_3}{b_1}}{b_3 - b_1} + \frac{h_3}{b_3}\right). \tag{3.6}$$

With this, the effect of the stator slots in the real stator is accounted for in the tangential reluctance of the stator model (Region III), while only a simple isotropic cylinder needs to be simulated. The effect of the stator slots in the air gap flux density field will be implemented with a permeance function in Section 3.2.4.

As was stated previously, the model is intended for use with both symmetrical and asymmetrical defects. The latter are defects where both rotors do not exhibit the same defects. Therefore, symmetry simplifications like only simulating one air gap cannot be used in this model. It is therefore necessary to simulate both air gaps, i.e. both region I and II and region IV and V. Furthermore, removing Region III by making $\varepsilon_3 = 0$ will prevent the tangential flux in the stator. In case of asymmetrical defects, a part of the magnetic flux closes through the stator tangentially. Although this flux is small due to the relatively high reluctance of the stator in the tangential direction, neglecting this flux would result in inaccuracies in case of asymmetrical defects. From this, it follows that $\varepsilon_3 > 0$. Note also that the model does not include induced currents in conducting parts such as the magnets and the stator cores.

Now that the regions are defined, the magnetic fields in these regions can be found by solving the magnetic scalar potential ϕ in every region. Based on [195], this magnetic potential is obtained by solving the following differential equation in all regions:

$$\frac{\partial^2 \phi}{\partial x^2} + \frac{\partial^2 \phi}{\partial y^2} = 0. \tag{3.7}$$

The solution of this differential equation for every region seen from the rotor reference frame can be written as:

$$\begin{cases} I : \phi_1(x,y) = \sum\limits_{m=-\infty}^{+\infty} \left(C_{1,m} e^{\frac{m\pi y}{\tau_\mathrm{m}}} + C_{2,m} e^{-\frac{m\pi y}{\tau_\mathrm{m}}} \right) e^{\frac{jm\pi x}{\tau_\mathrm{m}}} \\ II : \phi_2(x,y) = \sum\limits_{m=-\infty}^{+\infty} \left(C_{3,m} e^{\frac{m\pi y}{\tau_\mathrm{m}}} + C_{4,m} e^{-\frac{m\pi y}{\tau_\mathrm{m}}} \right) e^{\frac{jm\pi x}{\tau_\mathrm{m}}} \\ III : \phi_3(x,y) = \sum\limits_{m=-\infty}^{+\infty} \left(C_{5,m} e^{\frac{m\pi y}{\tau_\mathrm{m}}} + C_{6,m} e^{-\frac{m\pi y}{\tau_\mathrm{m}}} \right) e^{\frac{jm\pi x}{\tau_\mathrm{m}}} \\ IV : \phi_4(x,y) = \sum\limits_{m=-\infty}^{+\infty} \left(C_{7,m} e^{\frac{m\pi y}{\tau_\mathrm{m}}} + C_{8,m} e^{-\frac{m\pi y}{\tau_\mathrm{m}}} \right) e^{\frac{jm\pi x}{\tau_\mathrm{m}}} \\ V : \phi_5(x,y) = \sum\limits_{m=-\infty}^{+\infty} \left(C_{9,m} e^{\frac{m\pi y}{\tau_\mathrm{m}}} + C_{10,m} e^{-\frac{m\pi y}{\tau_\mathrm{m}}} \right) e^{\frac{jm\pi x}{\tau_\mathrm{m}}}. \end{cases} \tag{3.8}$$

with the unknown coefficients $C_{1,m}$ to $C_{10,m}$ also called the integration constants of the solution. From this, the magnetic fields can be deduced:

$$H_{\mathrm{PM},x} = -\frac{\partial \phi}{\partial x}, \qquad H_{\mathrm{PM},y} = -\frac{\partial \phi}{\partial y} \tag{3.9}$$

and the magnetic flux density can be found by the following constitutive equation:

$$\vec{B}_\mathrm{PM} = \mu(\vec{M} + \vec{H}_\mathrm{PM}) \tag{3.10}$$

with μ the permeability of the material and M the magnetization at the location where the equation is applied. In Region I and V, the magnetization will only have an axial (y-direction) component because the magnets are all positioned with their magnetization in the axial direction. In these regions, the axial component of the magnetization vector in both rotors is given by (3.3) as a function of x and t. In the other regions, there is no source of magnetization and therefore M will be zero in those regions.

In order to retrieve the scalar potential and thus the magnetic flux density at no-load, the integration coefficients $C_{1,m}$ to $C_{10,m}$ need to be determined. This requires solving a system of equations with as much equations as there are unknowns (i.e. the integration coefficients). In the case of (3.8), this means that 10 equations per harmonic order needs to be found. The equations can be extracted from the boundary conditions between the regions.

There are six boundaries between the regions: see figure 3.5. The two boundaries with the rotor back-irons $y = \varepsilon_1$ and $y = -\varepsilon_1$ have as condition that the magnetic field impinges the iron perpendicularly, meaning the magnetic field parallel to the iron surface must be zero. The four remaining boundary conditions at $y = \varepsilon_2$, $y = \varepsilon_3$, $y = -\varepsilon_3$ and $y = -\varepsilon_2$ enforce continuity of the normal flux density component and the tangential magnetic field component. In total, this results in ten boundary conditions for each considered harmonic:

$$
\begin{cases}
H_{\mathrm{PM},x\mathrm{I}}(x,y)|_{[y=\varepsilon_1]} = 0 \\
H_{\mathrm{PM},x\mathrm{V}}(x,y)|_{[y=-\varepsilon_1]} = 0
\end{cases}
$$

$$
\begin{cases}
B_{\mathrm{PM},y\mathrm{I}}(x,y)|_{[y=\varepsilon_2]} = B_{\mathrm{PM},y\mathrm{II}}(x,y)|_{[y=\varepsilon_2]} \\
H_{\mathrm{PM},x\mathrm{I}}(x,y)|_{[y=\varepsilon_2]} = H_{\mathrm{PM},x\mathrm{II}}(x,y)|_{[y=\varepsilon_2]}
\end{cases}
$$

$$
\begin{cases}
B_{\mathrm{PM},y\mathrm{II}}(x,y)|_{[y=\varepsilon_3]} = B_{\mathrm{PM},y\mathrm{III}}(x,y)|_{[y=\varepsilon_3]} \\
H_{\mathrm{PM},x\mathrm{II}}(x,y)|_{[y=\varepsilon_3]} = H_{\mathrm{PM},x\mathrm{III}}(x,y)|_{[y=\varepsilon_3]}
\end{cases}
\tag{3.11}
$$

$$
\begin{cases}
B_{\mathrm{PM},y\mathrm{III}}(x,y)|_{[y=-\varepsilon_3]} = B_{\mathrm{PM},y\mathrm{IV}}(x,y)|_{[y=-\varepsilon_3]} \\
H_{\mathrm{PM},x\mathrm{III}}(x,y)|_{[y=-\varepsilon_3]} = H_{\mathrm{PM},x\mathrm{IV}}(x,y)|_{[y=-\varepsilon_3]}
\end{cases}
$$

$$
\begin{cases}
B_{\mathrm{PM},y\mathrm{IV}}(x,y)|_{[y=-\varepsilon_2]} = B_{\mathrm{PM},y\mathrm{V}}(x,y)|_{[y=-\varepsilon_2]} \\
H_{\mathrm{PM},x\mathrm{IV}}(x,y)|_{[y=-\varepsilon_2]} = H_{\mathrm{PM},x\mathrm{V}}(x,y)|_{[y=-\varepsilon_2]}.
\end{cases}
$$

By combining (3.8) to (3.11), the following system of equations is found for the m-th harmonic:

$$
\begin{cases}
C_{1,m}e^{\frac{m\pi\varepsilon_1}{\tau_\mathrm{m}}} + C_{2,m}e^{-\frac{m\pi\varepsilon_1}{\tau_\mathrm{m}}} = 0 \\
C_{9,m}e^{-\frac{m\pi\varepsilon_1}{\tau_\mathrm{m}}} + C_{10,m}e^{\frac{m\pi\varepsilon_1}{\tau_\mathrm{m}}} = 0
\end{cases}
\begin{cases}
C_{1,m}\frac{\mu_M m\pi}{\tau_\mathrm{m}}e^{\frac{m\pi\varepsilon_2}{\tau_\mathrm{m}}} - C_{2,m}\frac{\mu_M m\pi}{\tau_\mathrm{m}}e^{-\frac{m\pi\varepsilon_2}{\tau_\mathrm{m}}} - C_{3,m}\frac{\mu_0 m\pi}{\tau_\mathrm{m}}e^{\frac{m\pi\varepsilon_2}{\tau_\mathrm{m}}} \\
+C_{4,m}\frac{\mu_0 m\pi}{\tau_\mathrm{m}}e^{-\frac{m\pi\varepsilon_2}{\tau_\mathrm{m}}} = \mu_M M_{\mathrm{R},m} \\
C_{3,m}\mu_0 e^{\frac{m\pi\varepsilon_3}{\tau_\mathrm{m}}} - C_{4,m}\mu_0 e^{-\frac{m\pi\varepsilon_3}{\tau_\mathrm{m}}} - C_{5,m}\mu_S e^{\frac{m\pi\varepsilon_3}{\tau_\mathrm{m}}} + C_{6,m}\mu_S e^{-\frac{m\pi\varepsilon_3}{\tau_\mathrm{m}}} = 0
\end{cases}
\begin{cases}
C_{5,m}\mu_S e^{-\frac{m\pi\varepsilon_3}{\tau_\mathrm{m}}} - C_{6,m}\mu_S e^{\frac{m\pi\varepsilon_3}{\tau_\mathrm{m}}} - C_{7,m}\mu_0 e^{-\frac{m\pi\varepsilon_3}{\tau_\mathrm{m}}} + C_{8,m}\mu_0 e^{\frac{m\pi\varepsilon_3}{\tau_\mathrm{m}}} = 0 \\
-C_{7,m}\frac{\mu_0 m\pi}{\tau_\mathrm{m}}e^{-\frac{m\pi\varepsilon_2}{\tau_\mathrm{m}}} + C_{8,m}\frac{\mu_0 m\pi}{\tau_\mathrm{m}}e^{\frac{m\pi\varepsilon_2}{\tau_\mathrm{m}}} + C_{9,m}\frac{\mu_M m\pi}{\tau_\mathrm{m}}e^{-\frac{m\pi\varepsilon_2}{\tau_\mathrm{m}}} \\
-C_{10,m}\frac{\mu_M m\pi}{\tau_\mathrm{m}}e^{\frac{m\pi\varepsilon_2}{\tau_\mathrm{m}}} = \mu_M M_{\mathrm{L},m}
\end{cases}
\begin{cases}
C_{1,m}e^{\frac{m\pi\varepsilon_2}{\tau_\mathrm{m}}} + C_{2,m}e^{-\frac{m\pi\varepsilon_2}{\tau_\mathrm{m}}} - C_{3,m}e^{\frac{m\pi\varepsilon_2}{\tau_\mathrm{m}}} - C_{4,m}e^{-\frac{m\pi\varepsilon_2}{\tau_\mathrm{m}}} = 0 \\
C_{3,m}e^{\frac{m\pi\varepsilon_3}{\tau_\mathrm{m}}} + C_{4,m}e^{-\frac{m\pi\varepsilon_3}{\tau_\mathrm{m}}} - C_{5,m}e^{\frac{m\pi\varepsilon_3}{\tau_\mathrm{m}}} - C_{6,m}e^{-\frac{m\pi\varepsilon_3}{\tau_\mathrm{m}}} = 0
\end{cases}
\begin{cases}
C_{5,m}e^{-\frac{m\pi\varepsilon_3}{\tau_\mathrm{m}}} + C_{6,m}e^{\frac{m\pi\varepsilon_3}{\tau_\mathrm{m}}} - C_{7,m}e^{-\frac{m\pi\varepsilon_3}{\tau_\mathrm{m}}} - C_{8,m}e^{\frac{m\pi\varepsilon_3}{\tau_\mathrm{m}}} = 0 \\
C_{7,m}e^{-\frac{m\pi\varepsilon_2}{\tau_\mathrm{m}}} + C_{8,m}e^{\frac{m\pi\varepsilon_2}{\tau_\mathrm{m}}} - C_{9,m}e^{-\frac{m\pi\varepsilon_2}{\tau_\mathrm{m}}} - C_{10,m}e^{\frac{m\pi\varepsilon_2}{\tau_\mathrm{m}}} = 0.
\end{cases}
\tag{3.12}
$$

Here, μ_S and μ_M are the absolute permeability of the stator and the magnets respectively. By solving this system of ten equations and ten unknowns per harmonic order, the integration constants $C_{1,m}$ to $C_{10,m}$ and therefore the solution of the scalar potential ϕ in every region is found. By utilizing (3.9) and (3.10), the magnetic flux density $B_{\mathrm{PM}}(x,y)$ can be found in every region:

$$
\begin{cases}
B_{\mathrm{PM},y\mathrm{I}}(x,y) = \sum\limits_{m=-\infty}^{+\infty} \left[\mu_M M_{\mathrm{R},m} - \frac{\mu_M m\pi}{\tau_\mathrm{m}} \left(C_{1,m} e^{\frac{m\pi y}{\tau_\mathrm{m}}} - C_{2,m} e^{-\frac{m\pi y}{\tau_\mathrm{m}}}\right)\right] \\
\cdot e^{\frac{jm\pi x}{\tau_\mathrm{m}}} \\
B_{\mathrm{PM},x\mathrm{I}}(x,y) = \sum\limits_{m=-\infty}^{+\infty} -j\frac{\mu_M m\pi}{\tau_\mathrm{m}} \left(C_{1,m} e^{\frac{m\pi y}{\tau_\mathrm{m}}} + C_{2,m} e^{-\frac{m\pi y}{\tau_\mathrm{m}}}\right) e^{\frac{jm\pi x}{\tau_\mathrm{m}}}
\end{cases}
$$

$$
\begin{cases}
B_{\mathrm{PM},y\mathrm{II}}(x,y) = \sum\limits_{m=-\infty}^{+\infty} -\frac{\mu_0 m\pi}{\tau_\mathrm{m}} \left(C_{3,m} e^{\frac{m\pi y}{\tau_\mathrm{m}}} - C_{4,m} e^{-\frac{m\pi y}{\tau_\mathrm{m}}}\right) e^{\frac{jm\pi x}{\tau_\mathrm{m}}} \\
B_{\mathrm{PM},x\mathrm{II}}(x,y) = \sum\limits_{m=-\infty}^{+\infty} -j\frac{\mu_0 m\pi}{\tau_\mathrm{m}} \left(C_{3,m} e^{\frac{m\pi y}{\tau_\mathrm{m}}} + C_{4,m} e^{-\frac{m\pi y}{\tau_\mathrm{m}}}\right) e^{\frac{jm\pi x}{\tau_\mathrm{m}}}
\end{cases}
$$

$$
\begin{cases}
B_{\mathrm{PM},y\mathrm{III}}(x,y) = \sum\limits_{m=-\infty}^{+\infty} -\frac{\mu_S m\pi}{\tau_\mathrm{m}} \left(C_{5,m} e^{\frac{m\pi y}{\tau_\mathrm{m}}} - C_{6,m} e^{-\frac{m\pi y}{\tau_\mathrm{m}}}\right) e^{\frac{jm\pi x}{\tau_\mathrm{m}}} \\
B_{\mathrm{PM},x\mathrm{III}}(x,y) = \sum\limits_{m=-\infty}^{+\infty} -j\frac{\mu_S m\pi}{\tau_\mathrm{m}} \left(C_{5,m} e^{\frac{m\pi y}{\tau_\mathrm{m}}} + C_{6,m} e^{-\frac{m\pi y}{\tau_\mathrm{m}}}\right) e^{\frac{jm\pi x}{\tau_\mathrm{m}}}
\end{cases}
$$

$$
\begin{cases}
B_{\mathrm{PM},y\mathrm{IV}}(x,y) = \sum\limits_{m=-\infty}^{+\infty} -\frac{\mu_0 m\pi}{\tau_\mathrm{m}} \left(C_{7,m} e^{\frac{m\pi y}{\tau_\mathrm{m}}} - C_{8,m} e^{-\frac{m\pi y}{\tau_\mathrm{m}}}\right) e^{\frac{jm\pi x}{\tau_\mathrm{m}}} \\
B_{\mathrm{PM},x\mathrm{IV}}(x,y) = \sum\limits_{m=-\infty}^{+\infty} -j\frac{\mu_0 m\pi}{\tau_\mathrm{m}} \left(C_{7,m} e^{\frac{m\pi y}{\tau_\mathrm{m}}} + C_{8,m} e^{-\frac{m\pi y}{\tau_\mathrm{m}}}\right) e^{\frac{jm\pi x}{\tau_\mathrm{m}}}
\end{cases}
$$

$$
\begin{cases}
B_{\mathrm{PM},y\mathrm{V}}(x,y) = \sum\limits_{m=-\infty}^{+\infty} \left[\mu_M M_{\mathrm{L},m} - \frac{\mu_M m\pi}{\tau_\mathrm{m}} \left(C_{9,m} e^{\frac{m\pi y}{\tau_\mathrm{m}}} - C_{10,m} e^{-\frac{m\pi y}{\tau_\mathrm{m}}}\right)\right] \\
\cdot e^{\frac{jm\pi x}{\tau_\mathrm{m}}} \\
B_{\mathrm{PM},x\mathrm{V}}(x,y) = \sum\limits_{m=-\infty}^{+\infty} -j\frac{\mu_M m\pi}{\tau_\mathrm{m}} \left(C_{9,m} e^{\frac{m\pi y}{\tau_\mathrm{m}}} + C_{10,m} e^{-\frac{m\pi y}{\tau_\mathrm{m}}}\right) e^{\frac{jm\pi x}{\tau_\mathrm{m}}}.
\end{cases}
\tag{3.13}
$$

This gives the magnetic flux density in the machine induced by the PMs only. So this is the no-load field without slots and without eccentricity. Modeling the slots will be included in Section 3.2.4 and the eccentricity in Section 3.3. The solutions can be written as a Fourier series with as base period again one mechanical rotation. As previously mentioned, this period is chosen because in defected state, the machine's magnetic field in the N_p pole pairs will not be identical.

The magnetic flux density distribution in (3.13) is seen in the rotor reference frame. It has no time dependency if the slotting effect is neglected.

When viewing from the stator reference frame, the rotation needs to be included. This will introduce a time component in the equations. Taking (3.1) into account, the resulting B_{PM} can be written in a Fourier series:

$$
B_{\mathrm{PM}}(x,y,t) = \sum_{m=-\infty}^{+\infty} B_{\mathrm{PM},m} e^{j(m\theta_m + m\omega_\mathrm{m} t)} \tag{3.14}
$$

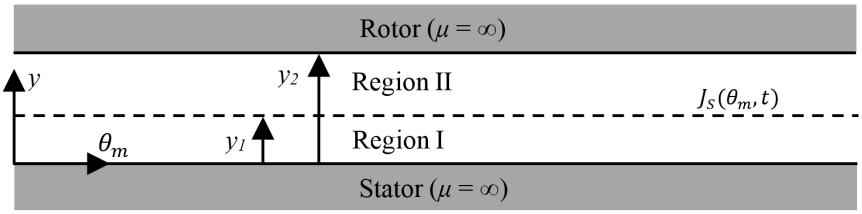

Figure 3.7: 2-region model for calculation of armature reaction [191].

with the B_{PM} as the harmonic components of this magnetic flux density. The circumferential axis is express in the mechanical circumference angle θ_m to make it conform with the remainder of this chapter. Beside the rotation, the magnetic field of the PMs cannot change over time. This means for this field that m is the harmonic number for both space and time. This is valid for each region and for both x and y components, i.e. for each equation in (3.13). Notice that because of the chosen base period of one rotation, there is no factor N_p in the equation.

3.2.3 Armature Reaction flux density field

For the modeling of the Armature Reaction (AR) magnetic field, the magnetic field induced by the stator currents in the stator coils, the method of [191] is used. There is no influence of demagnetization defects on the armature reaction flux density field if saturation is neglected. In Section 3.3, the influence of asymmetrical eccentricity defects on the armature flux density field will be accounted for. As there is no influence from demagnetization, this means only one air gap needs to be modeled because the AR magnetic field is symmetrical in both healthy and demagnetized situations. As previously mentioned, the sources of the armature flux density field are the stator currents. These are implemented by using a current sheet. This is a fictional plane splitting the air gap in two regions, i.e. region I and region II, as shown in figure 3.7. The currents are assumed to flow in this plane. The current sheet is written as:

$$J_{\mathrm{S}}(\theta_m, t) = \sum_{m=-\infty}^{+\infty} \sum_{u=-\infty}^{+\infty} J_{\mathrm{S},u,m} e^{j(u\theta_m + m\omega_{\mathrm{m}} t)}. \tag{3.15}$$

Here $J_{\mathrm{S},u,m}$ is a set of harmonic components in both space and time and u and m are the harmonic number in space and time respectively. The base period for space and time is again one mechanical revolution of the machine.

The magnetic field in the regions can be found by solving the magnetic vector potential A in every region:

$$\begin{cases} A_I(\theta_m, y, t) = \sum\limits_{m=-\infty}^{+\infty} \sum\limits_{u=-\infty}^{+\infty} -\mu_0 \frac{r}{u} \frac{\cosh\left(\frac{u}{r}[y_2 - y_1]\right)}{\sinh\left(\frac{u}{r} y_2\right)} \\ \cdot \cosh\left(\frac{u}{r} y\right) J_{\mathrm{S},u,m} e^{j(u\theta_m + m\omega_\mathrm{m} t)} \\ A_{II}(\theta_m, y, t) = \sum\limits_{m=-\infty}^{+\infty} \sum\limits_{u=-\infty}^{+\infty} -\mu_0 \frac{r}{u} \frac{\cosh\left(\frac{u}{r} y_1\right)}{\sinh\left(\frac{u}{r} y_2\right)} \\ \cdot \cosh\left(\frac{u}{r}[y_2 - y]\right) J_{\mathrm{S},u,m} e^{j(u\theta_m + m\omega_\mathrm{m} t)}. \end{cases} \tag{3.16}$$

From this, the magnetic field can be derived with:

$$H_{\mathrm{AR},\theta_m} = \frac{1}{\mu_0} \frac{\partial A}{\partial y}, \qquad H_{\mathrm{AR},y} = -\frac{1}{r\mu_0} \frac{\partial A}{\partial \theta_m}; \tag{3.17}$$

and the magnetic flux density as:

$$\vec{B}_\mathrm{AR} = \mu \vec{H}_\mathrm{AR}. \tag{3.18}$$

This results in a magnetic flux density for the AR as follows:

$$\begin{cases} B_{\mathrm{AR},y\mathrm{I}}(\theta_m, y, t) = \sum\limits_{m=-\infty}^{+\infty} \sum\limits_{u=-\infty}^{+\infty} j\mu_0 \frac{\cosh\left(\frac{u}{r}(y_2 - y_1)\right)}{\sinh\left(\frac{u}{r} y_2\right)} \\ \cdot \cosh\left(\frac{u}{r} y\right) J_{\mathrm{S},u} e^{j(u\theta_m + m\omega_\mathrm{m} t)} \\ B_{\mathrm{AR},\theta_m\mathrm{I}}(\theta_m, y, t) = \sum\limits_{m=-\infty}^{+\infty} \sum\limits_{u=-\infty}^{+\infty} -\mu_0 \frac{\cosh\left(\frac{u}{r}(y_2 - y_1)\right)}{\sinh\left(\frac{u}{r} y_2\right)} \\ \cdot \sinh\left(\frac{u}{r} y\right) J_{\mathrm{S},u} e^{j(u\theta_m + m\omega_\mathrm{m} t)} \end{cases} \tag{3.19}$$

$$\begin{cases} B_{\mathrm{AR},y\mathrm{II}}(\theta_m, y, t) = \sum\limits_{m=-\infty}^{+\infty} \sum\limits_{u=-\infty}^{+\infty} j\mu_0 \frac{\cosh\left(\frac{u}{r} y_1\right)}{\sinh\left(\frac{u}{r} y_2\right)} \\ \cdot \cosh\left(\frac{u}{r}(y_2 - y)\right) J_{\mathrm{S},u} e^{j(u\theta_m + m\omega_\mathrm{m} t)} \\ B_{\mathrm{AR},\theta_m\mathrm{II}}(\theta_m, y, t) = \sum\limits_{m=-\infty}^{+\infty} \sum\limits_{u=-\infty}^{+\infty} \mu_0 \frac{\cosh\left(\frac{u}{r} y_1\right)}{\sinh\left(\frac{u}{r} y_2\right)} \\ \cdot \sinh\left(\frac{u}{r}(y_2 - y)\right) J_{\mathrm{S},u} e^{j(u\theta_m + m\omega_\mathrm{m} t)} \end{cases}$$

with y_1 determining the position of the current sheet. The real current flows in the stator coils. Placing the current sheet adjacent to the stator in the air gap results in the required accuracy for this model, as can be seen in Section 3.5. The resulting B_AR can be written as a classical Fourier series:

$$B_\mathrm{AR}(\theta_m, y, t) = \sum_{m=-\infty}^{+\infty} \sum_{u=-\infty}^{+\infty} B_{\mathrm{AR},u,m} e^{j(u\theta_m + m\omega_\mathrm{m} t)} \tag{3.20}$$

with B_AR as $B_{\mathrm{AR},y\mathrm{I}}$, $B_{\mathrm{AR},\theta_m\mathrm{I}}$, $B_{\mathrm{AR},y\mathrm{II}}$ or $B_{\mathrm{AR},\theta_m\mathrm{II}}$ depending on the region and direction. Similarly, the harmonic amplitude in (3.20) – the factors between the summation symbols and the exponential factor – are generally represented by $B_{\mathrm{AR},u,m}$.

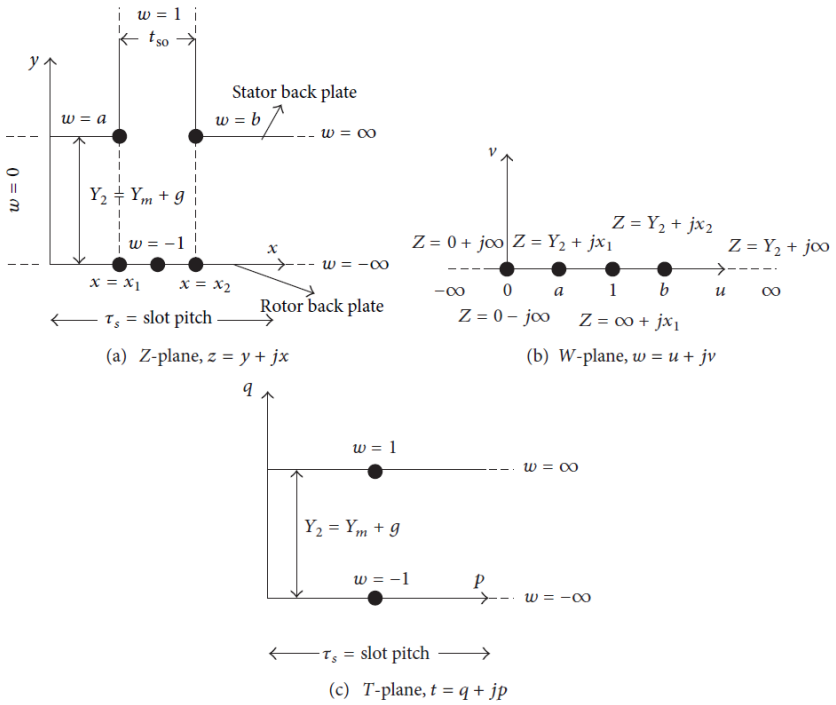

Figure 3.8: (a) The Z-plane representing the slotted air gap, (b) the W-plane representing the midplane and (c) the T-plane representing the smooth air gap [190, 196].

3.2.4 Magnetic field linked with the stator coils

As stated before, for the purpose of this work saturation can be neglected. This means the magnetic flux density field of the PMs and the AR can simply be added together. Based on Sections 3.2.2 and 3.2.3, the total air gap magnetic flux density becomes:

$$\vec{B}_{\text{airgap}} = \vec{B}_{\text{PM}} + \vec{B}_{\text{AR}} \tag{3.21}$$

where $\vec{B}_{\text{PM}}$ is the flux density of the PMs and $\vec{B}_{\text{AR}}$ is the flux density of the AR.

As mentioned, in Sections 3.2.2 and 3.2.3 the stator slotting effect in the air gap is not taken into account. The stator slots are accounted for by creating a permeance function that modifies the air gap flux density. This is introduced by [196] where the shape of the slot is transformed into a smooth air gap as depicted by figure 3.8. For this, a special case of conformal mapping is used: the Schwarz-Christoffel transformation. This transformation maps a complex half plane with only positive imaginary numbers on a polygon.

Both the slotted air gap and the smooth air gap are represented in a complex plane, being the Z-plane and the T-plane respectively. Schwarz-Christoffel con-

formal mapping is used to map the coordinates of the Z-plane on the T-plane. This requires two steps. Firstly, the Z-plane is mapped on a so called mid plane i.e. the W-plane. On this plane, the edges of the stator and rotor correspond with the u-axis. Secondly, this W-plane is transformed into the T-plane where it depicts a smooth air gap. The u-axis corresponds to the edges of the slotless stator and the rotor on this T-plane. The Z-plane is defined as $Z = y + jx$ to match the coordinate system defined in Section 3.2.1.

In [87], the equations for performing these transformations are worked out. These transformations are then inverted and condensed into a permeance function that corrects the axial and tangential flux density for the influence of the stator slots. The correction functions for the axial and the tangential component are combined in a complex function $\overline{\lambda_{\mathrm{sl}}}(\theta_m, y) = \lambda_{\mathrm{sl,real}}(\theta_m, y) + j\lambda_{\mathrm{sl,imag}}(\theta_m, y)$ so that the conjugate multiplied with the air gap flux density of the smooth air gap results in the flux density of the slotted air gap [190].

The real and imaginary part of the permeance function, $\lambda_{\mathrm{sl,real}}$ and $\lambda_{\mathrm{sl,imag}}$ resp. are shown in figure 3.9. This results in a total axial and tangential magnetic flux density without accounting for eccentricity as follows:

$$\begin{cases} B_{\mathrm{airgap,tot},y} = & B_{\mathrm{PM},y}\lambda_{\mathrm{sl,real}} - B_{\mathrm{PM},\theta_m}\lambda_{\mathrm{sl,imag}} \\ & +B_{\mathrm{AR},y}\lambda_{\mathrm{sl,real}} - B_{\mathrm{AR},\theta_m}\lambda_{\mathrm{sl,imag}} \\ B_{\mathrm{airgap,tot},\theta_m} = & B_{\mathrm{PM},\theta_m}\lambda_{\mathrm{sl,real}} + B_{\mathrm{PM},y}\lambda_{\mathrm{sl,imag}} \\ & +B_{\mathrm{AR},\theta_m}\lambda_{\mathrm{sl,real}} + B_{\mathrm{AR},y}\lambda_{\mathrm{sl,imag}}. \end{cases} \tag{3.22}$$

The above is valid for both air gaps. In order to calculate the back-EMF of the stator coils, the flux through the stator coils is needed. Because of the simplified stator modeling, the fluxes in the region III are not identical to the fluxes in the real stator.

The flux going through the stator coils can be found based on the air gap flux density fields. Because the stator is constructed symmetrically, the average flux density over the stator length can be approximated by:

$$B_{\mathrm{av},y} = \frac{B_{\mathrm{airgap,tot},y,\mathrm{L}} + B_{\mathrm{airgap,tot},y,\mathrm{R}}}{2}. \tag{3.23}$$

Here $B_{\mathrm{airgap,tot},y,\mathrm{L}}$ and $B_{\mathrm{airgap,tot},y,\mathrm{R}}$ are the left and the right air gap field at the edge of the stator respectively. This approximation is acceptable because region III in figure 3.5 is able to model tangential fluxes in case of demagnetization defects.

The instantaneous back-EMF in the stator coils can be written as:

$$E_{\mathrm{tooth},q}(t) = -N_{stator} S_T \frac{dB_{\mathrm{av},y}}{dt}. \tag{3.24}$$

were N_{stator} is the number of turns, and S_T is the area of the coil.

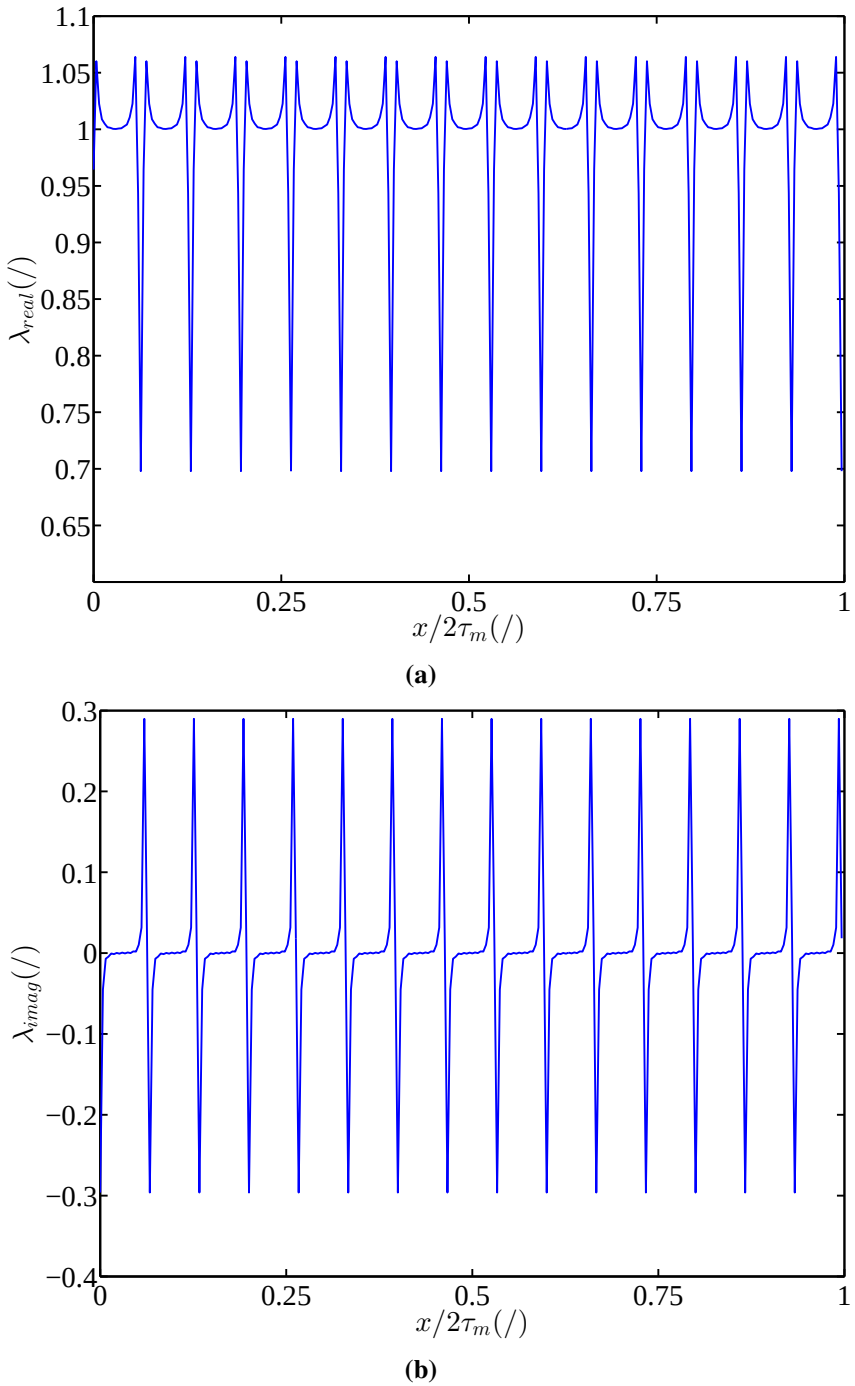

Figure 3.9: Permeance function $\overline{\lambda_{\mathrm{sl}}}$ [196]: (a) Real part $\lambda_{\mathrm{sl,real}}$ and (b) imaginary part $\lambda_{\mathrm{sl,imag}}$.

Section 3.5 shows the validation of the model and proves the acceptability of the approach. Because of stator symmetry, it can be said that:

$$\begin{aligned} \lambda_{\mathrm{sl,realR}} &= \lambda_{\mathrm{sl,realL}} = \lambda_{\mathrm{sl,real}} \\ \lambda_{\mathrm{sl,imagR}} &= -\lambda_{\mathrm{sl,imagL}} = \lambda_{\mathrm{sl,imag}}. \end{aligned} \tag{3.25}$$

By implementing the axial components of (3.22) in (3.23) and using (3.25), the average flux density in the axial direction can be written as:

$$B_{\mathrm{av},y} = B_{\mathrm{PM},y,\mathrm{av}}\lambda_{\mathrm{sl,real}} - B_{\mathrm{PM},\theta_m,\mathrm{av}}\lambda_{\mathrm{sl,imag}} + B_{\mathrm{AR},y,\mathrm{av}}\lambda_{\mathrm{sl,real}} - B_{\mathrm{AR},\theta_m,\mathrm{av}}\lambda_{\mathrm{sl,imag}} \tag{3.26}$$

with:

$$\begin{aligned} B_{\mathrm{PM},y,\mathrm{av}} &= \frac{B_{\mathrm{PM},y,\mathrm{L}} + B_{\mathrm{PM},y,\mathrm{R}}}{2} \\ B_{\mathrm{PM},\theta_m,\mathrm{av}} &= \frac{B_{\mathrm{PM},\theta_m,\mathrm{L}} + B_{\mathrm{PM},\theta_m,\mathrm{R}}}{2} \\ B_{\mathrm{AR},y,\mathrm{av}} &= \frac{B_{\mathrm{AR},y,\mathrm{L}} + B_{\mathrm{AR},y,\mathrm{R}}}{2} \\ B_{\mathrm{AR},\theta_m,\mathrm{av}} &= \frac{B_{\mathrm{AR},\theta_m,\mathrm{L}} + B_{\mathrm{AR},\theta_m,\mathrm{R}}}{2}. \end{aligned} \tag{3.27}$$

Based on (3.26), the back-EMF of the coils $E_{\mathrm{tooth},q}$ can be derived, but first, the impact of eccentricity on the magnetic flux density needs to be taken into account.

3.3 Adding eccentricity defects to the forward model

The influence of eccentricity is implemented by correcting the average magnetic flux density in the stator coils $B_{\mathrm{av},y}$ by means of a permeance function λ_{ecc}. To derive this permeance function, firstly a simple case of one stator tooth with the surrounding rotor magnets and rotor back-irons is solved. Secondly, the air gap flux density is written in function of the eccentricity defects in general. Lastly, the air gap equations are implemented into the simple case to express the influence of the eccentricity defects on the solution of the simple case into a permeance function.

3.3.1 Simple flux density field solution

In order to find a correct permeance function, eccentricity is modeled for a simple case: one stator tooth with the adjacent air gaps, magnets and rotor back-irons as shown in figure 3.10.

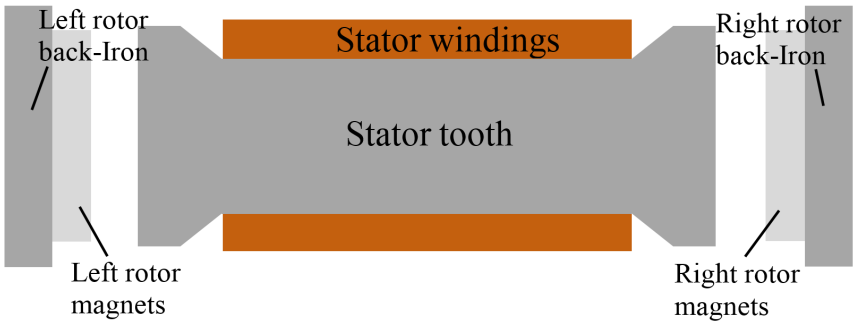

Figure 3.10: Representation of one stator tooth with adjacent left and right rotors.

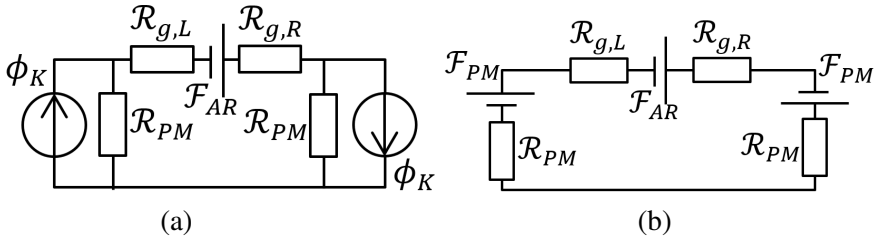

Figure 3.11: (a) Magnetic equivalent circuits of the magnetic situation of figure 3.10, and (b) the simplified circuit of (a).

The situation represents a simple magnetic circuit, which can be visualized as shown in figure 3.11a. This circuit can easily be converted to the circuit in figure 3.11b with:

$$\mathcal{F}_{\mathrm{PM}} = \phi_{\mathrm{PM}} \mathcal{R}_{\mathrm{PM}} \tag{3.28}$$

where:

$$\phi_{\mathrm{PM}} = B_{\mathrm{r}} S_{\mathrm{PM}}. \tag{3.29}$$

S_{PM} is the area of the magnet, $\mathcal{R}_{\mathrm{PM}}$ is the reluctance of the magnets, $\mathcal{R}_{\mathrm{g,L}}$ and $\mathcal{R}_{\mathrm{g,R}}$ are the reluctance of the left and the right air gap respectively, ϕ_{PM} is the residual flux of the magnets and $\mathcal{F}_{\mathrm{AR}}$ is the Magneto-Motive Force (MMF) of the stator coils for the fraction of the flux that crosses the air gap and $\mathcal{F}_{\mathrm{PM}}$ is the equivalent MMF of the magnets. The influence of eccentricity on the slot leakage and end-winding leakage is neglected. This circuit has become a simple serial network of four reluctances and three MMF sources, which can easily be solved. The flux density B_{ecc} in the circuit of figure 3.11b can be found by:

$$B_{\mathrm{ecc}} = \mu_0 \mu_{r,M} \frac{2\mathcal{F}_{\mathrm{PM}} + \mathcal{F}_{\mathrm{AR}}}{(\mu_{r,M} \cdot g_{\mathrm{L}} + h_{\mathrm{PM}}) + (\mu_{r,M} \cdot g_{\mathrm{R}} + h_{\mathrm{PM}})}. \tag{3.30}$$

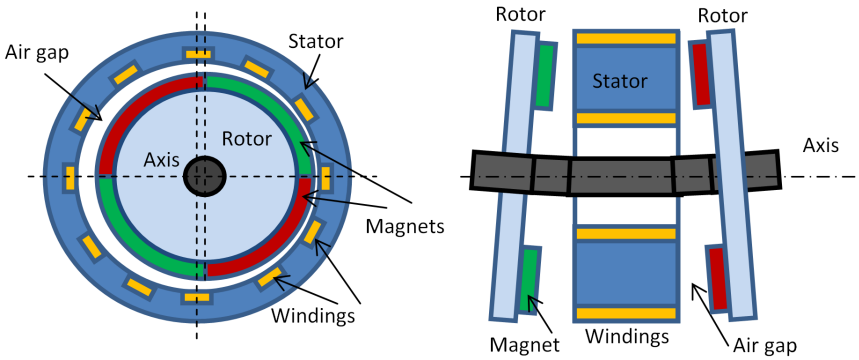

Figure 3.12: Visualization of static eccentricity in a radial flux machine (left) and dynamic eccentricity in an axial flux machine (right).

In a healthy state, the air gaps g_{L} and g_{R} are the healthy air gap $g_{\mathrm{L},0} = g_{\mathrm{R},0} = g_{healthy}$ of the machine. This leads to a magnetic flux density in healthy state:

$$B_{\mathrm{healthy}} = \frac{\mu_0 \mu_{r,M}}{2} \frac{2\mathcal{F}_{\mathrm{PM}} + \mathcal{F}_{\mathrm{AR}}}{\mu_{r,M} \cdot g_{healthy} + h_{\mathrm{PM}}}. \tag{3.31}$$

3.3.2 Air gap width variation due to eccentricity

There are three types of eccentricity:

1. Static Eccentricity (SE): This occurs when e.g. the bearings of the shaft shifts. The rotor is rotating around his own axis, but this axis is not aligned with the axis of the stator. The position in the air gap where the rotor is closest to the stator is fixed. This can be seen in the left part of figure 3.12.

2. Dynamic Eccentricity (DE): An example of this is a bended axis. The rotor is rotating around the axis of the stator, although the axis of the stator is not aligned with the axis of the rotor. The position in the air gap where the rotor is closest to the stator is not stationary but rotates at the same speed of the rotor. This can be seen in the right part of figure 3.12. The bending of the shaft itself is considered static for this study. The bending of the shaft can also be dynamic, for example due to vibrations, but this is not examined in this work.

3. Mixed Eccentricity (ME): This is a combination of SE and DE.

All three types can be tackled by writing the air gap as the healthy air gap corrected by the influence of SE and DE respectively:

$$g = g_{healthy} - g_{\Delta,\mathrm{SE}} - g_{\Delta,\mathrm{DE}} \tag{3.32}$$

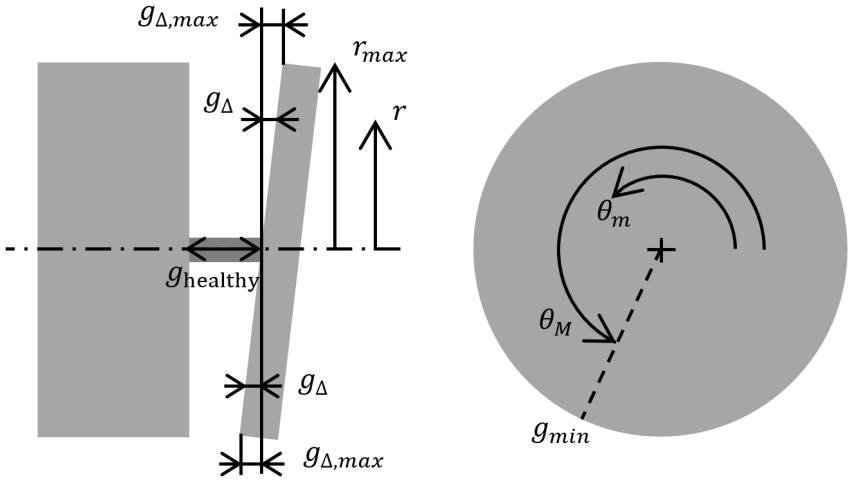

Figure 3.13: General definitions for rotor eccentricity. θ_{M} is the angle to the smallest air gap width $g_{\min}$ for both SE (θ_{MSE}) and DE (θ_{MDE}).

where $g_{\Delta,\mathrm{SE}}$ and $g_{\Delta,\mathrm{DE}}$ are the difference in air gap caused by SE and DE respectively and g is either g_{L} or g_{R}.

Figure 3.13 shows some definitions on an axial machine with an eccentric rotor. The differences in the air gap for SE and DE are dependent on the circumference angle. For DE, this difference is also time dependent. The following equation shows the evolution of the air gap over the circumferential direction for SE ($g_{\Delta,\mathrm{SE}}$) and DE ($g_{\Delta,\mathrm{DE}}$):

$$\begin{cases} g_{\Delta,\mathrm{SE}}(\theta_m) = \rho_{\mathrm{SE}} g_{healthy} \frac{r}{r_{\max}} cos(\theta_m + \theta_{\mathrm{MSE}}) \\ g_{\Delta,\mathrm{DE}}(\theta_m, t) = \rho_{\mathrm{DE}} g_{healthy} \frac{r}{r_{\max}} cos(\theta_m + \theta_{\mathrm{s}} + \omega_{\mathrm{m}} t + \theta_{\mathrm{MDE}}) \end{cases} \tag{3.33}$$

with θ_{MSE} and θ_{MDE} the angle of the position of minimum air gap for SE and DE respectively, and θ_{s} the mechanical start angle. ρ_{SE} and ρ_{DE} are called the eccentricity coefficient and can be defined as:

$$\rho_{\mathrm{SE}} = \frac{g_{\Delta,\mathrm{SE},max}}{g_{healthy}}; \qquad \rho_{\mathrm{DE}} = \frac{g_{\Delta,\mathrm{DE},max}}{g_{healthy}}. \tag{3.34}$$

with $g_{\Delta,\mathrm{SE},max}$ and $g_{\Delta,\mathrm{DE},max}$ being the maximal air gap size for SE and DE respectively. If either ρ_{SE} or ρ_{DE} is 1, the machine has 100% eccentricity at that air gap. In that case, the rotor will make contact with the stator. $r_{\max}$ is defined as the radius where this contact would occur. Notice that it is not possible to have 100% SE and 100% DE at the same time. The reason for this is that the air gap g is always greater or equal to zero. This means $g_{healthy} \geq g_{\Delta,\mathrm{SE}} + g_{\Delta,\mathrm{DE}}$.

3.3.3 Eccentricity Permeance function

Now the air gap equations are substituted into the simple flux density field solution to derive the eccentricity permeance function. Starting from (3.32) and (3.33), it can be seen that:

$$\mu_{r,M} g + h_{\mathrm{PM}} = (\mu_{r,M} g_{healthy} + h_{\mathrm{PM}}) \lambda_{\mathrm{gap}} \tag{3.35}$$

with

$$\begin{aligned} \lambda_{\mathrm{gap}} = 1 &- \rho_{\mathrm{SE}} \frac{\mu_{r,M} g_{healthy}}{\mu_{r,M} g_{healthy} + h_{\mathrm{PM}}} \frac{r}{r_{\max}} cos(\theta_m + \theta_{\mathrm{MSE}}) \\ &- \rho_{\mathrm{DE}} \frac{\mu_{r,M} g_{healthy}}{\mu_{r,M} g_{healthy} + h_{\mathrm{PM}}} \frac{r}{r_{\max}} cos(\theta_m + \theta_{\mathrm{s}} + \omega_{\mathrm{m}} t + \theta_{\mathrm{MDE}}) \end{aligned} \tag{3.36}$$

as the permeance function for the air gap. Combining this in (3.30) with (3.31) results in:

$$B_{\mathrm{ecc}} = B_{\mathrm{healthy}} \frac{2}{\lambda_{\mathrm{gap,L}} + \lambda_{\mathrm{gap,R}}} \tag{3.37}$$

with $\lambda_{\mathrm{gap,L}}$ and $\lambda_{\mathrm{gap,R}}$ the air gap permeance function of the left and right air gap respectively. This can be written as:

$$B_{\mathrm{ecc}} = B_{\mathrm{healthy}} \lambda_{\mathrm{ecc}} \tag{3.38}$$

with

$$\lambda_{\mathrm{ecc}} = \frac{2}{\lambda_{\mathrm{gap,L}} + \lambda_{\mathrm{gap,R}}}. \tag{3.39}$$

For the analytical model of this chapter, it can be written as:

$$B_{\mathrm{av,tot}} = B_{\mathrm{av}} \lambda_{\mathrm{ecc}}. \tag{3.40}$$

Similar to the flux density field of the PMs and the AR and the permeance function slots, λ_{ecc} can also be written in the form of a Fourier series:

$$\lambda_{\mathrm{ecc}}(\theta_m, t) = \sum_{w=-\infty}^{+\infty} \sum_{p=-\infty}^{+\infty} \lambda_{\mathrm{ecc},w,p} e^{j(w\theta_m + p\omega_{\mathrm{m}} t)} \tag{3.41}$$

with w and p the space and time harmonic number respectively. The eccentricity in the machine can be described by the two eccentricity coefficients (SE and DE) for both air gaps and their corresponding angles:

$$\begin{cases} [\rho_{\mathrm{SE,R}}; \theta_{\mathrm{MSE,R}}] \\ [\rho_{\mathrm{DE,R}}; \theta_{\mathrm{MDE,R}}] \\ [\rho_{\mathrm{SE,L}}; \theta_{\mathrm{MSE,L}}] \\ [\rho_{\mathrm{DE,L}}; \theta_{\mathrm{MDE,L}}]. \end{cases} \tag{3.42}$$

An eccentricity defect can be denoted by a set of four parameters $E = [e_1, e_2, e_3, e_4]$, where e_1 is the rotor on which the defect occurs rt, i.e. $e_1 \in [\mathrm{L}, \mathrm{R}]$ with 'L' and 'R' equal to the left and right air gap resp., e_2 is the type of eccentricity, i.e. $e_2 \in [SE, DE]$ with SE and DE corresponding with static and dynamic eccentricity resp., e_3 is the eccentricity coefficient for this rotor and type of eccentricity, i.e. $0 \leq e_3 \leq 1$ and e_4 is the angle to the minimum air gap width for this rotor and type of eccentricity, i.e. $e_4 \in [0°, 360°]$.

From now on, the parameters in (3.42) together with the magnetization factors K are called the defect information D_{info}.

3.4 Tooth back-EMF, phase back-EMF and terminal voltages

From the average flux density field, the flux in every stator tooth $\varphi_{stator,q}$ with tooth number q may be written as:

$$\varphi_{stator,q}(t) = \int_{S_T} B_{\mathrm{av,tot},y} dS_T = \sum_{l=0}^{n_{\mathrm{l}}} d_{\mathrm{l}} r_l \int_{\theta_q}^{\theta_{q+1}} B_{\mathrm{av,tot},y,l} d\theta_m \tag{3.43}$$

where S_T is the area of the stator tooth at the air gap, l is the index of the calculation plane through the stator tooth, n_{l} is the total number of calculation planes, d_{l} is the radial thickness of a calculation plane, θ_q and θ_{q+1} are the circumferential angles of the two slots around this tooth and $B_{\mathrm{av,tot},y,l}$ is the average flux density field for one calculation plane as described in (3.23). In this equation, the components can be inserted in Fourier form, which leads to:

$$\begin{aligned} B_{\mathrm{av,tot},y}(\theta_m, y, t) = & \sum_{m=-\infty}^{+\infty} \sum_{v=-\infty}^{+\infty} \sum_{w=-\infty}^{+\infty} \sum_{p=-\infty}^{+\infty} (B_{\mathrm{PM},y,\mathrm{av},m} \lambda_{\mathrm{sl,real},v} \\ & - B_{\mathrm{PM},\theta_m,\mathrm{av},m} \lambda_{\mathrm{sl,imag},v}) \lambda_{\mathrm{ecc},w,p} e^{j[(m+v+w)\theta_m + (m+p)\omega_{\mathrm{m}} t]} \\ & + \sum_{u=-\infty}^{+\infty} \sum_{m=-\infty}^{+\infty} \sum_{v=-\infty}^{+\infty} \sum_{w=-\infty}^{+\infty} \sum_{p=-\infty}^{+\infty} (B_{\mathrm{AR},y,\mathrm{av},u,m} \lambda_{\mathrm{sl,real},v} \\ & - B_{\mathrm{AR},\theta_m,\mathrm{av},u,m} \lambda_{\mathrm{sl,imag},v}) \lambda_{\mathrm{ecc},w,p} e^{j[(u+v+w)\theta_m + (m+p)\omega_{\mathrm{m}} t]}. \end{aligned} \tag{3.44}$$

Here v is the harmonic number of the slot permeance function in space. The back-EMF of every tooth can be found by:

$$E_{\text{tooth},q}(t) = -N_{stator}\frac{d\varphi_{stator,q}}{dt} = \sum_{m=-\infty}^{+\infty}\sum_{p=-\infty}^{+\infty} -N_{stator}j(m+p)\omega_{\text{m}} \cdot \varphi_{stator,q,m,p}e^{j(m+p)\omega_{\text{m}}t}. \tag{3.45}$$

By inserting (3.44) in (3.43) and calculating (3.45), the back-EMF in a tooth results in:

$$\begin{aligned} E_{\text{tooth},q}(t) = \sum_{m=-\infty}^{+\infty}\sum_{p=-\infty}^{+\infty} & -d_{\text{l}}\omega_{\text{m}}N_{stator}(m+p) \\ & \Bigg[\sum_{l=0}^{n_{\text{l}}}\sum_{v=-\infty}^{+\infty}\sum_{w=-\infty}^{+\infty}(B_{\text{PM},y,\text{av},m,l}\lambda_{\text{sl,real},v,l} - B_{\text{PM},\theta_m,\text{av},m,l}\lambda_{\text{sl,imag},v,l}) \\ & \lambda_{\text{ecc},w,p,l}\frac{r_l}{m+v+w}(e^{j(m+v+w)\theta_{q+1}} - e^{j(m+v+w)\theta_q}) \\ + \sum_{l=0}^{n_{\text{l}}}\sum_{u=-\infty}^{+\infty}\sum_{v=-\infty}^{+\infty}\sum_{w=-\infty}^{+\infty} & (B_{\text{AR},y,\text{av},u,m,l}\lambda_{\text{sl,real},v,l} - B_{\text{AR},\theta_m,\text{av},u,m,l}\lambda_{\text{sl,imag},v,l}) \\ & \lambda_{\text{ecc},w,p,l}\frac{r_l}{u+v+w}(e^{j(u+v+w)\theta_{q+1}} - e^{j(u+v+w)\theta_q})\Bigg]e^{j(m+p)\omega_{\text{m}}t}. \end{aligned} \tag{3.46}$$

The time indices m and p and their corresponding Fourier components can easily be converted to one time index n by adding the Fourier components together with $n = m + p$:

$$E_{\text{tooth},q}(t) = \sum_{n=-\infty}^{+\infty} E_{\text{tooth},q,n}e^{jn\omega_{\text{m}}t}. \tag{3.47}$$

The separate stator coils are connected to create the phases. To determine which coil to connect with which phase, the star of slot technique [197] is used. This places the back-EMFs of all coils in a vector plot and assigns a phase to each one based on the vector's position in the plot. This is shown in figure 3.14a for the 16-pole 15-slot example AFPMSM that will be further described in Section 3.5. From this, the winding arrangement can be determined (figure 3.14b) and the back-EMF of the phases can be derived from the back-EMF of the stator coils.

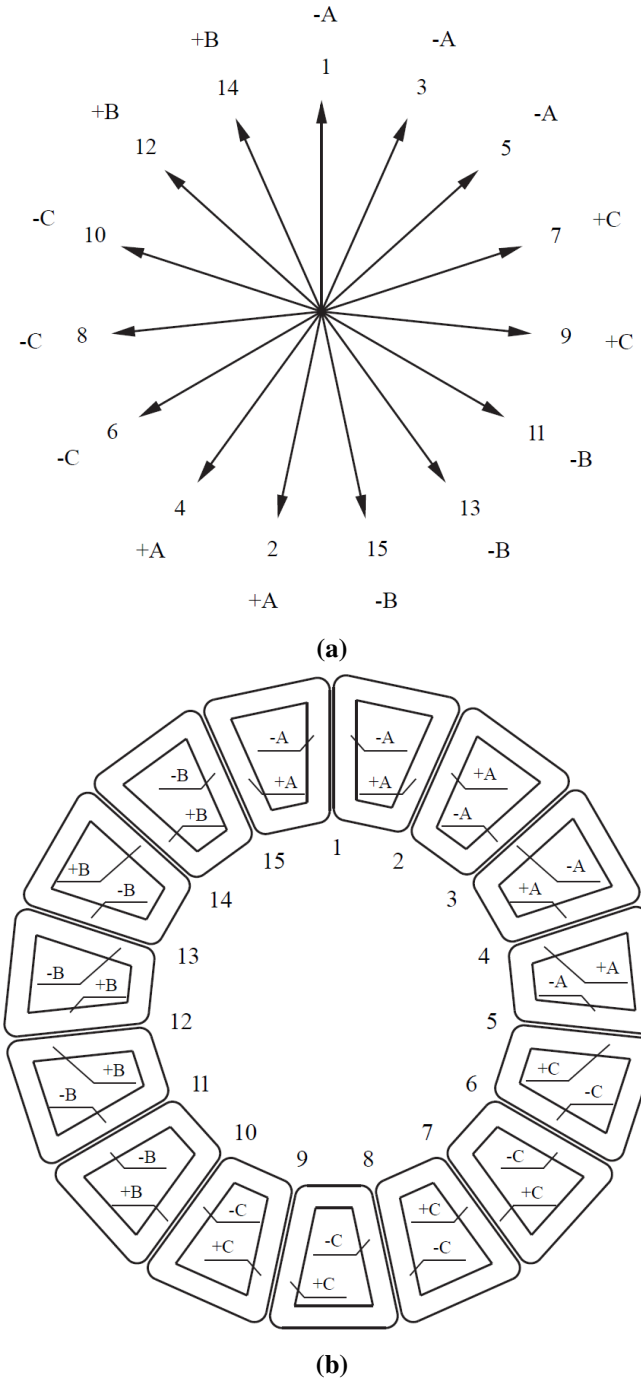

Figure 3.14: (a) Voltage vector representation based on the star of slot technique [197] and (b) stator winding arrangement following from (a) for the example 16-pole 15-slot AFPMSM in Section 3.5 [20].

Table 3.1: Characteristics and parameters of the example AFPMSM

Parameter	Value
Electrical output power (W)	4000
Rated speed (rpm)	2500
Rated torque (Nm)	15
Pole number	16
Slot/tooth number	15
Outer diameter (mm)	148
Inner diameter (mm)	100
Outer diameter housing (mm)	195
Magnet type	NdFeB SH40
Magnets remanence (T)	1.26
Magnet thickness (mm)	4.0
Magnet relative permeability	1.05
Rotor back-iron thickness (mm)	8.0
Air gap width (mm)	1.0
Number of serial turns per stator coil	57
Number of parallel branches per stator coil	2
Wire diameter (mm)	1.12
Stator resistance (Ω)	0.27
Rated current (A)	10.0
Stator laminates	0.23 mm Grain oriented Si-steel
Rotor back-iron mat.	Construction steel
Total mass (kg)	9

If the armature electrical circuit and the slot and end-winding flux leakage based on [198] and [199] are taken into account as leakage inductance (L_σ), the terminal voltages for each Fourier component become:

$$V_{\mathrm{term,ph,n}} = E_{\mathrm{phase,ph,n}} - (R_{\mathrm{a}} + jn\omega_{\mathrm{m}} L_\sigma) I_{phase,\mathrm{ph,n}} \tag{3.48}$$

where R_{a} is the armature resistance, $I_{phase,\mathrm{ph,n}}$ is the n-th harmonic component of the injected phase current and ph is the phase number.

The analytical model is now able to calculate the terminal voltages as output with the phase current, defect information, geometrical parameters and operation speed as inputs. This means the forward model, shown at the beginning of this chapter in figure 3.1 is now complete.

3.5 Validation

In order to verify the mathematical correctness of the analytical model, it needs to be validated. This is done with a FEM model of a 16-pole, 15-slot AFPMSM.

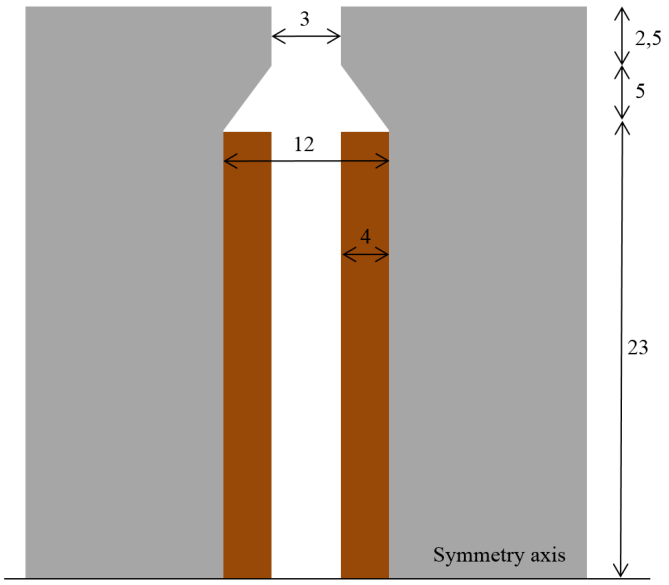

Figure 3.15: Dimensions of the stator slot of the example AFPMSM in millimeter. The machine has a variable air gap [76], which means that at lower radii, the air gap is wider to create a uniform flux density in the stator laminations, which reduces the iron losses. This means the stator tooth are shorter at lower radii. The dimensions shown in this figure correspond to the stator outer radius.

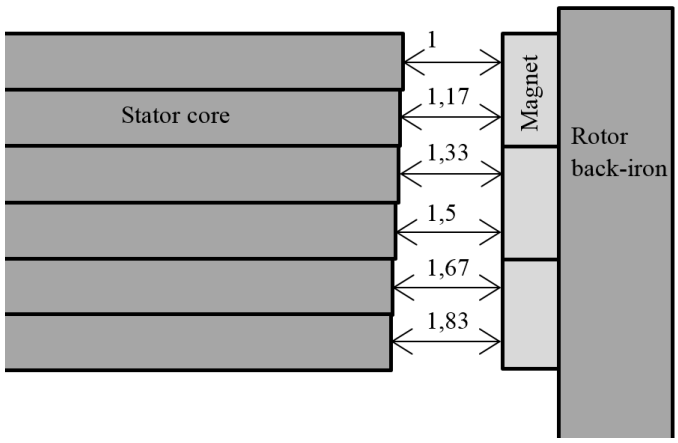

Figure 3.16: Dimensions of the variable air gap seen from the side as described in [76] of the example AFPMSM in millimeter.

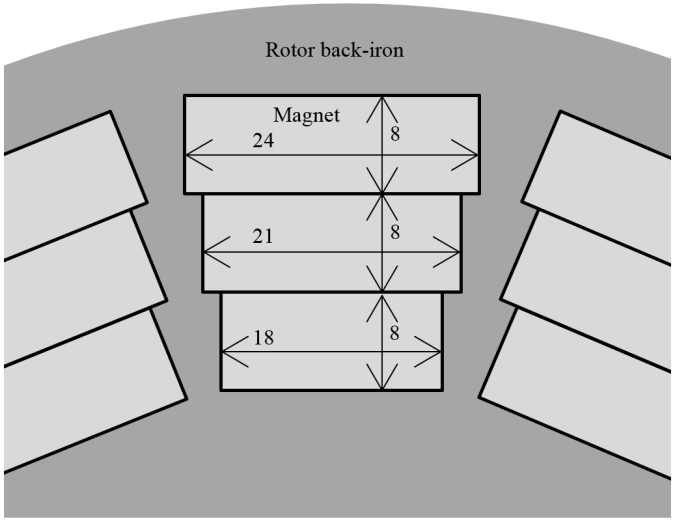

Figure 3.17: Dimensions of the PM lay-out of the example AFPMSM in millimeter.

The characteristics can be found in Table 3.1, figures 3.15, 3.16 and 3.17. Further information about this machine is present in [76]. The FEM model retrieves the magnetic flux density by calculating the vector potential differential equation in the same 2D calculation plane as the analytical model described in Section 3.2.1. Just as with the analytical model, the asymmetrical nature of the defects prevents any simplification by symmetry. The FEM model therefore also includes the complete geometry of the machine. Figure 3.18a shows the magnetic flux distribution in healthy operation at full-load while figure 3.18b shows the magnetic flux density distribution for an example of a combined demagnetization and eccentricity defect. One of the demagnetized magnets can be noticed due to the reduced flux flowing through it (third magnet on the right rotor). The eccentricity is harder to notice, but it can be seen that the rotors are not parallel to the stator. To obtain the 3D information, the model is solved at different radii [191]. Naturally, the FEM model is slower than the analytical model: one full simulation of the FEM model takes about 24h to calculate, while the analytical model only needs 1s. All the calculations have been done on a Intel Core i5-2540M processor with 8GB of RAM memory running a 64-bit Windows 7 operating system.

3.5.1 Healthy operations

The axial flux density field in the right air gap at full-load can be seen for a healthy machine in figure 3.19a. Full-load means that a sinusoidal three phase system of currents with rated amplitude is injected. The figure plots the flux density simulated by the analytical model and the FEM model. The two curves correspond very well. In the frequency domain, the curves differ 1.3% and 3.0% for the N_p-th and $3N_p$-th

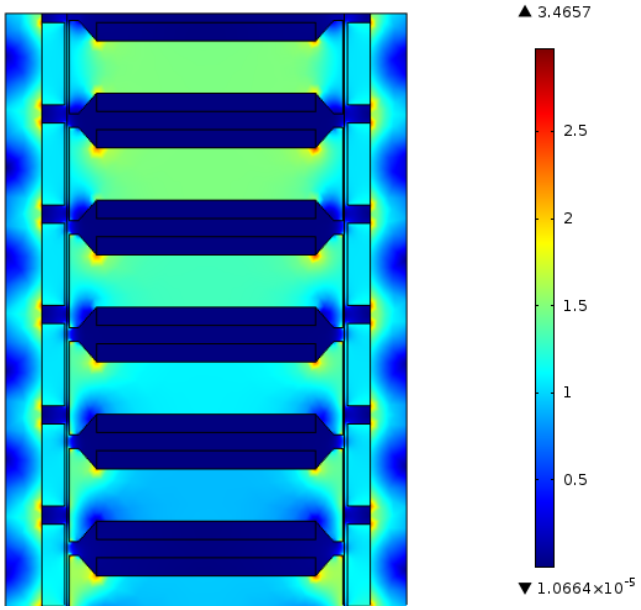

(a)

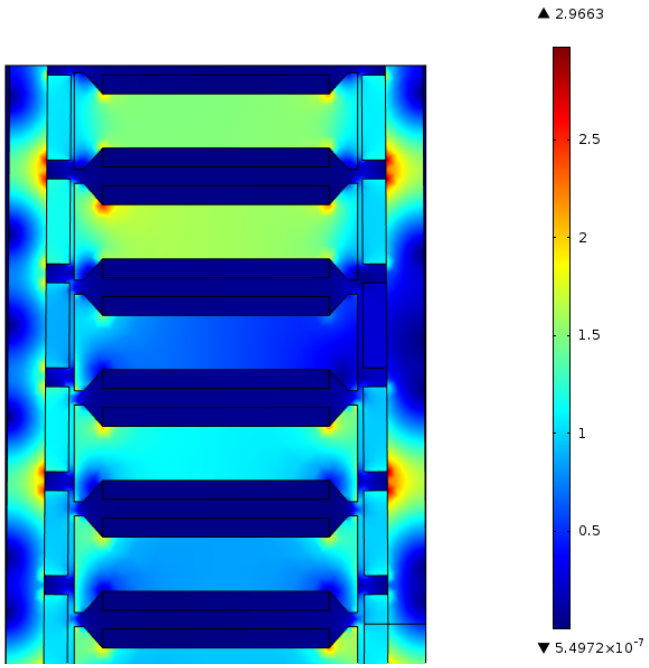

(b)

Figure 3.18: Color plot of the magnitude of the magnetic flux density in Tesla simulated with the FEM model in (a) the healthy situation and (b) with a combined demagnetization and eccentricity defect of $D\,[3, \mathrm{R}, 0.1]$, $D\,[8, \mathrm{R}, 0.2]$, $D\,[8, \mathrm{L}, 0.7]$, $D\,[14, \mathrm{L}, 0.4]$, $E\,[\mathrm{R}, \mathrm{SE}, 0.3, 0°]$, $E\,[\mathrm{R}, \mathrm{DE}, 0.5, 90°]$, $E\,[\mathrm{L}, \mathrm{SE}, 0.6, 45°]$ and $E\,[\mathrm{L}, \mathrm{DE}, 0.2, 0°]$, both at full-load.

harmonics respectively.

The terminal voltages are compared as well: figure 3.19b shows this at no-load operations. The analytical and FEM data correspond very well.

As the analytical model is constructed to be used for different YASA AFPMSM topologies, a validation for a different topology is required as well. Figure 3.20a shows a 35 pole pair 60 stator slots topology. Figure 3.20b plots the terminal voltages for this machine at full-load. The analytical and FEM data have a good agreement with each other.

3.5.2 Demagnetization

A demagnetization defect will alter the flux density in the air gaps of the machine. Figure 3.21 shows an example of the axial flux density of the right air gap with a certain demagnetization defect. The caption gives the details about the demagnetization defect of this plot. As previously explained e.g. $D\,[8, \mathrm{R}, 0.2]$ means that the 8th magnet in the right rotor has a magnetization of 0.2 times the rated magnetization, i.e. that it is 20% magnetized, or 80% demagnetized compared to a healthy magnet. Because in defining the magnet number on a circle the starting point can be chosen, the magnet number can only be interpreted as a relative value. This does not make it useless: this relative value can show us that e.g. $D\,[8, \mathrm{L}, 0.7]$ corresponds with a magnet on the left rotor that faces magnet number 8 on the right rotor. The plot clearly shows the modification of the axial flux density due to the demagnetization defect, and the analytical and FEM data have a good correspondence. In the frequency domain, the curves differ by 4.8% and 18.1% for the N_p-th and $3N_p$-th harmonics respectively.

Figure 3.22 plots the terminal voltages at no-load. The curves agree with each other. Because during a rotation a demagnetized magnet only passes over one phase at the time, the influence of the demagnetized magnet can only be seen in one phase at the time, as can be seen in figure 3.22. If 8 electrical periods or 1 mechanical period would have been plotted, it is possible to see the effect of the magnet cycle in all the three phases.

3.5.3 Eccentricity

The model has to be validated also for eccentricity defects. Section 3.3 explains that the eccentricity permeance function is applied to the average axial flux density, and not to the air gap axial flux density. This means that the air gap axial flux density is not a good indicator for validation. Therefore the average axial flux density is used for validation.

The average axial flux density for a case with an eccentricity defect at full-load is shown in figure 3.23. There is a good correspondence between the analytical and FEM data. In the frequency domain, the curves differ 1.1% and 3.1% for the N_p-th and $3N_p$-th harmonics respectively. In the plot of the average axial flux density,

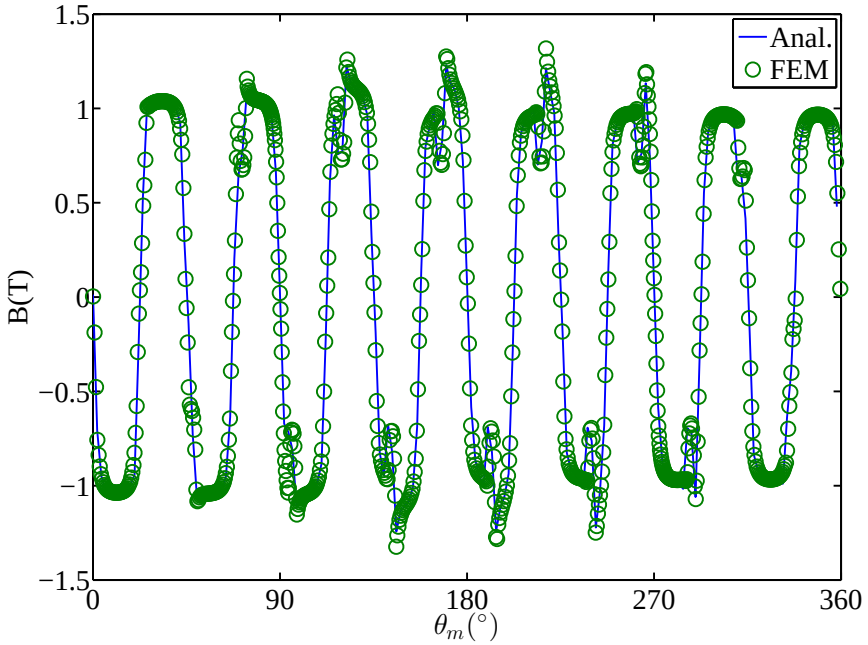

(a)

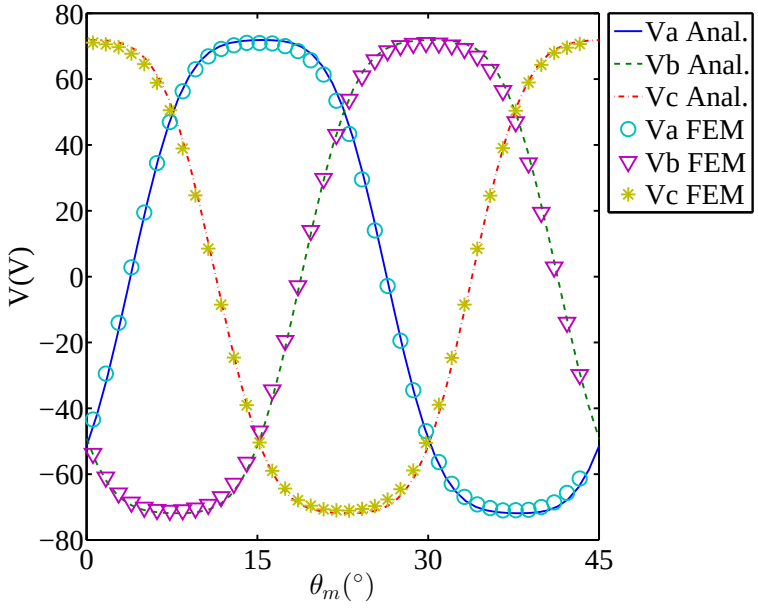

(b)

Figure 3.19: Analytical and FEM data for a healthy 8 pole pair 15 stator teeth topology. (a) The axial flux density at full-load as a function of the mechanical position φ and (b) the 3-phase terminal voltages at no-load for a speed of 746 rpm.

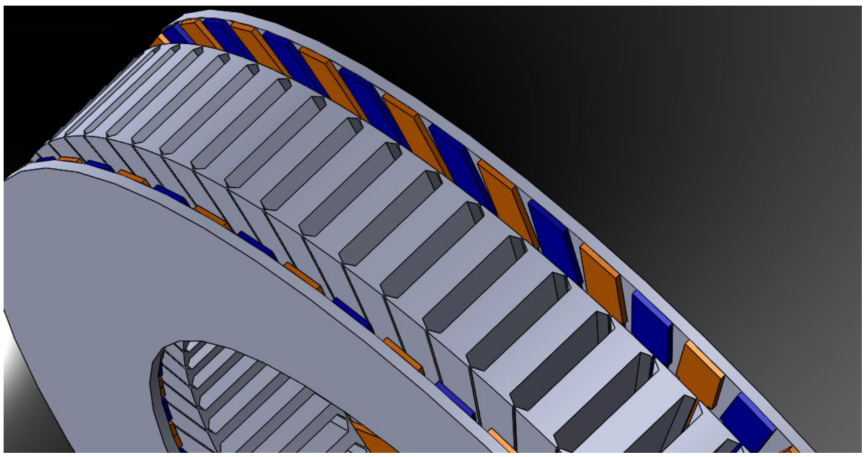

(a)

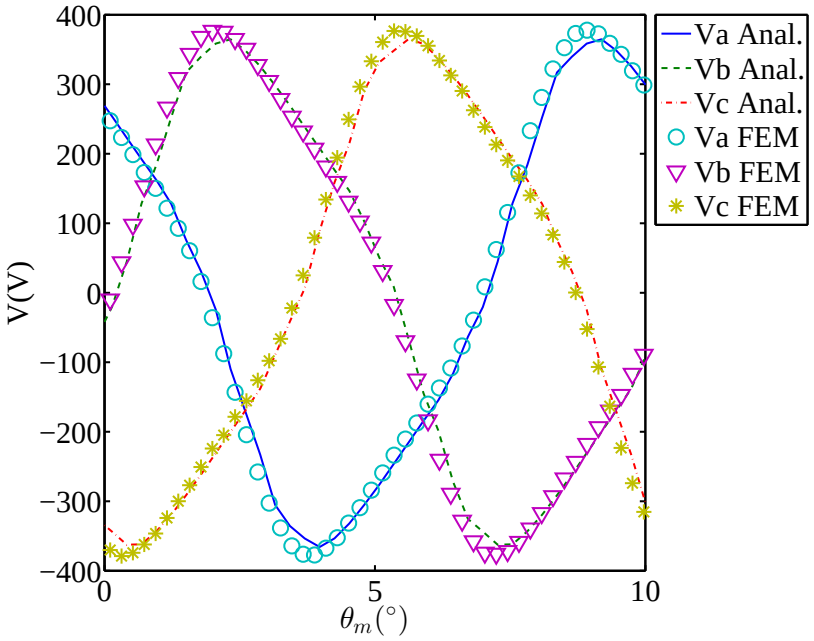

(b)

Figure 3.20: (a) The 35 pole pair 60 stator slots AFPMSM with an output power of 50 kW, a rated speed of 60 rpm and an outer diameter of 1100 mm [190, 200] and (b) the analytical and FEM 3-phase terminal voltages for the same machine at full-load and at the rated speed.

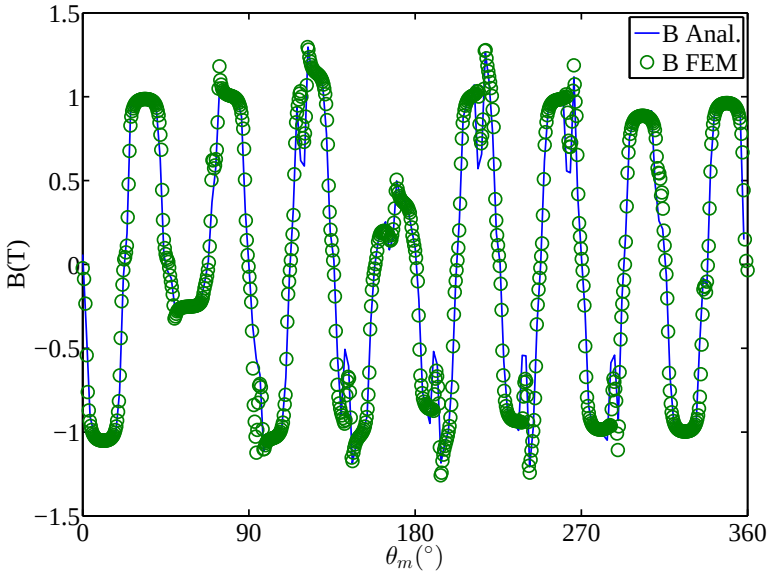

Figure 3.21: Analytical and FEM right air gap axial flux density at full-load with demagnetization defects $D\,[3, \mathrm{R}, 0.1]$, $D\,[8, \mathrm{R}, 0.2]$, $D\,[8, \mathrm{L}, 0.7]$ and $D\,[14, \mathrm{L}, 0.4]$, as a function of the mechanical position φ.

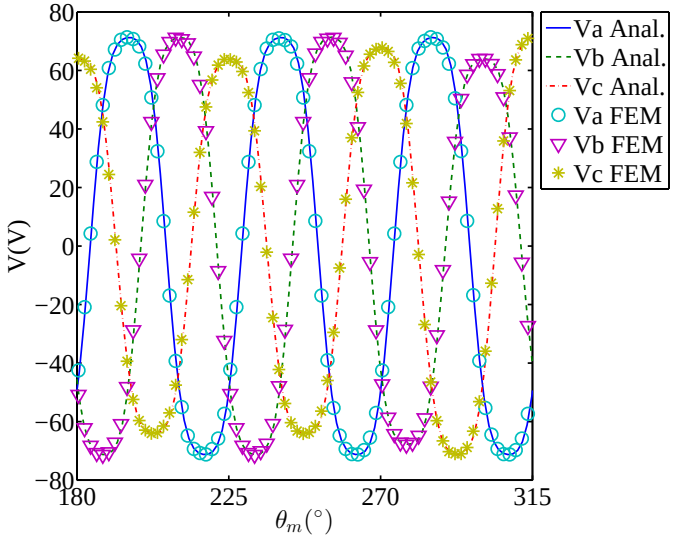

Figure 3.22: Analytical and FEM 3-phase terminal voltages at no-load for a speed of 746 rpm with a demagnetization defect $D\,[2, \mathrm{R}, 0]$.

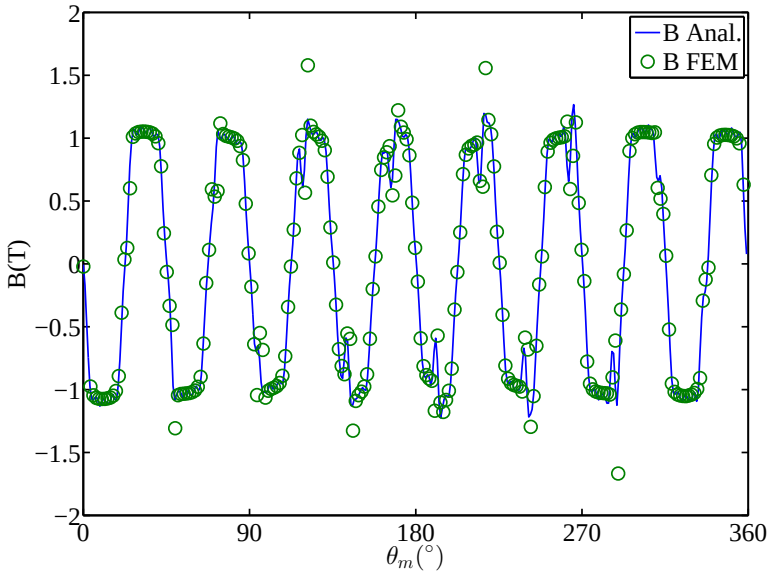

Figure 3.23: Analytical and FEM average axial flux density at full-load with an eccentricity defect of $E\,[\mathrm{R}, \mathrm{SE}, 0.3, 0°]$, $E\,[\mathrm{R}, \mathrm{DE}, 0.5, 90°]$, $E\,[\mathrm{L}, \mathrm{SE}, 0.6, 45°]$ and $E\,[\mathrm{L}, \mathrm{DE}, 0.2, 0°]$.

spikes of 1.6 T, -1.3 T and -1.6 T can be seen in the FEM data. These spikes are not visible in the analytical data. The reason for this is that the analytical model can only simulate a limited number of frequencies, thus filtering out the spikes in the analytical data. A second reason is that in the FEM model, local rises of the flux density occur at sharp edges like the stator slots, which are a result of numerical errors due to the finite size of the mesh.

3.5.4 Combined eccentricity and demagnetization

The ultimate validation with FEM is of course a combined defect of both demagnetization and eccentricity. Figure 3.24 shows the average axial flux density for this defect at full-load. In the frequency domain, the curves differ 1.0% and 3.8% for the N_p-th and $3N_p$-th harmonics respectively. Also in this combined case, the analytical and FEM data line up with each other. The same spikes as in figure 3.23 are here found as well. The reason for this is again the limited number of frequencies in the analytical model and the numerical errors in the FEM model at the sharp edges.

The terminal voltages in the healthy case are compared to those with the defect in figure 3.25, this time in the frequency spectrum. From this plot, it can be seen that the defect introduces subharmonics. These subharmonics could be monitored to perform real-time condition monitoring. Which subharmonics will occur due to

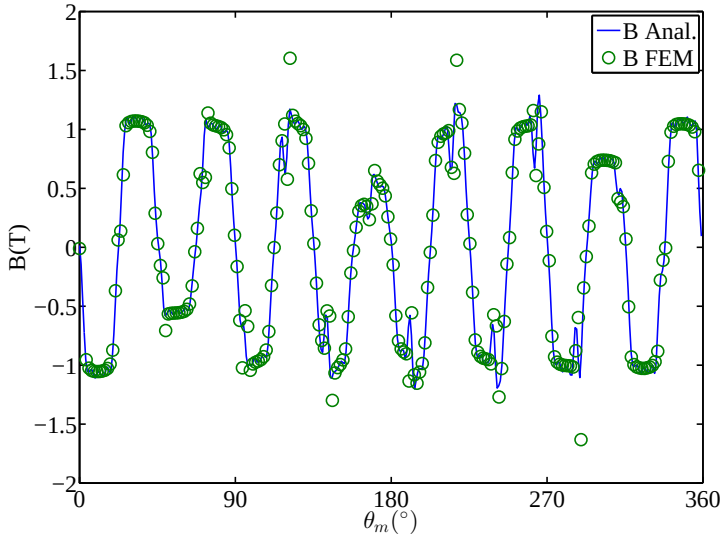

Figure 3.24: Analytical and FEM average axial flux density at full-load with a combined demagnetization and eccentricity defect of $D\,[3, \mathrm{R}, 0.1]$, $D\,[8, \mathrm{R}, 0.2]$, $D\,[8, \mathrm{L}, 0.7]$, $D\,[14, \mathrm{L}, 0.4]$, $E\,[\mathrm{R}, \mathrm{SE}, 0.3, 0°]$, $E\,[\mathrm{R}, \mathrm{DE}, 0.5, 90°]$, $E\,[\mathrm{L}, \mathrm{SE}, 0.6, 45°]$ and $E\,[\mathrm{L}, \mathrm{DE}, 0.2, 0°]$.

the defect is studied more extensively in Chapters 4 and 5.

3.6 Conclusion

Chapter 3 has presented a forward model that computes the terminal voltages of the YASA axial flux machine as a function of its geometry, injected currents, demagnetization defects and eccentricity defects.

More in detail, an analytical model is presented that computes the air gap flux density in a fast way, for a simplified, slotless machine geometry and without considering saturation. There are two models: one for the no-load flux density distribution caused by the permanent magnets, and one for the flux density distribution caused by the stator currents. The models can deal with a demagnetization coefficient in each of the magnets, for both rotors. The both flux densities are corrected via a permeance function for the slotting effect, and superimposed. A second permeance function is introduced to model eccentricity, and the EMF and terminal voltages are computed based on the air gap flux densities.

The forward model is validated via FEM on two machines of the YASA type: a 16 pole, 15 slot machine of 4 kW and a 70 pole, 60 slot machine of 50 kW.

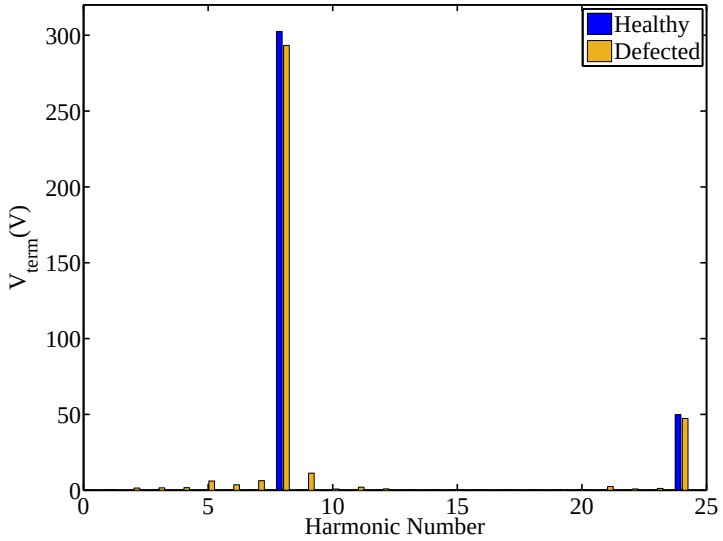

Figure 3.25: Analytical frequency data of the first terminal voltage at full-load for the healthy state and the combined demagnetization and eccentricity defect of $D\,[3, \mathrm{R}, 0.1]$, $D\,[8, \mathrm{R}, 0.2]$, $D\,[8, \mathrm{L}, 0.7]$, $D\,[14, \mathrm{L}, 0.4]$, $E\,[\mathrm{R}, \mathrm{SE}, 0.3, 0°]$, $E\,[\mathrm{R}, \mathrm{DE}, 0.5, 90°]$, $E\,[\mathrm{L}, \mathrm{SE}, 0.6, 45°]$ and $E\,[\mathrm{L}, \mathrm{DE}, 0.2, 0°]$.

Chapter 4

Inverse techniques for condition monitoring

Chapter 3 presented the forward model that computes several electromagnetic quantities for a motor with possible demagnetization and eccentricity defects. Chapter 4 uses this forward model to solve it in an inverse way to detect demagnetization and eccentricity defects. The overview of this chapter is the following.

In Section 4.1, the IP is described that uses the forward model. Secondly, Section 4.2 uses the forward model to perform an analysis of the sensitivity of the separate harmonics of the terminal voltages toward demagnetization defects with the goal of increasing the IP's calculation speed. Lastly, due to the geometry of the machine, the method using the terminal voltages is unable to determine in which rotor a certain defected magnet is located. To accommodate this, Section 4.3 offers an alternative approach of detecting demagnetization defects that is capable of detection in which rotor the defected magnets are located by means of sensing coils.

4.1 Inverse Problem and solvers

4.1.1 Inverse Problem formulation

First, we recall that the forward model in Chapter 3 takes the following inputs: the phase currents, the rotor speed, the geometrical and material properties, circuit parameters and information of the defect. The latter contains magnetization factors K and the eccentricity coefficients for SE and DE for both air gaps and their corresponding angles as explained in (3.42) in the previous chapter. This information is denoted by the variable (D_{info}). The outputs of the forward model are the phase terminal voltages.

In condition monitoring, the phase currents and phase terminal voltages can

be measured while the defect information is unknown. An electromagnetic IP as in [201] can identify the defect information.

The IP model functions are shown in figure 4.1. The IP solves the forward model with the measured phase currents and an initial value for the defect information. The forward model calculates the simulated phase terminal voltages. These are compared with the measured phase terminal voltages and based on this, the used defect information is altered until the difference between the measured and the simulated phase terminal voltages is lower than a threshold or any of the other the stop conditions is triggered. Section 4.1.4 will explain more about these stop conditions. In this last case, the defect information used in the forward model corresponds with the defect information of the measured case, which will be called the estimated defect information D_{info}. Notice that an IP is thus an iterative process. For condition monitoring with this IP, full knowledge of the machine is necessary. This means that the geometry and operating conditions must be known in the analytical model to simulate correctly the terminal voltages.

The deviation between the forward model values and the measured values is determined by an Objective Function (OF) based on the Euclidean Squared Distance of the measured and the simulated phase terminal voltages:

$$OF(D_{info}) = (V_{\mathrm{term,m}} - V_{\mathrm{term,s}}(D_{info}))^2 \tag{4.1}$$

where $V_{\mathrm{term,m}}$ and $V_{\mathrm{term,s}}$ are a compilation of the harmonic components magnitude and angle information in the form of their real and imaginary components of the measured and the simulated phase terminal voltages respectively. An example for a 3 phase system is:

$$\begin{aligned} V_{\mathrm{term}} = [&V_{\mathrm{term},a,1,real}, V_{\mathrm{term},b,1,real}, V_{\mathrm{term},c,1,real}, \\ &V_{\mathrm{term},a,1,imag}, V_{\mathrm{term},b,1,imag}, V_{\mathrm{term},c,1,imag}, \\ &V_{\mathrm{term},a,2,real}, ...] \end{aligned} \tag{4.2}$$

both for $V_{\mathrm{term,m}}$ and $V_{\mathrm{term,s}}$, where a, b and c are the index of the 3 phases and 1 and 2 are the harmonic number.

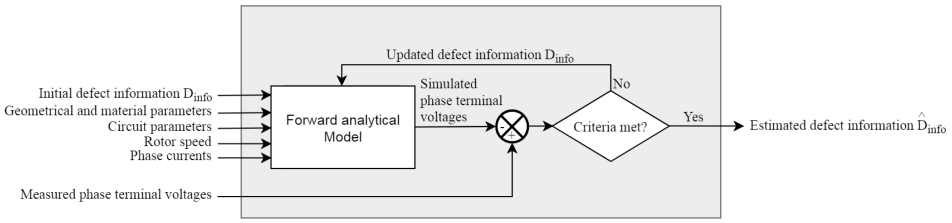

Figure 4.1: The scheme used by the IP to identify the defect information D_{info}, where $\hat{D}_{info}$ is the estimated value of the defect information D_{info}.

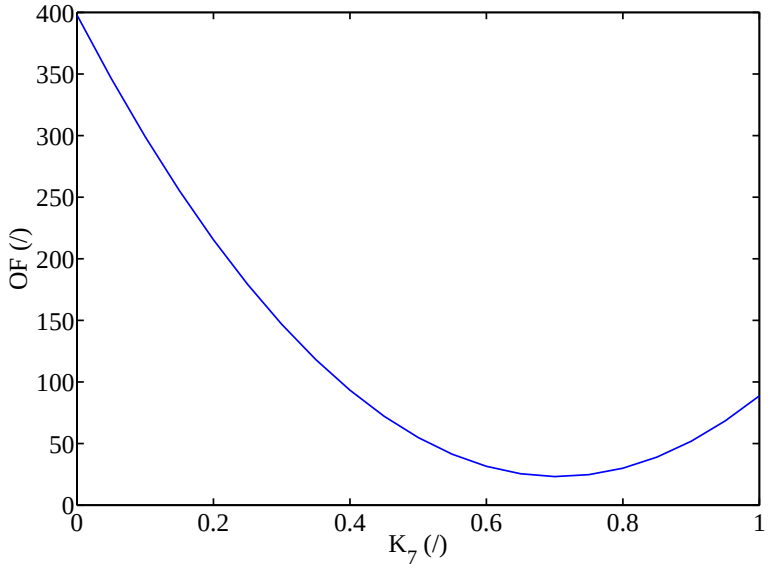

Figure 4.2: The value of the OF in function of the magnetization factor K_7 with a demagnetization defect of D[7, R, 0.7] and an eccentricity defect of E [R, SE, 0.2, 0°].

The minimization of this OF leads to the estimated defect information $\hat{D}_{info}$, which is the defect information corresponding to the measured phase currents and phase terminal voltages:

$$\hat{D}_{info} = \arg \min_{D_{info}} OF(D_{info}). \tag{4.3}$$

4.1.2 Line Search

As an introduction to the general methodology, the objective function's behavior is illustrated for the 3 kW axial flux machine that is also experimentally tested. With line searches, the relation between the OF value and the D_{info} parameters can be analyzed. As an example, figure 4.2 shows the OF value in function of K_7 with a defect of D[7, R, 0.7] and E [R, SE, 0.2, 0°]. We recall that this means a defect in magnet number 7 of the right rotor disc, having a magnetization coefficient of 0.7 and a static eccentricity defect with a magnitude of 0.2. The plot is created by changing only K_7 and keeping the other parameters at their healthy state. It shows that there is only one minimum located at $K_7 = 0.7$. A minimum is the value that best fits the measured situation. In case of a perfect match, the OF value would be zero. In reality, there will always be a difference due to measuring errors, noise, etc. Notice that there is only one minimum. There are no local minima in the curve beside the global minimum. It is observed that this is usually the case, not only for

Table 4.1: The coefficients of the polynomial curve with i the index of the polynomial corresponding with the definition of (4.4) for K_7 with the defect D[7, R, 0.7]

i	0	1	2	3	4	5
P_i	397.8	-1062.4	753.4	-2.5e-10	2.3e-10	7.6e-11

Table 4.2: The coefficients of the polynomial curve with i the index of the polynomial corresponding with the definition of (4.4) for $\rho_{\mathrm{SE,R}}$ with the defect E[R, SE, 0.2, 0°]

i	0	1	2	3	4	5	6
P_i	88.8	-228.3	586.4	-55.0	74.7	-56.5	17.6

the example in the figure, but also for other defects. Although the non-existence of local minima is not proven, the observed shapes of the OF make it easier to solve the minimization problem: solvers that find local minima are expected to be sufficient for solving the inverse problem.

As the curve suggests a polynomial trend, curve fitting has been performed, resulting in a polynomial of the form:

$$P(x) = P_n x^n + P_{n-1} x^{n-1} + ... + P_1 x + P_0 = \sum_{i=0}^{n} P_i x^i. \tag{4.4}$$

For the data of figure 4.2, a polynomial is fitted and the error ($\sqrt{\sum_i (\Delta y_i)^2}$) is plotted in figure 4.3(a). It shows that clearly that a 2th degree polynomial fits the data. The coefficients are shown in Table 4.1. Figure 4.4(a) shows the OF value in function of K_7 and K_8 for the defect D[7, R, 0.3], i.e. a 3D polynomial with a minimum at $K_7 = 0.3$ and $K_8 = 1.0$. This plot also shows that the OF has a valley shape. This is due to the fact that a defect of D[8, R, 0.3] has a very similar effect on the terminal voltages, resulting in a just slightly larger OF in the point $(K_7 = 1.0, K_8 = 0.3)$ than in the point $(K_7 = 0.3, K_8 = 1.0)$. Also the combinations of K_7 and K_8 between those two points have a similarly low OF value. This effect of course exist with every magnet pole, resulting in a $4N_p$-dimensional valley, with N_p the number of poles.

A similar analysis can be performed for eccentricity. Figure 4.4(b) shows the OF value in function of $\rho_{\mathrm{SE,R}}$ with a defect of E[R, SE, 0.2, 0°]. We recall that this means a static eccentricity of magnitude 0.2 in the right rotor with start angle of 0°. A minimum at $\rho_{\mathrm{SE,R}} = 0.2$ can be seen. There is again only one minimum. A polynomial is fitted to this data as well, and figure 4.3(b) shows that the error decreases when higher degrees are used. The OF for this eccentricity parameter is thus not pure quadratic. The coefficients of the polynomial trend line as described in (4.4) for the 6th degree polynomial are shown in Table 4.2.

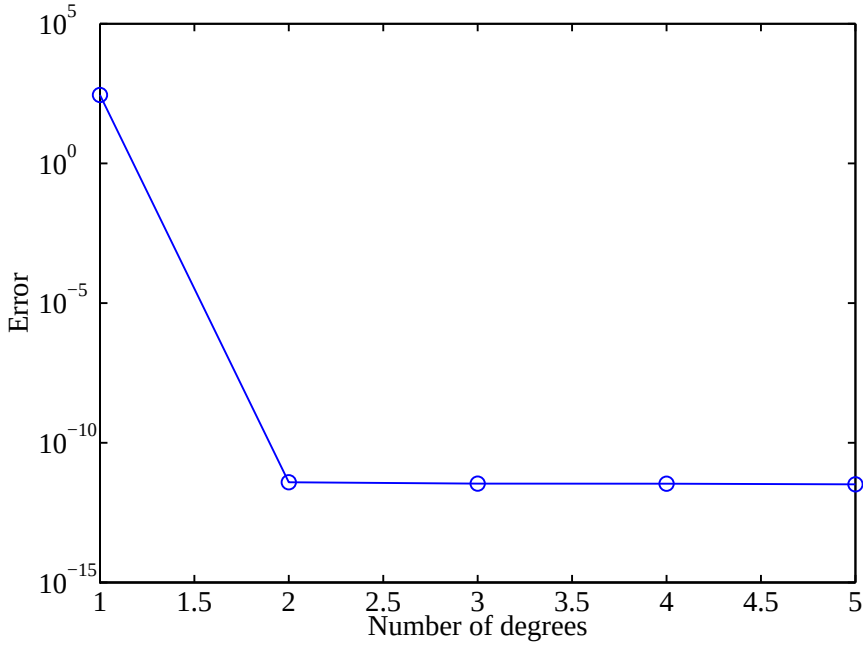

(a)

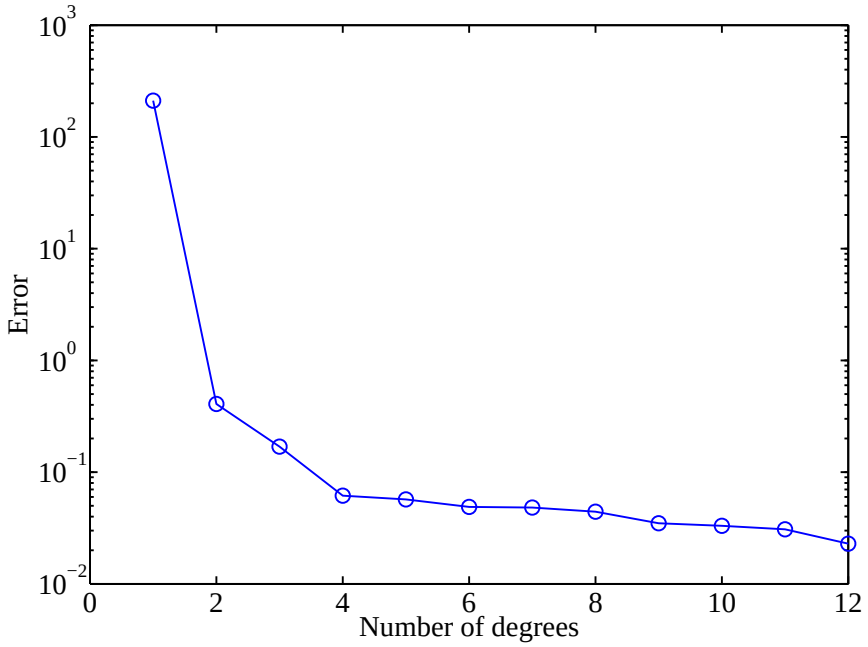

(b)

Figure 4.3: (a) The 35 pole pair 60 stator slots AFPMSM with an output power of 50 kW, a rated speed of 60 rpm and an outer diameter of 1100 mm [190, 200] and (b) the analytical and FEM 3-phase terminal voltages for the same machine at full-load and at the rated speed.

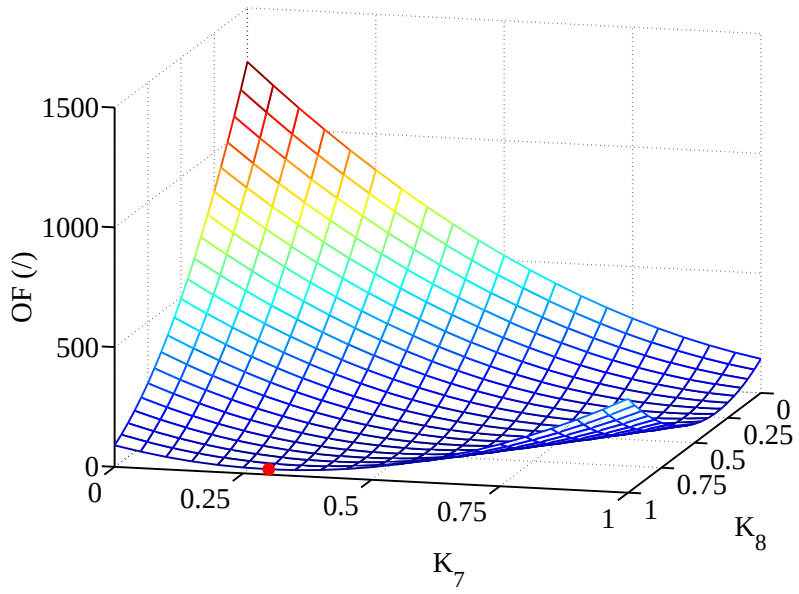

(a)

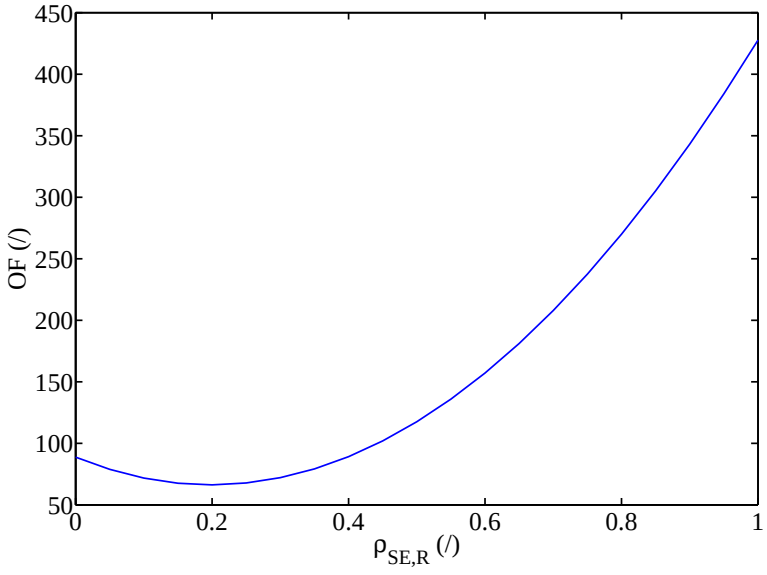

(b)

Figure 4.4: (a) 3D polynomial showing the OF value depending on K_7 and K_8. The minimum is located at $K_7 = 0.3$ and $K_8 = 1.0$. (b) The value of the OF in function of the static eccentricity coefficient $\rho_{\mathrm{SE,R}}$ with an eccentricity defect of E[R, SE, 0.2, 0°].

4.1.3 Solver choice

The minimization of the OF is done by a solver. There are many solvers, each with there benefits and disadvantages. The line searches shown in previous section give an indication of which solvers may be best suited for the considered type of optimization problem.

The choice of the solver depends mainly on two criteria: objective type and constraint type [202]. The objective type tries to categorize the shape of the OF value toward the D_{info} in increasing difficulty into 'Linear', 'Quadratic', 'Least Squares', 'Smooth Nonlinear' and 'Nonsmooth'. The analysis in Section 4.1.2 shows that the OF is not linear nor pure Quadratic. The OF could be approximated by a quadratic curve. The quadratic solver called Quadratic Programming solves a problem of the type [203]:

$$\arg\min_{x} \frac{1}{2} x^{\mathrm{T}} Q x + L^{\mathrm{T}} x \tag{4.5}$$

where Q and L are the quadratic and linear factor respectively and x is the variable that needs to be optimized (identified in IP). The solver requires Q and L as inputs. These factors can be acquired by curve fitting a polynomial to the OF as done in the previous section, but this requires solving an optimization algorithm as well. It is therefore better to solve the problem directly with the solvers in the 'Least Squares' objective type. Furthermore, because the polynomial behavior of the OF, all derivatives are adequately smooth so the use of gradient based solvers is justified.

The D_{info} is constrained with $0 \leq K \leq 1$ for each magnetization factor, and $0 \leq \rho \leq 1$ and $0 \leq \theta_{\mathrm{M}} \leq 360°$ for both SE and DE and for each air gap. This means this problem has boundary constraints of the type $LB \leq x \leq UB$ where LB en UB are the lower and upper bound of the variable x. From this objective type and constraint type, it can be concluded that the non-linear least-squares (Lsqnonlin) solver is recommended. Alternatively, a non-linear programming solver named 'fmincon' can also be used, although this is more intended for the 'Smooth Non-linear' objective type. It is not the purpose of this work to do a qualitative comparison between different solvers as this is widely covered in literature [204–210].

A quick comparison is done between the Lsqnonlin using the Trust-Region-Reflective (TRR) algorithm, the fmincon solver with the Sequential Quadratic Programming (SQP) algorithm and with the active-set algorithm, as those were the algorithms suggested by the solver documentation [211]. To have a fair comparison, the three solver-algorithm combinations have all been set up with equivalent stopping conditions, as described in Section 4.1.4. 300 randomly generated defect cases containing demagnetization, static and dynamic eccentricity have been considered and the results are shown in figure 4.5. If the actual magnetization factor of magnet i is $K_{\mathrm{actual},i}$ and the estimated magnetization factor is $K_{\mathrm{est},i}$, then the difference between those two for every magnet is:

$$\Delta K_i = K_{\text{actual},i} - K_{\text{est},i}. \tag{4.6}$$

The error in estimating the magnetization factors K is E_K and is defined as the Euclidean distance of the errors of every magnetization factor:

$$E_K = \sqrt{\Delta K_1^2 + \Delta K_2^2 + \ldots + \Delta K_{4N_p}^2} = \sqrt{\sum_{i=1}^{4N_p} \Delta K_i^2}. \tag{4.7}$$

In analogy of the approach of defining the error in the magnetization factors, the difference in the eccentricity defects can be defined:

$$\begin{cases} \Delta\rho_{\text{SE,R}} & = \rho_{\text{SE,R,actual}} - \rho_{\text{SE,R,est}} \\ \Delta\theta_{\text{MSE,R}} & = \theta_{\text{MSE,R,actual}} - \theta_{\text{MSE,R,est}} \\ \Delta\rho_{\text{DE,R}} & = \rho_{\text{DE,R,actual}} - \rho_{\text{DE,R,est}} \\ \Delta\theta_{\text{MDE,R}} & = \theta_{\text{MDE,R,actual}} - \theta_{\text{MDE,R,est}} \\ \Delta\rho_{\text{SE,L}} & = \rho_{\text{SE,L,actual}} - \rho_{\text{SE,L,est}} \\ \Delta\theta_{\text{MSE,L}} & = \theta_{\text{MSE,L,actual}} - \theta_{\text{MSE,L,est}} \\ \Delta\rho_{\text{DE,L}} & = \rho_{\text{DE,L,actual}} - \rho_{\text{DE,L,est}} \\ \Delta\theta_{\text{MDE,L}} & = \theta_{\text{MDE,L,actual}} - \theta_{\text{MDE,L,est}}. \end{cases} \tag{4.8}$$

But there is a problem with this definition. Consider the two parameters of e.g. SE in the right rotor: $[\rho_{\text{SE,R}}; \theta_{\text{MSE,R}}]$. They can be used to describe any SE defect in this rotor, but also to describe the lag of a SE defect in that rotor by setting $\rho_{\text{SE,R}} = 0$. This is a valid case situation, but posses a difficulty in the calculation of the error, i.e. any value of $\theta_{\text{MSE,R}}$ combined with $\rho_{\text{SE,R}} = 0$ describes the same situation. The angle parameter has no meaning if the eccentricity coefficient is zero. This means it is possible to have $\rho_{\text{SE,R}} = 0$ for both the actual and the estimated parameters but have $\Delta\theta_{\text{MSE,R}} \neq 0$, although the identical situation is described.

This should of course be prevented. As the eccentricity is determined with an amplitude $\rho_{\text{SE,R}}$ and an angle $\theta_{\text{MSE,R}}$, just like a regular complex number, it can easily be converted from this polar formulation to a Cartesian formulation like $\rho_{\text{SE,R,real}}$ and $\rho_{\text{SE,R,imag}}$. This can be done for both SE and DE in both air gaps. The difference in the eccentricity coefficients then becomes:

$$\begin{cases} \Delta\rho_{\mathrm{SE,R,real}} & = \rho_{\mathrm{SE,R,real,actual}} - \rho_{\mathrm{SE,R,real,est}} \\ \Delta\rho_{\mathrm{SE,R,imag}} & = \rho_{\mathrm{SE,R,imag,actual}} - \rho_{\mathrm{SE,R,imag,est}} \\ \Delta\rho_{\mathrm{DE,R,real}} & = \rho_{\mathrm{DE,R,real,actual}} - \rho_{\mathrm{DE,R,real,est}} \\ \Delta\rho_{\mathrm{DE,R,imag}} & = \rho_{\mathrm{DE,R,imag,actual}} - \rho_{\mathrm{DE,R,imag,est}} \\ \Delta\rho_{\mathrm{SE,L,real}} & = \rho_{\mathrm{SE,L,real,actual}} - \rho_{\mathrm{SE,L,real,est}} \\ \Delta\rho_{\mathrm{SE,L,imag}} & = \rho_{\mathrm{SE,L,imag,actual}} - \rho_{\mathrm{SE,L,imag,est}} \\ \Delta\rho_{\mathrm{DE,L,real}} & = \rho_{\mathrm{DE,L,real,actual}} - \rho_{\mathrm{DE,L,real,est}} \\ \Delta\rho_{\mathrm{DE,L,imag}} & = \rho_{\mathrm{DE,L,imag,actual}} - \rho_{\mathrm{DE,L,imag,est}}. \end{cases} \tag{4.9}$$

The error in the eccentricity defect E_{Ecc} can then be stated as the Euclidean distance of the Cartesian eccentricity parameters:

$$E_{Ecc} = \sqrt{\Delta\rho_{\mathrm{SE,R,real}}{}^2 + \Delta\rho_{\mathrm{SE,R,imag}}{}^2 + \ldots + \Delta\rho_{\mathrm{DE,L,imag}}{}^2}. \tag{4.10}$$

Section 4.1.4 will discuss the required accuracy of these calculations and performs a coarse tuning of the stop conditions. The figure 4.5 shows the tuning can be done more accurately as the Fmincon solver with the SQP algorithm is striving for a lower error then the other two solvers. Yet, a conclusion can already be made: the Lsqnonlin solver with TRR is considerably faster than the other two, which is an important factor in condition monitoring. This solver is therefore used for all further calculations.

4.1.4 Stopping conditions

In order to do a fair comparison as in figure 4.5, correct stopping conditions need to be established. For condition based maintenance, it is most important to know which defects occur, e.g. which magnets are demagnetized or what rotor has eccentricity. The actual amplitude of the defect is less important. As very strict stopping conditions will require more iterations to solve the problems choosing the correct stopping conditions can decrease the calculation time. Generally, the stopping conditions are determined by tuning them in a trail-and-error based methodology.

We start from a chosen deviation of 5% of the maximum value on the estimated value of the defect, as this is adequately accurate for this purpose. By means of the analytical model, the corresponding deviation in the OF can be found. A 5% deviation on one magnetization factor or on a eccentricity parameter results in a deviation on the OF of 0.8% and 0.5%. A deviation of 0.5% is the strictest case. The stopping conditions are tuned to result in a deviation on the OF smaller than 0.5%. The default stopping conditions of the solvers described previously are 10^{-6}. The stopping conditions fulfilling the requirements are shown in Table 4.3. The parameter $TolFun$ is the tolerance on the OF and is defined by (4.11) where i is the iteration number. The definition depends on whether the stopping condition

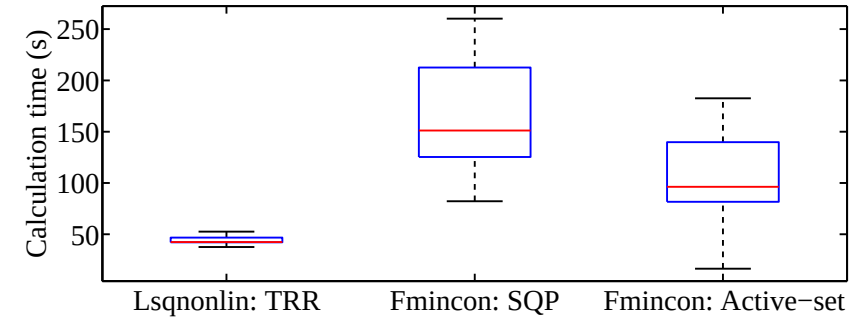

(a) Calculation time

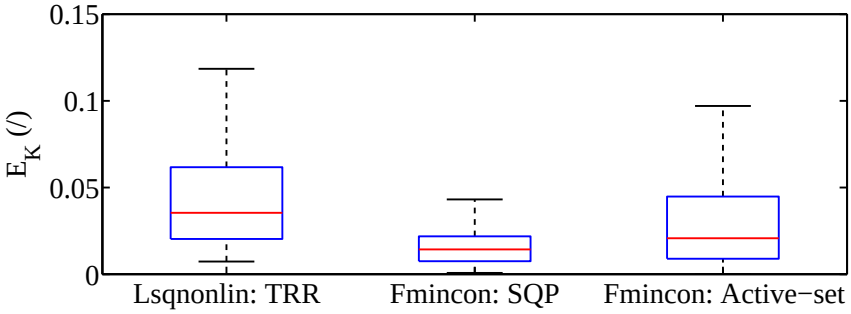

(b) Error on the magnetization factors

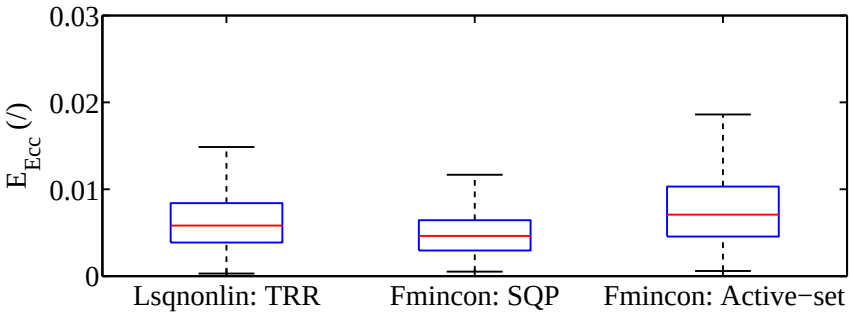

(c) Error on the eccentricity coefficients

Figure 4.5: The calculation time (a), the error on the magnetization factors defined in (4.7) (b), and the error on the eccentricity coefficients defined in (4.10) (c) for the three solver-algorithms combinations. The plots are based on 300 randomly generated defect cases containing demagnetization, static and dynamic eccentricity. Each solver calculated the same 300 cases.

Table 4.3: The tolerance on the OF $TolFun$ defined in (4.11) for every evaluated solver-algorithm combination. The last column describes if the tolerance value is either a relative or an absolute value.

Solver:algorithm	$TolFun$	Rel. or Abs. Tolerance
Lsqnonlin:TRR	10^{-1}	Rel.
fmincon:SQP	10^{-3}	Rel.
fmincon:active-set	10^{-1}	Abs.

is calculated as a relative or an absolute tolerance. The tolerance on the OF is set because this indicates the results are converging. The table shows that a significantly larger tolerance than the defaults values can be used due to the nature of the problem. The calculations in figure 4.5 are done with the stopping conditions described in this section. The previous section concluded: although the tuning can be improved, it is clear that the Lsqnonlin solver with TRR algorithm is the fastest of the three.

$$\begin{aligned} &\text{Abs.} : |OF(D_{info,i}) - OF(D_{info,i+1})| < TolFun \\ &\text{Rel.} : |OF(D_{info,i}) - OF(D_{info,i+1})| < TolFun * (1 + OF(D_{info,i})) \end{aligned} \tag{4.11}$$

4.2 Harmonic analysis

An analysis of harmonics that occur in the electric machine in case of defects, can be useful to speed up the inverse problem solving. As the solvers of the IP use an iterative process to determine the defect, the calculation time of the IP is a multiple of the calculation time of the forward model. It is therefore imperative that the forward model is as fast as possible, while still achieving the required accuracy to perform the defect detection. For this, it is interesting to look at the sensitivity of the harmonics toward the defects. More sensitive harmonics contain more information about the defect. By selecting the most sensitive harmonics first, less harmonics need to be calculated to achieve the required accuracy. This results in a faster forward model, and therefore an much faster IP, useful for condition monitoring.

This analysis is performed by first looking into the theoretical framework and determine what harmonics can be expected in a healthy and faulty machine. In the next section, an example case is examined in a practical investigation. After this, the harmonics are analyzed using the Cramér-Rao Lower Bound (CRLB) technique to have a sensitivity analysis of the harmonic content, which is the goal of this section. The CRLB technique is explained in Section 4.2.3

4.2.1 Theoretical framework

We start by exploring what harmonics can be expected in the AFPMSM. In order to draw conclusions for all topologies, the framework is presented in a general way, and is therefore valid for any YASA AFPMSM. The no-load field produced by the PMs is considered first. Afterwards, the influence of the magnetic field of the stator currents is examined. The harmonic content of an AFPMSM is well described in healthy conditions in e.g. [212].

Magnetic flux density and EMF at No-load

Chapter 3 states that the space harmonics and time harmonics in the no-load field are the same. The reason for this is that the magnetization of the PM can be considered constant. As the rotor rotates, the flux density field of the magnets simply rotates as well, but furthermore does not change in time. The stator slots will modify the air gap flux density field of the magnets, but this influence cannot be detected by the stator coils because the stator slots are obviously stationary. Therefore, both the space and the time harmonics of the no-load field are denoted by m.

If the machine is completely healthy, the following statements can be applied:

- The no-load field of the machine has N_p pole pairs, and as these are identical in healthy operation, the machine is N_p-periodic with the double pole pitch as one period. This means that the harmonics need to be a multiple of the number of pole pairs N_p.
- Because one double pole pitch contains two identical magnets, one facing with its north pole to the air gap and one facing with its south pole to the air gap, the magnetization square wave will always be an odd function. This implies that the harmonics can only be odd multiples of N_p.
- Gauss' law states that the total sum of the magnetic flux density crossing the air gap must always be zero. This implies that the air gap flux density field cannot contain the harmonic $m = 0$.

These conditions can all be condensed to one equation stating the possible harmonic content of the machines no-load field:

$$m/N_p = 2a + 1, \quad a \in \mathbb{Z}. \tag{4.12}$$

where m are the harmonics that can exist, and a is an integer number.

In this PhD, the machine can have defects. A demagnetization can break the periodicity of the pole pitches. The two magnets in one pole pair will not necessarily be identical. The only condition which does still hold is Gauss' law stating that the air gap flux density field cannot contain the harmonic $m = 0$. This means that the possible harmonics in an arbitrary defected state are:

$$m \in \mathbb{Z}_{\neq 0} \tag{4.13}$$

with $\mathbb{Z}_{\neq 0}$ as the integer numbers without zero. This criterion will therefore not result in a reduction of the number of harmonics needed for detection and gives no insight to what harmonics to expect in a defected case. This can be countered by examining the underlying principles on how the healthy magnetization pattern $M_{\mathrm{healthy}}(x)$ is modified by the "defects waveform" $f_{\mathrm{sq}}(x)$ to result in the demagnetized magnetization pattern $M_{\mathrm{demag}}(x)$. The waveform $f_{\mathrm{sq}}(x)$ is constructed with the magnetization factors K. The waveform is the value of corresponding magnetization factor at the location of the magnet, and is 1 between the magnets. This means the "defects waveform" is lower or equal to 1 at any point. This waveform is multiplied with the healthy magnetization pattern to create the demagnetized magnetization pattern.

Figure 4.6 shows this process for the defect D[8, R, 0] on the machine with 8 pole pairs, 15 stator slots, and 3 phases. Figure 4.6(a) and (b) shows the healthy magnetization in space and frequency domain respectively for the right rotor. The harmonic content of this waveform is defined by (4.12), but only the first 20 positive harmonics are shown for clarity, which results in only the 8th harmonic being non-zero in the plot. This waveform is multiplied by the "defect waveform" $f_{\mathrm{sq}}(x)$ shown in figure 4.6(c). This waveform has the value 1 at any x-value except for the x-values corresponding with magnet number 8. These values are set to the magnetization factor of that magnet K_8, which is 0. Figure 4.6(d) shows the harmonic content of the square wave. The 0th harmonic has the largest amplitude due to the consistent value 1 for all other magnets. The other harmonics create the square with value 0 at the 8th magnet's location. After multiplication, the resulting waveform is the demagnetized waveform in figure 4.6(e). This means the resulting $M_{\mathrm{demag}}(x)$ is the amplitude modulation of $M_{\mathrm{healthy}}(x)$, and in the frequency domain this leads to a convolution of the "defect waveform" frequencies with the healthy magnetization frequencies, shown in figure 4.6(f).

If $M_{\mathrm{healthy}}(x)$ is considered with all its harmonic content, the amplitude modulation can be written in general as:

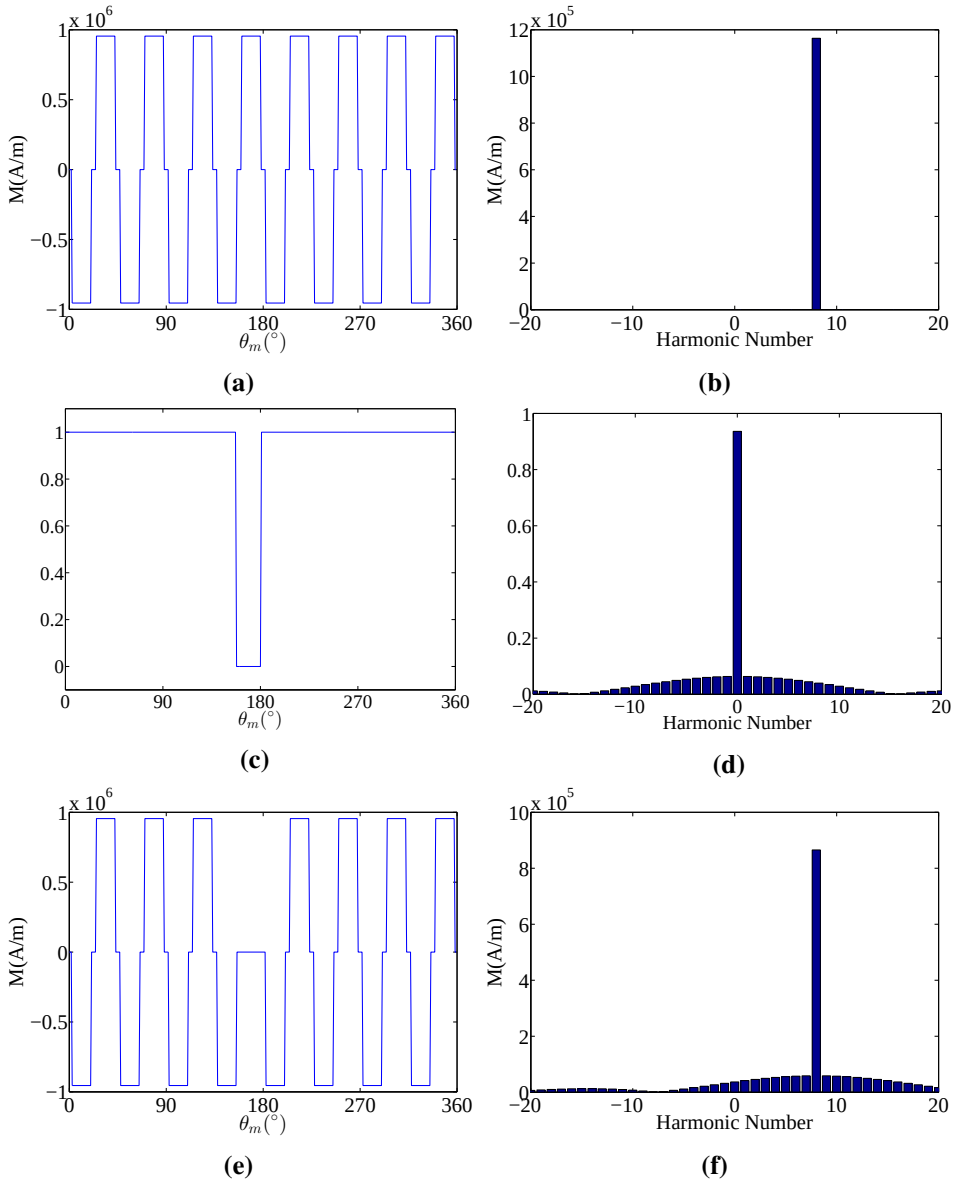

Figure 4.6: (a) The space domain waveform of the right rotor healthy magnetization pattern $M_{healthy}(x)$, (c) the "defects waveform" $A_{sq}(x)$ and (e) the right rotor magnetization pattern demagnetized by the "defects waveform" $A_{sq}(x)$. (b),(d) and (f) show the frequency domain of (a),(c) and (e) respectively. For clarity only the p-th harmonic is considered in (b). The represented defect is D[8, R, 0]. Note that the plots are denoted with θ_m instead of x, which can be done because of (3.1).

$$
\begin{aligned}
M_{\text{demag}}(x) &= M_{\text{healthy}}(x) f_{\text{sq}}(x) \\
&= \sum_{m=-\infty}^{+\infty} M_{\text{healthy},m} e^{\frac{jm\pi x}{\tau_{\text{m}}}} \sum_{m'=-\infty}^{+\infty} f_{\text{sq},m'} e^{\frac{jm'\pi x}{\tau_{\text{m}}}} \\
&= \sum_{m=-\infty}^{+\infty} \sum_{m'=-\infty}^{+\infty} M_{\text{healthy},m} f_{\text{sq},m'} e^{\frac{j(m+m')\pi x}{\tau_{\text{m}}}} \\
&= \sum_{m''=-\infty}^{+\infty} \left(\sum_{m=-\infty}^{+\infty} M_{\text{healthy},m} f_{\text{sq},m''-m} \right) e^{\frac{jm''\pi x}{\tau_{\text{m}}}} \\
&= \sum_{m''=-\infty}^{+\infty} M_{\text{demag},m''} e^{\frac{jm''\pi x}{\tau_{\text{m}}}}
\end{aligned}
\tag{4.14}
$$

with $m'' = m + m'$, where $M_{\text{healthy},m}$ is the harmonic component corresponding with the m-th harmonic of M_{healthy}, $f_{\text{sq},m'}$ is the harmonic component corresponding with the m'-th harmonic of f_{sq} and $M_{\text{demag},m''}$ is the harmonic component corresponding with the m''-th harmonic of M_{demag}.

The simplified case of figure 4.6 can easily be retrieved by stating that the healthy magnetization pattern is represented as a single sine wave with $m = N_p$ in (4.14). This results in the demagnetized magnetization pattern that is seen in figure 4.6(f):

$$
M_{\text{demag}}(x) = M_{\text{healthy},N_p} \sum_{m'=-\infty}^{+\infty} f_{\text{sq},m'} e^{\frac{j(N_p+m')\pi x}{\tau_{\text{m}}}}. \tag{4.15}
$$

The harmonic components of the "defect waveform" f_{sq} are shifted by $m = N_p$. The amplitude of the harmonic components of f_{sq} is scaled with M_{healthy,N_p}. This is seen in figure 4.6(f). It can also be observed that for this example defect, the harmonics that are influenced the most are the multiples of N_p and the sidebands around those multiples. These are the most sensitive harmonics to this demagnetization defect.

To understand how a defect with multiple demagnetized magnets will influence the magnetization patterns, the same procedure can be repeated for each demagnetized magnet one by one. It is clear that this will result in a similar harmonic content and state the same conclusion: the harmonics that are influenced the most are the multiples of N_p and the sidebands around those multiples. Note that in practice, f_{sq} can be modified in order to implement the demagnetization of every magnet simultaneously.

The harmonic content of the no-load flux density field in the air gap is reflected in the stator teeth back-EMFs, as this EMF is computed based on the air gap flux density. As described above, because the magnetic field of the magnets is simply

Table 4.4: Winding factors $k_{w,m}$ for the harmonics m of (a) a 5 pole pairs, 12 stator slots, 3 phase machines, and (b) 8 pole pairs, 15 stator slots, 3 phase machines both with double layer concentrated windings.

m	1	2	3	4	5	6	7	8	9
(a) $k_{w,m}$	0.07	0	0.5	0	0.93	0	0.93	0	0.5
(b) $k_{w,m}$	0.02	0.04	0.15	0.11	0.17	0.62	0.95	0.95	0.62

rotating, the back-EMF voltage has the same harmonic content as the no-load magnetic field. Because the stator slots are stationary, they will not introduce extra time harmonics in the back-EMF.

The back-EMF of a phase of the machine however can have a different harmonic content. By connecting the appropriate teeth back-EMFs in series to obtain the phase back-EMFs, the harmonic content is modified. The connections are chosen so that the N_p-th harmonics of the teeth per phase will amplify each other, but this has an impact on the other harmonics as well. The connections will amplify some harmonics and (partially) cancel out other harmonics. This process can be seen in figure 4.7, where (a) is the tooth back-EMF and (b) is the phase back-EMF for a 3 phase, 5 pole pair, 12 stator slot machine with as demagnetization defect D[4, R, 0] and D[4, L, 0]. The winding factor shows what the harmonic content of the back-EMF will be [198]. Table 4.4 shows the winding factors for two machines: (a) the machine shown in figure 4.7 and (b) a second machine where there is no complete canceling of the harmonics. When comparing the harmonic voltages in the figure, it is seen that amongst others even harmonics from the tooth coil back-EMF are not present in the phase back-EMF.

Stator current field

In full-load, the stator currents will introduce extra harmonics in the machine on top of the harmonics introduced by the no-load field. The correlation between the time and the space harmonic orders of the stator currents field is expressed by [213]:

$$u - m = c\zeta N_{ph}\upsilon, \quad c \in \mathbb{Z} \tag{4.16}$$

where υ is the periodicity of the machine, in respect to the number of stator slots and pole pairs by taking the greatest common divider of N_p and N_S, N_{ph} is the number of phases and ζ's value is 1 or 2 if N_S / υ is odd or even respectively.

If for instance a sinusoidal current with $m = N_p$ is injected in the 8 pole pair 15 stator slot 3 phase machine, then υ = 1 and ζ = 1. The occuring harmonic components armature reaction magnetic field will be described by:

$$u = N_p + 3c, \quad c \in \mathbb{Z}. \tag{4.17}$$

Note that this introduces asynchronous harmonics. This can be understood by considering a fixed point on one harmonic's sinusoidal wave in the air gap. For

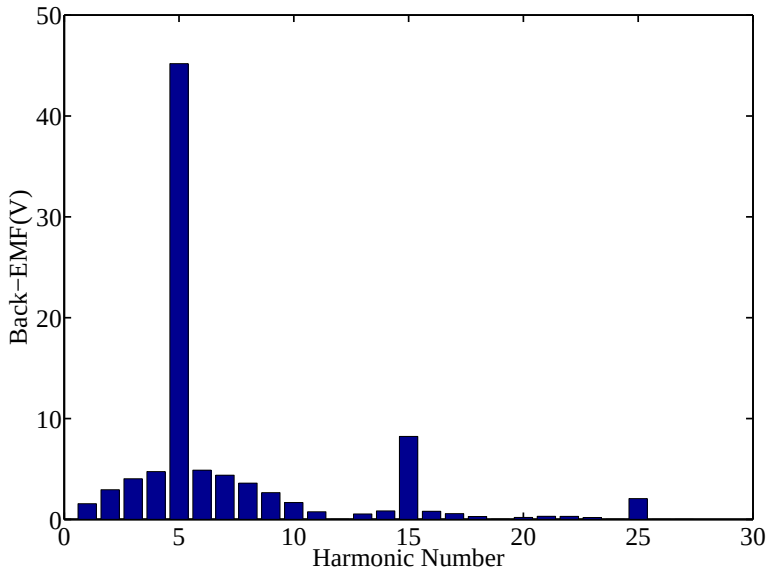

(a)

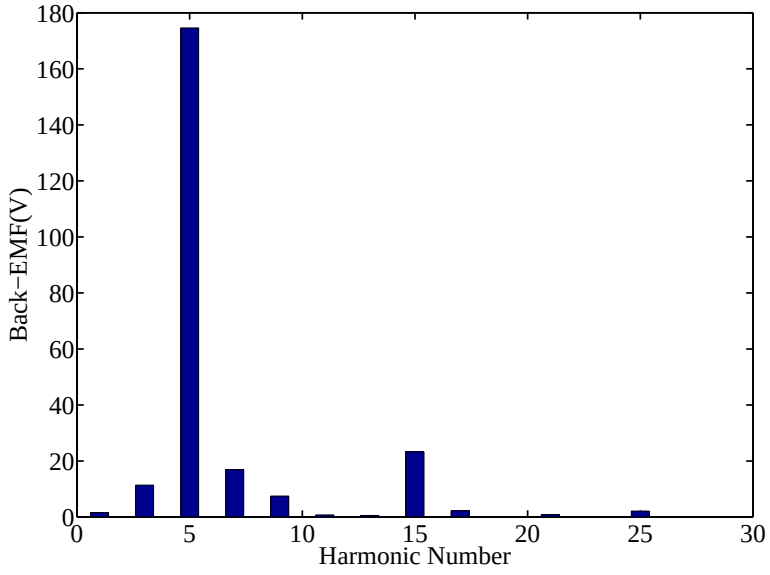

(b)

Figure 4.7: The harmonic content of the back-EMF voltage of (a) one stator tooth/coil and (b) one phase for the combined demagnetization defect D[4, R, 0] and D[4, L, 0]. Both plots are for a 3 phase, 5 pole pair, 12 stator slot machine simulated with the analytical model.

this point, the exponential terms $u\theta_m - m\omega_{\mathrm{m}}t$ are constant. From this, the angular velocity of the harmonics is derived as [213]:

$$\frac{d\theta_m}{dt} = \frac{m}{u}\omega_{\mathrm{m}}. \tag{4.18}$$

This means that the angular velocity of the harmonics equals the rotor angular velocity ω_{m} if $m = u$, which is only the case for $c = 1$ in the example in (4.17). The other space harmonics are asynchronous to the rotor and are therefore able to introduce eddy currents in the magnets and the rotor back-iron.

Because all these harmonics have the same time harmonic number m, the back-EMF generated by this stator current density field only has a m-th harmonic component. This is valid for every harmonic in a general non-sinusoidal current waveform. It can therefore be concluded that the harmonics of the back-EMF generated by the stator currents will be the same as those in the stator currents.

The harmonic content of the terminal voltages is the union of the harmonics generated by the no-load field of the PMs and the AR field of the stator currents.

4.2.2 Case study

The theoretical analysis of the previous section is now applied to a specific case. The 8 pole pair, 15 stator slot, 3 phase machine that was introduced in Section 3.5 is again used for this study. A fully sinusoidal stator current with the nominal magnitude is injected in the machine. The defect D[8, R, 0] is applied, which means the 8th magnet on the right rotor has been completely demagnetized. The machine is considered both with and without the defect, so that the healthy and the defected case can be compared.

Applying N_p = 8 to (4.12) predicts for the healthy machine that the harmonics with $m = ..., -40, -24, -8, 8, 24, 40, ...$ will occur due to the no-load field caused by the PMs. Based on the previous section, the stator currents will introduce only an 8th harmonic. Figure 4.8(a) shows the results of the analytical model for this particular case. The figure shows only the harmonics in the range [0,40[, and confirms the results of (4.12).

For the defected case, the theoretical framework in (4.13) predicts that every harmonic except 0 can occur, but based on the methodology explained in figure 4.6, the sideband harmonics around the harmonics of the healthy case are expected to show up. Figure 4.8(b) shows the results for the defected case and confirms the expectations of the theoretical framework. Because only one magnet is demagnetized in figure 4.8(b), the effect is small. In figure 4.8(c), multiple demagnetization defects have been introduced: D[6, R, 0], D[7, R, 0], D[8, R, 0], D[9, R, 0], D[6, L, 0], D[7, L, 0], D[8, L, 0], D[9, L, 0]. In this case, the side bands around the healthy case harmonics are much larger.

The next section will now define a more general methodology to determine the most sensitive harmonics in the terminal voltages toward a certain demagnetization

defect.

4.2.3 Sensitivity Analysis: Cramér-Rao Lower Bound

The CRLB technique is used to determine what harmonic orders of the terminal voltages are the most sensitive to the defect. In order to understand how this is done, the next sections will first give a brief recapitulation of the generally known likelihood function, the score and the CRLB to then use this for the sensitivity analysis.

Likelihood function

When rolling a die, the chance a certain number is thrown is determined by its probability or probability function. Questions like "What is the chance to roll a '6' 5 times in a row with a fair die?" try to determine this probability. But the opposite question can be asked as well: "If the die rolls a '6' 5 times in a row, what is the likelihood that this die is loaded or not fair?" This last question tries to determine the likelihood that a certain parameter resulted in a set of outcomes of the experiment. The parameter in this example is the fairness of the die. Although probability and likelihood are linguistic synonyms, in statistics, there is a distinction in their use. The likelihood function, which is sometimes called the likelihood, is in general a function of the parameters of a statistical model and can be used to estimate certain parameters of this model [214].

In general, the probability function can be described as a function of the set of sample data X_m, given a certain set of parameters β:

$$X_m \rightarrow f(X_m|\beta) = P(X_m|\beta). \tag{4.19}$$

Similarly, the likelihood function can be described as a function of the parameters to be estimated β, given a certain set of sample data X_m:

$$\beta \rightarrow f(X_m|\beta) = \mathcal{L}(\beta|X_m). \tag{4.20}$$

This means that if the function $f(X_m|\beta)$ is used as a function in X_m with a fixed β, it is called the probability function, while if this same function is used as a function in β with a fixed X_m, it is called the likelihood function.

The likelihood is very useful in parameter estimation. The maximum of the likelihood for a set of parameters corresponds with the values for those parameters that results in the highest agreement of the model with the measured data. The general methodology that maximizes the likelihood to estimate parameters is called maximum-likelihood estimation (MLE) [215].

To find the maximum of the likelihood function, the derivative of the likelihood function is calculated. This is then equaled to zero and solved for the parameters that need to be estimated. As many distributions contain products and exponential factors, it is often more convenient to use the natural logarithm of the likelihood

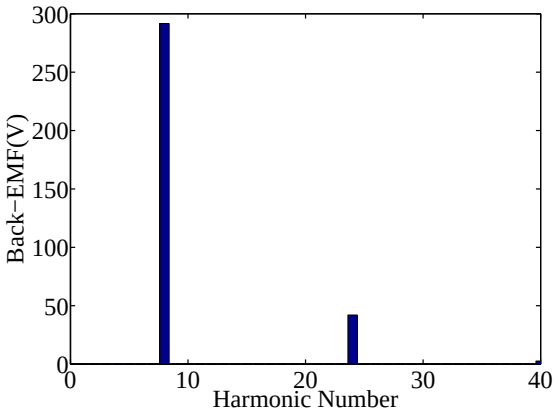

(a)

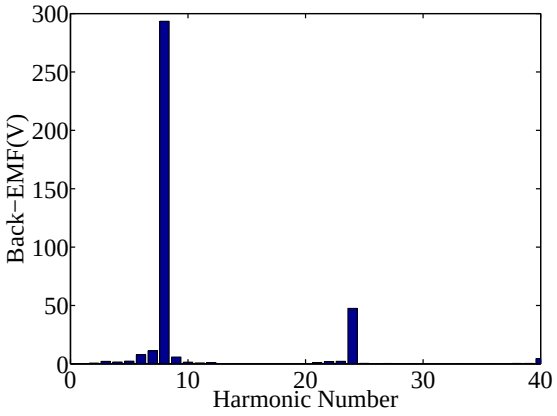

(b)

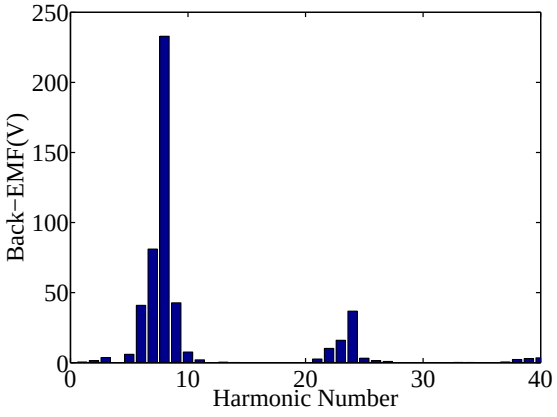

(c)

Figure 4.8: The harmonic spectrum of the terminal voltage at load of the (a) healthy, and (b) defected state with defect D[8, R, 0] and (c) defected state with defect D[6, R, 0], D[7, R, 0], D[8, R, 0], D[9, R, 0], D[6, L, 0], D[7, L, 0], D[8, L, 0], D[9, L, 0]. All these plots are for the 3 phase, 8 pole pair, 15 stator slot machine simulated with the analytical model.

function, called the log-likelihood function or log-likelihood. This is justified because the logarithm is a monotonically increasing function. This means the maximum of the log-likelihood function corresponds with the same parameter values as the likelihood function. Solving the derivative of the log-likelihood is generally easier to compute.

Score

The derivative of the log-likelihood is called the score or score function [216]. The score is then:

$$S(\beta|X_m) = \frac{\partial}{\partial\beta}\ln\mathcal{L}(\beta|X_m) = \frac{1}{\mathcal{L}(\beta|X_m)}\frac{\partial\mathcal{L}(\beta|X_m)}{\partial\beta}. \tag{4.21}$$

Because the score is the gradient of the likelihood function with respect to the parameters β normalized by the value of the likelihood itself, it is indicative for the sensitivity of a likelihood function $\mathcal{L}(\beta, X_m)$ toward the parameters β.

Assuming β contains only one parameter, the variance of the score function is called the Fisher Information $F(\beta)$:

$$F(\beta) = \mathrm{Var}(\mathrm{S}|\beta) = \mathbb{E}\left[(\mathrm{S} - \mu_{\mathrm{S}})^2\right] \tag{4.22}$$

where Var is the variance function, μ_S is the mean value of the score and $\mathbb{E}$ is the expected value of the data. The expected value is the value corresponding with the average value of a set of sample data if the size of the set goes to infinity. For a set of sample data X_m, the mean of that data is thus $\mu = \mathbb{E}[X_m] = \int_{-\infty}^{+\infty} X_m P(X_m) dX_m$. Based on this, the mean of the score μ_S can be determined:

$$\begin{aligned}\mu_S = \mathbb{E}[S(\beta|X_m)] &= \int_{-\infty}^{+\infty} S(\beta|X_m)P(X_m|\beta)dX_m \\ &= \int_{-\infty}^{+\infty} \frac{1}{\mathcal{L}(\beta|X_m)}\frac{\partial\mathcal{L}(\beta|X_m)}{\partial\beta}P(X_m|\beta)dX_m\end{aligned}. \tag{4.23}$$

Using (4.19) and (4.20), this becomes:

$$\int_{-\infty}^{+\infty} \frac{1}{f(X_m|\beta)}\frac{\partial f(X_m|\beta)}{\partial\beta}f(X_m|\beta)dX_m = \int_{-\infty}^{+\infty}\frac{\partial f(X_m|\beta)}{\partial\beta}dX_m. \tag{4.24}$$

As the Leibniz integral rule is fulfilled, the differential may be placed outside the integral [217]. Furthermore, because the integral of a complete probability function is by definition always 1, the mean of the score results in zero:

$$\int_{-\infty}^{+\infty}\frac{\partial f(X_m|\beta)}{\partial\beta}dX_m = \frac{\partial}{\partial\beta}\int_{-\infty}^{+\infty} f(X_m|\beta)dX_m = \frac{\partial 1}{\partial\beta} = 0. \tag{4.25}$$

If this is used in (4.22), $F(\beta)$ becomes:

$$F(\beta) = \mathbb{E}\left[(S-0)^2\right] = \mathbb{E}\left[S^2\right] = \mathbb{E}\left[\left(\frac{\partial}{\partial\beta}\ln(\mathcal{L}(\beta|X_m))\right)^2\middle|\beta\right]. \tag{4.26}$$

Notice that $F(\beta)$ is not dependent on the sample data X_m because this is averaged out by the $\mathbb{E}$-function.

Intuitively, a higher $F(\beta)$ indicates more extreme values of the score. As the score is the derivative of the likelihood function, this means the likelihood function has steeper slopes. Because the area of a distribution is always 1, steeper slopes indicate a high peak value of the likelihood function, increasing the agreement that the corresponding values of β at this peak are the correct values. F is therefore an indication of how much information of β is contained in the sample data X_m. This means that F is an indicator of how sensitive X_m is for the parameter β.

If more than one parameter is examined, the F can be expanded to a matrix called the Fisher Information Matrix F_m. Instead of calculating the variance of the score, the covariance matrix of the score in respect to all the parameters β is determined. An element in this matrix at the i-th row and j-th column is defined by:

$$F_{m,ij} = \mathrm{Cov}(\mathrm{S_i}, \mathrm{S_j}) = \mathbb{E}\left[(\mathrm{S_i} - \mu_{\mathrm{S,i}})\,(\mathrm{S_j} - \mu_{\mathrm{S,j}})\right]. \tag{4.27}$$

In the principal diagonal i equals j, which means these elements are the variances of the score for all the parameters. Just like before, the mean of the score is 0. In matrix notations, the F_m becomes:

$$F_m = \mathbb{E}\left[SS^T\right] = \mathbb{E}\left[\left[\frac{\partial}{\partial\beta}\ln(\mathcal{L}(\beta|X_m))\right]\left[\frac{\partial}{\partial\beta}\ln(\mathcal{L}(\beta|X_m))\right]^{\mathrm{T}}\right]. \tag{4.28}$$

According to the authors of [201, 218, 219], this can be solved to:

$$F_m = \left(\frac{\partial X_s(\overline{\beta})}{\partial\beta}\right)V^{-1}\left(\frac{\partial X_s(\overline{\beta})}{\partial\beta}\right)^{\mathrm{T}} \tag{4.29}$$

with $\overline{\beta}$ being the assumed values of the parameters β, X_s the simulated data of the model and V the measurement variance of the likelihood function:

$$V = \mathbb{E}\left[\frac{1}{K} = \sum_{k=1}^{K}\left(X_m - X_s(\overline{\beta})\right)^2\right] \tag{4.30}$$

with K the number of samples and k the sample number.

Cramér-Rao Lower Bound

The CRLB states a lower bound on the variance of estimators of the deterministic parameters β. This is also known as the information inequality or the Cramér-Rao inequality [220].

This theory expresses that the variance of any unbiased estimator is equal or greater than the CRLB denoted as C_r. If β contains a set of deterministic parameters that are unknown and need to be estimated from a set of measurements X_m, the unbiased estimators are $\hat{\beta}$. In the unbiased case, the CRLB is defined as the inverse of the Fisher Information Matrix $F_m(\beta)$:

$$\mathrm{Cov}(\hat{\beta}) \geq \mathrm{C_r} = \mathrm{F_m}(\beta)^{-1}. \tag{4.31}$$

If an unbiased estimator succeeds in achieving this bound, it is called fully efficient, where the efficiency is defined as:

$$e(\hat{\beta}) = F_m(\beta)^{-1}\mathrm{Cov}(\hat{\beta})^{-1} \tag{4.32}$$

combined with (4.31):

$$e(\hat{\beta}) \leq 1. \tag{4.33}$$

The solution that has the lowest possible mean squared error of all other unbiased solutions is called the Minimum Variance Unbiased (MVU) estimator. However, it is possible that even the MVU estimator does not reach the bound. As the CRLB is the inverse of the Fisher Information Matrix, it also can be used to determine the sensitivity of output of a model toward a certain input parameter. More information about the CRLB technique can be found in [221].

Using the Cramér-Rao Lower Bound to determine the sensitivity of harmonics

The purpose is to determine what voltage harmonics are the most sensitive for the occurrence of a demagnetization defect, i.e. the relative sensitivity of the terminal voltage harmonics to the magnetization factors. The terminal voltages depend on the magnetization factors, so in respect to the previous sections the terminal voltages V_{term} correspond with the sample data X_m and the array of magnetization factors K corresponds with the deterministic parameter β.

The likelihood function $\mathcal{L}(K|V_{\mathrm{term}})$ determines the likelihood that the given terminal voltages V_{term} are the result of a certain demagnetization defect described by K. This means the relative sensitivity can be found with the CRLB based on (4.31):

$$\mathrm{Cov}(\hat{\mathrm{K}}) \geq \mathrm{F_m}(\mathrm{K})^{-1} \tag{4.34}$$

where $\hat{K}$ is the unbiased estimators for K. Here the Fisher Information Matrix based on (4.29) becomes:

$$F_m = \left(\frac{\partial V_{\text{term}}(\overline{K})}{\partial K} \right) V^{-1} \left(\frac{\partial V_{\text{term}}(\overline{K})}{\partial K} \right)^{\text{T}} \tag{4.35}$$

with $\overline{K}$ being the assumed values of the parameters K. Notice that because the sensitivity of the voltage to the defect as a whole is studied, K is treated as one deterministic parameter. The sensitivity of the harmonics toward every magnet separately will not be examined. This means the matrix version of the Fisher Information is therefore not really required. Therefore, from now on, the scalar Fisher Information F will be used.

As the analytical model in Chapter 3 is built in the frequency domain, every terminal voltage frequency can be retrieved separately. This means that both (4.34) and (4.35) can be calculated for every harmonic component of the terminal voltages. The CRLB values can then be sorted from the most to the least sensitive terminal voltage harmonic component. Furthermore, it should be noted that the CRLB technique is a qualitative technique, and not a quantitative technique. This means that the ratios of the values of the CRLB give an indication of the relative sensitivity of the harmonic components, but the magnitude of the CRLB values have no absolute meaning. Furthermore, as the CRLB calculation is non-iterative, it is not time demanding compared to the IP.

4.3 Fault detection with sensing coils

The techniques in Section 4.1 are based on measurement and analytical data retrieved from the stator coils. These data are then used to diagnose a defect by means of an IP. Although this is a very solid technique, it has a shortcoming that is inherent to using stator coils: an identical defect in the left or the right rotor is seen by the stator coils as identical. This means that the stator coils do not contain any data to diagnose in which of both rotors the defect has occurred. It can be argued that detecting the magnitude of the defect and the progression of it with the aim of predictive maintenance is much more important than diagnosing the rotor side of the defect, especially because the machine needs to be taken offline for repairs just the same no matter what rotor contains the defect.

But prior knowledge of what rotor has the defect can decrease the maintenance time and resulting costs, especially in machines with non-identical rotors. The last situation can occur due to a combination of the rotor mounting system and the inverse polarization of opposing magnets. This is the case in the machine described in Chapter 7. Although this could be taken into consideration in the design process of the machine, it can also be accounted for by using a detecting technique that can determine in which rotor the defect is present.

As described in Section 2.3.3, the authors of [54] use three sensing coils in a SSSR machine equally distributed over the machine circumference. By connecting the three coils in series, the total voltage vector can be used to determine the

eccentricity magnitude and location. Because sensing coils at the air gap measure the flux in the air gap and not the flux in the stator coils, which is the average of the two air gap fluxes, this technique could be extended for a YASA machine and determine in what rotor the eccentricity defect occurs.

Similarly, sensing coils at the air gaps can be used to detect the demagnetization defects, including determining in what rotor they occur. The back-EMF of the sensing coils is used in a IP similar to the technique described in Section 4.1. This approach is explained in this section. First the sensing coils and their positions are determined. Then the forward model is adapted to include these sensing coils and lastly the IP is updated to work with the sensing coils back-EMF.

4.3.1 Sensing coil positions

The flux through the stator coils is the average flux of both air gap flux density fields entering or leaving the stator teeth. Furthermore, the influence of demagnetization on this average flux in the stator teeth is the same for both air gaps. This is why the stator coils cannot distinguish between the two rotors. To determine what rotor is defected, a measurement must be done where the magnetic flux density field is not the average and the influence of the two rotors is not the same. This can be done by measuring the stator flux more closely to the air gaps.

Some of the techniques used for measuring the flux through a material are [222] [54]:

- Sensing coils method: A coil is placed around the area of interest. An alternating magnetic field generates a back-EMF in the windings of the coil. The back-EMF is measured and can be used to derive the flux through the coil. Because the current in the coil is negligible, the diameter of the wire can be very small. Also, less windings than for instance the stator coils are needed to have a good signal. This allows for the coil to be placed at narrow areas.
- Fluxgate sensors: Two coils are wound around a high-permeable material. One coil is fed with an alternating current, pushing the core to the point of saturation. The second coil measures the back-EMF induced by this magnetic field. If no external field is applied, the back-EMF is symmetrical. If this external field is non-zero, this will result in an asymmetry in the back-EMF waveform, which can be measured. This requires the external field to be quasi-static compared to the injected alternating current waveform.
- Hall sensors: A current flows in a conductive plate.If a magnetic field passes through the plate normal to its surface, the electrons in the current will experience a Lorenz force perpendicularly to the direction of the current. This will in turn result in a voltage difference perpendicularly to the current direction. This voltage difference can be measured and, in case of a constant current, is proportional only to the magnetic flux density field through the plate.

- Needle probes: If a time-varying magnetic field passes through the plate normal to its surface, this will result – according to Faraday's law – in an electric field in the plane of the plate surface. Between two different points on the surface, the electric field causes a potential difference. This voltage difference can be measured and is proportional to the magnetic flux density field through (half of) the plate. The voltage can be used to locally estimate the flux in the material.

Firstly, the geometry of the machine does not provide much space to insert sensors. Secondly, the flux needs to be measured in the complete stator tooth section, as this is the useful part of the air gap magnetic field involved in the torque generation. Local measurement are not adequate. Due to these criteria, winding a sensing coil around the stator tooth adjacent to the stator coils is the simplest method that fulfills the requirements [223]. By placing this coil around the stator tooth near the air gaps, it can pick up the magnetic flux very easily [54]. Because the sensing coil is very compact, it can easily be placed in the machine without altering anything to the design of the machine.

For a sensing coil to be able to pick up the magnetic flux density originating from a specific PM, this magnet needs to pass in front of the tooth with the sensing coil near that air gap. This requires that both air gaps need at least one sensing coil. Furthermore, from the viewpoint of one stator tooth, all the PMs pass in front of this tooth in one complete revolution. This means that one sensing coil per air gap is enough to capture the magnetization data of every magnet in the machine. This setup can be seen in figure 4.9. Note that the two sensing coils do not have to be installed on the same stator tooth. This setup enforces an extra requirement on this technique: the back-EMF of one revolution is needed in order to diagnose the machine. By adding more evenly distributed sensing coils per air gap, the magnetization data of the magnets can be captured simultaneously. For instance, if three sensing coils per air gap are placed uniformly in the machine, every coil only needs to measure the data of 1/3th of a revolution. This means the measurement time is cut in three. Although condition monitoring prefers swift defect detection, increasing the number of sensing coils in the air gaps will have negligible influence because the gross part of the detection time is attributable to the IP using the analytical model iteratively.

4.3.2 Sensing coil forward model

Chapter 3 describes an analytical model that calculates the terminal voltages of that stator coils. The sensing coil approach requires an analytical model that calculates the back-EMF of the sensing coils instead. Figure 4.10 shows a flowchart of this sensing coil analytical model. The no-load and the stator current flux density can again be found with the scalar and the vector potential respectively as in Sections 3.2.2 and 3.2.3. From this, Section 3.2.4 superposes the no-load flux density with

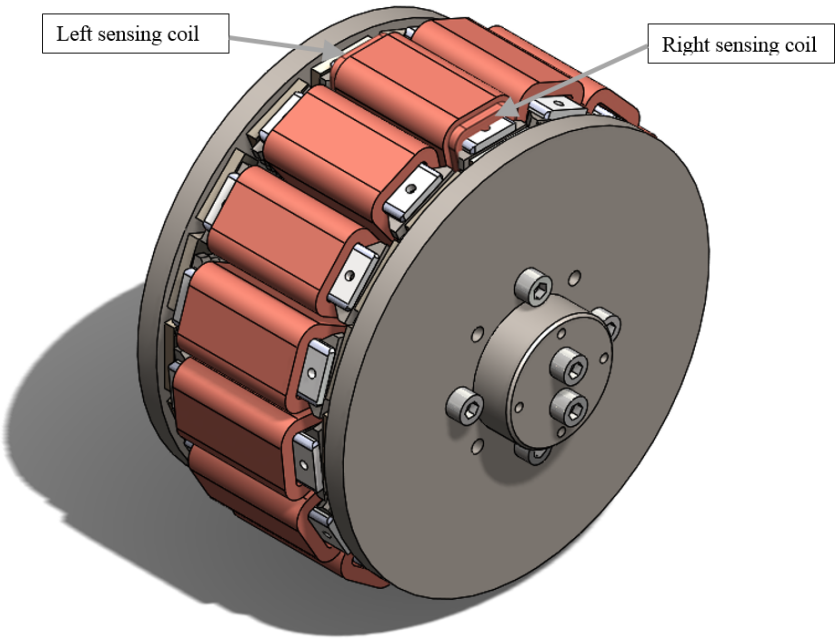

(a)

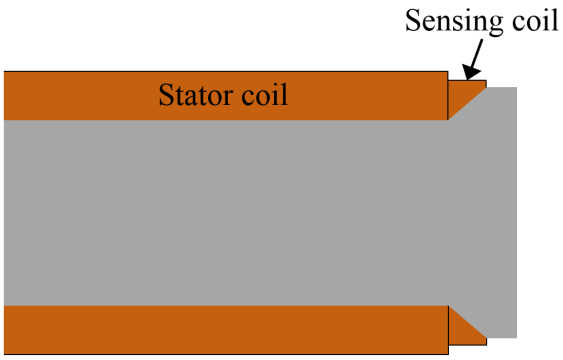

(b)

Figure 4.9: (a) The machine setup including the minimum required amount of sensing coils: one for each air gap [224]. The shown machine is the single-stator double-rotor YASA AFPMSM with 3 phases, 8 pole pairs and 15 stator coils explained in Section 3.5, and (b) a cross-section of the tooth with the sensing coil at the right air gap.

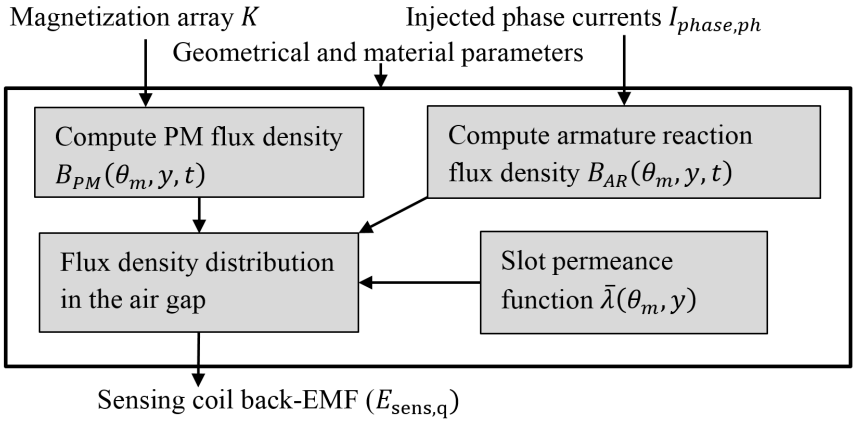

Figure 4.10: Flowchart of the sensing coil analytical model.

the stator current flux density as saturation is negligible for our purposes. Furthermore, the air gap flux density is corrected with the stator slot permeance function. The next step is the averaging of the air gap flux density to retrieve the required flux in the stator coils φ_{stator}. This is not needed for the sensing coil technique. The flux in the sensing coils φ_{sens} is required instead. This can be done by an adaptation of (3.43), where the axial component of the air gap flux density is integrated over the surface S_T of a stator tooth:

$$\varphi_{\mathrm{sens},q}(t) = \int_{S_T} B_{\mathrm{airgap,tot}y} dS_T = \sum_{l=0}^{n_{\mathrm{l}}} d_{\mathrm{l}} r_l \int_{\theta_q}^{\theta_{q+1}} B_{\mathrm{airgap,tot}y,l} d\theta_m \tag{4.36}$$

To compute the integral over the surface S_T, the geometry is discretized in n_{l} slices with thickness d_{l} as explained in Chapter 3. The axial component of the air gap flux density $B_{\mathrm{airgap,tot}}$ is similar to (4.37):

$$\begin{aligned} B_{\mathrm{airgap,tot},y}(\theta_m, y, t) = & \sum_{m=-\infty}^{+\infty} \sum_{v=-\infty}^{+\infty} (B_{\mathrm{PM},y,m} \lambda_{\mathrm{sl,real},v} - B_{\mathrm{PM},\theta_m,m} \lambda_{\mathrm{sl,imag},v}) \\ & e^{j[(m+v)\theta_m + m\omega_{\mathrm{m}} t]} \\ & + \sum_{u=-\infty}^{+\infty} \sum_{m=-\infty}^{+\infty} \sum_{v=-\infty}^{+\infty} (B_{\mathrm{AR},y,u,m} \lambda_{\mathrm{sl,real},v} - B_{\mathrm{AR},\theta_m,u,m} \lambda_{\mathrm{sl,imag},v}) \\ & e^{j[(u+v)\theta_m + m\omega_{\mathrm{m}} t]}. \end{aligned} \tag{4.37}$$

In the above equation, $B_{\mathrm{PM},y,m}$, $B_{\mathrm{PM},\theta_m,m}$, $B_{\mathrm{AR},y,u,m}$and $B_{\mathrm{AR},\theta_m,u,m}$ are the axial and tangential component of the PM and AR flux density field of the air

gap in front of the sensing coil respectively. Note that the permeance function of eccentricity is not included in this equation. This is because the permeance function is designed to be included on the average flux as it contains the information of both air gaps equally. The effect of eccentricity on the air gap flux density field is not accounted for and therefore this analytical model for the sensing coils is not useful for eccentricity defect detection.

The back-EMF in the sensing coils can then be derived:

$$E_{\mathrm{tooth},q}(t) = \sum_{m=-\infty}^{+\infty} -N_{\mathrm{sens}} j m \omega_{\mathrm{m}} \varphi_{\mathrm{sens},q,m} e^{jm\omega_{\mathrm{m}}t}, \tag{4.38}$$

where N_{sens} is the number of turns of the sensing coils. This results in a similar equation as (4.37):

$$\begin{aligned} E_{\mathrm{sens},q}(t) = & \sum_{m=-\infty}^{+\infty} -d_{\mathrm{l}} \omega_{\mathrm{m}} N_{\mathrm{sens}} m \\ & \Bigg[\sum_{l=0}^{n_{\mathrm{l}}} \sum_{v=-\infty}^{+\infty} (B_{\mathrm{PM},y,m,l} \lambda_{\mathrm{sl,real},v,l} - B_{\mathrm{PM},\theta_m,m,l} \lambda_{\mathrm{sl,imag},v,l}) \\ & \frac{r_l}{m+v} (e^{j(m+v)\theta_{q+1}} - e^{j(m+v)\theta_q}) \\ & + \sum_{l=0}^{n_{\mathrm{l}}} \sum_{u=-\infty}^{+\infty} \sum_{v=-\infty}^{+\infty} (B_{\mathrm{AR},y,u,m,l} \lambda_{\mathrm{sl,real},v,l} - B_{\mathrm{AR},\theta_m,u,m,l} \lambda_{\mathrm{sl,imag},v,l}) \\ & \frac{r_l}{u+v} (e^{j(u+v)\theta_{q+1}} - e^{j(u+v)\theta_q}) \Bigg] e^{jm\omega_{\mathrm{m}}t}. \end{aligned} \tag{4.39}$$

Because the sensing coils are used with a high impedance voltage measurement, no current will flow in the coils and therefore there will be no voltage drop in the coil electrical circuit. The back-EMFs are the terminal voltages of the sensing coils. Note that the position of the sensing coils in figure 4.9 shows that they are not exactly adjacent to the air gap, but because of construction considerations are placed next to the stator coils. This means not only the AR air gap flux density field will pass through the coil, but also a part of the tooth tip and end winding leakage flux, which have not been accounted for in equations derived above. Some deviation due to this is to be expected, but Section 4.3.3 shows that this approximation is acceptable.

4.3.3 Model validation

This sensing coil analytical model needs to be validated as well. In order to do this, the same machine is used as in Section 3.5, i.e. the 3 phase, 8 pole pair, 15 stator

slot YASA type AFPMSM. All machine data can be found in Section 3.5. The FEM model of that section is expanded with the sensing coils so the back-EMF of the sensing coils can be simulated numerically. As the analytical model with the stator coils is already validated with the air gap flux density field and the terminal voltages of the FEM model, only the sensing coil back-EMF calculation needs to be validated.

Figure 4.11(a) shows the back-EMF of the sensing coil calculated both with the analytical model and the FEM model. The data has a very good agreement. Furthermore, the expected deviation explained in the previous section due to the difference in sensing coil position between the two models is visible but acceptable.

In the FEM model, it is possible to place the sensing coils adjacent to the air gap as in the analytical model although this is construction-wise not realistic. Figure 4.11(b) shows the result of this simulation for the same situation as figure 4.11(a). Now, both data align without the previous deviation.

The model is also validated in a defected state. The defect D[8, R, 0] is applied, which means the 8th magnet of the right rotor is completely demagnetized. Figure 4.12 shows the back-EMF of the sensing coil at the left and right air gap. The sensing coils in the FEM models are placed as shown in figure 4.9. Again a good agreement is found between the analytical and numerical data except for the previous explained deviation.

Again it is possible to place the sensing coils adjacent to the air gaps. These results are shown in figure 4.13 and again there is a good correspondence between the analytical and numerical data.

Figure 4.14 shows a comparison of the frequency components of the back-EMF of the sensing coil of the right air gap for the healthy case and defected case. The harmonic content is similar as that of the terminal voltages: the defect introduces extra harmonics around the healthy harmonics.

As the analytical model is now validated, the next section will describe how this model is used to detect demagnetization defects.

4.3.4 Demagnetization identification

The methodology of the IP finding the defect information with the analytical model of Chapter 3 and the measured terminal voltages remains similar if the sensing coils are used. A new IP is defined, similar to the one described in Section 4.1.1. This new IP will use the sensing coil analytical model in previous section and the back-EMF measured from the sensing coils on the actual machine to determine the demagnetization defect in the machine. The inputs of the sensing coil analytical model are the magnetization array K, the phase currents, the rotor speed, the geometrical and circuit parameters.

The general structure of the IP is the same and follows a scheme shown in figure 4.15, which is based on figure 4.1. The difference is that now the OF determines the deviation between the sensing coil analytical model and the measured sensing

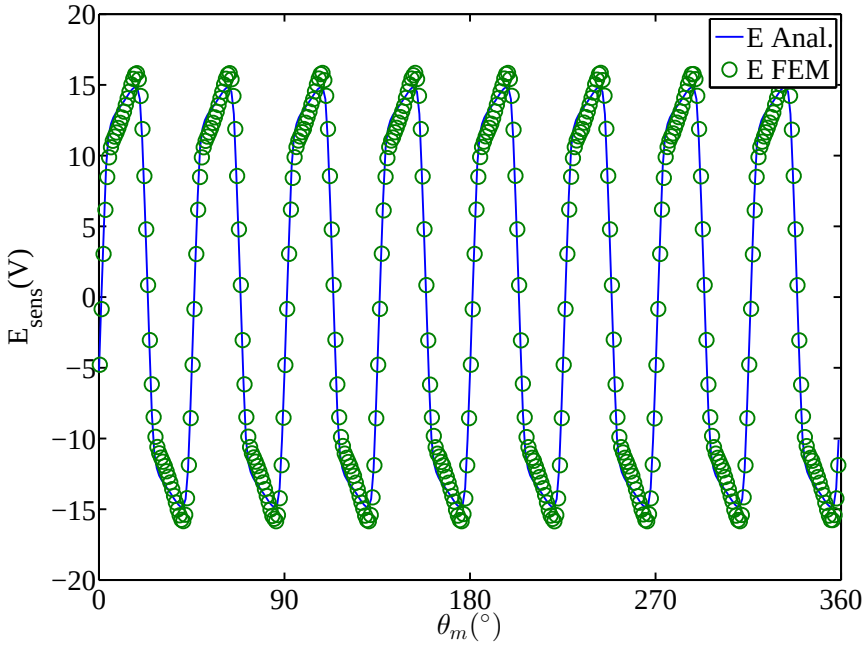

(a)

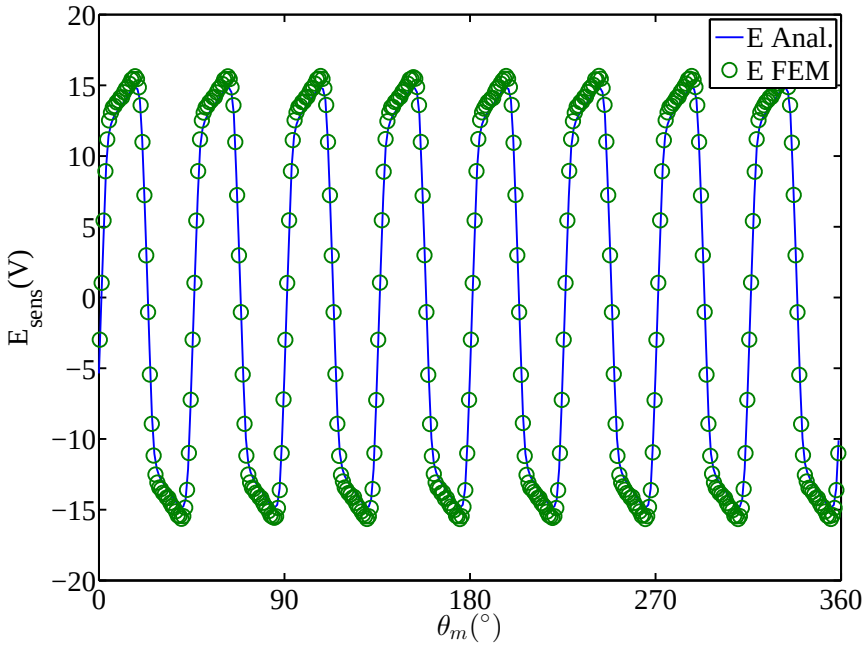

(b)

Figure 4.11: The back-EMF of the sensing coil in the right air gap simulated by the analytical and the FEM for a 3 phase, 8 pole pair, 15 stator slot machine in healthy state. With the sensing coils in the FEM model placed (a) as shown in figure 4.9 and (b) placed directly adjacent to the air gap.

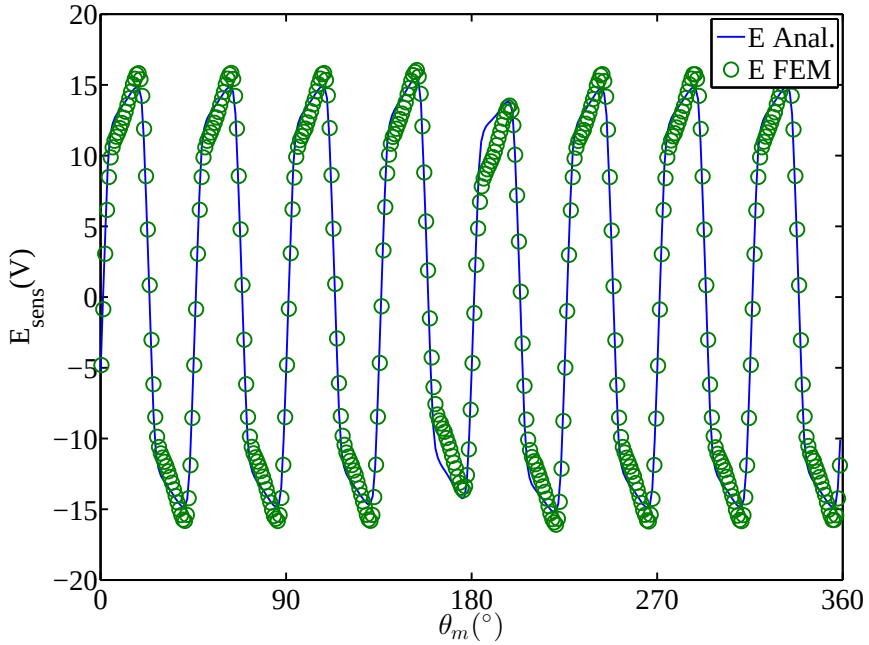

(a)

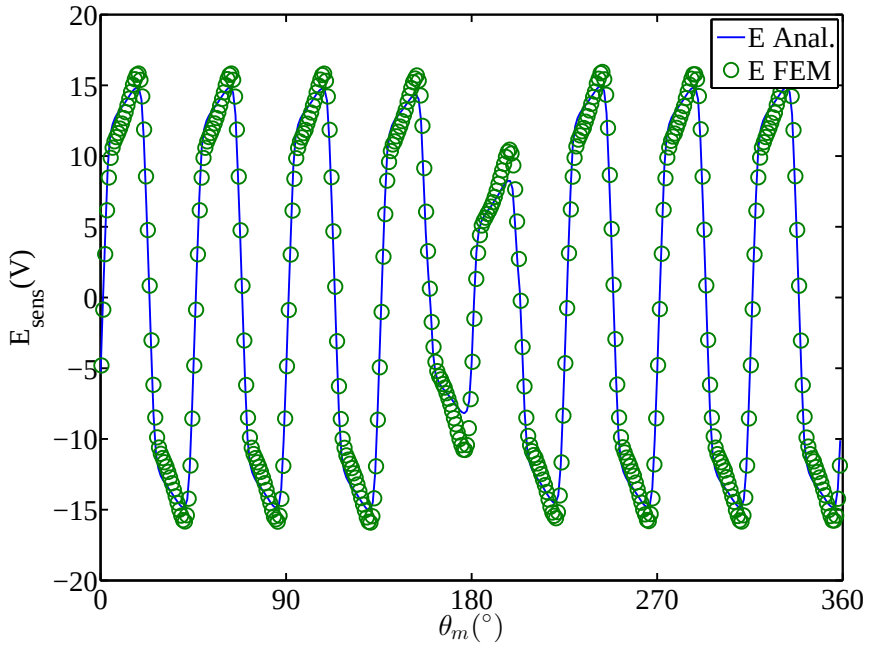

(b)

Figure 4.12: The back-EMF of the sensing coil in (a) the left and (b) the right air gap simulated by the analytical and the FEM model for a 3 phase, 8 pole pair, 15 stator slot machine with the D[8, R, 0] defect applied.

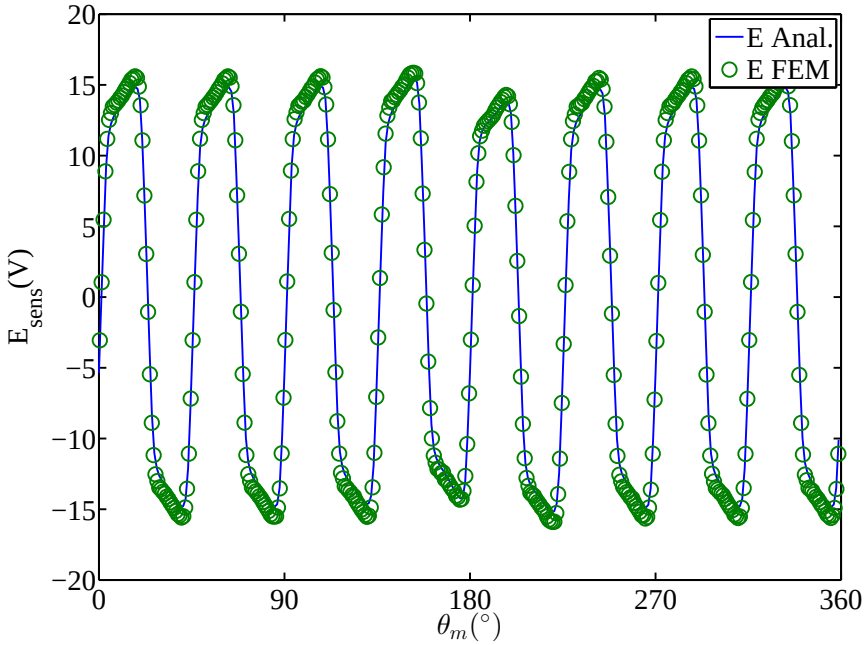

(a)

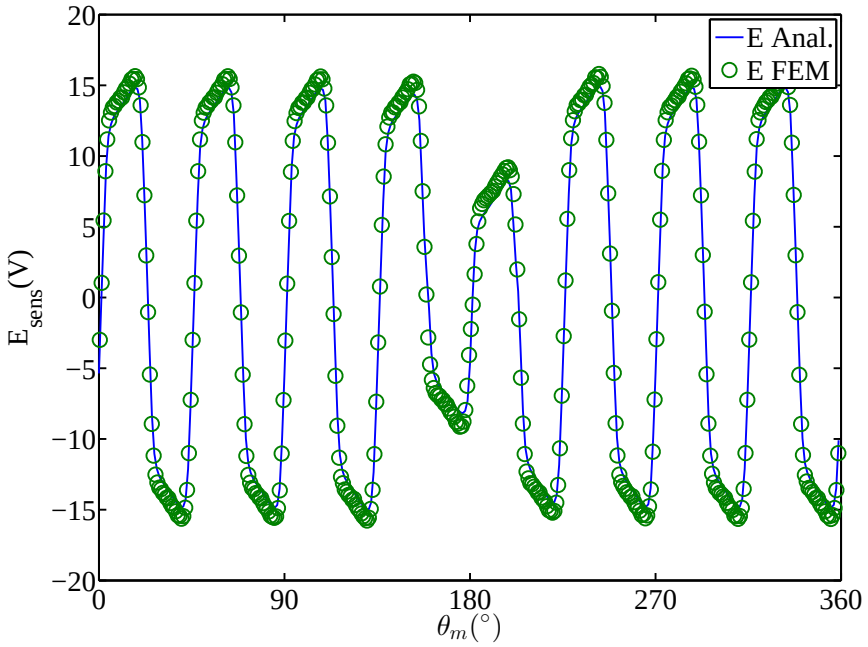

(b)

Figure 4.13: The back-EMF of the sensing coil in (a) the left and (b) the right air gap simulated by the analytical and the FEM model for a 3 phase, 8 pole pair, 15 stator slot machine with the D[8, R, 0] defect applied. In this figure, the sensing coils in the FEM model are placed directly adjacent to the air gap.

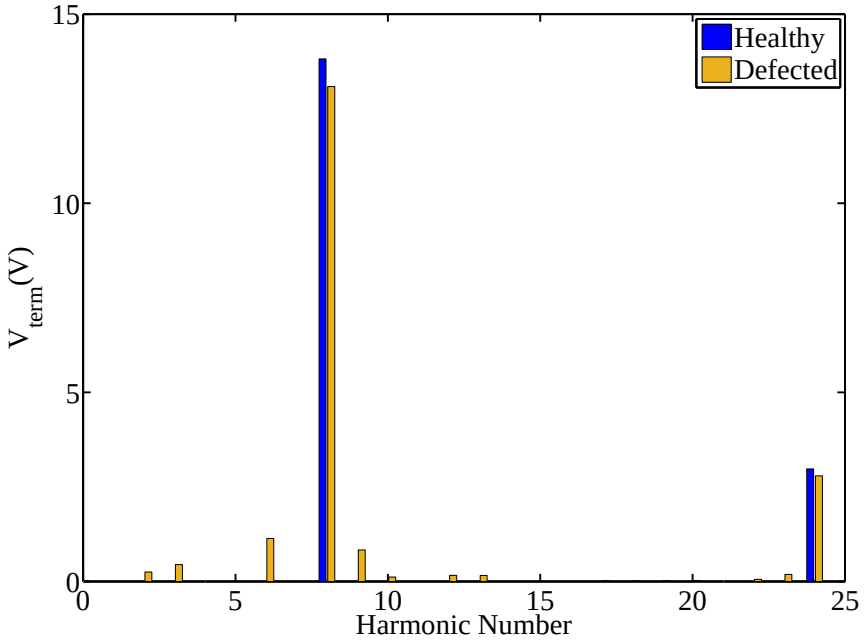

Figure 4.14: Analytical frequency data of the back-EMF of the sensing coil on the right air gap at full-load for the healthy state and with the defect $D\,[8, \mathrm{R}, 0]$.

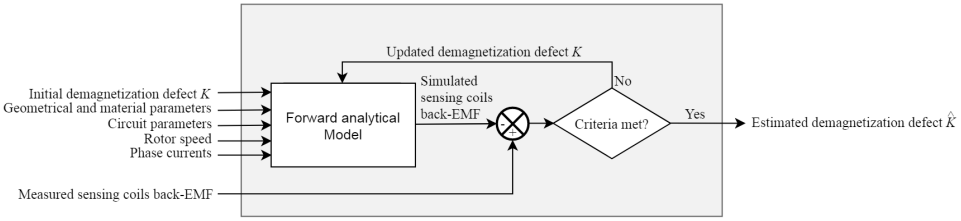

Figure 4.15: The scheme used by the sensing coil IP together with the sensing coil analytical model to diagnose the demagnetization defect by determining the magnetization array K.

coil back-EMFs, which is the Squared Euclidean Distance between the measured and the simulated sensing coil back-EMFs:

$$OF(K) = \left(E_{\mathrm{sens,m}} - E_{\mathrm{sens,s}}(K)\right)^2 \tag{4.40}$$

Here, $E_{\mathrm{sens,m}}$ and $E_{\mathrm{sens,s}}$ are a compilation of the harmonic components magnitude and angle information in the form of their real and imaginary components of the measured and the simulated phase terminal voltages respectively. An example for a 3 phase system is:

$$E_{\text{sens}} = [E_{\text{sens,R,1,real}}, E_{\text{sens,L,1,real}}, E_{\text{sens,R,1,imag}}, E_{\text{sens,L,1,imag}}, E_{\text{sens,R,2,real}}, ...] \tag{4.41}$$

both for $E_{\text{sens,m}}$ and $E_{\text{sens,s}}$, where R and L refer to the sensing coil in the right and left air gap resp. and 1 and 2 are the harmonic number.

The minimization of the OF will lead to the recovered array of magnetization coefficients $\hat{K}$, which is the output of the IP:

$$\hat{K} = \arg\min_{K} OF(K). \tag{4.42}$$

As the back-EMFs of the sensing coils placed in both air gaps are used for this IP – containing the magnetization information of all the PMs – the IP is able to detect and locate asymmetrical defects.

4.4 Conclusion

In this chapter, the methodology for the inverse problem is explained. The methodology uses the forward model from Chapter 3, to determine the demagnetization and eccentricity defects from measured stator winding voltages.

A harmonic analysis is made as this can reduce the CPU time for solving the inverse problem. By selecting the harmonics that are most sensitive to faults, the inverse algorithm can focus on these harmonics, not wasting time to compute harmonics that contain almost no relevant information. Theoretical framework and the case study conclude that the harmonics that are influenced the most are the multiples of N_p and the sidebands around those multiples. The Cramér-Rao bound technique is explained, as well as the Fisher information matrix. It is shown how this method can determine the sensitivity of harmonics.

Finally, an alternative methodology for the inverse problem is presented where the stator winding voltages are replaced by voltages measured in dedicated sensing coils. The latter requires additional windings to be added in the machine, but has the advantage that it can determine in which of both rotors the defect occurs. A validation of the induced voltages is presented by comparing the analytical model with a Finite Element model.

Chapter 5

Detection of demagnetization defects

This chapter first studies the detection of defects with the IP of Chapter 4 and the forward model of Chapter 3. In Chapter 5, the considered defects are only demagnetization defects. Chapter 6 will focus more on the detection of eccentricity defects and the distinction between demagnetization and eccentricity defects.

Secondly, the CRLB technique will be used to examine which harmonics are the most sensitive to a defect and how this is used to accelerate the detection of the demagnetization defects.

Finally, the technique for detecting demagnetization defects with the sensing coils is studied. This technique requires the modified forward model and IP introduced in Chapter 4. Results obtained with this technique are shown and compared with the results of the technique using the stator coils.

5.1 Numerical evaluation of the demagnetization detection technique with the IP and the terminal voltages

In the previous chapter, the IP was thoroughly explained. It was shown how it works, and how it uses the analytical model of Chapter 3 and measurement data of the stator coils of the AFPMSM.

In order to test this technique, measurement data is generated simply by calculating the terminal voltage with the analytical model and adding noise to the data. This is done by multiplying the noise level nl with the maximum value of the terminal voltage waveform.

$$nl_{ampl} = nl \cdot \max(V_{\text{term}}) \tag{5.1}$$

where nl_{ampl} is the amplitude of the noise waveform and the noise level nl is a number between 0 and 1. This noise waveform is created by generating a uniformly

Table 5.1: An example of a defect found by the IP with an error of 0.08267 and 5% noise on the terminal voltage data. The introduced defect is $D\,[2, \mathrm{R}, 0.45]$, $D\,[5, \mathrm{R}, 0.06]$, $D\,[12, \mathrm{R}, 0.33]$. Only the magnetization factors of the right rotor are shown. All the magnetization factors of the left rotor are 1.

Actual K [/]	Estimated K [/]	$\Delta(10^{-1})$ [%]
1.00	1.00	1.8
0.45	0.48	30.7
1.00	0.99	7.1
1.00	0.96	43.4
0.06	0.10	43.0
1.00	1.00	0.0
1.00	0.99	5.6
1.00	0.99	7.2
1.00	1.00	2.4
1.00	0.98	23.3
1.00	0.98	16.6
0.33	0.35	21.4
1.00	1.00	2.1
1.00	0.98	18.8
1.00	0.98	19.3
1.00	1.00	2.7

distributed random waveform with nl_{ampl} as amplitude. This noise waveform is then converted to the frequency domain and is added to the terminal voltages harmonics.

All calculations in this section are performed at the rated load and speed of the machine. The full description of the machine can be found in Section 3.5.

As indicator of the error in detecting the demagnetization defect, the definition of (4.7) in the previous chapter is used again.

As an example, we consider a number of different demagnetization defects. Table 5.1 shows the magnetization array K for a 3 phase 8 pole pair 15 stator slot machine. Because this method cannot differentiate between the magnets of two rotors, the magnets from the second rotor have been fixed to 1, meaning healthy. First the actual defect is shown. This is the defect used in the analytical model with added noise to generate the terminal voltages that can be used as measurement data in this test. 5% noise has been used in this example. The second column shows the estimated magnetization factors and the third column presents the absolute difference between the actual and estimated K relative to their maximum value. It can be seen that the technique succeeds in estimating the magnetization factors quite accurately. The method also finds that some healthy magnets are not 100% magnetized. This deviation is of course to be expected. The total error in the magnetization defects E_K of this case can be calculated with (4.7) and is 0.08267.

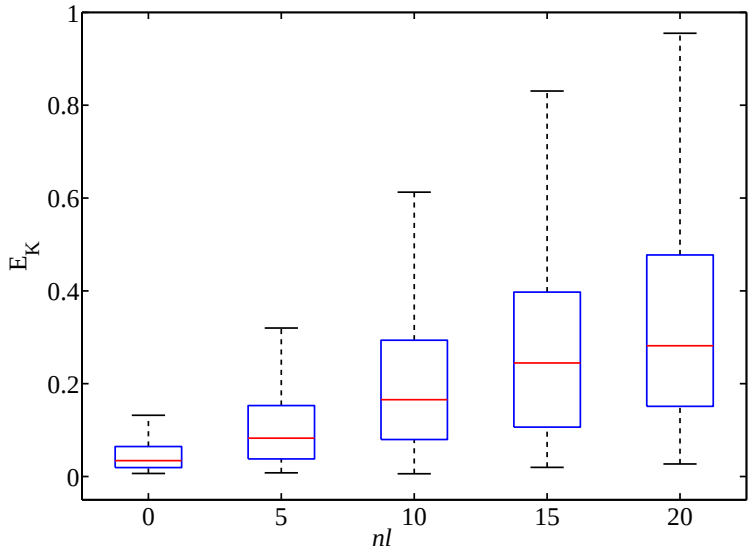

Figure 5.1: On a 3 phase 8 pole pair 15 stator slot machine 1, 3 and 7 magnets have been demagnetized respectively. For every situation, 100 random defects have been generated. The noise level nl was varied from 0% to 20%. The median is indicated by the red line, while the 25th and 75th percentile are shown by the box borders. The lower and upper adjacent value are indicated by the dashed lines and outliers are not shown for clarity sake.

The case presented in Table 5.1 is an example; it does not give a general overview of the performance of the technique. To achieve a more general indication of the identification accuracy, for resp. 1, 3 and 7 demagnetized magnets, 100 random generated demagnetization defects have been tested. For each case, the IP was solved and the error in the magnetization factors was calculated. These are then compiled into a boxplot per evaluated noise level. The errors in the magnetization defects E_K for for instance 5% noise are shown in figure 5.1 at $nl = 5$. To get a better idea of the physical meaning of the error values shown in this figure, we can consider the following example: if every magnetization factor is deviating 5% of the maximum magnetization factor value from the real value, still assuming only one rotor has defects, then the error equation (4.7) gives a result of $E_K = 0.20$ for this machine. It can be seen that the majority of defects are more accurate than this: the 75th percentile has $E_K = 0.1529$.

Of course, the accuracy is also influenced by the noise on the terminal voltage data. Figure 5.1(b) shows the accuracy of the demagnetization detection for five different noise levels. The results are as expected: with increasing noise levels, the average accuracy decreases and the variance on the accuracy increases. It is therefore important for defect detection that good measurements with limited noise can be performed. The correlation is also verified with Pearson Correlation test,

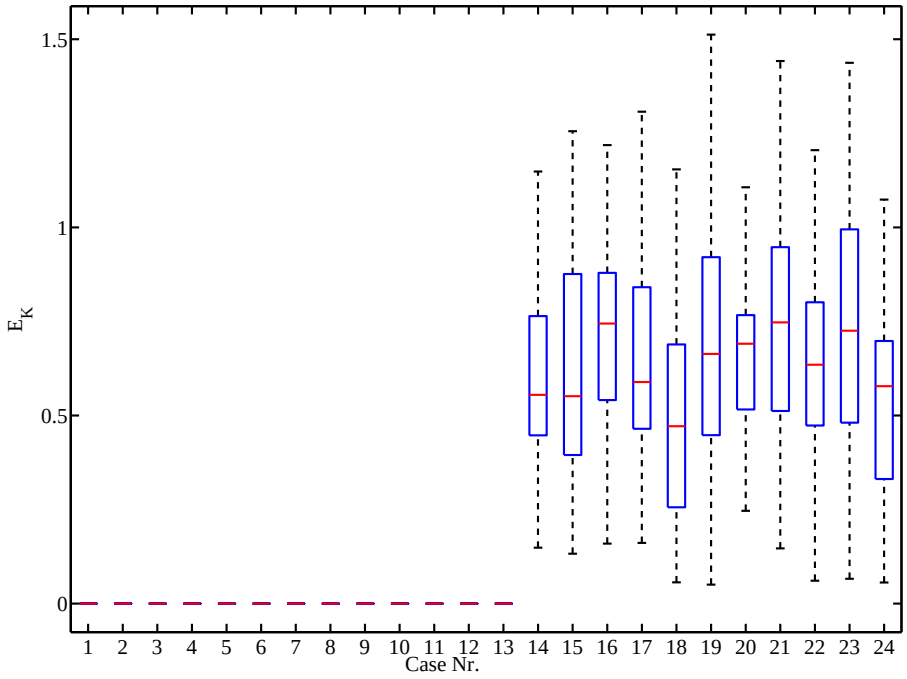

Figure 5.2: Overview of the error in the magnetization factors for 24 different topologies. The meaning of the different lines and colors is identical to figure 5.1.

which shows that the correlation is significant at the 0.01 level. A linear regression can be placed on the data. The constant and first order coefficient for this regression are respectively 0.060 and 0.014 with an standard error of 0.008 and 0.001.

It can be concluded that the technique is able to detect the demagnetization defects with adequate accuracy as long as the noise level is acceptably low.

5.1.1 Evaluation of different topologies

The previous paragraphs describe the performance of the demagnetization detection technique for the 3 phase 8 pole pair 15 stator slot machine. Figure 5.2 shows an overview of the accuracy of the technique for 24 different topologies. The number of stator slots, pole pairs and phases of each topology in the figure is given in Table 5.2. The figures show a very clear trend: case 14 to 24 have a very big error compared to case 1 to 13. The IP is not able to solve the detection technique for case 14 to 24 in an acceptable accuracy. The noise level was set to 0% and the stop conditions are set to the default stop conditions of the solver, i.e. 10e-6, to exclude these as the causes.

The trend is explained by the periodicity $\gcd(2N_p, N_S)$. The last column of

Table 5.2: The number of stator slots, pole pairs and phases for each case in figure 5.2. The last column shows the periodicity determined by $\gcd(2N_p, N_S)$ for each case.

Case Nr.	N_S	N_p	N_{ph}	$\gcd(2N_p, N_S)$
1	15	8	3	1
2	9	4	3	1
3	9	5	3	1
4	15	7	3	1
5	21	10	3	1
6	21	11	3	1
7	15	7	5	1
8	15	8	5	1
9	25	12	5	1
10	25	13	5	1
11	7	4	7	1
12	21	10	7	1
13	21	11	7	1
14	12	7	3	2
15	12	5	3	2
16	18	7	3	2
17	18	8	3	2
18	10	4	5	2
19	10	6	5	2
20	20	8	5	4
21	14	5	7	2
22	14	6	7	2
23	14	9	7	2
24	36	3	3	6

Table 5.2 calculates this periodicity for each case and a clear trend emerges. The demagnetization detection technique cannot function properly for machines with a periodicity higher than 1. This is an inherent feature of the machine as this means that machines with high periodicity are constructed by repeating the base machine several times throughout the circumference. Because all teeth are connected to the same set of phases, the information that determines in which repeated base machine the demagnetization defect occurred is lost.

Demagnetization detection on machines with a periodicity higher than 1 can be performed when working with a 'modular n-phase' configuration. This means that $N_{ph} = N_S$, or that every stator tooth is a phase on its own. The author of [91] show the advantages of the modular n-phase configuration. By using this modular n-phase configuration, the IP has access to all the information in the separate stator tooth back-EMF. Both the analytical model as the IP are constructed in a flexible

way to allow such topology changes and improve the versatility of the technique. This means that in the modular n-phase configuration the algorithm is able to detect demagnetization in a machine with a periodicity higher than 1.

5.1.2 Effect of uncertainties in model parameters

Until now, the model and its parameters are always assumed to be known except for the defect information (the magnetization factors and the eccentricity parameters). This means that all physical phenomena are taken into account and all model parameters are assumed to be determined perfectly. But in reality, the parameters of the model may have some uncertainty. For example, the uncertainty on geometrical parameters like the air gap have already been studied [225, 226]. The influence of the uncertainty of the armature resistance (R_a) and the leakage inductance (L_σ) are studied and published in [227].

Basically, the model can be written as a function resulting in the terminal voltages based on the 'well-known' parameters w, the uncertain parameters u and the unknown parameters the IP is trying to determine, which in this case is the defect information D_{info}:

$$V_\mathrm{term} = f(w, u, D_{info}) \tag{5.2}$$

If this model is solved by the IP with the traditional OF (4.1), the uncertain parameters will influence the solution. A possibility to counter this is to compensate for the uncertainty within the OF, as is done in the Minimum Path of the Uncertainty (MPU) OF:

$$OF_{MPU}(D_{info}) = \left(V_\mathrm{term,m} - V_\mathrm{term,s}(w, u^\bullet, D_{info}) - \alpha \frac{\partial V_\mathrm{term,s}(w, u, D_{info})}{\partial u} \right)^2 \tag{5.3}$$

where $u^\bullet$ is the mean value of the uncertain parameter, α is the fitting constant that is at every iteration obtained by setting $OF_{MPU} = 0$. More information about this technique can be found in [226], but to show how effective this technique is, figure 5.3 compares the accuracy of the traditional OF with that of the MPU OF for both the armature resistance R_a and the leakage inductance L_σ [227]. The effect of each parameter is studied individually. The sensitivity of the model to the uncertain parameter is determined with finite difference with a step of 10% of the nominal value. The enforced defect is a demagnetization defect $D\,[6, \mathrm{L}, 0.5]$ The relative error is defined:

$$E_{K,\mathrm{perc}} = \left| \frac{(\overline{K} - \hat{K})}{\overline{K}} \right| \times 100\%. \tag{5.4}$$

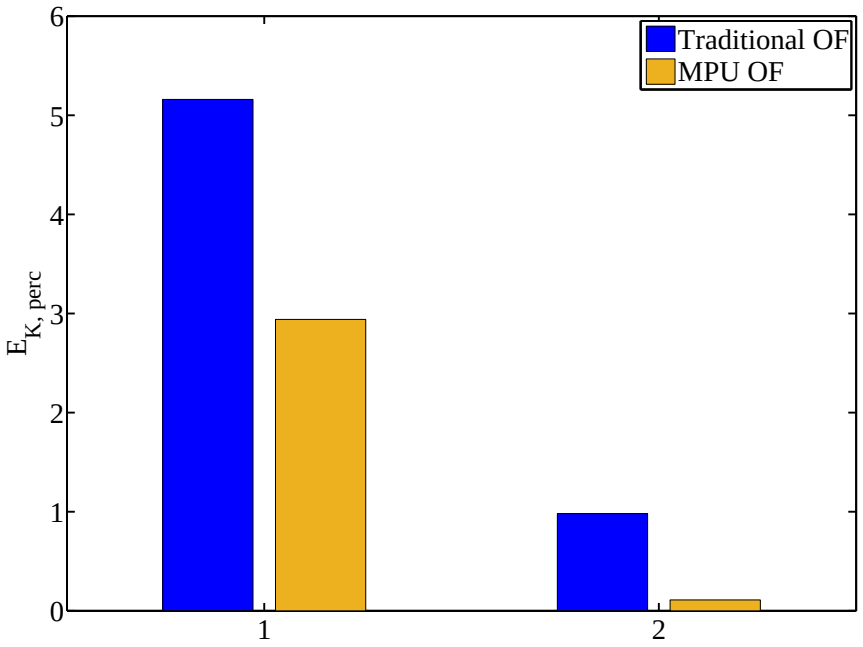

Figure 5.3: The relative error in the magnetization factors solved with the traditional OF and the MPU OF respectively of the armature resistance R_{a} (1) and the leakage inductance L_{σ} (2) for an enforced defect $D\,[6, \mathrm{L}, 0.5]$ [227].

5.2 Evaluation of the sensitivity of the terminal voltage harmonics with the CRLB technique

The previous chapter gave the fundamentals of the harmonic content of the terminal voltages in a machine with demagnetization defects. This was first done with a theoretical framework and secondly by examining an example case. Both gave insight in the harmonic content and its origin within the machine, but they did not give precise and general answers to the question which harmonics are the most sensitive, and how much of these harmonics are needed to retrieve the demagnetization defects. For this, the CRLB technique was introduced in Section 4.2.3. This technique results in an array of harmonics with descending sensitivity.

In this section, this technique will be examined to draw some conclusions. Firstly, it is determined that solving the IP with the most sensitive harmonics only, can result in faster solutions. By eliminating less sensitive harmonics, the amount of harmonics needed to find a good solution can be reduced. Secondly, a general trend of sensitive harmonics is found, independent of the demagnetization defect. And lastly, this conclusion is broadened over different topologies.

5.2.1 Influence of the selection of the harmonics on the convergence of the IP

The IP uses the terminal voltages delivered by the analytical model to find the defects by solving a system of equations. But it does not need every harmonic to find the solution. This means a selection in this harmonics needs to be made.

The minimal number of required harmonics

No matter how this selection is made, there is one constraint that always must be fulfilled: the number of equations delivered by the analytical model must be greater than or equal to the number of unknowns of the IP. If this is not fulfilled, there is no unique solution for the IP to find. In this, the equations are of the form $f(K) = V_{\mathrm{term}}$ where f is a function based on the magnetization array K and resulting in the terminal voltages V_{term}. This function is thus the analytical model of the AFPMSM where the magnetization array K contains the unknown parameters. The number of equations is determined by the number of elements in V_{term}.

The number of equations: The terminal voltages consist of N_{ph} phases, each with N_{har} harmonics in it. Furthermore, as harmonics are complex numbers, they are always described by two numbers: either a real and a imaginary part if they are shown in a Cartesian system, or an amplitude and an angle if they are shown in a polar system. So the terminal voltages always result in $2N_{ph}N_{\mathrm{har}}$ data points or equations for the IP.

The number of unknowns: As the goal of the IP in this section is to detect demagnetization defects, the magnetization factors of the magnets are the unknowns for the IP. As mentioned in Chapter 3, the magnetization array contains all the magnetization factors K. As there is one magnetization factor for each magnet, the number of unknowns is equal to the number of magnets that are considered for the evaluation.

Notice that in the previous section, one rotor was considered healthy because the IP cannot differentiate between the two rotors. In this case, the IP will not evaluate the values of the magnetization factors of these magnets and thus only the magnets from the defected rotor are considered as unknown.

Of course this is a consideration meant for the sake of simplicity. In reality, all magnets can become defected. So in the most general case, there are two rotors with each $2N_p$ magnets on them, resulting in $4N_p$ unknowns. This results in:

$$\begin{aligned} 2N_{ph}N_{\mathrm{har}} &\geq 4N_p \\ N_{\mathrm{har}} &\geq \frac{4N_p}{2N_{ph}} = \frac{2N_p}{N_{ph}} \\ N_{\mathrm{har}} &\geq N_{\mathrm{har,min}} = \lceil \frac{2N_p}{N_{ph}} \rceil \end{aligned} \tag{5.5}$$

where $N_{\mathrm{har,min}}$ is the minimum amount of time harmonics that the terminal voltages must contain in order for the IP to be able to solve the problem. If less harmonics are used, it is impossible to solve the problem. But using $N_{\mathrm{har,min}}$ time harmonics for the terminal voltages does not guarantee an accurate result from the IP. It is possible that the chosen $N_{\mathrm{har,min}}$ harmonics simply did not contain enough information about the defects to perform detection accurately. This means the sensitivity of these harmonics toward the defect was too low for an accurate detection.

Selection of appropriate harmonics

In order to have the error on the magnetization factors E_K low enough, a minimum of information about the defect must reside in the selected terminal voltage harmonics. If not, the estimated magnetization factors may be completely different to the actual magnetization factors. This means there is a minimum amount of harmonics $N_{\mathrm{har,acc}}$ needed in order to find a good solution to the problem.

$$N_{\mathrm{har,acc}} \geq N_{\mathrm{har,min}} \tag{5.6}$$

Combining the two equations (5.5) and (5.6), we obtain as main inequality constraint:

$$N_{\mathrm{har}} \geq N_{\mathrm{har,acc}} \geq N_{\mathrm{har,min}}. \tag{5.7}$$

Practically, N_{har} harmonics will be selected to solve the IP. How this selection is made, has an impact on the value of $N_{\mathrm{har,acc}}$. Two ways are considered:

a) "First N_{har} harmonics" — The Fourier series is truncated to N_{har} harmonic components. This results in an array of harmonics with the harmonic number ranging 0 to $N_{\mathrm{har}} - 1$. This is the most used option.

b) "N_{har} well-selected harmonics" — The selected harmonic components are the N_{har} most sensitive harmonics. Therefore, the sensitivity is first computed with the CRLB technique explained in Section 4.2.3. This technique results in a sensitivity value for each harmonic. These values can be used to make a sorted array of the time harmonics in descending order of sensitivity toward the introduced demagnetization defect. From this array, the first $N_{\mathrm{har,acc}}$ elements are selected. An example of such an array is given in Table 5.3. This is the result of the CRLB technique for a 3 phase 8 pole pair 15 stator slot machine with one magnet on the right rotor demagnetized for 30%. As mentioned in the previous chapter, the actual F_m and C_r values are not important, but rather their ratio. It is a qualitative and not a quantitative study. This means different defects will result in different values, but similar sorted array of harmonics.

Table 5.3: The Fisher Information Matrix F and The Cramér-Rao Lower Bound C_r values for each time harmonic in a sorted order of descending F_m for a 3 phase 8 pole pair 15 stator slot machine with one magnet on the right rotor 30% demagnetized.

m	7	8	6	9	5	3	23
$F\ (10^3)$	86.8	64.2	43.5	21.6	3.1	2.7	2.1
$C_r(10^{-3})$	3.4	3.9	4.8	6.8	18.0	19.1	21.6

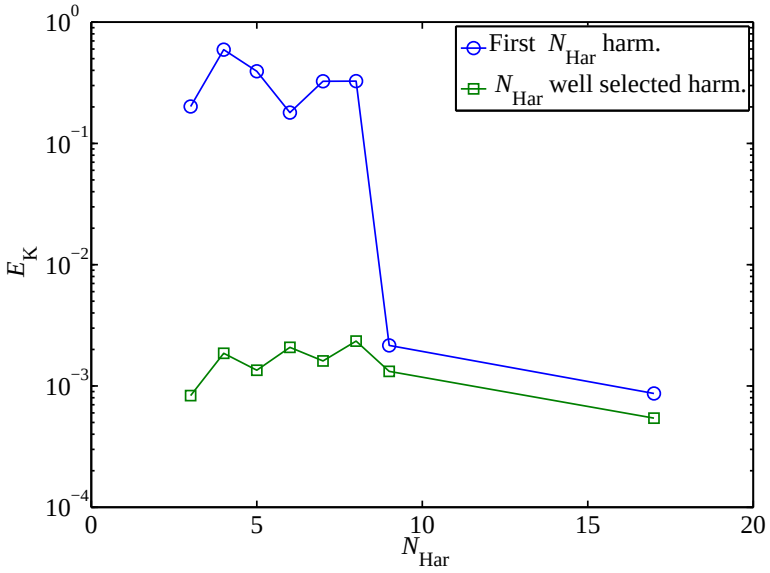

Figure 5.4: The error on the magnetization array for both explained ways of selecting the set of harmonics on a 3 phase 8 pole pair 15 stator slot machine with one magnet on the right rotor 30% demagnetized. The curve called 'First N_{har} harm.' corresponds with the previously explained option (a) while the curve called 'N_{har} well selected harm.' corresponds with option (b).

The harmonics selected by option (b) have a higher F than those of option (a), unless the most sensitive harmonics are contained in the first N_{har} harmonics of the terminal voltages. The theoretical and practical analysis of Chapter 4 indicate that this last exception is not the case. These higher F result in lower total C_r values for the complete selection. But will this result in a convergence of the IP with less needed harmonics meaning lower N_{har}?

This is examined in figure 5.4. Here, the error on the magnetization array E_K is determined depending on the number of selected harmonics N_{har} for the simulations. Both options of selecting the harmonics described previously are compared, where option (a) is called 'First N_{har} harm.' and option (b) is called 'N_{har} well selected harm.' on this plot. In the example, only one rotor with defects is con-

sidered. This means only $2N_p$ magnetization factors are unknown in this problem. The minimum amount of harmonics needed to solve this problem based on (5.5) becomes $N_{\mathrm{har,min}} = \lceil \frac{N_p}{N_{ph}} \rceil$. Notice that because one rotor is considered healthy, there is no '2' in the equation. As it is a machine with 3 phases and 8 pole pairs, $N_{\mathrm{har,min}} = 3$. In figure 5.4, it can be seen that the curves don't have any data for $N_{\mathrm{har}} < 3$.

The figure shows that for option (a), the IP does not find an accurate solution for $N_{\mathrm{har}} < 9$. It is only when the harmonic with harmonic number 8 is used, which is the harmonic corresponding with $m = N_p$, that an accurate solution is found. This means that in this case for option (a), $N_{\mathrm{har,acc}} = N_p + 1 = 9$. On the other hand, option (b) is able to find a solution at $N_{\mathrm{har}} = 3$, which is $N_{\mathrm{har,min}}$. This means $N_{\mathrm{har,acc}} = N_{\mathrm{har,min}}$ for option (b). This can be explained due to the fact that the most sensitive harmonics, including the harmonic with $m = N_p$ is already selected at $N_{\mathrm{har}} = 3$.

Consequently, less harmonics are needed to solve the IP when selecting the harmonics as in option (b) – the most sensitive harmonics – than with option (a). This will result in shorter calculation times for the analytical model, and because of the iterative nature of the IP, shorter calculation times for finding the demagnetization defect. For example, the solution with $N_{\mathrm{har}} = 9$ for option (a) took 66.8 seconds while the solution with $N_{\mathrm{har}} = 3$ for option (b) took 58.2 seconds. Although this is only a 12.9% reduction, it is an advantage with as only drawback the calculation of the sensitive sequence. This is a one-time calculation for the machine and only took 1.55 seconds.

5.2.2 Generalization of the sensitivity sequence over almost all demagnetization defects

A logical next questing is "Can such a sorted array of sensitive harmonics be found for all demagnetization defects in a machine?". This is an important question as the sequence of sensitive harmonics for a given defect needs to be determined in advance in order to select the harmonics when solving the IP. But the actual demagnetization defect in reality is not known a priori, so that the proposed technique may not be useful if different defects would result in totally different sets of sensitive harmonics.

To find out the relationship between given defects on the one hand and the corresponding set of most sensitive harmonics on the other hand, a large set of calculations has been performed on the 3 phase 8 pole pair 15 stator slot machine. For resp. 1, 3, 7 and 16 demagnetized magnets 5000 uniformly distributed random defects have been generated. For each defect, the CRLB technique is applied. The normalized F_m data is shown in figure 5.5.

A sequence from high to low sensitivity can be found for every defect. Figure 5.5 shows that generally the same harmonics tend to be sensitive toward demagnetization defects: the N_p-th harmonic and its multiples, each with its sidebands.

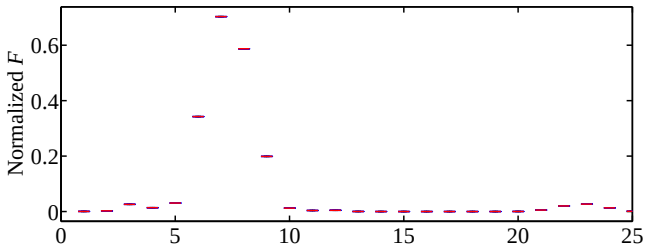

(a) 1 magnet demagnetized

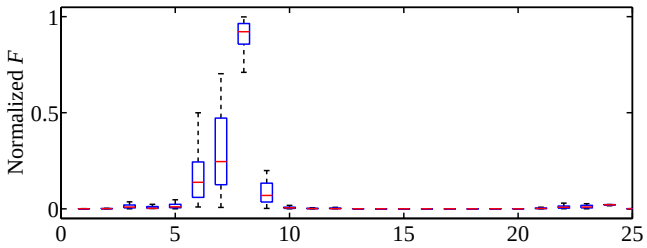

(b) 3 magnets demagnetized

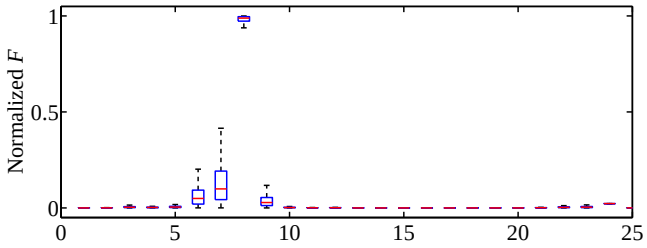

(c) 7 magnets demagnetized

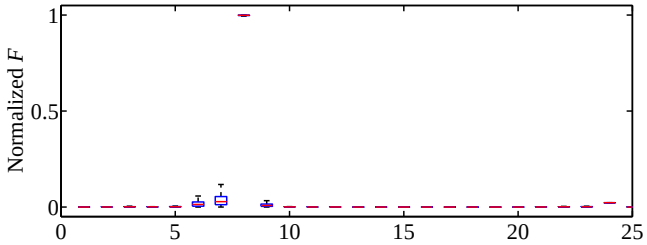

(d) 16 magnets demagnetized

Figure 5.5: On a 3 phase 8 pole pair 15 stator slot machine 1, 3, 7 and 16 magnets have been demagnetized respectively. For every situation, 5000 uniformly distributed random defects have been generated and with the CRLB technique, the normalized F_m have been calculated. These are then compiled into boxplots with the harmonic numbers on the x-axis. The meaning of the different lines and colors is identical to figure 5.1.

The amplitudes of the sideband harmonics are sometimes referred to as the ASBC. Higher multiples of N_p are significantly less sensitive to the defects. The sidebands form a pyramid-like shape on the plots as their sensitivity decreases if they are further away from the N_p-th harmonic or its multiple respectively.

If only one magnet is demagnetized, like in figure 5.5(a), the variance on the data is very small. The reason for this is that a different defect magnet only produces a shift in time in the terminal voltage waveforms, giving rise to similar harmonic components. Because the sensitivity is found by the variation of the voltage toward the variation in the defect, the amplitude of the defect has very little influence on these results as well.

A trend is visible in figures 5.5(b) and 5.5(c). Although there is some variance on the results, the same set of harmonics seem to be sensitive to the enforced defects.

In figure 5.5(d), all magnets are demagnetized. The plot shows a low variance as well. This means that for all examined defects, the terminal voltages are influenced similarly. As described above, because the gradient of the voltage toward the defect is studied, the magnetization factor value does not influence the results. Furthermore, the figure shows that the sidebands have a very small sensitivity compared to the N_p-th harmonic. This can be understood by recalling the theoretical framework of Section 4.2.1: the sidebands are a result of the convolution of the square wave with the magnetization waveform. In the CRLB, the gradient of the voltage toward one magnet will similarly result in the sidebands being sensitive, as clearly shown in figure 5.5(a). But if all magnets are demagnetized, the gradient of the voltage will be toward all magnets simultaneously. Which is sensitivity-wise the same as an uniformal demagnetization over all magnets, and thus results in hardly any sidebands in figure 5.5(d).

As a conclusion, figure 5.5 shows that – with an acceptable accuracy – the same set of most sensitive harmonics can be used for different magnet defects. By consequence, the suggested approach of option (b) based on the a priori selection of the most sensitive harmonics - can be recommended.

5.2.3 Generalization of the sensitivity sequence over different topologies

Although finding this conclusion for the 3 phase 8 pole pair 15 stator slot machine is interesting, a general conclusion for all YASA AFPMSMs is recommended. To examine this, the previous analysis has been performed for 16 topologies in total. The number of phases of these topologies is 3, 5 or 7 phases. The number op pole pairs ranges from 2 to 9 pole pairs. As for the stator slots, these topologies range from 10 to 56 slots. These selection consists of topologies with both fractional-slot and integral-slot machines.

Figure 5.6 shows four cases from this analysis. The plots are again a compilation of the normalized F_m values of 5000 uniformly distributed faults, each with 3

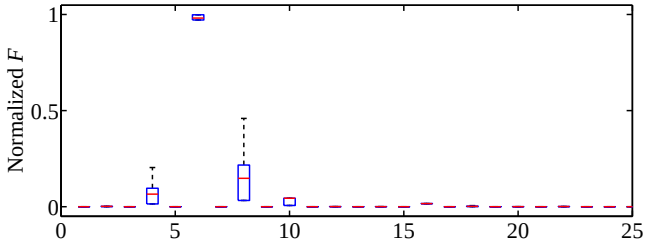

(a) 3 phases, 5 pole pairs and 12 stator slots

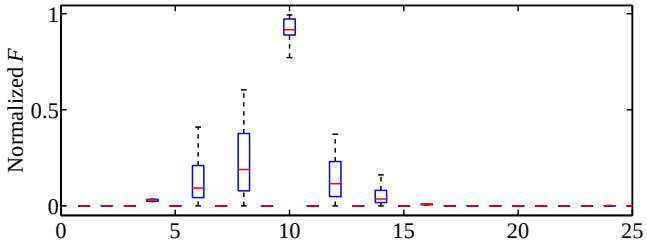

(b) 5 phases, 9 pole pairs and 20 stator slots

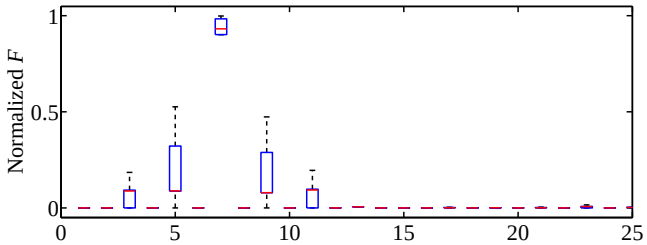

(c) 7 phases, 6 pole pairs and 14 stator slots

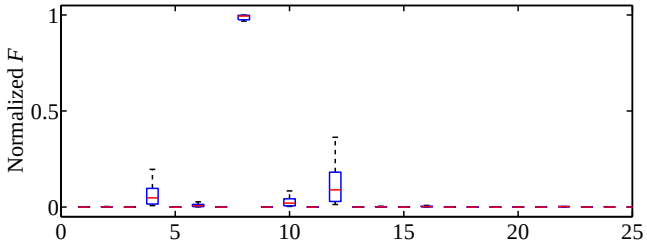

(d) 3 phases, 7 pole pairs and 18 stator slots

Figure 5.6: Four different machine topologies have been displayed. For every situation, 5000 uniformly distributed random defects have been generated, every one of them with 3 demagnetized magnets. With the CRLB technique, the normalized F_m have been calculated. These are then compiled into boxplots with the harmonic numbers as the x-axis. The meaning of the different lines and colors is identical to figure 5.1.

magnets demagnetized.

First of all, this figure confirms the theory explained in Section 4.2.1 about how the connections of the tooth via the star of slot theory can filter certain harmonics so they will not appear in the phase back-EMF and the terminal voltages. For example, the case of figure 5.6(a) has no odd voltage harmonics, and consequently the sensitivity of those harmonics toward the defects is zero. This is shown in the figure by a zero-valued normalized F_m for those harmonics.

Aside from this filtering effect, a similar trend as in the previous section can be observed. Again, the N_p-th harmonic is the most sensitive, followed by its sidebands and then the multiples of N_p and their sidebands.

As a general conclusion, the sensitivity decreases for higher multiples of N_p and with a larger distance from the N_p-th harmonic or its multiples. The sensitivity is maximal for the N_p-th harmonic and also high for its sidebands.

5.3 Numerical evaluation of the demagnetization detection technique using sensing coils

In the previous chapter, the modified forward model that calculates the sensing coil back-EMF was introduced. It was explained where these sensing coils were located in the machine and how the IP for the sensing coil method uses the measurement data and the simulated sensing coil back-EMF to detect demagnetization defects.

In this section, this technique is tested and the influence of noise on the results is analyzed. Furthermore, the method is compared to the detection technique that uses the model of Chapter 3 together with the IP based on the terminal voltages to detect defects.

5.3.1 Influence of the noise level on the accuracy of the demagnetization detection

The technique is tested at different noise levels. The level of noise nl is defined as in Section 5.1. The error E_K in the resulting magnetization array K is again defined by (4.7). We recall that this is the Euclidean distance between the estimated and the actual magnetization array.

Figure 5.7 shows the average error E_K for different noise levels. It is clear that the IP can solve the problem and find the defects at low noise level. Once the noise level increases, the accuracy decreases, but is still acceptable.

5.3.2 Symmetrical versus asymmetrical defect, sensing coil technique versus terminal voltage technique

To recapitulate, two techniques have been explained in previous chapters:

- Chapter 3 introduced an analytical model for simulating the machine, which resulted in the terminal voltages. Chapter 4 then proposed an IP to detect demagnetization and eccentricity defects with this model. It used geometrical data, rotation speed, phase current and the terminal voltages to retrieve the defect information. For the next comparison, this method will be called the 'terminal voltage technique'.

- Chapter 4 modified the terminal voltage model of Chapter 3 to create an analytical model that can simulate the back-EMF of the sensing coils. It then modifies the IP so it uses the geometrical data, rotation speed, phase current and the sensing coil back-EMF to retrieve the demagnetization defect. For the next comparison, this method will be called the 'sensing coil technique'.

The two techniques are compared in figure 5.8. The horizontal axis is the number of demagnetized magnets. The defects are again generated randomly and contain 1% noise on the terminal voltages for the terminal voltage technique and on the back-EMF for the sensing coil technique. The figure shows the average of the error E_K. In figure 5.8(b), the error of the terminal voltage technique has been divided by 50 for the sake of clarity.

When first only discussing the sensing coil technique results, it can be seen that there is very little difference between the results for symmetrical and asymmetrical defects. Both can be detected very accurately. The accuracy is slightly better when fewer magnets are demagnetized.

Secondly, we compare both methods. Figure 5.8 also shows a comparison between the two techniques. The sensing coil technique clearly outperforms the terminal voltage technique for both symmetrical and asymmetrical defects. In the former, the difference is limited but noticeable. In the latter, the difference is huge.

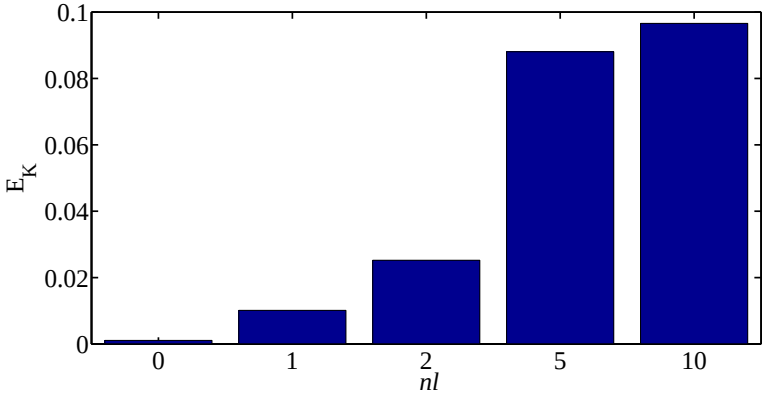

Figure 5.7: The average error on the magnetization array E_K is shown in function of increasing percentual noise levels nl. The calculations were performed on the 3 phase 8 pole pair 15 stator slot machine.

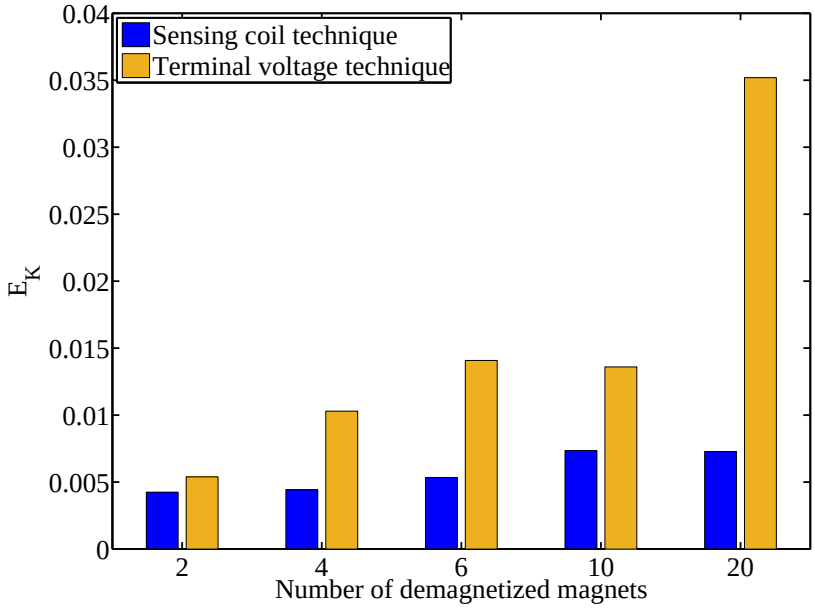

(a) Symmetrical demagnetization

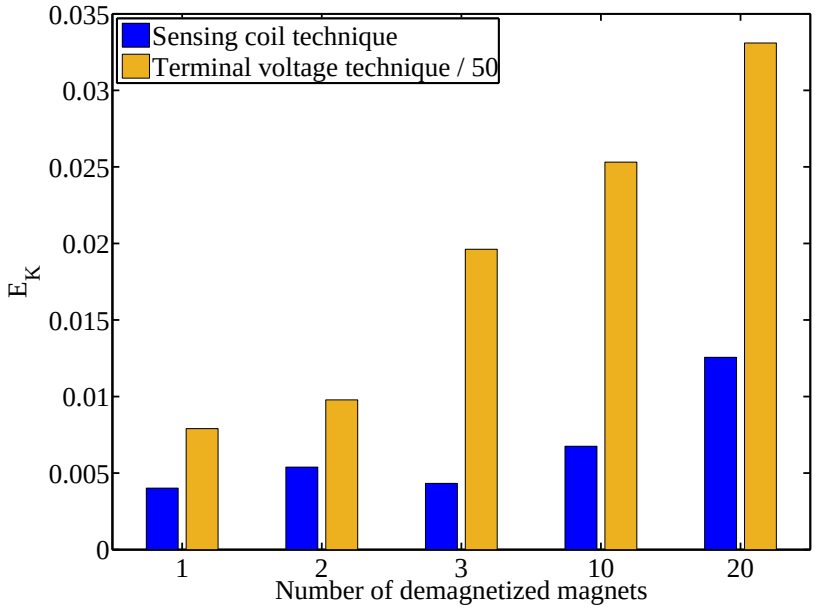

(b) Asymmetrical demagnetization

Figure 5.8: The average error on the magnetization array E_K in function of the number of demagnetized PMs for both the terminal voltage technique and the sensing coil technique. All defects are randomly generated and have 1% noise. (a) Shows only the symmetrical demagnetization defects while (b) shows only the asymmetrical demagnetization defects. Notice that for clarity sake, the data of the terminal voltage technique in (b) has been divided by a factor 50.

Remember that the error of the terminal voltage technique has been scaled down. It is clear that the terminal voltage technique cannot accurately detect asymmetrical defects. This was expected because the stator coils are in the middle of the stator tooth and cannot differentiate between the magnetic fields of the left and right rotor respectively.

It can be concluded that the sensing coil technique outperforms the terminal voltage technique, especially for asymmetrical defects, which are an inherent limitation of the terminal voltage technique. On the other hand, adding sensing coils to a machine increases the cost and they can go defected as well.

5.4 Conclusion

In this chapter, the focus is on detection of demagnetization defects in axial flux permanent magnet machines.

Firstly, the terminal voltage technique, which is explained in the previous chapters, is tested. It is clear that the technique is able to detect demagnetization defects when only one rotor with defects is considered or with symmetrical defects. Also the impact of noise is examined.

Secondly, the previously proposed tool for analyzing the harmonic's sensitivity toward the defects is used to determine a general trend about which harmonics are sensitive. The tool was also used to show that choosing the sensitive harmonics results in smaller computational burden. The general trend states that the harmonics of the healthy machine, i.e. the N_p-th harmonic and its multiples together with their sidebands are the most sensitive. This is in line with what was expected in the theoretical framework and the case study in Chapter 4.

Lastly, the modified analytical model and IP for the sensing coils is tested. It proves to be able to detect demagnetization defects better than the terminal voltage technique, especially with asymmetrical defects. It manages to deal with the inherent short-coming of the terminal voltage technique toward asymmetrical defect. But the technique with sensing coils has as downside the extra two sensing coils that have to be added in the machine.

Chapter 6

Detection of eccentricity defects and combined demagnetization and eccentricity defects

Chapter 4 introduced a detection technique for detecting demagnetization and eccentricity defects using an IP and an analytical model explained in Chapter 3. This technique was tested for demagnetization defects in Chapter 5.

In the following sections the technique that uses the terminal voltages will first be evaluated for SE, DE and ME. Afterwards, defects with both demagnetization and eccentricity are put to the test in order to determine that the detection technique can distinguish between the two types of defects.

6.1 Detection of eccentricity defect

For this chapter, the same methodology of Section 5.1 is used. Measurement data is again generated by calculating the terminal voltages with the analytical model of Chapter 3 and adding an uniformly distributed random noise to this data. The details on how this is performed are explained in Section 5.1.

All calculations in this chapter are performed at the rated load and speed of the machine. The full description of the machine can be found in Section 3.5.

To determine the accuracy of the technique, the error in the defect information is determined using the error in the magnetization factors E_K defined in (4.7) and the error in the eccentricity parameters E_{Ecc} defined in (4.10).

In Sections 6.1.3 and 6.2, distinguishing between the error in the SE and the DE parameters resp. is important. Therefore, both errors are defined:

$$E_{Ecc,\mathrm{SE}} = \sqrt{\Delta\rho_{\mathrm{SE,L,real}}{}^2 + \Delta\rho_{\mathrm{SE,L,imag}}{}^2 + \Delta\rho_{\mathrm{SE,R,real}}{}^2 + \Delta\rho_{\mathrm{SE,R,imag}}{}^2} \tag{6.1}$$

Table 6.1: An example of an eccentricity defect found by the IP with an error in the SE parameters of 0.0168. The calculation is done with 5% noise on the terminal voltage data. The introduced defect is $E\,[\mathrm{R}, \mathrm{SE}, 0.41, 2.640\ \mathrm{rad}]$. Only the SE parameters of the right rotor are shown. All the eccentricity parameters of the left rotor and the DE parameters of the right rotor are 0.

	Actual ecc. defect	Estimated ecc. defect	$\Delta(10^{-1})$ [%]
$\rho_{\mathrm{SE,R}}$ [/]	0.41	0.39	16.1
$\theta_{\mathrm{MSE,R}}$ [rad]	2.640	2.628	11.9

$$E_{Ecc,\mathrm{DE}} = \sqrt{{\Delta\rho_{\mathrm{DE,L,real}}}^2 + {\Delta\rho_{\mathrm{DE,L,imag}}}^2 + {\Delta\rho_{\mathrm{DE,R,real}}}^2 + {\Delta\rho_{\mathrm{DE,R,imag}}}^2} \tag{6.2}$$

with of course:

$$E_{Ecc} = \sqrt{{E_{Ecc,\mathrm{SE}}}^2 + {E_{Ecc,\mathrm{DE}}}^2}. \tag{6.3}$$

Furthermore, because the technique uses the stator coils, an inherent shortcoming is the disability of determining in which rotor the defect has occurred. Therefore, in this chapter, all shown defects will occur on the right rotor. The left rotor is assumed to be healthy, meaning $\rho_{\mathrm{SE,L}}$ and $\rho_{\mathrm{DE,L}}$ are always zero.

6.1.1 Static eccentricity defects

Table 6.1 shows a SE defect in a 3 phase 8 pole pair 15 stator slot machine. First, the actual defect is shown. This is the defect used in the analytical model with added noise to generate the terminal voltages that is used as measurement data in this test. 5% noise is used in this example. The next column shows the estimated eccentricity parameters and the last column presents the absolute difference between the actual and estimated parameters relative to their maximum value. It shows that the technique succeeds in estimating the SE amplitude and angle quite accurately. The error in the SE parameters $E_{Ecc,\mathrm{SE}}$ of this case is calculated with (6.1) and is 0.0168.

The case presented in Table 6.1 is an example; it does not give a general overview of the performance of the technique. To achieve this 100 random SE defects are tested. For each case, the IP is solved and the error in the SE parameters is calculated. These are then compiled into a boxplot per evaluated noise level. The errors in the SE defects $E_{Ecc,\mathrm{SE}}$ for for instance 5% noise are shown in figure 6.1 at $nl = 5$. To get a better idea of the physical meaning of the error values shown in this figure, we can consider the following example: if every SE parameter is deviating 5% of the maximum parameter value from the real value, still assuming only one rotor has defects, then the error equation (6.1) gives a re-

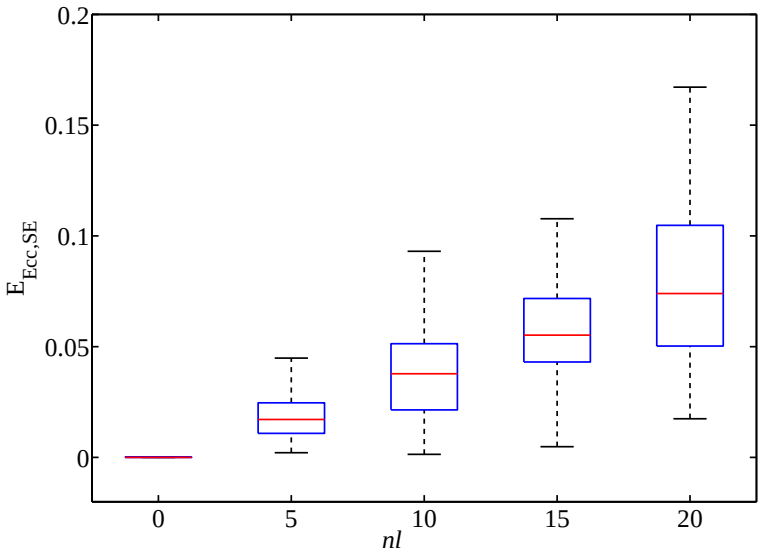

Figure 6.1: On a 3 phase 8 pole pair 15 stator slot machine, 100 random SE defects have been generated. The noise level nl was varied from 0% to 20%. The meaning of the different lines and colors is identical to figure 5.1.

sult of $E_{Ecc,\mathrm{SE}} = 0.0700$ for this machine. It can be seen that the defects are more accurate than this.

Of course, the accuracy is also influenced by the noise on the terminal voltage data. Figure 6.1 shows the accuracy of the SE defect detection for five different noise levels. The results are as expected: with increasing noise levels, the average accuracy decreases and the variance on the accuracy increases. It is therefore important for defect detection that good measurements with limited noise can be performed. The Pearson Correlation test shows here as well that the correlation is significant at the 0.01 level. Also here, a linear regression can be placed on the data. The constant and first order coefficient for this regression are respectively -0.001 and 0.004 with an standard error of 0.002 and 0.000.

6.1.2 Dynamic eccentricity defects

The same approach can be taken for DE. Table 6.2 shows a DE defect in a 3 phase 8 pole pair 15 stator slot machine. Again, the actual defect is first shown: the terminal voltages are produced by evaluating the forward analytical model with the given defect parameters as input, and then adding noise to better mimic realistic measured voltage waveforms. 5% noise is used in this example as well. The next two columns again show the estimated eccentricity parameters and the absolute difference between the actual and estimated parameters relative to their maximum

Table 6.2: An example of an eccentricity defect found by the IP with an error in the DE parameters of 0.0171. The calculation was done with 5% noise on the terminal voltage data. The introduced defect is $E\,[\mathrm{R}, \mathrm{DE}, 0.81, 0.612\ \mathrm{rad}]$. Only the DE parameters of the right rotor are shown. All the eccentricity parameters of the left rotor and the SE parameters of the right rotor are 0.

	Actual ecc. defect	Estimated ecc. defect	$\Delta(10^{-1})$ [%]
$\rho_{\mathrm{DE,R}}$ [/]	0.81	0.79	16.2
$\theta_{\mathrm{MDE,R}}$ [rad]	0.612	0.605	6.5

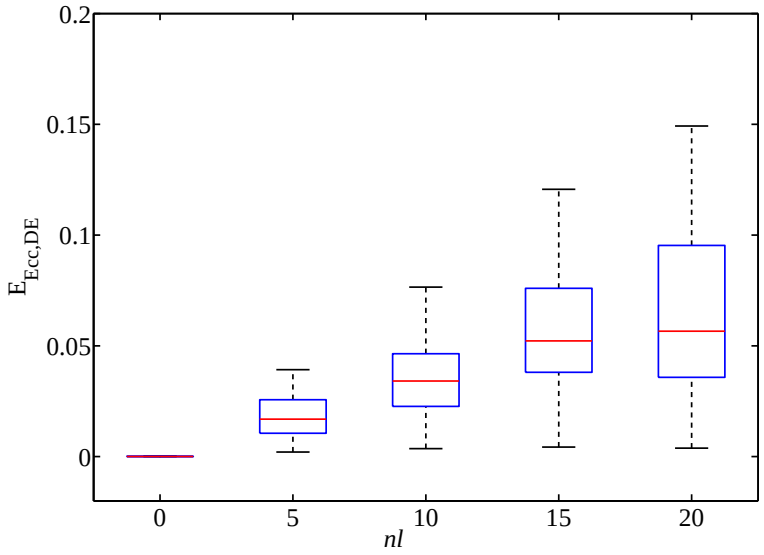

Figure 6.2: On a 3 phase 8 pole pair 15 stator slot machine 100 random DE defects have been generated. The noise level nl was varied from 0% to 20%. The meaning of the different lines and colors is identical to figure 5.1.

value. It shows that the technique succeeds in estimating the DE amplitude and angle quite accurately. The error in the DE parameters $E_{Ecc,\mathrm{DE}}$ of this case is calculated with (6.2) and is 0.0171.

Again, the case presented in Table 6.2 is an example and does not give a general overview of the performance of the technique for DE. To achieve this, 100 random DE defects are tested. For each case, the IP is solved and the error in the DE parameters is calculated. These are then compiled into a boxplot per evaluated noise level. The errors in the DE defects $E_{Ecc,\mathrm{DE}}$ for 5% noise are shown in figure 6.2 at $nl = 5$. Again, the physical meaning of the error can be understood by an example: if every DE parameter is deviating 5% of the maximum parameter value from the real value, still assuming only one rotor has defects, then the error equation (6.2) again gives a result of $E_{Ecc,\mathrm{DE}} = 0.0700$ for this machine. It can

Table 6.3: An example of an eccentricity defect found by the IP with an error in the SE parameters of 0.0167 and an error in the DE parameters of 0.0243. The calculation was done with 5% noise on the terminal voltage data. The introduced defect is $E\,[\mathrm{R}, \mathrm{SE}, 0.36, 3.563\ \mathrm{rad}],\ E\,[\mathrm{R}, \mathrm{DE}, 0.35, 2.438\ \mathrm{rad}]$. Only the eccentricity parameters of the right rotor are shown. All the eccentricity parameters of the left rotor are 0.

	Actual ecc. defect	Estimated ecc. defect	$\Delta(10^{-1})$ [%]
$\rho_{\mathrm{SE,R}}$ [/]	0.36	0.34	16.7
$\theta_{\mathrm{MSE,R}}$ [rad]	3.563	3.564	0.7
$\rho_{\mathrm{DE,R}}$ [/]	0.35	0.37	22.3
$\theta_{\mathrm{MDE,R}}$ [rad]	2.438	2.465	26.7

be seen that the defects are more accurate than this.

And again, the influence to the accuracy by the noise on the terminal voltage data is examined. Figure 6.2 shows the accuracy of the DE defect detection for five different noise levels. The results show again that with increasing noise levels, the average accuracy decreases an the variance on the accuracy increases. Just as with SE, The Pearson Correlation test shows the correlation is significant at the 0.01 level. The constant and first order coefficient for the linear regression are respectively 0.001 and 0.003 with an standard error of 0.002 and 0.000, which is very similar to the linear regression for SE.

6.1.3 Mixed ecccentricity defects

ME consists of a SE and a DE defect. Table 6.3 shows both defects on a 3 phase 8 pole pair 15 stator slot machine. Again, the actual defect is first shown, produced in the same way as in previous sections, followed by the estimated eccentricity parameters and the absolute difference between the actual and estimated parameters relative to their maximum value. It shows that the technique succeeds in estimating the ME amplitudes and angles quite accurately. The errors in the SE and DE parameters of this case, $E_{Ecc,\mathrm{SE}}$ and $E_{Ecc,\mathrm{DE}}$ resp., is calculated with (6.1) and (6.2) and are 0.0167 and 0.0243 respectively.

Just as before, the case presented in Table 6.3 is an example and does not give a general overview of the performance of the technique for ME. To achieve this 100 random ME defects are tested. For each case, the IP is solved and the error in the SE parameters and the error in the DE parameters is calculated. These are then compiled into a boxplot per evaluated noise level. The errors in the SE and the DE defects, $E_{Ecc,\mathrm{SE}}$ and $E_{Ecc,\mathrm{DE}}$ resp., for 5% noise are shown in figure 6.3 at $nl = 5$. For getting a better idea for the accuracy, the same calculated example of Sections 6.1.1 and 6.1.2 can be used, which results in 0.0700 for both $E_{Ecc,\mathrm{SE}}$ and $E_{Ecc,\mathrm{DE}}$. It can be seen that even in the ME case, the results are more accurate than this.

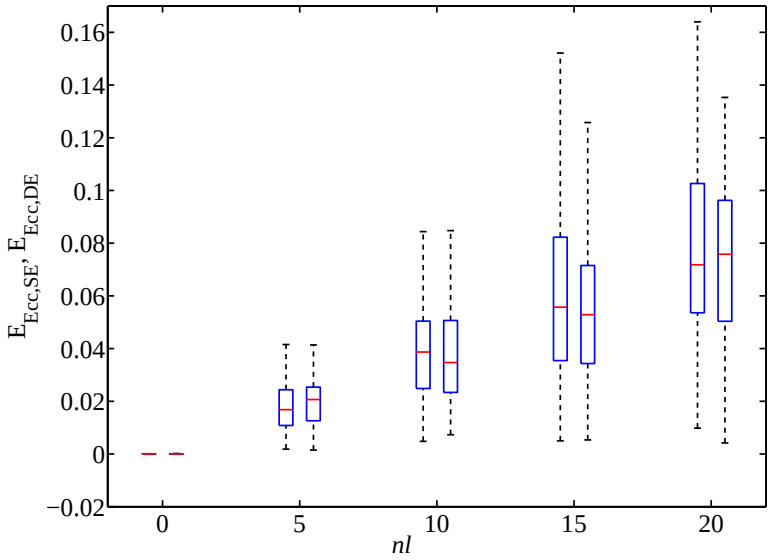

Figure 6.3: On a 3 phase 8 pole pair 15 stator slot machine 100 random ME defects have been generated. The noise level nl was varied from 0% to 20%. The meaning of the different lines and colors is identical to figure 5.1. For each noise level, first the boxplot of the error in the SE parameters is shown, following by the boxplot of the error in the DE parameters.

And again, the influence to the accuracy by the noise on the terminal voltage data is examined. Figure 6.3 shows the accuracy of the SE and the DE defect detection for five different noise levels. For each noise level, two boxplots are shown, corresponding to the $E_{Ecc,\mathrm{SE}}$ and $E_{Ecc,\mathrm{DE}}$ values respectively. The results show that even for ME the same conclusion as in previous sections are drawn. The Pearson Correlation test has a significance at the 0.01 level for both SE as DE and the linear regression coefficients are the same as in section 6.1.1 and 6.1.2.

6.1.4 Evaluation of different topologies

The previous paragraphs describe the performance of the eccentricity detection technique for the 3 phase 8 pole pair 15 stator slot machine. Figure 6.4 shows an overview of the accuracy of the technique for 24 different topologies for mixed eccentricity. Plot (a) and (b) show the error on the SE parameters $E_{Ecc,\mathrm{SE}}$ and the DE parameters $E_{Ecc,\mathrm{DE}}$ respectively of these defects. The number of stator slots, pole pairs and phases of each topology in the figure are the same as in figure 5.2 and are given in Table 5.2. The figures show the same trend as in figure 5.2: case 14 to 24 have a very big error compared to case 1 to 13. The IP is again not able to solve the detection technique for case 14 to 24 in an acceptable accuracy. Just as before, the noise level was set to 0% and the stop conditions are set to the default

stop conditions of the solver, i.e. 10e-6, to exclude these as the causes.

The trend is again explained by the periodicity $\gcd(2N_p, N_S)$ shown in the last column of Table 5.2. The eccentricity detection technique cannot function properly for machines with a periodicity higher than 1. This is an inherent feature of the machine as this means that machines with high periodicity are constructed by repeating the base machine several times throughout the circumference. Because all teeth are connected to the same set of phases, the information that determines in which repeated base machine the eccentricity defect occurred is lost.

In Section 5.1.1, using a modular n-phase configuration on machines with a periodicity higher than 1 was suggested as a possible solution for demagnetization detection. Modular n-phase configurations will also allow eccentricity detection to be performed on these machines. This configuration sets $N_{ph} = N_S$, which means that every stator tooth is a phase on its own. The modular n-phase configuration has several advantages [91], among others giving the IP access to all the information in the separate stator tooth back-EMF. As stated in Section 5.1.1, both the analytical model as the IP are constructed in a flexible way to allow such topology changes and improve the versatility of the technique. This means that in the 'modular n-phase' configuration the algorithm is able to detect eccentricity in a machine with a periodicity higher than 1.

6.2 Detections of combined demagnetization and eccentricity defects

Finally, the big question is "Can the technique differentiate between demagnetization and eccentricity?" To determine this, the technique is tested with combined demagnetization and ME defects. Table 6.4 shows an example of this on a 3 phase 8 pole pair 15 stator slot machine. Firstly, the array of magnetization factors K is shown with from left to right the actual defect, the estimated defect and the absolute difference between the actual and estimated factors relative to their maximum value. Still the left rotor is kept healthy, so all magnetization factors of that rotor are 1. Underneath that, the ME is shown as before, again showing both the actual and estimated defect, followed by the absolute difference between the actual and estimated parameters relative to their maximum value. In this case 5% noise on the generated terminal voltages is used again. It can be seen that the technique succeeds in estimating the magnetization factors as well as the ME amplitudes and angles quite accurately. The error in the magnetization factors E_K is calculated with (4.7) and is 0.0428. The error in the SE and DE parameters, $E_{Ecc,\mathrm{SE}}$ and $E_{Ecc,\mathrm{DE}}$ resp., are calculated with (6.1) and (6.2) and are 0.0209 and 0.0186 respectively.

Again, after the case presented in Table 6.4, a general overview of the performance of the technique for combined demagnetization and eccentricity defects is required. This is achieved by testing 100 random defects containing both demagne-

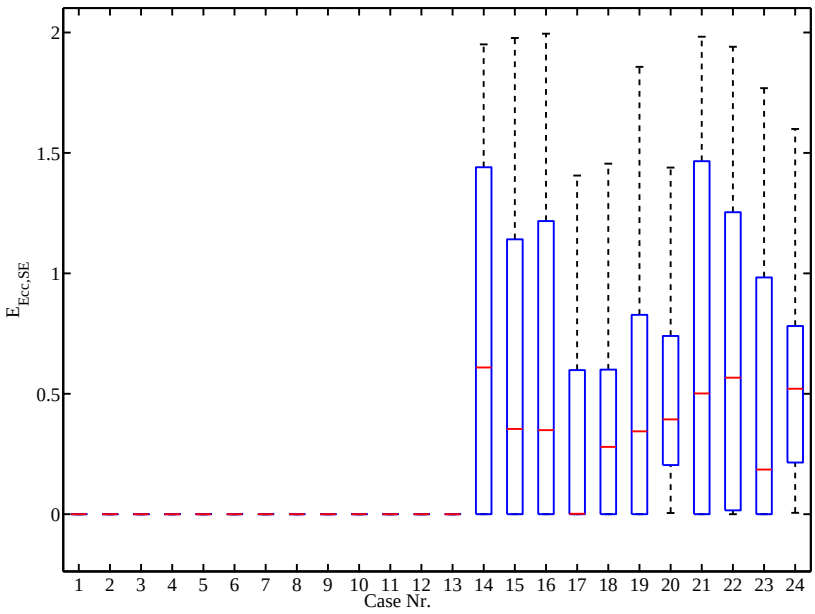

(a)

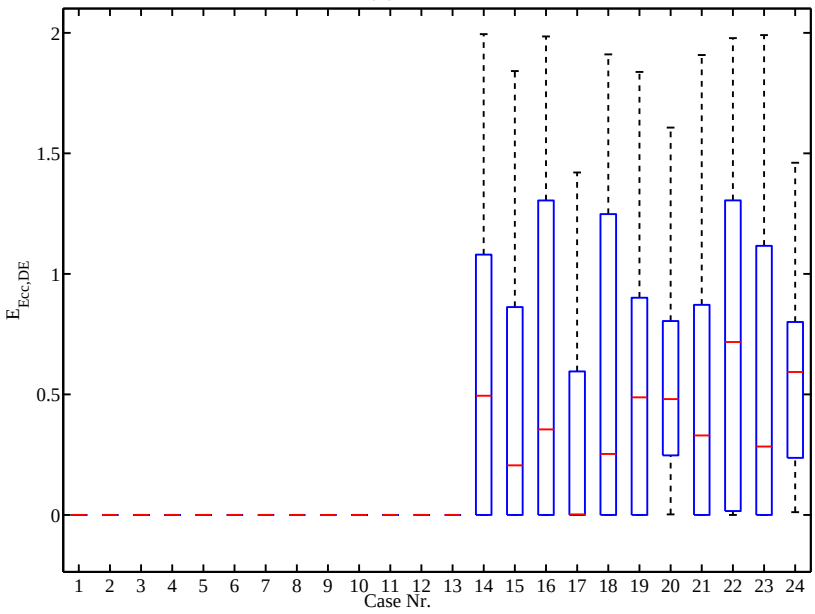

(b)

Figure 6.4: Overview of the error in (a) the static eccentricity parameters and (b) the dynamic eccentricity parameters for 24 different topologies. The meaning of the different lines and colors is identical to figure 5.1. For topology 1 to 13, the error is under 1.5e-9.

Table 6.4: An example of a defect found by the IP with an error in the magnetization factors E_K of 0.0428, an error in the SE parameters of 0.0209 and an error in the DE parameters of 0.0186. The calculation was done with 5% noise on the terminal voltage data. The introduced defect is $D\,[11, \mathrm{R}, 0.08]$, $E\,[\mathrm{R}, \mathrm{SE}, 0.65, 1.143\ \mathrm{rad}]$, $E\,[\mathrm{R}, \mathrm{DE}, 0.89, 1.519\ \mathrm{rad}]$. Only the defect information of the right rotor are shown. On the left rotor, all the magnetization factors are 1 and all the eccentricity parameters are 0.

Actual K [/]	Estimated K [/]	$\Delta(10^{-1})$ [%]
1.00	1.00	4.0
1.00	1.00	1.8
1.00	0.99	6.0
1.00	0.99	6.0
1.00	1.00	3.2
1.00	1.00	2.2
1.00	1.00	2.3
1.00	1.00	1.3
1.00	1.00	4.6
1.00	0.98	21.4
0.08	0.11	34.1
1.00	1.00	0.2
1.00	0.99	6.0
1.00	0.99	6.1
1.00	1.00	1.9
1.00	1.00	2.3

	Actual ecc. defect	Estimated ecc. defect	$\Delta(10^{-1})$ [%]
$\rho_{\mathrm{SE,R}}$ [/]	0.65	0.64	9.5
$\theta_{\mathrm{MSE,R}}$ [rad]	1.143	1.171	28.8
$\rho_{\mathrm{DE,R}}$ [/]	0.89	0.89	1.0
$\theta_{\mathrm{MDE,R}}$ [rad]	1.519	1.540	20.9

tization and ME. For each case, the IP is solved and the error in the magnetization factors, the error in the SE parameters and the error in the DE parameters is calculated. These are then compiled into a boxplot per evaluated noise level. The errors in the magnetization factors, in the SE and the DE defects, E_K $E_{Ecc,\mathrm{SE}}$ and $E_{Ecc,\mathrm{DE}}$ resp., for 5% noise are shown in figure 6.5 at $nl = 5$. As reference for the accuracy, we recollect that for a deviation of 5% of the maximum parameter value on the magnetization factors and the eccentricity parameters, the resulting error is 0.2000 for E_K and 0.0700 for both $E_{Ecc,\mathrm{SE}}$ and $E_{Ecc,\mathrm{DE}}$. This is calculated with (4.7), (6.1) and (6.2) respectively. It can be seen that for the demagnetization defect, the majority of the results are more accurate than this, while for the SE and the DE defect, all the results are more accurate than this example.

Lastly, the influence to the accuracy by the noise on the terminal voltage data

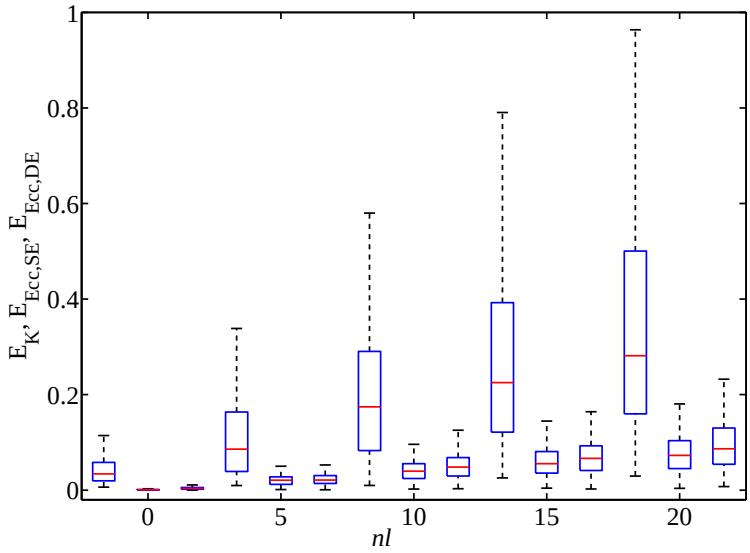

Figure 6.5: On a 3 phase 8 pole pair 15 stator slot machine 100 random defects have been generated. The noise level nl was varied from 0% to 20%. The meaning of the different lines and colors is identical to figure 5.1. For each noise level, first the boxplot of the error in the magnetization factors is shown, following by the boxplot of the error in the SE parameters and the boxplot of the error in the DE parameters.

for these combined defects is examined as well. Figure 6.3 shows the accuracy of the demagnetization defect, the SE and the DE defect detection for five different noise levels. For each noise level, three boxplots are shown, corresponding to the E_K, $E_{Ecc,\mathrm{SE}}$ and $E_{Ecc,\mathrm{DE}}$ values respectively. The same conclusions as in previous paragraphs can be taken. For this combined defect the Pearson Correlation test has a significance at the 0.01 level for all three defects and the linear regression coefficients are 0.057 and 0.015 with standard error of 0.008 and 0.001 for demagnetization, 0.002 and 0.004 with standard error of 0.001 and 0.000 for SE and 0.003 and 0.004 with standard error of 0.001 and 0.000 for DE. This results are very similar to the results for the defects separately.

6.2.1 Evaluation of different topologies

The previous paragraph describes the performance of the combined demagnetization and eccentricity detection technique for the 3 phase 8 pole pair 15 stator slot machine. Figure 6.6 shows an overview of the accuracy of the technique for 24 different topologies for combined demagnetization and eccentricity defects. Plot (a) and (b) show the error on the magnetization factors E_K and the eccentricity parameters E_{Ecc} respectively of these defects. The number of stator slots, pole

pairs and phases of each topology in the figure are the same as in figure 5.2 and are given in Table 5.2. The figures show the same trend as in figures 5.2 and 6.4: case 14 to 24 have a very big error compared to case 1 to 13. The IP is again not able to solve the detection technique for case 14 to 24 in an acceptable accuracy. Just as before, the noise level was set to 0% and the stop conditions are set to the default stop conditions of the solver, i.e. 10e-6, to exclude these as the causes.

The trend is again explained by the periodicity $\gcd(2N_p, N_S)$ shown in the last column of Table 5.2. The combined demagnetization and eccentricity detection technique cannot function properly for machines with a periodicity higher than 1 for the reasons explained in Section 6.1.4.

In Section 5.1.1, using a modular n-phase configuration on machines with a periodicity higher than 1 was suggested as a possible solution for demagnetization detection. Modular n-phase configurations will allow combined demagnetization and eccentricity detection to be performed on these machines because it gives the IP access to all the information in the separate stator tooth back-EMF. In this way, the technique is able to detect combined demagnetization and eccentricity in a machine with a periodicity higher than 1.

6.3 Conclusion

In the previous chapter, the focus was on the demagnetization defects only. In this chapter, the focus is on the eccentricity defects and on the combined demagnetization and eccentricity defects. The technique uses the stator coil waveforms as inputs, and is based on the analytical model of Chapter 2 and the IP.

Although for simplicity, only one rotor with defects was considered, the results show an adequate accuracy to detect SE, DE and ME as well as the combination of demagnetization defects and ME. For the combined defect, the technique does not only detect the presence of the combined defect, but it is also able to *distinguish* between demagnetization and eccentricity.

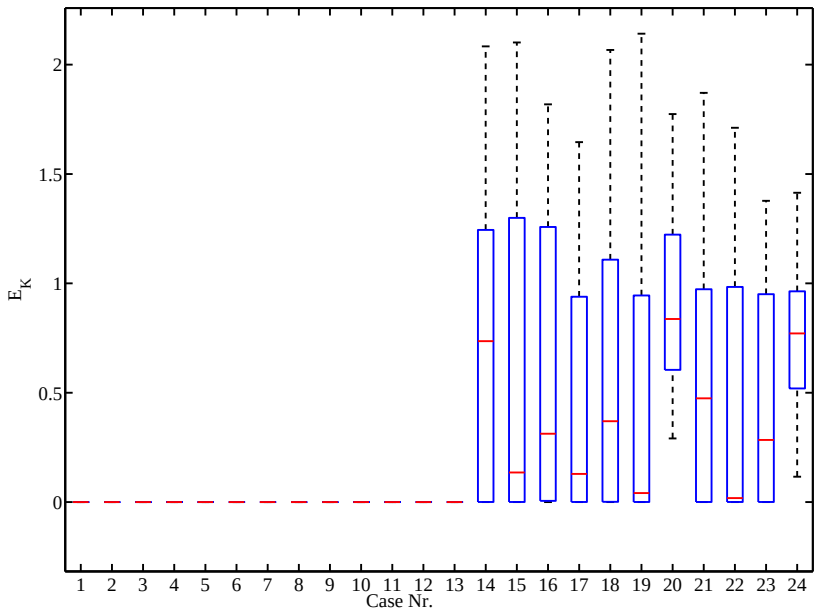

(a)

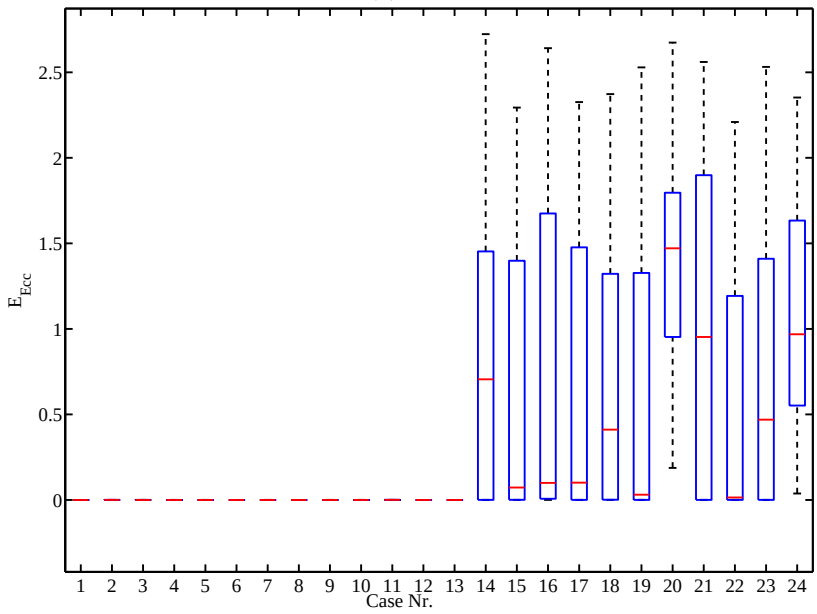

(b)

Figure 6.6: Overview of the error in (a) the magnetization factors and (b) the eccentricity parameters for 24 different topologies. The meaning of the different lines and colors is identical to figure 5.1. For topology 1 to 13, the error is under 3e-4.

Chapter 7

Experimental validation

The previous chapters introduced a demagnetization and eccentricity detection technique that is created to be general, i.e. not limited to a certain topology. The analytical models have been validated with FEM models.

For further validation, a prototype was built that is described in this chapter. The prototype is a 3 phase YASA AFPMSM with a power of 4 kW. The complete construction of the machine is outside the scope of this work, but the implementation of demagnetization and eccentricity is explained.

This setup allows performing measurements of the three phase terminal voltages of the stator coils and the back-EMF of six sensing coils, which will be used to validate the models described in Chapter 3 and Section 4.3.2. Afterwards, the detection technique based on the terminal voltage of Section 4.1 and the demagnetization detection technique based on the sensing coils of Section 4.3.4 are applied on the measured data.

Finally, just as an illustration, the terminal voltage technique is used with a Deadbeat (DB) controller as a fault-tolerant control.

7.1 Prototype of the YASA AFPMSM

The prototype machine is a 3 phase YASA AFPMSM. It has 8 pole pairs and 15 stator slots. The specific machine is a 4 kW 2500 RPM YASA AFPMSM optimized for energy efficiency, and designed [20]. This machine is already used for the validation of the analytical model with a FEM model in Section 3.5, where more information about this machine can be found. The same topology will now be used in the experimental validation of the model and the technique to detect defects.

Figure 7.1 shows the general structure of the machine. The machine is electromagnetically based on the description of Section 2.1.4, shown in figure 2.10. Of course a global machine design accounts for much more [3, 20]: mechanical strength (high axial forces and torque), thermal design (heat evacuation), ease of assembly, production cost, etc.

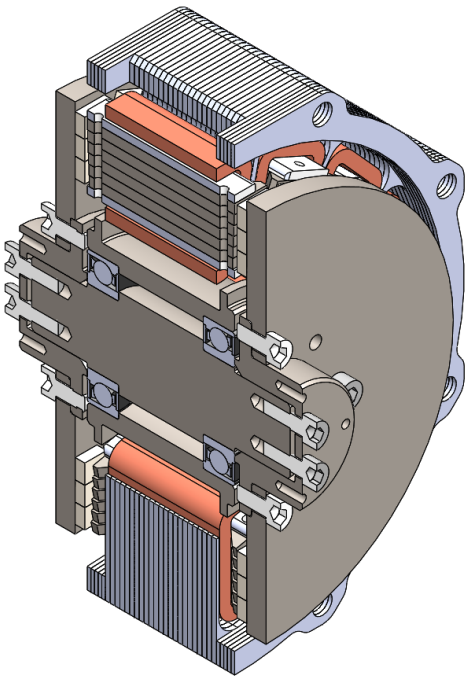

Figure 7.1: Cross-section of the CAD model of the 4 kW 2500 RPM YASA AFPMSM [20, 228].

The complete design of the machine is outside the scope of this work, more information about the construction of the machine can be found in [229].

7.1.1 Implementation of the demagnetization and eccentricity

The machine contains two rotors. Each rotor consists of an iron disc made of C45 steel with high magnetic permeability. The discs have NdFeB magnets glued to their surface. Each rotor has 16 poles, constructed with an alternating polarization, resulting in 8 pole pairs. The two rotors are constructed in such a way that after the mounting opposite poles align with each other in the axial direction as shown in the flux path diagram of figure 2.6(a). The two rotors are connected to the shaft with bolts. The rotors are attached to the shaft in such a way that the air gap can be adjusted. The construction does not only allow varying the air gap uniformally, but also to apply dynamic eccentricity to the machine, which is required to examine eccentricity defects. Demagnetization defects can be implemented by changing the healthy rotors with rotors with missing magnets as shown in figure 7.2.

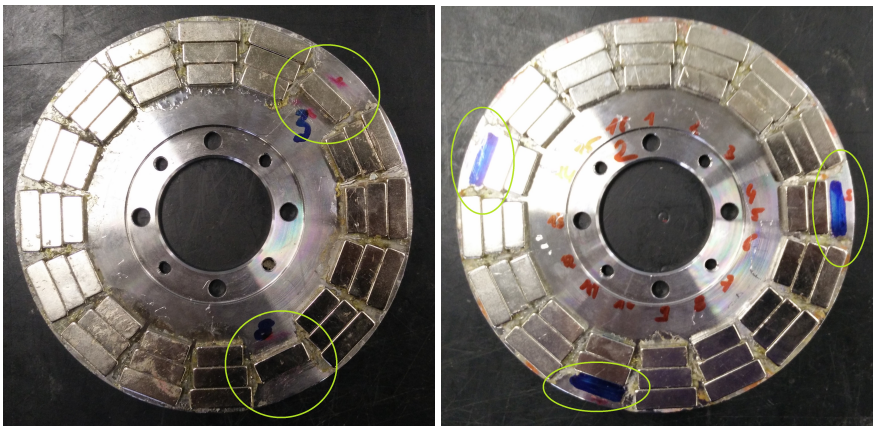

Figure 7.2: Two demagnetized rotors: some poles have missing magnets.

7.1.2 Sensing coils for air gap flux measurement

For research purposes, sensors were added during the construction of the machine. Several RTD-sensors are integrated into different parts of the machine to study the temperatures; six sensing coils are placed near the air gaps to measure the back-EMF caused by the main flux of the machine, and one sensing coil is placed on top of a stator tooth core near the air gap to study the fringing flux of the machine. The sensing coils for measuring the main flux are positioned on the stator teeth as described in Section 4.3.1.

Only the sensing coils measuring the main flux will be used in this research. Three sensing coils are placed around a stator tooth, and axially positioned close to the air gap. The three coils are at 120 mechanical degrees from each other along the circumference of the machine. The three coils give redundancy in data as only one sensing coil per air gap is needed for the demagnetization defect detection of the sensing coil technique. Each sensing coil is constructed of 20 turns of wire with a diameter of 0.2 mm.

7.1.3 Test setup

The described machine is placed in a test setup to perform the measurements. This setup is shown in figure 7.3. The machine is connected with an asynchronous motor rated at 7.5 kW and 3000 RPM. This asynchronous motor acts as a load machine and is controlled by a commercial drive. The drive of this machine is controlled by a dSPACE 1104 platform. An incremental encoder measures the speed and, together with a Lorenz DR2112 torque sensor, the mechanical power can be measured.

The AFPMSM can also be controlled, which is done by a dSPACE controlled custom-designed inverter based on a Semikron SEMiX101GD12E4s IGBT-

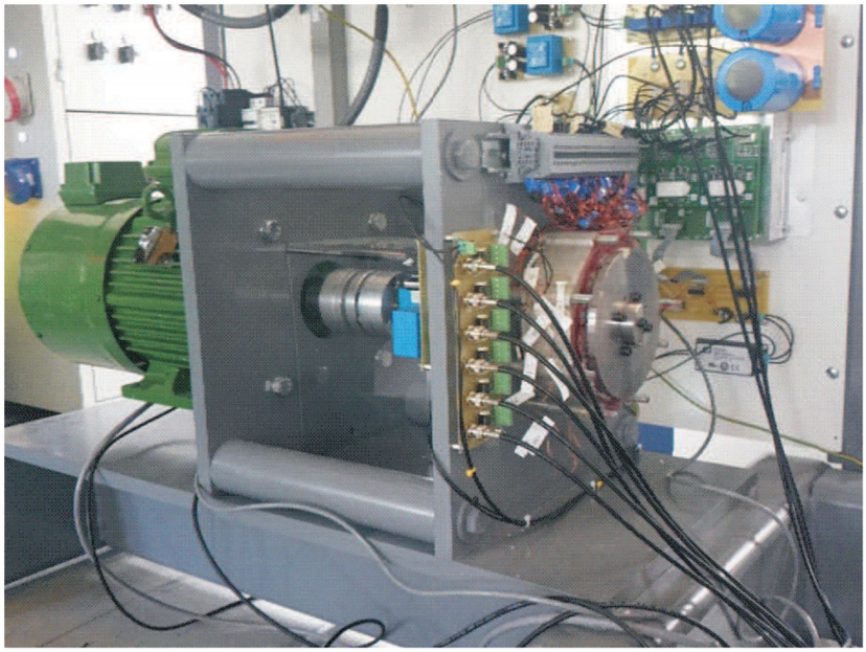

Figure 7.3: An overview of the laboratory setup with the AFPMSM working as generator.

module. Alternatively, a fully-programmable three-phase load can be connected to the machine when it is used as a generator. The lack of pulse-width modulation in the load is an advantage for the noise on the measurements.

Furthermore, the three phase terminal voltages and the three phase currents are measured with two Yokogawa DLM2024 scopes. The currents data are converted to a voltage signal by using LEM LA55-P current transducers. The back-EMFs of the sensing coils are also measured with the same scopes, but because these coils always function in no-load, no current measurements are needed.

7.2 Validation with experimental data

7.2.1 Validation of the terminal voltage analytical model

The setup described in previous section is used to perform measurements of the three phase terminal voltages of the stator coils in healthy, demagnetized, eccentric and combined demagnetization and eccentricity situations. This data is useful to perform a validation of the analytical model with experimental data.

Figures 7.4 and 7.5 shows the waveforms and their harmonic spectrum of the terminal voltage data at no-load and at 7 A load for a speed of 1500 RPM. There is a good correspondence between the analytical and the experimental data. At 7 A load, the analytical model overestimates the terminal voltage slightly.

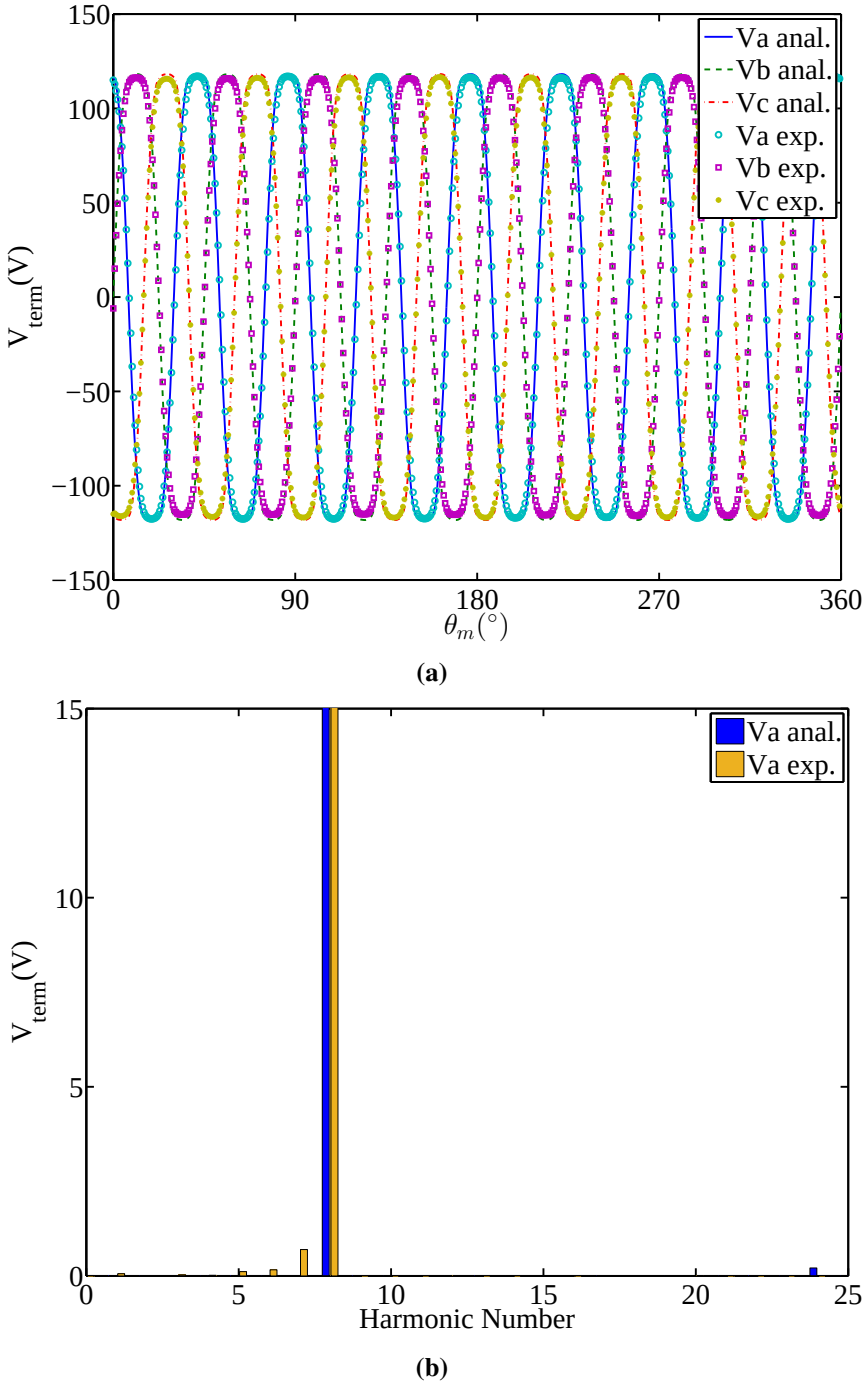

Figure 7.4: (a) Waveforms and (b) harmonic spectrum of the three phase terminal voltage of the analytical and experimental data at 1500 RPM and in healthy condition at no-load.

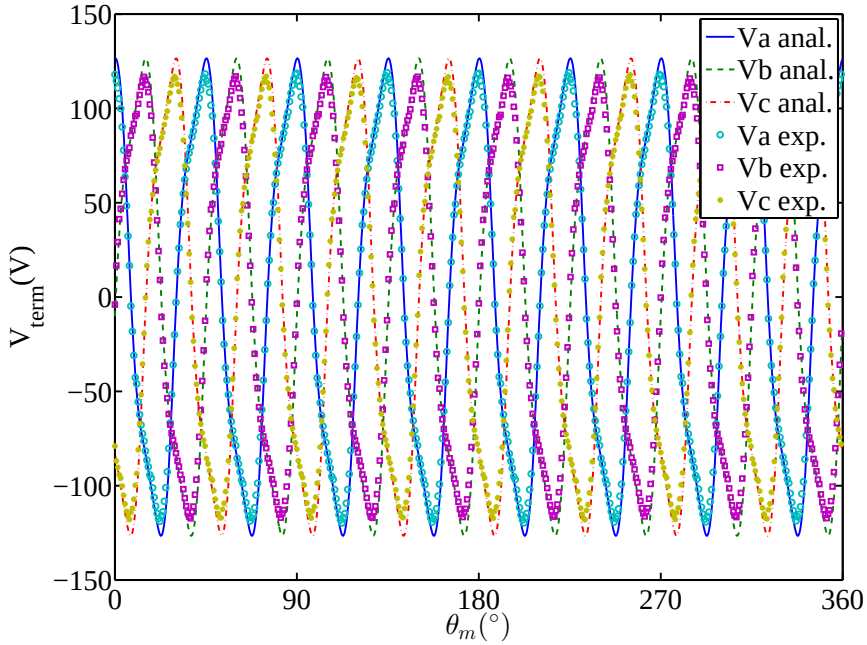

(a)

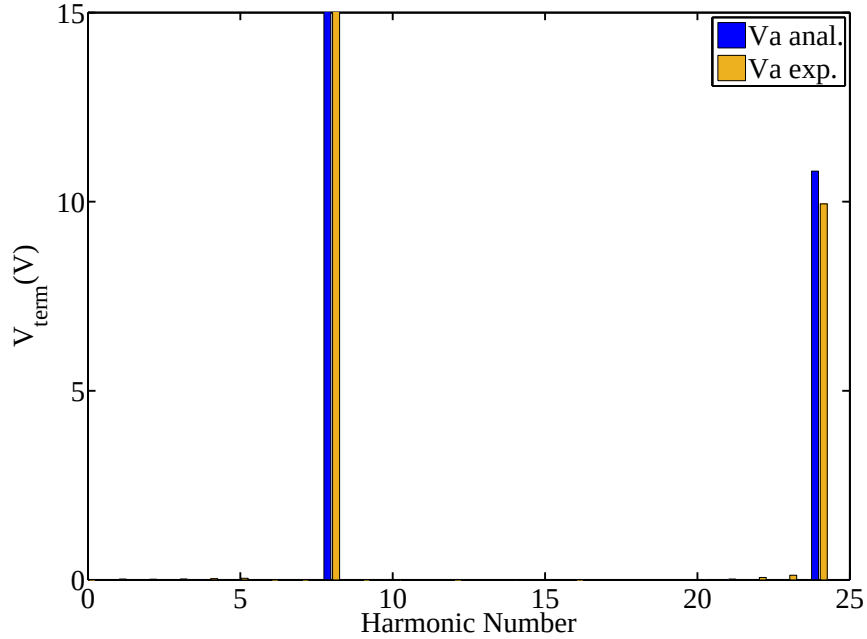

(b)

Figure 7.5: (a) Waveforms and (b) harmonic spectrum of the three phase terminal voltage of the analytical and experimental data at 1500 RPM and in healthy condition at 7 A load.

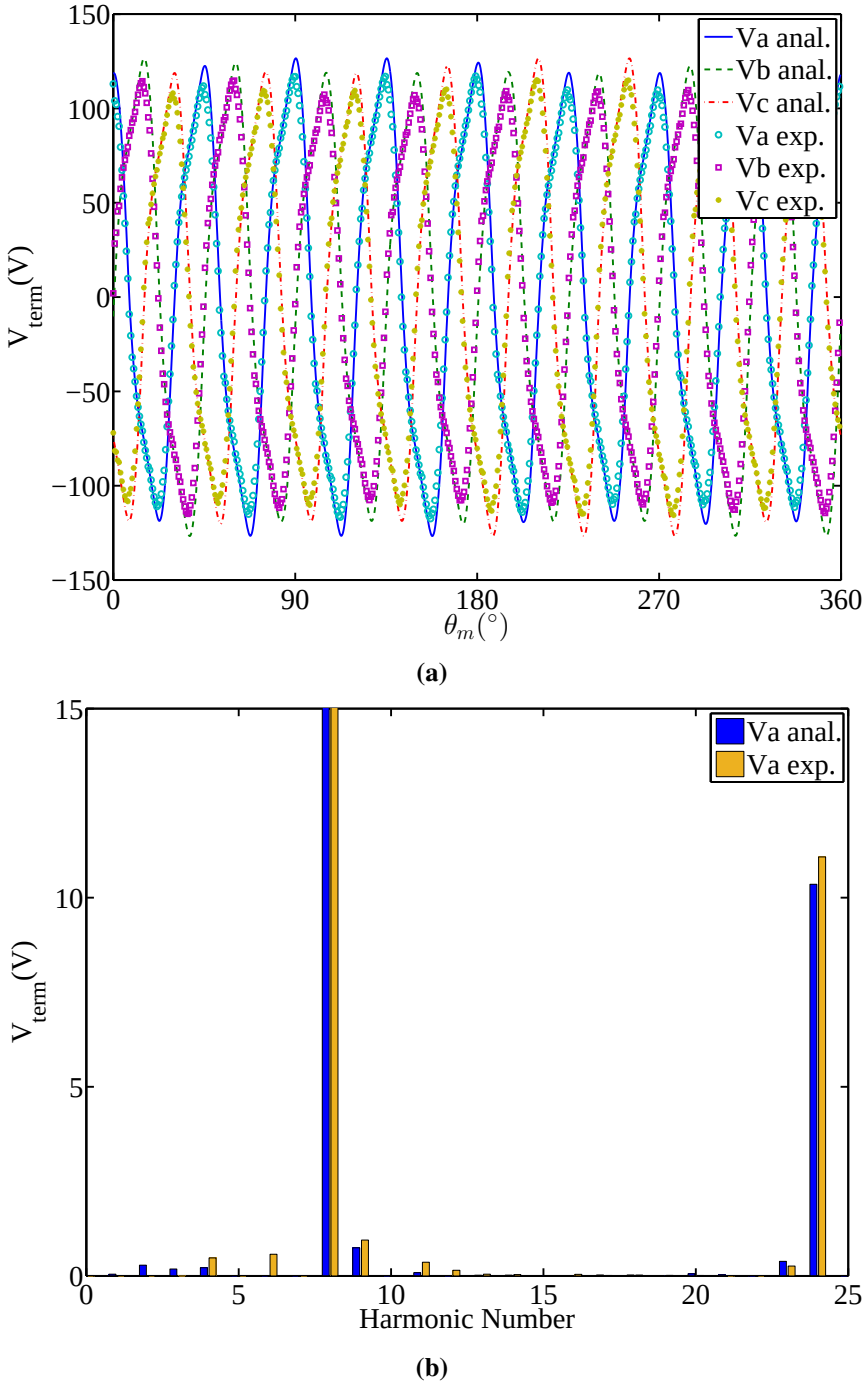

Figure 7.6: (a) Waveforms and (b) harmonic spectrum of the three phase terminal voltage of the analytical and experimental data at 1500 RPM and 7 A load with a demagnetization defect $D\,[3, \mathrm{L}, 0.33]$, $D\,[8, \mathrm{L}, 0.33]$.

The same situation of 7 A load and a speed of 1500 RPM is shown with a demagnetization defect in figure 7.6. Beside the slight overestimation shown before, the data agrees with each other.

Figure 7.7 shows a dynamic eccentricity defect at the operating point of 7 A load and 1500 RPM. Again a good correspondence between the analytical and the experimental data is found.

In figure 7.8, both a demagnetization defect and an eccentricity defect are implemented at the same operating point with 7 A current and a speed of 1500 RPM. Here as well, the experimental data agrees with the analytical data.

7.2.2 Validation of the sensing coil analytical model

In the machine, three sensing coils per air gap are implemented. Although this is more than needed for the sensing coil detection technique, it is useful to validate the sensing coil analytical model with the experimental data.

Figure 7.9 shows the sensing coil back-EMF of the left and right air gap. The machine is operating at no-load at 2500 RPM in a healthy situation. Although the agreement between the analytical and experimental data is good, the analytical model overestimates the back-EMF slightly. This is explained by the difference of the position of the sensing coils in the analytical model compared to the actual machine. This difference is already described in Section 4.3.3. Furthermore, especially visible in the right air gap, all sensing coils do not have the same amplitude, although the machine is completely healthy. Due to the low number of turns, the data is sensitive to small manufacturing differences, which lead to differences in the induced voltage in the coils.

Figure 7.10 shows the same situation as figure 7.9, but at a load of 5 A. The same deviation as in the previous figure can be seen. Beside this, the data agrees well with each other. Notice that it is to be expected that this deviation will be visible in every figure of the sensing coil back-EMF.

In the situation of figure 7.11, one of the three magnets of a pole was reversed in polarity due to a manufacturing error, which is a demagnetization defect. The plots are at no-load and at a speed of 2500 RPM. The effect of the defect is clearly visible in both the analytical and the experimental data. Also, beside the previously explained deviations, the analytical and experimental data have a good correspondence. Notice that the defect (which is in the left rotor) has a greater effect in the experimental data than in the analytical data in the right air gap. This is again due to the sensing coils position on the stator teeth.

Figure 7.12 shows the same defect at a load of 8.5 A and again a speed of 2500 RPM. The left air gap still has a good agreement between the analytical and the experimental data. In the right air gap, both the effect of the defect and the flux of the stator currents create a deviation between the analytical and experimental data. On top of that, we again have the deviation between the amplitudes of the three sensing coil signals in that air gap. This phenomenon disrupts the data too much

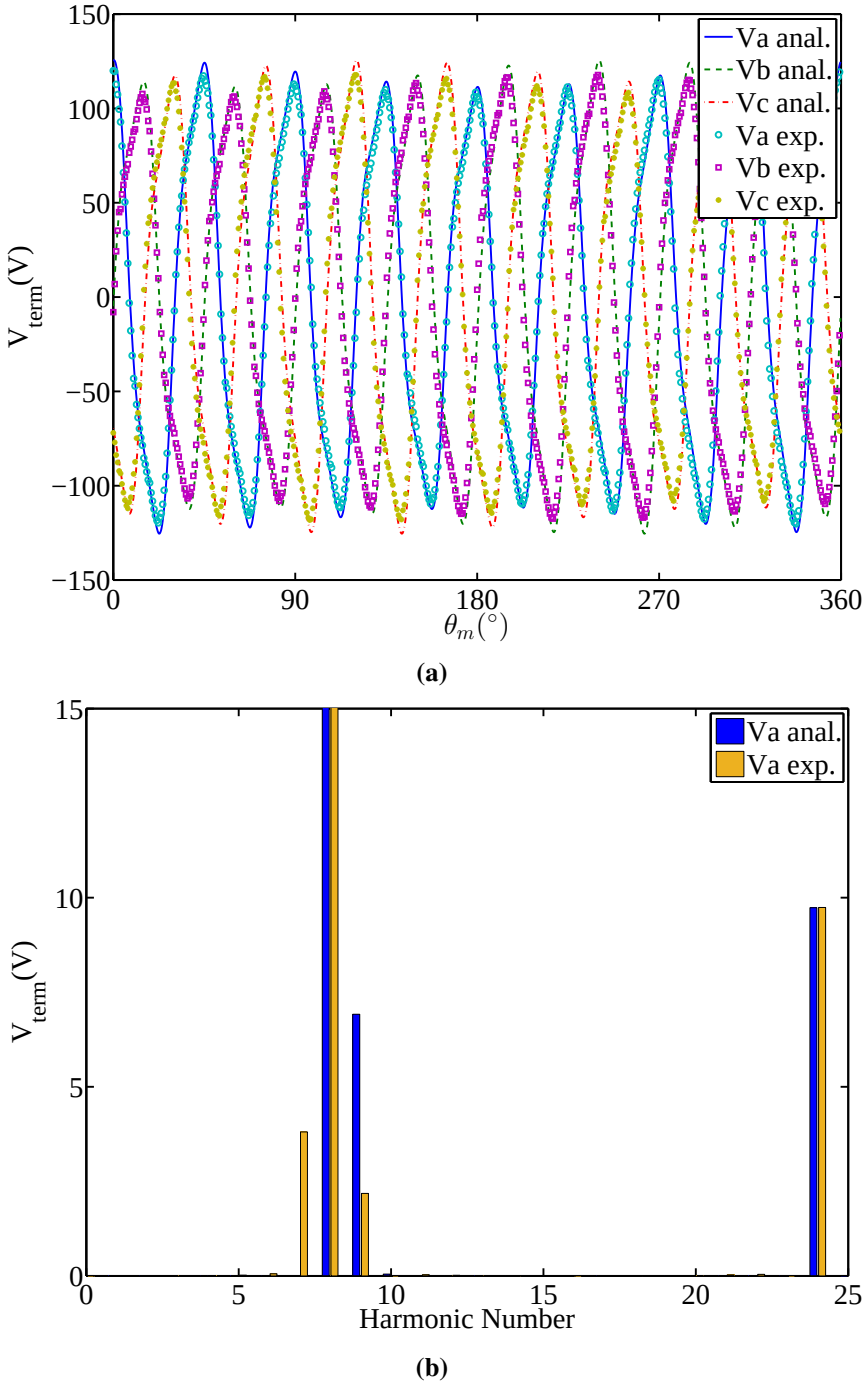

Figure 7.7: (a) Waveforms and (b) harmonic spectrum of the three phase terminal voltage of the analytical and experimental data at 1500 RPM and 7 A load with an eccentricity defect $E\,[\mathrm{L}, \mathrm{DE}, 0.78, 135^\circ]$.

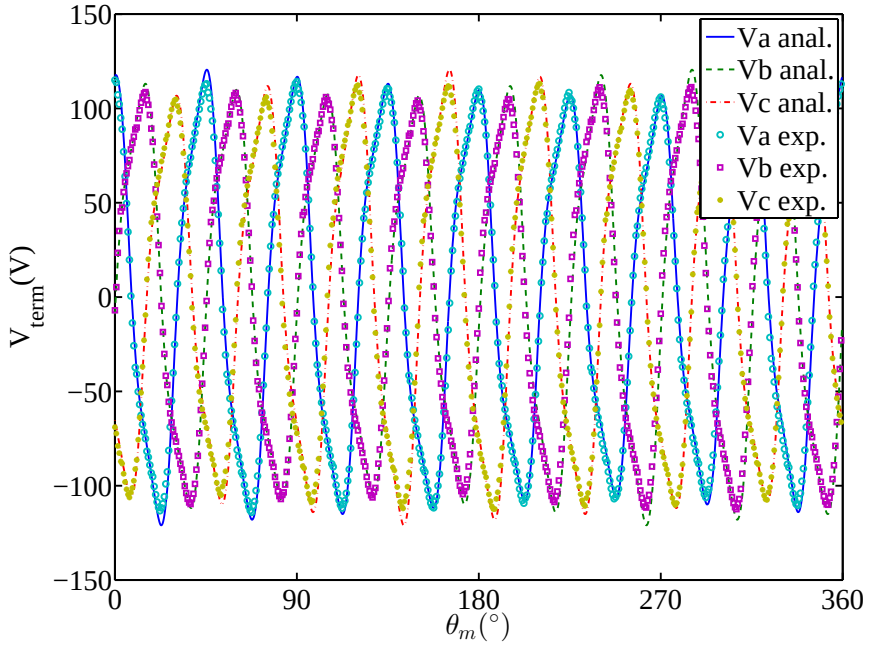

(a)

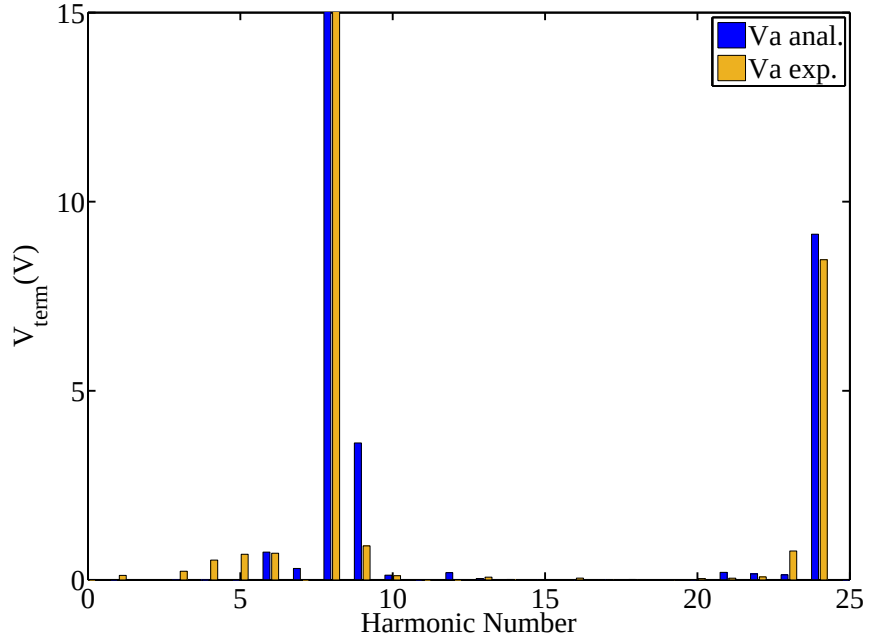

(b)

Figure 7.8: (a) Waveforms and (b) harmonic spectrum of the three phase terminal voltage of the analytical and experimental data at 1500 RPM and 7 A load with a combined demagnetization and eccentricity defect $D\,[5, \mathrm{L}, 0.62]$, $D\,[10, \mathrm{L}, 0.62]$, $D\,[14, \mathrm{L}, 0.62]$, $E\,[\mathrm{L}, \mathrm{DE}, 0.59, 270^\circ]$.

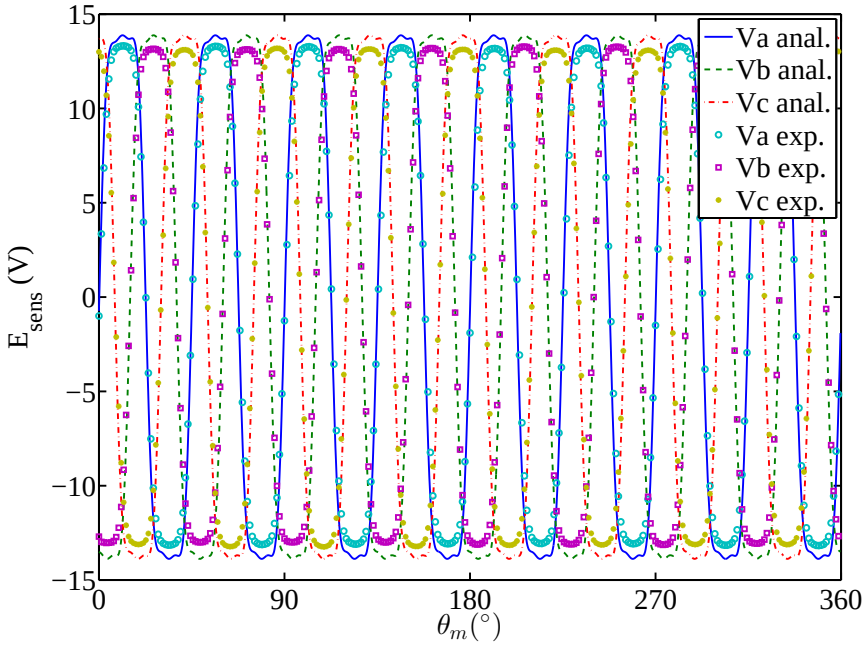

(a)

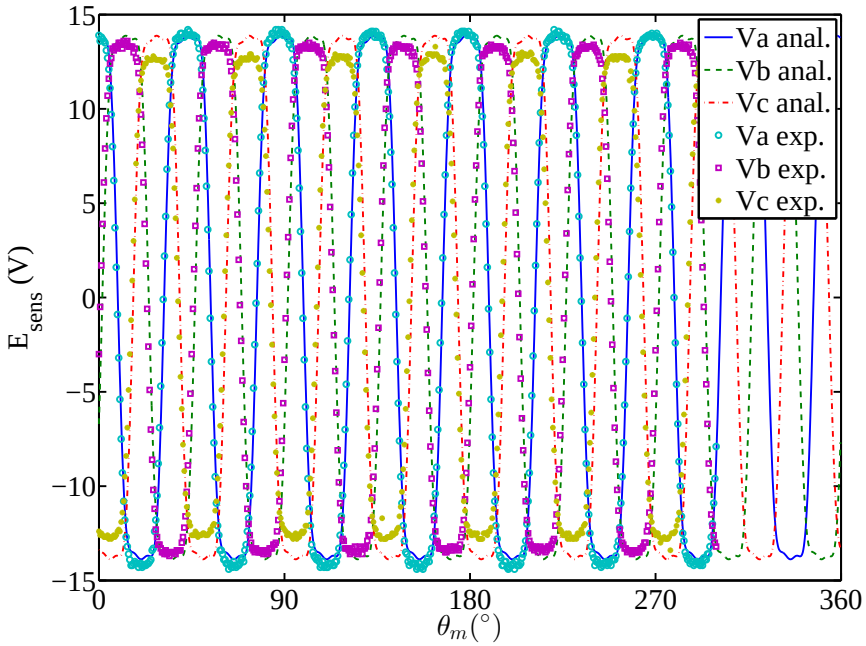

(b)

Figure 7.9: Analytical and experimental sensing coil back-EMF data at tooth 4, 9 and 14 for a healthy machine at 2500 RPM and no-load for (a) the left air gap and (b) the right air gap.

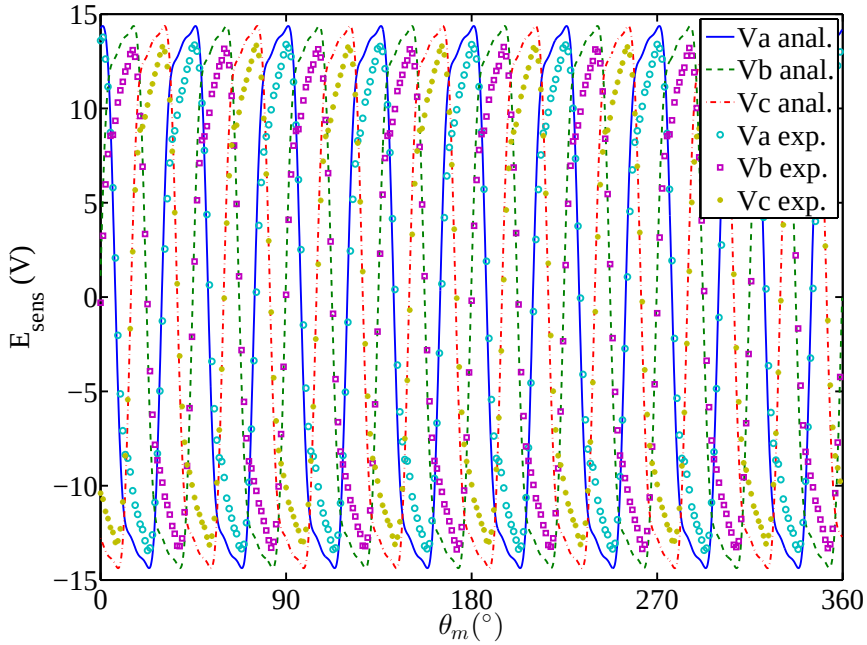

(a)

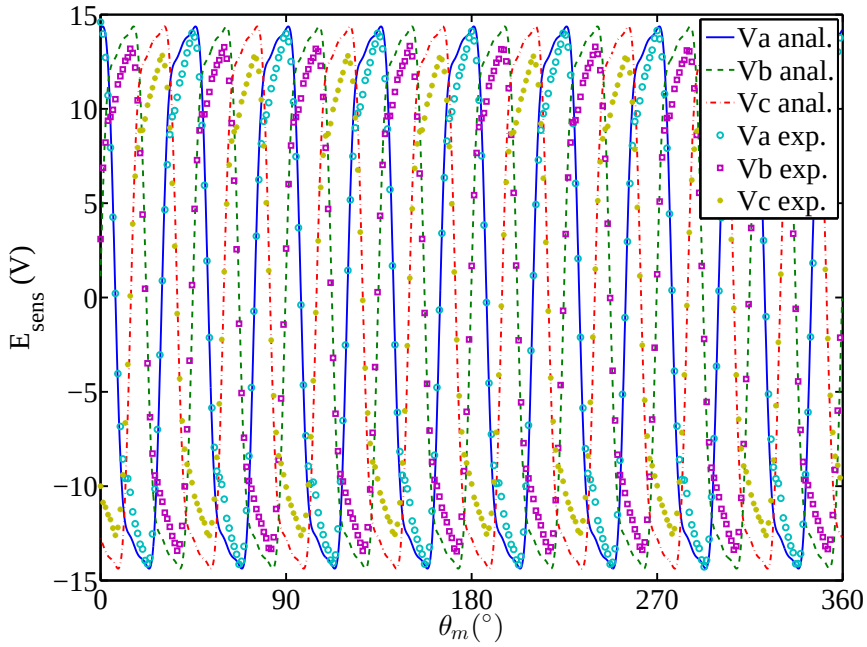

(b)

Figure 7.10: Analytical and experimental sensing coil back-EMF data at tooth 4, 9 and 14 for a healthy machine at 2500 RPM and 5 A load for (a) the left air gap and (b) the right air gap.

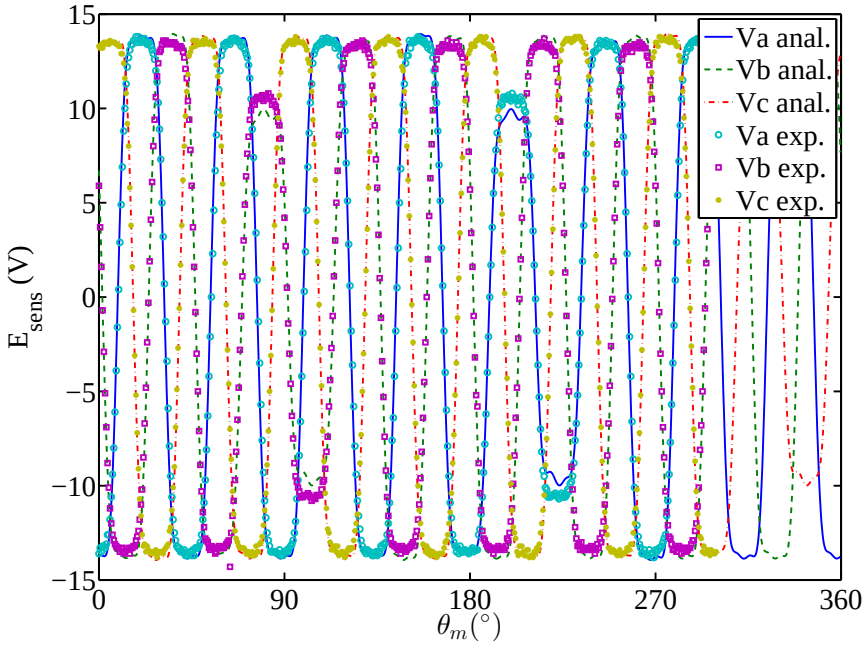

(a)

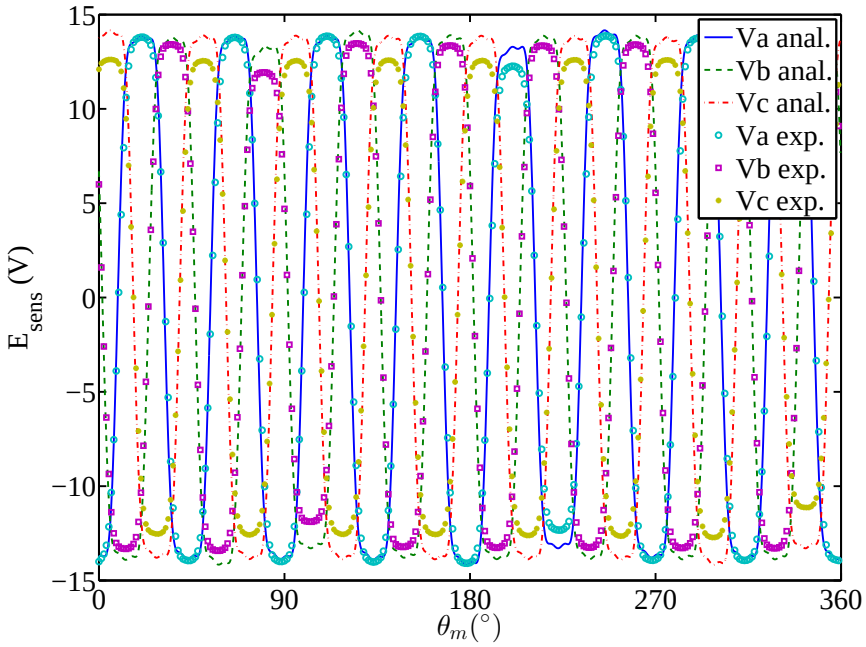

(b)

Figure 7.11: Analytical and experimental sensing coil back-EMF data at tooth 4, 9 and 14 for a machine with one magnet of a pole reversed in polarity at 2500 RPM and no-load for (a) the left air gap and (b) the right air gap.

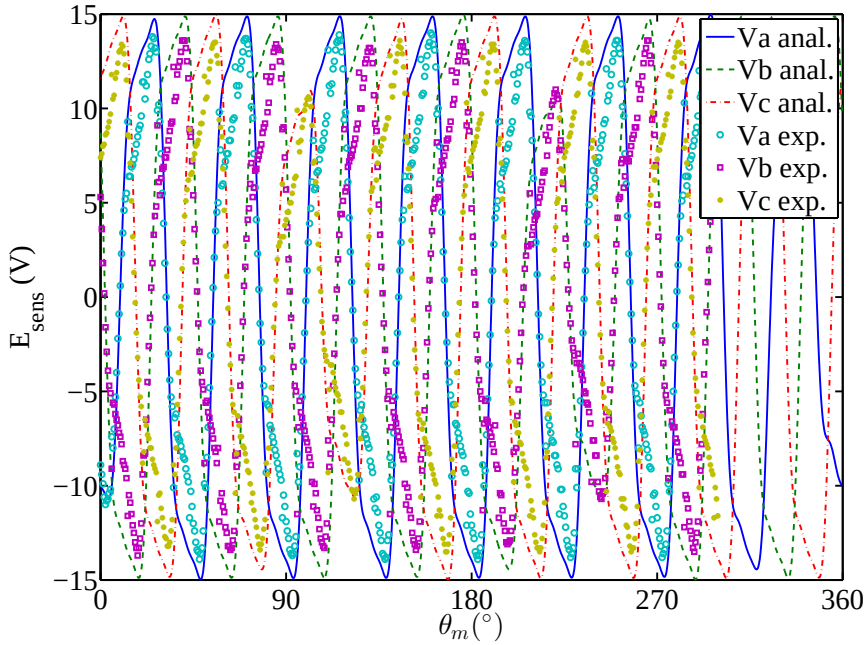

(a)

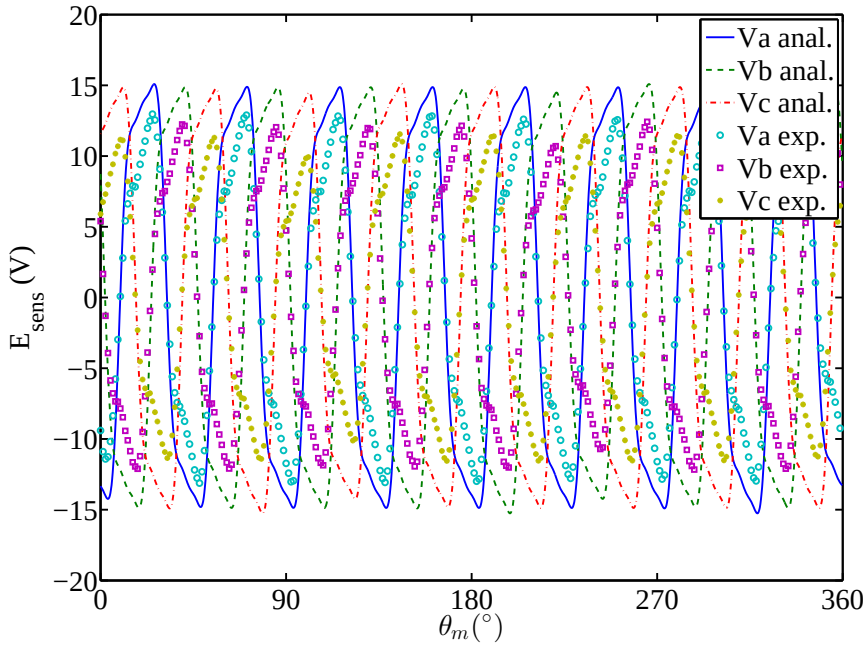

(b)

Figure 7.12: Analytical and experimental sensing coil back-EMF data at tooth 4, 9 and 14 for a machine with one magnet of a pole reversed in polarity at 2500 RPM and 8.5 A load for (a) the left air gap and (b) the right air gap.

Table 7.1: Results of the IP on measurement data with a demagnetization defect. Only the defect information of the right rotor are shown. On the left rotor, all the magnetization factors are 1.

Actual K [/]	Estimated K [/]	$\Delta(10^{-1})$ [%]
1.00	1.00	0.0
1.00	1.00	0.0
1.00	0.99	8.6
0.62	0.61	7.1
1.00	0.99	12.0
1.00	0.97	34.5
1.00	1.00	0.8
0.62	0.62	2.3
1.00	1.00	0.0
1.00	1.00	0.0
1.00	1.00	0.0
1.00	1.00	0.0
0.62	0.65	30.0
1.00	0.96	38.7
1.00	0.98	15.4
1.00	1.00	0.0

for a good correspondence between the analytical and experimental data in figure 7.12(b).

7.2.3 Validation of the defect detection techniques

In the previous section, the analytical model has been validated with experimental data. In order to validate the technique completely, the IP is used with measurement data to see if it can extract the defect information from a real case. The figures 7.4 to 7.8 of Section 7.2.1 show that even though there is a very good validation between the analytical model and the experimental data, the analytical model overestimates the terminal voltages slightly. Because this will prevent the IP from finding a good solution, the analytical model is first tuned to the healthy measurement data. Afterwards, this tuned model is used on the measurement data of the defected case.

In Table 7.1, a demagnetization defect has been applied to the machine. This is done by replacing one rotor by the rotor on the right in figure 7.2. The first column shows the magnetization factors for the defected rotor. It can be seen that three poles have been demagnetized partially by removing the most outward magnet. The second column shows the retrieved defect by the IP based on the terminal voltage and phase current measurements of this case. The measurements are done at 1500 RPM and at 7 A load. The IP estimated that three magnets are demagnetized,

Table 7.2: Results of the IP on measurement data with a dynamic eccentricity defect. Only the defect information of the right rotor are shown. On the left rotor all the eccentricity parameters are 0. The last column expresses the difference between the actual and the estimated parameters relative to the maximum value of that parameter, i.e. 1 and 2π of the amplitude and angle parameter respectively.

	Actual ecc. defect	Estimated ecc. defect	$\Delta(10^{-1})$ [%]
$\rho_{\mathrm{SE,R}}$ [/]	0	0.13	128.4
$\theta_{\mathrm{MSE,R}}$ [rad]	0	2.205	350.9
$\rho_{\mathrm{DE,R}}$ [/]	0.64	0.38	255.8
$\theta_{\mathrm{MDE,R}}$ [rad]	0	0.028	4.5

and estimates the magnitude of the demagnetization quite accurate. The last column shows the absolute difference between the actual and estimated magnetization factors relative to the maximum value.

In Table 7.2, a dynamic eccentricity defect has been applied to the machine. The measurements are done at 1500 RPM and at 7 A load. The first two columns show the actual and estimated eccentricity parameters respectively, while the last column shows the absolute difference between the actual and estimated magnetization factors relative to the maximum value. Notice that the values of the last column no not exceed 100% as they are expressed in 10^{-3} %. The IP is able to detect that dynamic eccentricity has occurred, and also estimates the angle of the defect accurately. But the IP is not able to estimate the magnitude of the eccentricity defect correctly. This can be explained by the construction of the rotor: figure 7.1 shows the mechanism by which eccentricity is applied to the machine. The rotor contains a set of bolts, some pushing the rotor away from the stator while other pulling the rotor toward the stator. By adjusting these bolts adequately, the rotor is placed in an eccentric position. By doing this, the average air gap width is increased as shown in figure 7.13.

The IP does not account for this change and assumes that both the left and right air gap have the same average air gap width, being the air gap at healthy conditions. Furthermore, the IP detects a static eccentricity on the machine of magnitude 0.13, but when using the IP on the healthy case, it detects a static eccentricity with magnitude of 0.15 and an angle of 2.2339 rad. This means that even though for this study no static eccentricity was implemented in the machine, the machine already has a static eccentricity defect.

7.3 Illustration of a fault-tolerant control

Although the analytical model and the defect detection technique are mainly built for detecting an occurring defect and performing predictive maintenance, they open doors for a variety of possibilities. To illustrate this, the model and the technique are used in a fault-tolerant control based on a DB control [90, 92].

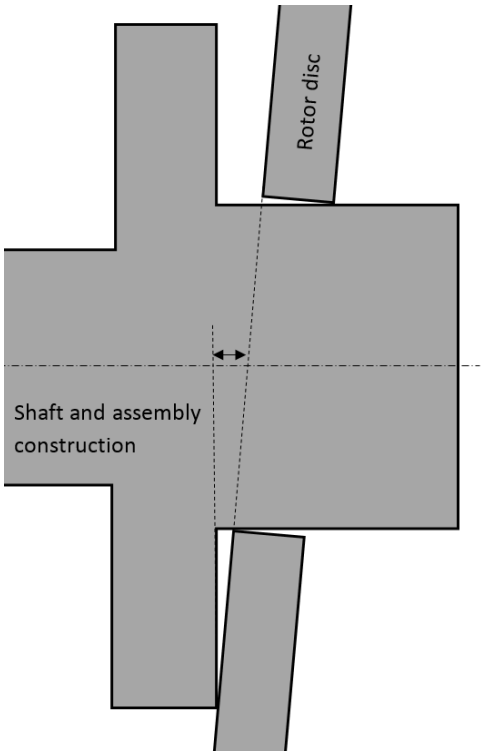

Figure 7.13: Illustration of the rotor disc connection to the shaft in eccentricity. More details can be found about the actual geometry in figure 7.1.

Since the application fields of AFPMSMs require high dynamic performance, they are often used in combination with high-performance current controls to achieve a fast and accurate control with low current ripple. DB control is particularly suitable for this purpose. This model-based predictive control strategy makes use of a concise system model to determine which voltage needs to be applied to the system in order to reach the required current level in one time step. However, the performance of DB control heavily depends on the model accuracy, especially on the rotor flux, and consequently the back-EMF [230]. Because demagnetization and eccentricity faults alter the back-EMF of the AFPMSM, they would thus deteriorate the performance of the DB controller if the system model is not adequately updated. To overcome this issue, the proposed analytical model proves very useful.

Since the applied voltage is known, and the stator currents, rotor position and mechanical speed of the AFPMSM are measured to carry out the DB control, sufficient information is present to identify demagnetization and eccentricity faults by means of the inverse analytical model. Subsequently, the forward model can be used to determine the back-EMF of the AFPMSM under these faulty circum-

stances. By constantly running the inverse model in parallel with the DB controller to check for faults, and updating the simplified system model of the DB controller by means of a lookup table of the latest back-EMF obtained by the forward model, the input voltages computed by the controller remain adequate, even in case of demagnetization and eccentricity faults.

Simulation results for the DB controller at a mechanical speed of 1000 RPM and a DC-bus voltage of 300 V are presented in figure 7.14. Band-limited white noise is added to the current and speed values in these simulations, in order to make them more representative for a real-case scenario. Figure 7.14(a) shows the stator current component i_q for a healthy machine. This current component is proportional to the torque according to the field orientation principle. The simulated current follows its reference value closely, with almost no current ripple.

However, when the third and fourth magnet of the left rotor disc, and the ninth magnet of the right rotor disc are completely demagnetized, and the system model of the DB controller is not updated, i_q shows increased current ripple and a systematic deviation from its reference value, as can be seen in figure 7.14(b). Figure 7.14(c) shows that these issues are solved by adapting the lookup table of the back-EMF used by the DB controller by means of the analytical model: the performance of the DB controller shows almost no degradation in comparison with the healthy case.

7.4 Conclusion

This chapter describes the construction of a prototype YASA AFPMSM with a power of 4 kW and a speed of 2500 RPM. The machine has 8 pole pairs, 15 stator slots and 3 phases. The laboratory setup makes it possible to measure the three phase terminal voltages and currents of the stator coils and the back-EMF of six sensing coils.

This is used to perform an extensive validation of both the analytical model for the terminal voltage technique and the analytical model for the sensing coil technique. It is clear that although the sensing coils can distinguish defects between the two rotors, they are more prone to manufacturing differences, resulting in less accurate measurement data. After this, both the terminal voltage technique and the sensing coil technique are run with actual measured data from the setup to show the applicability of the techniques.

Lastly, the terminal voltage technique is used in a DB controller and evaluated for its fault-tolerant control.

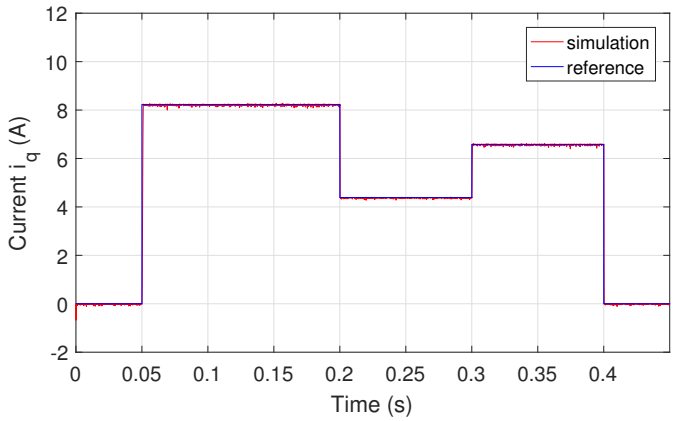

(a) Healthy machine

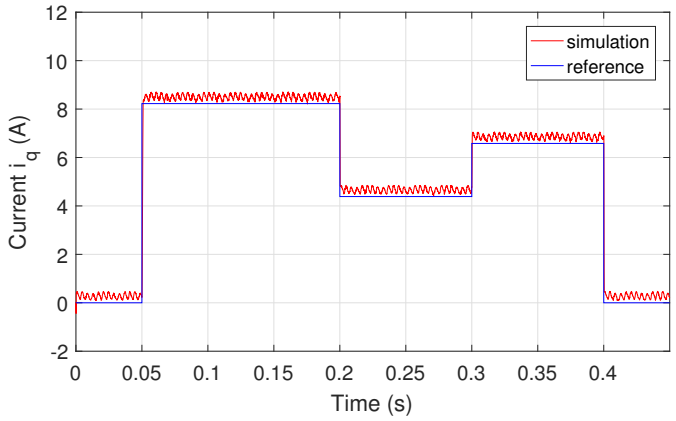

(b) Faulty machine, without model update

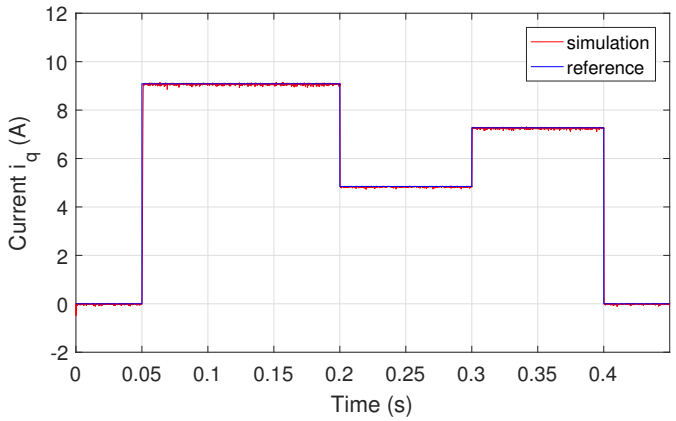

(c) Faulty machine, with model update

Figure 7.14: Simulations for the current component i_q [90, 92].

Chapter 8

Concluding Remarks and Further Research

This last chapter summarizes the conclusions about the techniques of this work and points out the future work that is required for the further development of this technology.

8.1 Overall conclusion

The first chapter started by explaining the motivation, objectives and outline of this dissertation.

Then, the second chapter explains the working principles of AFPMSMs. After explaining the different possible topologies, the focus was placed on the YASA type AFPMSMs. This machine is appreciated because of its high power density, high efficiency and modular stator design. Afterwards, the several maintenance strategies are explained and based on this, it is explained why condition monitoring is so important. Then, the condition monitoring techniques described in literature are shown: a broad overview of existing techniques to detect several types of defects, and a more specific overview of detection techniques for demagnetization and eccentricity. It is clear that internationally there is a lot of research on condition monitoring techniques. From this study, it has become clear that there was a lack of techniques for demagnetization and eccentricity detection in AFPMSMs with two air gaps. The first goal of this dissertation is therefore to build analytical models for this type of machines. The second goal is to develop flexible defect detection techniques that can handle both demagnetization and eccentricity defects at the same time.

Chapter 3 starts with a comparison of three typical analytical modeling techniques for of AFPMSMs. It was concluded that for the goal of this study, the Schwarz-Christoffel Model was the best compromise between calculation time and accuracy. Then, the model of the machine was mathematically constructed and all

technical details were explained thoroughly. Afterwards, the model was validated with FEM simulations performed on different topologies, for both healthy and several defected situations.

Chapter 4 proposed an IP that uses the analytical model of the previous chapter to detect demagnetization and eccentricity defects. Several elements like a line search, solver choice, stop conditions, etc. were briefly touched upon, but for this study, a thorough analysis of solvers and IPs was outside the scope of this dissertation. As calculation time is such an important element, the chapter explains the theoretical elements for analyzing what harmonics are more sensitive to the occurrence of demagnetization defects. The last part of this chapter provides an alternative technique using sensing coils that counters the inherent limitation of the terminal voltage technique: the inability of determining in which rotor the defect has occurred. For the sensing coil technique, the analytical model of Chapter 3 and the IP are modified to work with sensing coils for demagnetization detection.

The next chapter, Chapter 5, applies the techniques explained in the previous chapter for demagnetization defects. The IP with the terminal voltage analytical model is tested for a wide variety of demagnetization defects, and concluded that as long as the noise level is adequately low, the demagnetization defect can be found. For topologies with periodicity, the technique can only find the demagnetization defects if a 'modular n-phase' configuration is used. In the second part of this chapter, the technique for analyzing the sensitivity has been used on demagnetization defects. It is shown that working with the most sensitive harmonics only can reduce the calculation time. Furthermore, a general conclusion of what harmonics will be sensitive for demagnetization defects over a wide set of defects and topologies is drawn: the N_p-th harmonics and its multiples, each with its sidebands are the most sensitive harmonics. Lastly, the sensing coil technique is applied on demagnetization defects, and the results are compared with the terminal voltage technique. It is clear that the sensing coil technique is more accurate, especially with asymmetrical defects. Of course the downside of this technique is the extra sensing coils needed to perform the measurements.

In Chapter 6, the terminal voltage technique is applied on eccentricity defects. It can be concluded that the technique can detect the eccentricity defect with sufficient accuracy, given that the noise levels on the terminal voltage data are not too high. Furthermore, the technique is applied on combined demagnetization and eccentricity defects, and the results show that the technique can differentiate between the two types of defects quite easily. In both situations, the technique can only find the defects in topologies with periodicity if a 'modular n-phase' configuration is used.

Finally, the last chapter introduced the prototype AFPMSM constructed at the Electrical Energy Laboratory of Ghent University and describes the test setup in the laboratory. The setup allows measurements of the three phase terminal voltages and the sensing coils back-EMF. This data is then used to validate the terminal voltage and the sensing coil analytical model with experimental data, proving the

correctness of the models. The data is also utilized to test the terminal voltage technique. Lastly, an example is given of the advantages of having this detection technique and the analytical model by using it in a deadbeat control.

From this all, some conclusions about the objectives of this dissertation can be drawn. The required analytical model was build and the model is capable of simulating both demagnetization as eccentricity defects adequately accurate and fast enough for condition monitoring. The model is able to simulate both symmetrical and asymmetrical defects correctly.

Secondly, this work succeeds in developing a detection technique based on solving an inverse problem using measurement data and the analytical model. The detection techniques requires only the terminal voltages and phase currents and does not require extra sensors in the machine. The method is able to differentiate between demagnetization and eccentricity and can also detect combined defects. It cannot detect in which rotor the defects are occurring as that information is not stored in the measured signals. In machines with periodicity, the technique cannot detect the defect correctly using only the three phase voltages and currents. This can be solved by using a modular n-phase configuration. The detection technique is capable of working with such a configuration.

8.2 Recommendations for Further Research

Although the analytical model already accounts for demagnetization and eccentricity defects, extending it with inter-turn short-circuit defects will allow studying combined demagnetization, eccentricity and inter-turn defects. This is especially interesting because these defects are the three most occurring defects in the electromagnetic part of the machine.

The model gives insight in the defects in the machine, but it focuses on condition monitoring. Further study of the effect of defects on performance would be interesting to evaluate how the defects influence torque and torque ripple, efficiency, losses, etc. Better knowledge of these elements can be incorporated in the machine design to reduce the influence of the defects on the machine's performance. The analytical model of this dissertation is not built to calculate these variables accurately. The reason for this is that studying e.g. machine losses requires knowledge of the exact flux density within the stator teeth, which is not calculated in this model. Future work can be to develop very accurate models.

Thirdly, improvements can be done to increase the convergence speed of the IP. Small alterations can have an substantial impact due to the relatively simple OF waveform shape. Increasing the power of the OF will steepen the waveform, which is an incentive for the solver to take larger steps when it is yet far away from the optimum. Also scaling the error of each harmonic component by its sensitivity toward defects, could result in faster conversion because it emphasizes the most sensitive harmonics.

The next logical step in the evolution of this technology is real-time monitoring. This requires the technique to be adequately fast and accurate, which is a difficult requirement. The standard motor controllers do not have enough processing power to solve the IP within a reasonable amount of time, and certainly not within every time step of the controller. Previously explained improvements to the IP may help, but will definitely not be enough. An alternative approach can be to run the detection algorithm in parallel on a separate computer and use the retrieved conclusions to either report to the maintenance staff, or in more severe cases, prompt an alarm or even shut down the machine to prevent further damage. But in any case, the speed of the technique is very important. In today's industry, more and more applications require a very high dynamic behavior of the machines. In those cases, the technique will simply not suffice as it requires a stationary operating point during measurements.

Manufacturing inaccuracies and uncertainties on the parameters can be compensated with the Minimum Path of the Uncertainty technique. Alternatively, they can be accounted for by tuning the model at first use. This means the IP tries to find all crucial parameters (e.g. air gap width) by matching the model terminal voltages with the real machine measurements. This will initially require some time at start-up to determine these parameters with the IP. Afterwards the impact of uncertainty on the parameters will be reduced because of this tuning of the parameters. This method could also be used to retrieve data on the deviation of parameters due to the manufacturing process. This study of course first requires examining the sensitivity of the terminal voltage harmonics toward these crucial parameters. Based on this information, the parameters that influence the terminal voltages significantly can be retrieved.

Once the defects can be detected quickly and accurately, this technique and model can be used in countering the consequences of the defects in the machine. Examples of this are the fault-tolerant control of Section 7.3, reduction of the torque ripple to prevent metal fatigue or other damage in the rest of the drivetrain, etc.

In the context of predictive maintenance, the lifetime of the machine could be estimated. This requires detecting the condition of the machine at regular time instances. In a simple method, the trend of degradation of the machine could be extrapolated to predict the lifetime of the machine. More advanced methods require knowledge of the complete drivetrain to have insight in the origin of the defects. For example, the progression of eccentricity in the machine can be detected by analyzing the amplitudes of mechanical shocks that increase the eccentricity and how frequently they occur.

References

[1] P. Waide and C. Brunner, "Energy-Efficiency Policy Opportunities for Electric Motor-Driven Systems," in *Internation Energy Agency*, 2011.

[2] BEMAS, *Challenges for industry in North-West Europe*. BEMAS, 2016.

[3] B. Scheerlinck, "Fringing Flux Losses in Axial Flux Permanent Magnet Synchronous Machines," Ph.D. dissertation, Ghent University, 2017.

[4] F. G. Capponi, G. De Donato, and F. Caricchi, "Recent advances in axialflux permanent-magnet machine technology," *IEEE Transactions on Industry Applications*, vol. 48, no. 6, pp. 2190–2205, 2012.

[5] C. H. Lim, "Thermal modelling of the ventilation and cooling inside axial flux permanent magnet generators," Ph.D. dissertation, Durham University, 2010.

[6] F. Libert, "Design, optimization and comparison of permanent magnet motors for a low-speed direct-driven mixer," Ph.D. dissertation, Royal Institute of Technology, Stockholm, 2004.

[7] F. Sahin, A. Tuckey, and A. Vandenput, "Design, development and testing of a high-speed axial-flux permanent-magnet machine," in *IEEE Industry Applications Conference*, 2001, pp. 1640–1647.

[8] K. Akatsu and S. Wakui, "A comparison between axial and radial flux PM motor by optimum design method from the required output NT characteristics," *The International Journal for Computation and Mathematics in Electrical and Electronic Engineering (COMPEL)*, vol. 25, no. 2, pp. 496–509, 2006.

[9] T. J. Woolmer and M. D. McCulloch, "Analysis of the yokeless and segmented armature machine," in *International Electric Machines and Drives Conference (IEMDC)*, vol. 1, 2007, pp. 704–708.

[10] F. Caricchi, F. G. Capponi, F. Crescimbini, and L. Solero, "Experimental study on reducing cogging torque and no-load power loss in axial-flux

permanent-magnet machines with slotted winding," *IEEE Transactions on Industry Applications*, vol. 40, no. 4, pp. 1066–1075, 2004.

[11] W. Fei, P. Luk, and K. Jinupun, "A new axial flux permanent magnet segmented-armature-torus machine for in-wheel direct drive applications," in *Power Electronics Specialists Conference*, 2008, pp. 2197–2202.

[12] H. Kierstead, R. Wang, and M. Kamper, "Design optimization of a single sided axial flux permanent magnet in-wheel motor with non-overlap concentrated winding," in *Southern African Universities Power Engineering Conference*, 2009.

[13] B. Chalmers and E. Spooner, "An axial-flux permanent-magnet generator for a gearless wind energy system," *IEEE Transaction on Energy Conversion*, vol. 14, no. 2, pp. 251–257, 1999.

[14] A. Di Gerlando, G. M. Foglia, M. F. Iacchetti, and R. Perini, "Axial flux pm machines with concentrated armature windings: Design analysis and test validation of wind energy generators," *IEEE Transactions on Industrial Electroncs*, vol. 58, no. 9, pp. 3795–3805, 2011.

[15] Y. Chen, P. Pillay, and A. Khan, "Pm wind generator topologies," *IEEE on Industry Applications*, vol. 22, no. 1, pp. 86–94, 2007.

[16] T. Chan and L. Lai, "An axial-flux permanent-magnet synchronous generator for a direct-coupled wind-turbine system," *IEEE Transactions on Energy Conversion*, vol. 22, no. 1, pp. 86–94, 2007.

[17] G. F. Price, T. D. Batzel, M. Comanescu, and B. A. Muller, "Design and testing of a permanent magnet axial flux wind power generator," in *Proceedings of the 2008 IAJC-IJME International Conference*, 2008.

[18] A. Parviainen, J. Pyrhönen, and P. Kontkanen, "Axial flux permanent magnet generator with concentrated winding for small wind power applications," in *IEEE International Conference on Electric Machines and Drives*, 2005, pp. 1187–1191.

[19] D. Moreels and P. Leijnen, "High Efficiency Axial Flux Machines," Magnax, pp. 1–21, November 2018.

[20] H. Vansompel, "Design of an energy efficient axial flux permanent magnet machine," Ph.D. dissertation, Ghent University, 2013.

[21] A. Hemeida, "Electromagnetic and Thermal Design of Axial Flux Permanent Magnet Synchronous Machines," Ph.D. dissertation, Ghent University, 2017.

[22] S. Kahourzade, A. Mahmoudi, and H. W. Ping, "A comprehensive review of axial-flux permanent-magnet machines," *Canadian Journal of Electrical and Computer Engineering*, vol. 37, no. 1, pp. 19–33, 2014.

[23] M. Tapia, A. Hoffer, and J. Tapia, "Simulation and Analysis of an Axial Flux Induction Machine," *IEEE Latin America Transactions*, vol. 15, no. 7, pp. 1263–1269, 2017.

[24] J. H. J. Potgieter, F. J. Marquez-Fernandez, A. G. Fraser, and M. D. McCulloch, "Performance Evaluation of a High Speed Segmented Rotor Axial Flux Switched Reluctance Traction Motor," in *International Conference on Electrical Machines (ICEM)*, 2016, pp. 531–537.

[25] M. Aydin, S. Huang, and T. Lipo, "Axial flux permanent magnet disc machines: A review," in *Symposium on Power Electronics, Electrical Drives, Automation, and Motion (SPEEDAM)*, 2004, pp. 61–71.

[26] C. Chan, "Axial-Field Electrical Machines - Design and Applications," *IEEE Transactions on Energy Conversion*, vol. EC-2, no. 2, pp. 294–300, 1987.

[27] S. M. Mirimani, A. Vahedi, and F. Marignetti, "Effect of Inclined Static Eccentricity Fault in Single Stator-Single Rotor," *IEEE Transactions on Magnetics*, vol. 48, no. 1, pp. 143–149, 2012.

[28] M. Aydin, S. Huang, and T. A. Lipo, "Torque quality and comparison of internal and external rotor axial flux surface-magnet disc machines," *IEEE Transactions on Industrial Electronics*, vol. 53, no. 3, pp. 822–830, 2006.

[29] C. Du-Bar, "Design of an axial flux machine for an in-wheel motor application," Ph.D. dissertation, Chalmers University of Technology, 2011.

[30] F. Profumo, Zheng Zhang, and A. Tenconi, "Axial flux machines drives: a new viable solution for electric cars," *IEEE Transactions on Industrial Electronics*, vol. 44, no. 1, pp. 39–45, 1997.

[31] A. Parviainen, "Design of axial-flux permanent-magnet low-speed machines and performance comparison between radial-flux and axial-flux machines," Ph.D. dissertation, Lappeenranta University of Technology, 2005.

[32] F. Caricchi, F. Crescimbini, O. Honorati, G. L. Bianco, and E. Santini, "Performance of coreless-winding axial-flux permanent-magnet generator with power output at 400 hz, 3000 r/min," *IEEE Transactions on Industry Applications*, vol. 34, no. 6, pp. 1263–1269, 1998.

[33] S. M. Hosseini, M. Agha-Mirsalim, and M. Mirzaei, "Design, prototyping, and analysis of a low cost axial-flux coreless permanent-magnet generator," *IEEE Transactions on Magnetics*, vol. 44, no. 1, pp. 75–80, 2008.

[34] M. J. Kamper, R.-J. Wang, and F. G. Rossouw, "Analysis and performance of axial flux permanent-magnet machine with air-cored nonoverlapping concentrated stator windings," *IEEE Transactions on Industry Applications*, vol. 44, no. 5, pp. 1495–1504, 2008.

[35] J. Brown, "High Efficiency Permanent Magnet Motor," Marand Precision Engineering, October 2010, powerpoint Accessed: 2018-08-02. [Online]. Available: http://www.ata.org.au/wp-content/uploads/marand_high_efficiency_motor.pdf

[36] "Csiro 2007 world solar challenge," CSIRO Science Image, October 2007, website accessed: 02-08-2018. [Online]. Available: http://www.scienceimage.csiro.au/mediarelease/mr07-205.html

[37] F. Caricchi, F. Crescimbini, K. Mezzetti, and E. Santini, "Multi-stage axial-flux PM machine for wheel direct drive," in *IEEE Industry Applications Conference*, 1995, pp. 679–684.

[38] S. T. Vun, M. D. McCulloch, and C. Y. Leong, "The development of an electromagnetic analytical design tool for megawatt-scale YASA generators," in *IET Conference on Renewable Power Generation*, 2011, p. 44.

[39] S. T. Vun and M. D. McCulloch, "Optimal Design Method for Large-Scale YASA Machines," *IEEE Transactions on Energy Conversion*, vol. 30, no. 3, pp. 900–907, 2015.

[40] S. Huang, M. Aydin, and T. A. Lipo, "TORUS concept machines: pre-prototyping design assessment for two major topologies," in *IEEE Industry Applications Conference*, 2001, pp. 1619–1625.

[41] A. S. Fawzal, R. M. Cirstea, K. N. Gyftakis, T. J. Woolmer, M. Dickison, and M. Blundell, "The Fan Design Impact on the Rotor Cooling of Axial Flux Permanent Magnet Machines," in *International Conference on Electrical Machines (ICEM)*, 2016, pp. 2725–2731.

[42] ——, "Fan Performance Analysis for Rotor Cooling of Axial Flux Permanent Magnet Machines," *IEEE Transaction on Industry Applications*, vol. 53, no. 4, pp. 3295–3304, 2017.

[43] A. S. Fawzal, R. M. Cirstea, T. J. Woolmer, M. Dickison, M. Blundell, and K. N. Gyftakis, "Air inlet/outlet arrangement for rotor cooling application of axial flux PM machines," *Applied Thermal Engineering*, vol. 130, pp. 1520–1529, feb 2018.

[44] P. Salminen, A. Parviainen, M. Niemela, and J. Pyrhönen, "Influence of Air Gap Diameter to the Performance of Concentrated Wound Permanent Magnet Motors," in *Advanced Computer Techniques in Applied Electromagnetics*, Wiak, S and Krawczyk, A and Dolezel, I, Ed., vol. 30, 2008.

[45] H. Jussila, P. Salminen, A. Parviainen, J. Nerg, and J. Pyrhönen, "Concentrated Winding Axial Flux Permanent Magnet Motor with Plastic Bonded Magnets and Sintered Segmented Magnets," in *International Conference on Electrical Machines (ICEM)*, 2009, paper ID 1113.

[46] H. Jussila, *Concentrated Winding Multiphase Permanent Magnet Machine Design and Electromagnetic PropertiesCase Axial Flux Machine*. Lappeenranta University of Technology, 2009.

[47] M. Valtonen, A. Parviainen, and J. Pyrhönen, "Influence of the Air-Gap Length to the Performance of an Axial-Flux Induction Motor," in *International Conference on Electrical Machines (ICEM)*, 2009, paper ID 1103.

[48] F. G. Capponi, G. De Donato, G. Borocci, and F. Caricchi, "Axial-Flux Hybrid-Excitation Synchronous Machine: Analysis, Design, and Experimental Evaluation," *IEEE Transactions on Industry Applications*, vol. 50, no. 5, pp. 3173–3184, 2014.

[49] F. G. Capponi, G. Borocci, G. De Donato, and F. Caricchi, "Flux Regulation Strategies for Hybrid Excitation Synchronous Machines," *IEEE Transactions on Industry Applications*, vol. 51, no. 5, pp. 3838–3847, 2015.

[50] ——, "Closed-Loop, Flux Weakening Control for Hybrid Excitation Synchronous Machines," in *Energy Conversion Congress and Exposition (ECCE)*, 2015, pp. 5271–5278.

[51] G. De Donato, F. G. Capponi, G. Borocci, F. Caricchi, L. Beneduce, L. Fratelli, and A. Tarantino, "Omega-Shaped Axial-Flux Permanent-Magnet Machine for Direct-Drive Applications With Constrained Shaft Height," *IEEE Transactions on Industry Applications*, vol. 51, no. 4, pp. 3050–3058, 2015.

[52] F. Marignetti, A. Vahedi, and S. M. Mirimani, "An Analytical Approach to Eccentricity in Axial Flux Permanent Magnet Synchronous Generators for Wind Turbines," *Electric Power Components and Systems*, vol. 43, no. 8-10, pp. 1039–1050, 2015.

[53] S. M. Mirimani, A. Vahedi, F. Marignetti, and E. De Santis, "Static Eccentricity Fault Detection in Single-StatorSingle-Rotor Axial-Flux Permanent-Magnet Machines," *IEEE Transactions on Industry Applications*, vol. 48, no. 6, pp. 1838–1845, 2012.

[54] S. M. Mirimani, A. Vahedi, F. Marignetti, and R. Di Stefano, "An Online Eccentricity Fault Detection Method for Axial Flux Machines," in *Internation Symposium on Power Electronics, Electrical Drives, Automation and Motion (SPEEDAM)*, 2014, pp. 285–289.

[55] A. Di Gerlando, K. ElShawarby, G. M. Foglia, and R. Perini, "DC Side Current and Torque Ripples Reduction in Multi-Modular PMSG for Wind Applications," in *International Conference on Electrical Machines (ICEM)*, 2016, pp. 252–258.

[56] A. Di Gerlando, G. M. Foglia, and M. F. Iacchetti, "Design Guidelines for Wound Inter-Phase Reactors in High-Power Rectifier Systems," in *International Conference on Electrical Machines (ICEM)*, 2016, pp. 1506–1512.

[57] A. Di Gerlando, G. M. Foglia, M. F. Iacchetti, and R. Perini, "Thermal Modeling for the Design and Check of an Axial Flux PM Motor," in *International Conference on Electrical Machines (ICEM)*, 2014, pp. 1441–1447.

[58] ——, "Evaluation of Manufacturing Dissymmetry Effects in Axial Flux Permanent-Magnet Machines: Analysis Method Based on Field Functions," *IEEE Transactions on Magnetics*, vol. 48, no. 6, pp. 1995–2008, jun 2012.

[59] A. Di Gerlando, G. M. Foglia, and R. Perini, "Analytical Modelling of Unbalanced Magnetic Pull in Isotropic Electrical Machines," in *International Conference on Electrical Machines (ICEM)*, 2009, pp. 984–989.

[60] A. Di Gerlando, G. M. Foglia, R. Perini, and M. Ubaldini, "Permanent magnet synchronous machines with concentrated coil armature windings: analysis and test validation of single stator-double rotor, axial flux machines," *Electrical Engineering*, vol. 90, no. 1, pp. 65–77, nov 2007.

[61] B. M. Ebrahimi, J. Faiz, and M. J. Roshtkhari, "Static-, Dynamic-, and Mixed-Eccentricity Fault Diagnoses in Permanent-Magnet Synchronous Motors," *IEEE Transactions on Industrial Electronics*, vol. 56, no. 11, pp. 4727–4739, nov 2009.

[62] B. M. Ebrahimi and J. Faiz, "Demagnetization Fault Diagnosis in Surface Mounted Permanent Magnet Synchronous Motors," *IEEE Transactions on Magnetics*, vol. 49, no. 3, 2, pp. 1185–1192, 2013.

[63] B. M. Ebrahimi, J. Faiz, M. Javan-Roshtkhari, and A. Zargham Nejhad, "Static Eccentricity Fault Diagnosis in Permanent Magnet Synchronous Motor Using Time Stepping Finite Element Method," *IEEE Transactions on Magnetics*, vol. 44, no. 11, pp. 4297–4300, 2008.

[64] B. M. Ebrahimi and J. Faiz, "Configuration Impacts on Eccentricity Fault Detection in Permanent Magnet Synchronous Motors," *IEEE Transactions on Magnetics*, vol. 48, no. 2, pp. 903–906, 2012.

[65] B. M. Ebrahimi, M. Etemadrezaei, and J. Faiz, "Dynamic eccentricity fault diagnosis in round rotor synchronous motors," *Energy Conversion and Management*, vol. 52, no. 5, pp. 2092–2097, may 2011.

[66] B. M. Ebrahimi, M. J. Roshtkhari, J. Faiz, S. Member, and S. V. Khatami, "Advanced Eccentricity Fault Recognition in Permanent Magnet Synchronous Motors Using Stator Current Signature Analysis," *IEEE Transactions on Industrial Electronics*, vol. 61, no. 4, pp. 2041–2052, 2014.

[67] B. M. Ebrahimi and J. Faiz, "Feature Extraction for Short-Circuit Fault Detection in Permanent-Magnet Synchronous Motors Using Stator-Current Monitoring," *IEEE Transactions on Power Electronics*, vol. 25, no. 10, pp. 2673–2682, 2010.

[68] X. Song, D. Liu, H. Polinder, N. Mijatovic, J. Holboll, and B. B. Jensen, "Short Circuits of a 10-MW High-Temperature Superconducting Wind Turbine Generator," *IEEE Transactions on Applied Superconductivity*, vol. 27, no. 4, jun 2017.

[69] M. van der Geest, H. Polinder, J. A. Ferreira, A. Veltman, J. J. Wolmarans, and N. Tsiara, "Analysis and Neutral Voltage-Based Detection of Interturn Faults in High-Speed Permanent-Magnet Machines With Parallel Strands," *IEEE Transaction on Industrial Electronics*, vol. 62, no. 6, pp. 3862–3873, jun 2015.

[70] U. Shipurkar, J. Dong, H. Polinder, and J. A. Ferreira, "Availability of Wind Turbine Converters With Extreme Modularity," *IEEE Transaction on Sustainable Energy*, vol. 9, no. 4, pp. 1772–1782, 2018.

[71] U. Shipurkar, H. Polinder, and J. A. Ferreira, "Modularity in Wind Turbine Generator Systems - Opportunities and Challenges," in *European Conference on Power Electronics and Applications (EPE'16 ECCE EUROPE)*, 2016.

[72] J. Wolmarans, H. Polinder, J. A. Ferreira, and D. Clarenbach, "Design of a Fault Tolerant Permanent Magnet Machine for Airplanes," in *Conference on Electrical Machines and Systems (ICEMS)*, 2008, pp. 2882+.

[73] H. V. Xuan, H. Polinder, D. Lahaye, and J. A. Ferreira, "Modeling for the Design of Fractional Slot PM Machines with Concentrated Windings Protected from Demagnetization during Three-phase Short Circuit," in *Energy Conversion Congress and Exposition (ECCE)*, 2012, pp. 1276–1283.

[74] ABB, "Condition Monitoring of Electrical Machines," ABB Group, July 2012.

[75] SKF, "Integrated Condition Monitoring," SKF Group, January 2016.

[76] H. Vansompel, P. Sergeant, L. Dupré, and A. Van Den Bossche, "Axial-Flux PM Machines With Variable Air Gap," *IEEE Transactions on Industrial Electronics*, vol. 61, no. 2, pp. 730–737, 2014.

[77] H. Vansompel, P. Sergeant, and L. Dupré, "Optimized Design Considering the Mass Influence of an Axial With Concentrated Pole Windings," *IEEE Transactions on Magnetics*, vol. 46, no. 12, pp. 4101–4107, 2010.

[78] H. Vansompel, P. Sergeant, L. Dupré, and A. Van Den Bossche, "Improving the Torque Output in Radial- and Machines with Concentrated Windings by using a Combined Wye-Delta Connection," in *International Electric Machines and Drives Conference (IEMDC)*, no. c, 2011, pp. 336–341.

[79] B. Scheerlinck, H. De Gersem, and P. Sergeant, "3-d eddy current and fringing-flux distribution in an axial-flux permanent-magnet synchronous machine with stator in laminated iron or smc," *IEEE Transactions on Magnetics*, vol. 51, no. 11, p. 4, 2015.

[80] ——, "Reducing losses due to fringing flux in a yokeless and segmented armature axial-flux permanent-magnet synchronous machine," *IEEE Transactions on Magnetics*, vol. 52, no. 10, p. 8, 2016.

[81] A. Rasekh, P. Sergeant, and J. Vierendeels, "Fully predictive heat transfer coefficient modeling of an axial flux permanent magnet synchronous machine with geometrical parameters of the magnets," *Applied Thermal Engineering*, vol. 110, pp. 1343–1357, 2017.

[82] ——, "Cfd-parametric study in stator heat transfer of an axial flux permanent magnet machine," *International Word Academy of Science, Engineering and Technology*, vol. 11, pp. 61–65, 2017.

[83] ——, "Development of correlations for windage power losses modeling in an axial flux permanent magnet synchronous machine with geometrical features of the magnets," *Energies*, vol. 9, no. 12, p. 17, 2016.

[84] H. Vansompel, A. Hemeida, A. Rasekh, P. Sergeant, and J. Vierendeels, "Coupled electromagnetic and thermal analysis of an axial flux pm machine," *IEEE Transactions on Magnetics*, vol. 51, no. 11, p. 2, 2015.

[85] A. Rasekh, P. Sergeant, and J. Vierendeels, "Convective heat transfer prediction in disk-type electrical machines," *Applied Thermal Engineering*, vol. 91, pp. 778–790, 2015.

[86] A. H. Mohamed, A. Hemeida, A. Rashekh, H. Vansompel, A. Arkkio, and P. Sergeant, "A 3D dynamic lumped parameter thermal network of air-cooled yasa axial flux permanent magnet synchronous machine," *Energies*, vol. 11, no. 4, pp. 1–16, 2018.

[87] A. Hemeida and P. Sergeant, "Analytical Modeling of Surface PMSM Using a Combined Solution of Maxwell's Equati ons and Magnetic Equivalent

Circuit (MEC)," *IEEE Transactions on Magnetics*, vol. 50, no. 12, pp. 1–13, 2014.

[88] A. Hemeida, P. Sergeant, and H. Vansompel, "Comparison of methods for permanent magnet eddy current loss computations with and without reaction field considerations in axial flux pmsm," *IEEE Transactions on Magnetics*, vol. 51, no. 9, 2015.

[89] A. Hemeida, P. Sergeant, A. Rasekh, H. Vansompel, and J. Vierendeels, "An optimal design of a 5mw afpmsm for wind turbine applications using analytical model," in *International Conference on Electrical Machines (ICEM)*, 2016, pp. 1290–1297.

[90] L. Verkroost, H. Vansompel, P. Sergeant, F. De Belie, and J. De Bisschop, "Active Demagnetization Fault Compensation for Axial Flux Permanent Magnet Synchronous Machines Using an Analytical Inverse Model," *IEEE Transactions on Energy Conversion*, submitted October 2018.

[91] L. Verkroost, J. Van Damme, H. Vansompel, F. De Belie, and P. Sergeant, "Module Connection Topologies and Interleaving Strategies for Integrated Modular Motor Drives," *International Electric Machines and Drives Conference (IEMDC)*, submitted 2018.

[92] L. Verkroost, J. Druant, H. Vansompel, F. De Belie, and P. Sergeant, "Predictive current control vs. pi control for surface mounted permanent magnet machines," in *International Conference on Electrical Machines (ICEM)*, 2018, p. 7.

[93] P. J. Tavner, "Review of condition monitoring of rotating electrical machines," *IET Electric Power Applications*, vol. 2, no. 4, pp. 215–247, 2008.

[94] B. Corne, "Condition Monitoring with Motor Current Signature Analysis," Ph.D. dissertation, Ghent University, 2018.

[95] 'IEEE Press', *Recommended practice for design of reliable industrial and commercial power systems*. IEEE Press, 1990.

[96] W. H. Dickinson, "IEEE reliability working group, report on reliability of electric plant. Part I, II and III," *IEEE Transactions on Industry Applications*, vol. 10, pp. 201–252, 1974.

[97] D. L. Evans, "IEEE reliability working group, report on problems with hydrogenerator thermoset stator windings. Part I, II and III," *IEEE Transactions on Power Application Systems*, vol. 100, pp. 3284–3303, 1981.

[98] P. O'Donnell, "IEEE reliability working group, report of large motor reliability survey of industrial and commercial installations. Part I, II and III," *IEEE Transactions on Industry Applications*, vol. 21, pp. 853–872, 1985.

[99] P. F. Albrecht, R. M. McCoy, E. L. Owen, and D. K. Sharma, "Assessment of the reliability of motors in utility applications-updated," *IEEE Transactions on Energy Conversion*, vol. 1, pp. 39–46, 1986.

[100] A. H. Bonnett and G. C. Soukup, "Cause and analysis of stator and rotor failures in three-phase squirrel-cage induction motors," *IEEE Transactions on Industry Applications*, vol. 28, no. 4, pp. 921–937, 1992.

[101] O. V. Thorsen and M. Dalva, "A survey of faults on induction motors in offshore oil industry, petrochemical industry, gas terminals and oil refineries," *IEEE Transactions on Industry Applications*, vol. 31, no. 5, pp. 1186–1196, 1995.

[102] ——, "Failure identification and analysis for high-voltage induction motors in the petrochemical industry," *IEEE Transactions on Industry Applications*, vol. 35, no. 4, pp. 810–818, 1999.

[103] P. J. Tavner and J. P. Hasson, "Predicting the design life of high integrity rotating electrical machines," in *IEE International Conference Electrical Machines and Drives (EMD)*, 1999.

[104] P. J. Tavner, G. J. W. Van Bussel, and F. Spinato, "Machine and converter reliabilities in wind turbines," in *IET International Conference Power Electronics Machines and Drives (PEMD)*, 2006.

[105] A. Cordoba-Arenas, J. Zhang, and G. Rizzoni, "Diagnostics and Prognostics Needs and Requirements for Electrified Vehicles Powertrains," *IFAC Proceedings Volumes*, vol. 46, no. 21, pp. 524–529, 2013.

[106] P. W. Thamke, N. M. Yewale, U. B. Vaidya, and G. Prashant, "Faults Associated With Permanent Magnet Synchronous Motor," *International Journal Of Core Engineering & Management (IJCEM)*, vol. 2, no. 3, pp. 211–217, 2015.

[107] J.-C. Urresty, J.-R. Riba, and L. Romeral, "A back-emf based method to detect magnet failures in PMSMs," *IEEE Transactions on Magnetics*, vol. 49, no. 1, pp. 591–598, 2013.

[108] J. Faiz and H. Nejadi-Koti, "Demagnetization Fault Indexes in Permanent Magnet Synchronous Motors-An Overview," *IEEE Transactions on Magnetics*, vol. 52, no. 4, 2016.

[109] J. Faiz and E. Mazaheri-Tehrani, "Demagnetization Modeling and Fault Diagnosing Techniques in Permanent Magnet Machines Under Stationary and Nonstationary Conditions: An Overview," *IEEE TRANSACTIONS ON INDUSTRY APPLICATIONS*, vol. 53, no. 3, pp. 2772–2785, 2017.

[110] J. Hong, S. Park, D. Hyun, T.-j. Kang, S. B. Lee, C. Kral, and A. Haumer, "Detection and Classification of Rotor Demagnetization and Eccentricity Faults for PM Synchronous Motors," *IEEE Transactions on Industry Applications*, vol. 48, no. 3, pp. 923–932, 2012.

[111] ISO10816-3, *Mechanical vibration - Evaluation of machine vibration by measurements on non-rotating parts - part 3: Industrial machines with nominal power above 15 kW and nominal speeds between 120 r/min and 15000 r/min.* ISO, 2009.

[112] Frost&Sullivan, "Importance of Condition Monitoring Unveiled," Frost&Sullivan Market Insight, July 2005, website Accessed: 17-08-2018. [Online]. Available: http://www.frost.com/sublib/display-market-insight.do?id=42013958

[113] Allen's Tri-State, "The Importance Of Condition Monitoring For Industrial Equipment," Allen's Tri-State Mechanical, January 2016, website accessed: 17-08-2018. [Online]. Available: http://www.allenstristate.com/the-importance-of-condition-monitoring-for-industrial-equipment/

[114] Scanimetrics, "Equipment condition monitoring of increasing importance," Scanimetrics News, website accessed: 17-08-2018. [Online]. Available: https://www.scanimetrics.com/index.php/scanimetrics-news-menu-item/12-methods-and-applications/268-equipment-condition-monitoring-of-increasing-importance

[115] R. Mocanu and A. Onea, "Determination of Stator Temperature for Thermal Protection in a Permanent Magnet Synchronous Machine," in *Mediterranean Conference on Control and Automation*, 2017, pp. 1321–1325.

[116] A. J. Rogers, "Distributed optical-fibre sensing," *Measurement Science and Technology*, vol. 10, no. 8, pp. R75–R99, 1999.

[117] D. J. T. Siyambalapitiya, P. G. McLaren, and P. J. Tavner, "Transient thermal characteristics of induction machine rotor cage," *IEEE Transactions on Energy Conversion*, vol. 3, no. 4, pp. 849–854, 1988.

[118] M. Fabian, D. M. Hind, C. Gerada, T. Sun, and K. T. V. Grattan, "Comprehensive Monitoring of Electrical Machine Parameters Using an Integrated Fiber Bragg Grating-Based Sensor System," *Journal of Lightwave Technology*, vol. 36, no. 4, SI, pp. 1046–1051, feb 2018.

[119] S. E. Zocholl, "Motor analysis and thermal protection," *IEEE Transactions on Power Delivery*, vol. 5, no. 3, pp. 1275–1280, 1990.

[120] P. Milanfar and J. H. Lang, "Monitoring the thermal condition of permanent-magnet synchronous motors," *IEEE Transactions Aerospace Electronic Systems*, vol. 32, no. 4, pp. 1421–1429, 1996.

[121] P. H. Mellor, D. Roberts, and D. R. Turner, "Lumped parameter thermal model for electrical machines of TEFC design," *IEE Proceedings B - Electric Power Applications*, vol. 138, no. 5, pp. 205–218, 1991.

[122] G. B. Brandt and M. Gottlieb, "Fiber optic temperature sensors using optical fibers," *Abstracts of Papers of the American Chemical Society*, vol. 184, p. 64, 1982.

[123] C. C. Carson, S. C. Barton, and F. S. Echeverria, "Immediate warning of local overheating in electrical machines by the detection of pyrolysis products," *IEEE Transactions on Power Application Systems*, vol. 92, pp. 533–542, 1973.

[124] P. J. Tavner, B. G. Gaydon, and D. M. Ward, "Monitoring generators and large motors," *IEE Proceedings B - Electric Power Applications*, vol. 133, no. 3, pp. 169–180, 1986.

[125] D. M. Ryder, J. W. Wood, and P. L. Gallagher, "The detection and identification of overheated insulation in turbo-generators," *IEEE Transactions on Power Application Systems*, vol. 98, no. 7, pp. 333–336, 1979.

[126] D. J. A. Dear, A. F. Dillon, and A. N. Freedman, "Determination of organic compounds in the hydrogen used for cooling large electricity generators," *Journal of Chromatograms*, vol. 137, pp. 315–322, 1977.

[127] J. K. Kelley, J. W. Auld, V. J. Herter, K. A. Hutchinson, and W. A. Rugenstein, "Early detection and diagnosis of overheating problems in turbine generators by instrumental chemical analysis," *IEEE Transactions on Power Application Systems*, vol. 95, no. 3, pp. 879–886, 1976.

[128] R. Bowen, D. Scott, W. Siefert, and V. C. Westcott, "Ferrography," *Tribology International*, vol. 9, no. 3, pp. 109–115, 1976.

[129] I. W. Mayes, "Use of neutral networks for online vibration monitoring," *Proceedings of the Institution of Mechanical Engineers, Part A: Journal of Power and Energy*, vol. 208, no. A4, pp. 267–274, 1994.

[130] R. G. Herbert, "Computer techniques applied to the routine analysis of run-down vibration data for condition monitoring of turbine-alternators," *British Journal of non-destructive testing*, vol. 28, no. 6, pp. 371–375, 1986.

[131] S. A. S. Al Kazzaz and G. K. Singh, "Experimental investigations on induction machine condition monitoring and fault diagnosis using digital signal

processing techniques," *Electric Power Systems Research*, vol. 65, no. 3, pp. 197–221, 2003.

[132] G. K. Singh and S. A. S. Al Kazzaz, "Vibration signal analysis using wavelet transform for isolation and identification of electrical faults in induction machine," *Electric Power Systems Research*, vol. 68, no. 1, pp. 119–136, 2004.

[133] D. N. Walker, S. L. Adams, and R. J. Placek, "Torsional vibration and fatigue of turbine-generator shafts," *IEEE Transactions on Power Apparatus and Systems*, vol. 100, no. 11, pp. 4373–4380, 1981.

[134] A. Y. Ben Sasi, F. Gu, Y. Li, and A. D. Ball, "A validated model for the prediction of rotor bar failure in squirrel-cage motors using instantaneous angular speed," *Journal for Mechanical Systems and Signal Processing*, vol. 20, pp. 1572–1589, 2006.

[135] B. Corne, B. Vervisch, S. Derammelaere, J. Knockaert, and J. Desmet, "Emulating single point bearing faults with the use of an active magnetic bearing," *IET Science, Measurement & Technology*, vol. 12, no. 1, pp. 39–48, 2018.

[136] N. Tandon and B. C. Nakra, "Comparison of vibration and acoustic measurement techniques for the condition monitoring of rolling element bearings," *Tribology International*, vol. 25, no. 3, pp. 205–212, 1992.

[137] N. Tandon, G. S. Yadava, and K. M. Ramakrishna, "A comparison of some condition monitoring techniques for the detection of defect in induction motor ball bearings," *Mechanical Systems and Signal Processing*, vol. 21, no. 1, pp. 244–256, 2007.

[138] J. R. Stack, T. G. Habetler, and R. G. Harley, "Fault classification and fault signature production for rolling element bearings in electric machines," *IEEE Transactions on Industry Applications*, vol. 40, no. 3, pp. 735–739, 2004.

[139] M. R. Shahriar, P. Borghesani, and A. C. C. Tan, "Electrical Signature Analysis-Based Detection of External Bearing Faults in Electromechanical Drivetrains," *IEEE Transactions on Industrial Electronics*, vol. 65, no. 7, pp. 5941–5950, jul 2018.

[140] E. M. H. Kamerbeek, "Torque measurements on induction motors using Hall generators or measuring windings," *Philips Technology Revision*, vol. 34, no. 7, pp. 152–162, 1974.

[141] D. R. Albright, "Inter-turn short circuit detector for turbine generator rotor windings," *IEEE Transactions on Power Application Systems*, vol. 50, pp. 478–483, 1971.

[142] C. Hargis, "Steady-state analysis of 3-phase cage motors with rotor-bar and end-ring faults," *IEE Proceedings B - Electric Power Applications*, vol. 130, no. 3, pp. 225–225, 1983.

[143] M. Jufer and M. Abdulaziz, "Influence d'une rupture de barre ou d'un anneau sur les characteristiques externes d'un moteur asynchrone a cage," *Bulletin SEV/VSE Switzerland*, vol. 69, no. 17, 1978.

[144] W. T. Thomson and M. Fenger, "Current signature analysis to detect induction motor faults," *IEEE Industry Applications Magazine*, vol. 7, no. 4, pp. 26–34, 2001.

[145] J. L. Kohler, J. Sottile, and F. C. Trutt, "Condition monitoring of stator windings in induction motors. II. Experimental investigation of voltage mismatch detectors," *IEEE Transactions on Industry Applications*, vol. 38, no. 5, pp. 1454–1459, 2002.

[146] H. Jordan and K. Kovacs, "Messungen des schlupfes von asynchronmaschinen mit einer spule," *Elektrotech. Z.*, vol. 86, pp. 294–296, 1965.

[147] M. S. Erlicki, Y. Porat, and A. Alexandrovitz, "Leakage field changes of an induction motor as indication of nonsymmetric supply," *lEEE Trans. Gen. Appl.*, vol. 7, no. 6, pp. 713–717, 1971.

[148] C. D. Rickson, "Protecting motors from overload due to asymmetrical fault conditions," *Electrical Revision*, pp. 778–780, 1983.

[149] J. Penman, G. Hadwick, and A. F. Stronach, "Protection strategy against faults in electrical machines," in *IEE International Conference on Developments in Power System Protection*, 1980.

[150] A. M. Trzynadlowski, M. Ghassemzadeh, and S. F. Legowski, "Diagnostics of mechanical abnormalities in induction motors using instantaneous electric power," *IEEE Transactions on Energy Conversion*, vol. 14, no. 4, pp. 1417–1423, 1999.

[151] D. J. Hunter, P. J. Tavner, D. M. Ward, and D. S. Benaragama, "Measurements of the harmonic components of the instantaneous electrical power delivered at the terminals of a 500 MW turbogenerator," in *IEE International Conference on Sources and Effects of Power System Disturbances*, 1982.

[152] R. Giussani, L. Renforth, M. Seltzer-Grant, and C. Zachariades, "A Holistic Combined Electrical and Mechanical Condition Monitoring Technique for Oil and Gas High Voltage Rotating Machines," in *IEEE Electrical Insulation Conference (EIC)*. IEEE, 2015, pp. 283–287.

[153] R. T. Harrold, F. T. Emery, F. J. Murphy, and S. A. Drinkut, "Radio frequency sensing of incipient arcing faults within large turbine generators," *IEEE Transactions on Power Application Systems*, vol. 98, no. 4, pp. 1167–1173, 1979.

[154] F. T. Emery, B. N. Lenderking, and R. D. Couch, "Turbine- generator on-line diagnostics using RF monitoring," *IEEE Transactions on Power Application Systems*, vol. 100, no. 12, pp. 4974–4982, 1981.

[155] R. T. Harrold and F. T. Emery, "Radio frequency diagnostic monitoring of electrical machines," *IEEE Electrical Insulation Magazine*, vol. 2, no. 2, pp. 18–24, 1986.

[156] M. Kurtz and G. C. Stone, "In-service partial discharge testing of generator insulation," *IEEE Transactions on Electrical Insulation*, vol. 14, no. 2, pp. 94–100, 1979.

[157] M. Kurtz, G. C. Stone, D. Freeman, V. R. Mulhall, and P. Lonseth, "Diagnostic testing of generator insulation without service interruption," *CIGRE*, 1980.

[158] G. C. Stone, H. G. Sedding, N. Fujimoto, and J. M. Braun, "Practical implementation of ultrawideband partial dischargedetectors," *IEEE Transactions on Electrical Insulation1*, vol. 27, no. 1, pp. 70–81, 1992.

[159] A. Romanenko, A. Muetze, and J. Ahola, "Incipient Bearing Damage Monitoring of 940-h Variable Speed Drive System Operation," *IEEE Transaction on Energy Conversion*, vol. 32, no. 1, pp. 99–110, 2017.

[160] G. C. Stone and J. Kapler, "Condition-based maintenance for the electrical windings of large motors and generators," in *IEEE Pulp and Paper Conference*, 1997, pp. 57–63.

[161] M. E. H. Benbouzid and H. Nejjari, "A simple fuzzy logic approach for induction motors stator condition monitoring," in *IEEE Electric Machines and Drives Conference*, 2001, pp. 634–639.

[162] S. Caldara, S. Nuccio, G. R. Galluzzo, and M. Trapanese, "A fuzzy diagnostic system: application to linear induction motor drives," in *IEEE Instrumentation and Measurement Technology Conference*, 1997, pp. 257–262.

[163] F. Filippetti, G. Franceschini, and C. Tassoni, "Neural networks aided online diagnostics of induction motor rotor faults," *IEEE Transactions on Industry Applications*, vol. 31, no. 4, pp. 892–899, 1995.

[164] J. Penman and C. M. Yin, "Feasibility of using unsupervised learning, artificial neural networks for the condition monitoring of electrical machines,"

IEE Proceedings B - Electric Power Applications, vol. 141, no. 6, pp. 317–322, 1994.

[165] J. Ben Ali, L. Saidi, S. Harrath, E. Bechhoefer, and M. Benbouzid, "Online automatic diagnosis of wind turbine bearings progressive degradations under real experimental conditions based on unsupervised machine learning," *Applied Acoustics*, vol. 132, pp. 167–181, 2018.

[166] D. Train, *IEEE Guide for Diagnostic Field Testing of Electric Power Apparatus- Part 1 : Oil Filled Power Transformers , Regulators , and Reactors*. IEEE, 2005, vol. 1995.

[167] J.-C. Urresty, R. Atashkhooei, J.-R. Riba, L. Romeral, and S. Royo, "Shaft Trajectory Analysis in a Partially Demagnetized Permanent-Magnet Synchronous Motor," *IEEE Transactions on Industrial Electronics*, vol. 60, no. 8, pp. 3454–3461, aug 2013.

[168] Z. Hou, J. Huang, H. Liu, Z. Liu, M. Ye, and J. Yang, "No-load losses based method to detect demagnetisation fault in permanent magnet synchronous motors with parallel branches," *IET Electric Power Applications*, vol. 11, no. 3, pp. 471–477, 2017.

[169] S. Rajagopalan, W. le Roux, T. G. Habetler, and R. G. Harley, "Dynamic eccentricity and demagnetized rotor magnet detection in trapezoidal flux (Brushless DC) motors operating under different load conditions," *IEEE Transactions on Power Electronics*, vol. 22, no. 5, pp. 2061–2069, sep 2007.

[170] M. Karami, N. Mariun, M. R. Mehrjou, M. Z. A. Ab Kadir, N. Misron, and M. A. M. Radzi, "Static Eccentricity Fault Recognition in Three-Phase Line Start Permanent Magnet Synchronous Motor Using Finite Element Method," *Mathematical Problems in Engineering*, 2014.

[171] C. Ruschetti, C. Verucchi, G. Bossio, C. De Angelo, and G. Garcia, "Rotor demagnetization effects on permanent magnet synchronous machines," *Energy Conversion and Management*, vol. 74, pp. 1–8, 2013.

[172] W. Le Roux, R. G. Harley, and T. G. Habetler, "Detecting Rotor Faults in Low Power Permanent Magnet Synchronous Machines," *IEEE Transactions on Power Electronics*, vol. 22, no. 1, pp. 322–328, jan 2007.

[173] T. Goktas, M. Zafarani, and B. Akin, "Discernment of Broken Magnet and Static Eccentricity Faults in Permanent Magnet Synchronous Motors," *IEEE Transactions on Energy Conversion*, vol. 31, no. 2, pp. 585–594, 2016.

[174] "Direct-quadrature-zero transformation," Wikipedia, April 2018, website accessed: 03-08-2018. [Online]. Available: https://en.wikipedia.org/wiki/Direct-quadrature-zero_transformation

[175] J. Hong, D. Hyun, S. B. Lee, J.-Y. Yoo, and K.-W. Lee, "Automated Monitoring of Magnet Quality for Permanent-Magnet Synchronous Motors at Standstill," *IEEE Transactions on Industry Applications*, vol. 46, no. 4, pp. 1397–1405, 2010.

[176] J. R. Riba Ruiz, J. A. Rosero, A. Garcia Espinosa, and L. Romeral, "Detection of demagnetization faults in permanent-Magnet synchronous motors under nonstationary conditions," *IEEE Transactions on Magnetics*, vol. 45, no. 7, pp. 2961–2969, 2009.

[177] T. Ishikawa, Y. Seki, and N. Kurita, "Analysis for Fault Detection of Vector-Controlled Permanent Magnet Synchronous Motor With Permanent Magnet Defect," *IEEE Transactions on Magnetics*, vol. 49, no. 5, pp. 2331–2334, 2013.

[178] A. G. Espinosa, J. A. Rosero, J. Cusid, L. Romeral, and J. A. Ortega, "Fault Detection by Means of Hilbert Huang Transform of the Stator Current in a PMSM With Demagnetization," *IEEE Transactions on Energy Conversion*, vol. 25, no. 2, pp. 312–318, 2010.

[179] M. Delgado Prieto, A. Garcia Espinosa, J.-R. Riba Ruiz, J.-C. Urresty, and J. Antonio Ortega, "Feature Extraction of Demagnetization Faults in Permanent-Magnet Synchronous Motors Based on Box-Counting Fractal Dimension," *IEEE Transactions on Industrial Electronics*, vol. 58, no. 5, pp. 1594–1605, 2011.

[180] J. Rosero Garcia, J. Luis Romeral, and E. Rosero Garcia, "Detecting eccentricity faults in a PMSM in non-stationary conditions," *Ingenieria e Investigacion*, vol. 32, no. 1, pp. 5–10, apr 2012.

[181] K.-T. Kim, Y.-S. Lee, and J. Hur, "Transient Analysis of Irreversible Demagnetization of Permanent-Magnet Brushless DC Motor With Interturn Fault Under the Operating State," *IEEE Transactions on Industry Applications*, vol. 50, no. 5, pp. 3357–3364, 2014.

[182] Y.-S. Lee, K.-T. Kim, and J. Hur, "Finite-Element Analysis of the Demagnetization of IPM-Type BLDC Motor With Stator Turn Fault," *IEEE Transactions on Magnetics*, vol. 50, no. 2, feb 2014.

[183] J. A. Farooq, A. Djerdir, and A. Miraoui, "Analytical Modeling Approach to Detect Magnet Defects in Permanent-Magnet Brushless Motors," *IEEE Transactions on Magnetics*, vol. 44, no. 12, pp. 4599–4604, dec 2008.

[184] ——, "Identification of demagnetization faults in a permanent magnet synchronous machine by permeance network," *International Journal for Computation and Mathematics in Electrical and Electronic Engineering (COMPEL)*, vol. 28, no. 6, pp. 1619–1631, 2009.

[185] J.-C. Urresty, J.-R. Riba, M. Delgado, and L. Romeral, "Detection of Demagnetization Faults in Surface-Mounted Permanent Magnet Synchronous Motors by Means of the Zero-Sequence Voltage Component," *IEEE Transactions on Energy Conversion*, vol. 27, no. 1, pp. 42–51, 2012.

[186] J.-C. Urresty, J.-R. Riba, and L. Romeral, "Influence of the Stator Windings Configuration in the Currents and Zero-Sequence Voltage Harmonics in Permanent Magnet Synchronous Motors With Demagnetization Faults," *IEEE Transactions on Magnetics*, vol. 49, no. 8, 2, pp. 4885–4893, aug 2013.

[187] R. Z. Haddad, C. A. Lopez, S. N. Foster, and E. G. Strangas, "A Voltage-Based Approach for Fault Detection and Separation in Permanent Magnet Synchronous Machines," *IEEE Transactions on Industry Applications*, vol. 53, no. 6, pp. 5305–5314, 2017.

[188] J. F. Bangura, R. J. Povinelli, N. A. O. Demerdash, and R. H. Brown, "Diagnostics of eccentricities and bar/end-ring connector breakages in polyphase induction motors through a combination of time-series data mining and time-stepping coupled FE-State-Space techniques," *IEEE Transactions on Industry Applications*, vol. 39, no. 4, pp. 1005–1013, 2003.

[189] H. A. Toliyat and G. B. Kliman, *Handbook of Electric Motors*. Marcel Dekker, 2004.

[190] A. Hemeida, B. Hannon, and P. Sergeant, "Comparison of three analytical methods for the precise calculation of cogging torque and torque ripple in axial PM machines," *Mathematical Problems in Engineering*, pp. 1–14, 2016.

[191] H. Vansompel, P. Sergeant, and L. Dupré, "A Multilayer 2-D 2-D Coupled Model for Eddy Current Calculation in the Rotor of an Axial-Flux PM Machine," *IEEE Transactions on Energy Conversion*, vol. 27, no. 3, pp. 784–791, 2012.

[192] X. Tang, X. Wang, Y. Li, and Y. Yang, "Study on Demagnetization of Permanent Magnets in Line-start Permanent Magnet Synchronous Motors During Starting Process," *IEEE Transactions on Energy Conversion*, p. 8, 2014.

[193] B. Hannon, P. Sergeant, and L. Dupré, "2-D Analytical Subdomain Model of a Slotted PMSM With Shielding Cylinder," *IEEE Transactions on Magnetics*, vol. 50, no. 7, pp. 1–10, 2014.

[194] Y. Yang, B. Yan, N. Wang, and X. Wang, "Analytical Prediction of Electromagnetic Performance of Vernier Machine with Rotor Eccentricity," *Electric Power Components and Systems*, vol. 44, no. 15, pp. 1693–1706, 2016.

[195] T. F. Chan, L. L. Lai, and S. Xie, "Field Computation for an Axial Flux Permanent-Magnet Synchronous Generator," *IEEE Transactions on Energy Conversion*, vol. 24, no. 1, pp. 1–11, 2009.

[196] D. Zarko, D. Ban, and T. A. Lipo, "Analytical Calculation of Magnetic Field Distribution in the Slotted Air Gap of a Surface Permanent-Magnet Motor Using Complex Relative Air-Gap Permeance," *IEEE Transactions on Magnetics*, vol. 42, no. 7, pp. 1828–1837, 2006.

[197] N. Bianchi and M. Dai Pré, "Use of the star of slots in designing fractional-slot single-layer synchronous motors," *IEEE Transactions on Power Electronics*, vol. 153, no. 3, pp. 459–466, 2006.

[198] J. Pyrhönen, T. Jokinen, and V. Hrabovcva, *Design of Rotating Electrical Machines*. Wiley, 2008.

[199] H. Jussila, *Concentrated Winding Multiphase Permanent Magnet Machine Design and Electromagnetic PropertiesCase Axial Flux Machine*. Lappeenranta University of Technology, 2009.

[200] A. Hemeida, P. Sergeant, A. Rasekh, H. Vansompel, and J. Vierendeels, "An Optimal Design of a 5MW AFPMSM for Wind Turbine Applications Using Analytical Model," in *International Conference on Electrical Machines (ICEM)*, 2016, pp. 1290–1297.

[201] A. M. A.-E. Abdallh, G. Crevecoeur, and L. Dupré, "Selection of measurement modality for magnetic material characterization of an electromagnetic device using stochastic uncertainty analysis," *IEEE Transactions on Magnetics*, vol. 47, no. 11, pp. 4564–4573, nov 2011.

[202] "Optimization decision table," MathWorks, website accessed: 31-08-2018. [Online]. Available: https://nl.mathworks.com/help/optim/ug/optimization-decision-table.html

[203] "Quadratic programming," MathWorks, website accessed: 31-08-2018. [Online]. Available: https://nl.mathworks.com/help/optim/ug/quadprog.html

[204] S. Nassirpour, P. Chang, A. Fillmer, and A. Henning, "A comparison of optimization algorithms for localized in vivo B-0 shimming," *Magnetic Resonance in Medicine*, vol. 79, no. 2, pp. 1145–1156, feb 2018.

[205] B. Morini and M. Porcelli, "TRESNEI, a Matlab trust-region solver for systems of nonlinear equalities and inequalities," *Computational Optimization and Applications*, vol. 51, no. 1, pp. 27–49, jan 2012.

[206] T. Montanher, A. Neumaier, and F. Domes, "A computational study of global optimization solvers on two trust region subproblems," *Journal of Global Optimization*, vol. 71, no. 4, SI, pp. 915–934, aug 2018.

[207] E. Segredo, B. Paechter, C. Segura, and C. I. Gonzalez-Vila, "On the comparison of initialisation strategies in differential evolution for large scale optimisation," *Optimization Letters*, vol. 12, no. 1, pp. 221–234, jan 2018.

[208] R. M. Lima and I. E. Grossmann, "On the solution of nonconvex cardinality Boolean quadratic programming problems: a computational study," *Computational Optimization and Applications*, vol. 66, no. 1, pp. 1–37, jan 2017.

[209] E. G. Birgin and J. M. Gentil, "Evaluating bound-constrained minimization software," *Computational Optimization and Applications*, vol. 53, no. 2, SI, pp. 347–373, 2012.

[210] S. Pan, T. Tan, and Y. Jiang, "A global continuation algorithm for solving binary quadratic programming problems," *Computational Optimization and Applications*, vol. 41, no. 3, pp. 349–362, dec 2008.

[211] "Choosing the algorithm," Mathworks, 2018, website accessed: 06-02-2019. [Online]. Available: https://nl.mathworks.com/help/optim/ug/choosing-the-algorithm.html

[212] B. Hannon, P. Sergeant, and L. Dupré, "Harmonic Study of a Diametrically-Wound Permanent-Magnet Synchronous Machine," *IEEE Young Researcher Symposium*, 2014.

[213] B. Hannon, P. Sergeant, and L. Dupre, "Time- and Spatial-Harmonic Content in Synchronous Electrical Machines," *IEEE Transactions on Magnetics*, vol. 53, no. 3, 2017.

[214] "Likelihood function," Wikipedia, June 2018, website accessed: 28-08-2018. [Online]. Available: https://en.wikipedia.org/wiki/Likelihood_function

[215] "Maximum likelihood estimation," Wikipedia, July 2018, website accessed: 28-08-2018. [Online]. Available: https://en.wikipedia.org/wiki/Maximum_likelihood_estimation

[216] "Score (statistics)," Wikipedia, August 2018, website accessed: 28-08-2018. [Online]. Available: https://en.wikipedia.org/wiki/Score_(statistics)

[217] "Leibniz integral rule)," Wikipedia, December 2018, website accessed: 28-12-2018. [Online]. Available: https://en.wikipedia.org/wiki/Leibniz_integral_rule

[218] M. A. A. Abdallh, G. Crevecoeur, and L. Dupré, "Optimal needle placement for the accurate magnetic material quantification based on uncertainty analysis in the inverse approach," *Measurement Science & Technology*, vol. 21, no. 11, p. 16, 2010.

[219] A. M. A. Abdallh, "An inverse problem based methodology with uncertainty analysis for the identification of magnetic material characteristics of electromagnetic devices," Ph.D. dissertation, Ghent University, 2012.

[220] "Cramér-Rao bound," Wikipedia, August 2018, website accessed: 28-08-2018. [Online]. Available: https://en.wikipedia.org/wiki/Cramér-Rao_bound

[221] G. Goodwin and R. Payne, "Dynamic system identification. experiment design and data analysis," *Mathematics in Science and Engineering*, vol. 136, 1977.

[222] A. A.-E. Abdallh and L. Dupre, "Local magnetic measurements in magnetic circuits with highly non-uniform electromagnetic fields," *Measurement Science and Technology*, vol. 21, no. 4, apr 2010.

[223] K. Abbaszadeh and A. Rahimi, "Analytical quasi 3D modeling of an axial flux PM motor with static eccentricity fault," *Scientia Iranica*, vol. 22, no. 6, pp. 2482–2491, 2015.

[224] J. De Bisschop, H. Vansompel, P. Sergeant, and L. Dupré, "Demagnetization Fault Detection in Axial Flux PM Machines by using Sensing Coils and an Analytical Model," *IEEE Transactions on Magnetics*, vol. 53, no. 6, pp. 1–4, 2017.

[225] V. Simon-Sempere, M. Burgos-Payan, and J.-R. Cerquides-Bueno, "Influence of Manufacturing Tolerances on the Electromotive Force in Permanent-Magnet Motors," *IEEE Transactions on Magnetics*, vol. 49, no. 11, pp. 5522–5532, nov 2013.

[226] A. A.-E. Abdallh, G. Crevecoeur, and L. Dupre, "A Robust Inverse Approach for Magnetic Material Characterization in Electromagnetic Devices With Minimum Influence of the Air-Gap Uncertainty," *IEEE Transactions on Magnetics*, vol. 47, no. 10, pp. 4364–4367, 2011.

[227] J. De Bisschop, A. Abdallh, P. Sergeant, and L. Dupré, "Identification of demagnetization faults in axial flux permanent magnet synchronous machines using an inverse problem coupled with an analytical model," *IEEE Transactions on Magnetics*, vol. 50, no. 11, pp. 1–4, 2014.

[228] H. Vansompel, P. Sergeant, and P. Leijnen, "Stator for an axial flux machine and method for producing the same," Patent WO2018/015 293, 2018.

[229] H. Vansompel, P. Leijnen, and P. Sergeant, "Multiphysics Analysis of a Stator Construction Method in Yokeless and Segmented Armature Axial Flux PM Machines," *IEEE Transactions on Energy Conversion*, vol. 34, no. 1, pp. 139–146, 2019.

[230] M. Yang, X. Lang, J. Long, and D. Xu, "Flux immunity robust predictive current control with incremental model and extended state observer for pmsms drive," *IEEE Transactions on Power Electronics*, vol. 32, no. 12, pp. 9267–9279, 2017.